THE UNIVERSITY *of* EDINBURGH

Colloidal Cluster Phases and Solar Cells

Alastair Mailer

Doctor of Philosophy
The University of Edinburgh
2012

Abstract

The arrangement of soft materials through solution processing techniques is a topic of profound importance for next generation solar cells; the resulting morphology has a major influence on construction, performance and lifetime. This thesis investigates the connections between the soft matter physics of colloidal systems and solid state dye sensitised (SSDS) and bulk heterojunction (BHJ) solar cells.

A study of aqueous titanium dioxide nanoparticulate suspensions was carried out in order to observe how suspension structure can be controlled by altering the inter-colloid potential via pH-induced electrostatic charging. Measurements were performed at volume fractions between 0.025% and 8.2% with the solution pH set to 3.1, 3.5 or 4.5 before mixing. Suspensions with a volume fraction above 4% formed self-supporting gels regardless of the set pre-mix pH. These gels displayed shear thinning behaviour with a power law exponent of 0.8, a yield stress of 11(1) Pa and rheological response consistent with an aggregated fractal network. At lower volume fractions, suspensions exhibited consolidation interpreted as the collapse of a gel of fractal clusters with a fractal dimension of 2.36. The velocity of the suspension/supernatant interface exhibited delayed sedimentation behaviour, as well as further fractal-based power law scalings with volume fraction. Lower volume fraction suspensions were explored using dynamic light scattering. Limited aggregation of 'stable' suspensions was observed when compared to primary aggregate radii measured from electron microscopy images.

To connect suspension structure and cell manufacture, the behaviour of more concentrated suspensions was observed during the drying of thin films, a process which forms an essential part of a SSDS solar cell. Lowering the pH of the suspension after mixing from 4 to 3 resulted in an ordering of observed crack domains. An increase in film delamination was also observed. Rates of mass loss during drying followed the expected three phase process, although there was

an unexpected increase in rate during the initial phase (where rate is usually constant in time).

Dynamic light scattering was found to be a useful but demanding technique for studying cluster formation in titanium dioxide suspensions. A non-linear fitting technique utilising the method of moments was thoroughly explored using computer simulated datasets. The algorithm reduced the systematic error in fitted parameters for moderately polydisperse ($0.2 < \sigma < 0.4$) datasets as compared to the commonly applied linear algorithm. The fitting algorithm was also robust to bad initial estimates of parameters.

Finally, test solar cells have been built using blends of titanium dioxide and poly-3-hexylthiophene. Device performance was reduced with blend standing time after mixing but could be improved by remixing the blend before spin coating, implicating a reversible process (e.g. aggregation of titanium dioxide or crystallisation of P3HT) in the loss of performance. Addition of a titanium dioxide hole blocking layer before spin coating reduced cell performance. Combining the above studies and these device designs provides a future platform for continuation of this work in the context of real devices.

Declaration

I declare that this thesis was composed by myself, that the work contained herein is my own except where explicitly stated otherwise in the text, and that this work has not been submitted for any other degree or professional qualification except as specified.

(*Alastair Mailer*)

Acknowledgements

There are many people who I wish to thank for their help and support throughout the execution of the work which this thesis represents:

- My supervisor, Paul Clegg, for his guidance, assistance and support throughout this project.
- The students and staff of the Robertson Group, at the School of Chemistry, for their help with characterising my test cells and making me feel welcome in a new workplace. Most particularly I would like to thank Charlotte Linfoot, for her clear instruction in cell construction and characterisation techniques.
- Peter Pusey, for introducing me to the dynamic light scattering technique and its application to polydisperse systems.
- Michael Butler, of the University of the West of Scotland, for help with the profilometry measurements.
- Andrew Garrie, for his technical assistance in evaporative deposition.
- Patrick Nicholson, Fernando Castro and Alan Turbull at the National Physical Laboratory, Teddington, for access to equipment and useful discussions about solar cells.
- The Engineering and Physical Sciences Research Council and National Physical Laboratory, Teddington, for their financial support.
- My postgraduate peers in the School of Physics, for stimulating discussion, camaraderie and nachos.
- My parents, for their understanding and support through it all.

Contents

List of Figures

List of Tables

Chapter 1

Introduction

Interest in renewable energy sources, including solar energy technologies, is rising rapidly across the world as economic, social and environmental pressures expose major problems with the long term viability of fossil fuel sources. To achieve significant reductions in our dependence on fossil fuels will require inexpensive renewable technologies. First generation (silicon) solar photovoltaics have now become a mature and widespread technology, ubiquitous in applications from pocket calculators to space stations. However, improvements in these cells are now incremental, with cost reductions now primarily tied to economies of scale and material supply despite intensive research in the area. The best cells in use today can generate a price per peak kilowatt-hour of US$ 0.20 – US$ 0.80, compared to US$ 0.10 for wholesale electricity [47]. Thin-film photovoltaic technology attempts to address this problem by reducing the amount of material required in a cell, but these cells require components constructed from scarce materials and processing at high vacuum, which still contribute significantly to costs. Given this, it is difficult to see how current solar technologies can achieve cost parity with conventional power sources.

The last twenty years have seen several new concepts emerge in the field, igniting a widespread surge in research. By using cheap materials and low temperature production techniques which do not require a vacuum, significant reductions in production cost are possible. Due to the strong influence of interfacial interactions between components in these new cells on performance there are opportunities for soft condensed matter research to make useful contributions to the understanding required to optimise these devices [91]. This thesis aims to explore these routes

to cheap and efficient solar cells utilising two of the new design concepts in the field, with an emphasis on heading towards completed cells.

The **Dye Sensitised Solar Cell (DSSC)** concept emerged [75] in 1991, with research led by Michael Grätzel at the EPFL, Lausanne [78], although the basic principles of operation had been known about since the 19th century. By abandoning silicon and the crystalline semiconductor junction concept and instead using nanocolloidal titanium dioxide and solution processing techniques production costs have been significantly reduced. Although rapid progress has been achieved, with cell power conversion efficiencies now above 10% [42] (often seen as the threshold for commercial development) these cells still lag behind silicon cell efficiencies (ca. 20%) and suffer from long-term stability problems due to the need to encapsulate volatile solvents.

The **Bulk Heterojunction (BHJ)** concept [17] also emerged in the 1990s through concurrent studies at Cambridge, Santa Barbara and Osaka. A BHJ cell is fabricated from a blend of components in solution, as opposed to the DSSC in which a rigid porous layer of one component is fabricated first and backfilled with the second. This has the advantage that all processing occurs directly in solution and therefore can be achieved using similar technologies as are currently used in the plastic film industry. An added benefit is the possibility of producing flexible and coloured films which increase the possible applications of this technology.

Research work in this area proceeds under three broad drivers: synthesis of new materials, understanding of how these materials are combined into cells and understanding of the fundamental processes which result in photovoltaic action. All three areas act synergistically to allow advance in device design; understanding of fundamental processes informs and is informed by gaining control over device assembly processes, both of which are implemented practically using appropriately designed synthetic materials. At the heart of the operation of DSSCs and BHJ cells are the shapes of the two phases and the nature of the interface between them. The nature of the charge photogeneration process demands control of these shapes on the length scale of tens of nanometers. In BHJ cells, this is the diffusion length scale set by the lifetime of photo-excited electronic states in the blended materials (ca. 20 nm). In DSSCs, this is the length scale which balances the need to allow diffusive transport of electrolyte ions away from the dye and the need to incorporate as much sensitised interface per unit volume as possible. Accordingly, scientists working with nanoscopic colloids and interfaces are beginning to contribute to the debate over how to

raise device efficiencies [2, 47, 77, 90, 91, 96].

This thesis investigates the colloidal interactions which affect the behaviour and structure of aqueous solutions of titanium dioxide, a semiconducting material used widely to conduct research into these technologies [17]. Chapter 2 discusses the properties of this material in suspension, a form in which it can be easily manipulated and processed and which ultimately affects the final structure of cells. Chapter 3 investigates the behaviour of these suspensions as they are dried to form a solid porous structure; the structure formed during this process is essential for DSSC operation and strongly affects the performance characteristics of the cell. Chapter 4 investigates dynamic light scattering, a powerful technique for examining the dynamic structure of suspensions on scales well below the diffraction limit of light. Finally, chapter 5 relates an approach to the task of applying the knowledge gained in previous chapters to real devices and the challenges of reliable cell construction.

Recently, governments across the world (including in the UK) have indicated a serious economic commitment to developing solar power as a viable large-scale energy source[1]. Industrial production of DSSCs for micro- and macrogeneration has begun in Australia, Japan and the UK. The evidence points to DSSC and BHJ cells playing a significant role in the move away from a fossil fuel-based energy market. The intense level of research in the area and the rate of progress in cell efficiency over the last 20 years demonstrates that there is still important work to be done in the field.

[1]See *The Guardian*: 'China puts its faith in solar power with huge renewable investment', 26 May 2009; 'Sunnier times ahead for solar energy as MPs back tariff boost for photovoltaic power', 15 June 2009.

Chapter 2

Self Assembly of Colloidal Titanium Dioxide

Colloidal titanium dioxide is an important component of many industrial systems, electrochemical and otherwise. In a photoelectrochemical cell, it usually forms the electron accepting electrode. Titanium dioxide is well suited to be an electrode material; it is semiconducting with a deep valence band, cheap, non-toxic, chemically stable, environmentally friendly and transparent to much of the solar spectrum, preventing light being absorbed in the wrong part of the cell. In colloidal form, it becomes easy to solution process.

One route to producing new functionality in a material is to change its structure. Changing material structure on the atomic scale (e.g. controlling individual molecules on length scales of a nanometer or less) is difficult due to the energies and resolutions of manipulation required. Colloidal processing opens up new opportunities for the control of self-assembly due to the rescaling of characteristic lengths and times to much more accessible regimes.

Colloids have been described in many textbooks [31, 49, 57]. As a summary, a colloidal mixture is a mix of two phases (solid in liquid, solid in gas, liquid in gas etc.) in which the dimensions of the domains of one phase are in the range 10 nm to 10 000 nm, small enough that Brownian motion is important, yet large enough that the discrete nature of the medium they are suspended in can be averaged out to a continuum.

The current drive towards producing commercially viable photoelectrochemical

photovoltaics is motivated by the discovery that replacing a single, flat electrode with a porous electrode structured on mesoscopic (e.g. colloidal) length scales vastly improved the efficiency of these cells [41]. Now that the concept of the system has been proved, part of the process of optimisation is in understanding the colloidal interactions which produce the porous film that has made this a viable PV technology.

This chapter will detail how studying the self assembly of an aqeuous colloidal titanium dioxide system was approached. In section 2.1 the material properties of titanium dioxide and the science of colloidal systems will be introduced. The titanium dioxide pastes used in screen-printed and doctor-bladed cell electrodes demonstrate gel-like properties and therefore this basic colloidal science will be extended to explore the structures and processes behind gel formation. The materials and methods used to undertake this study are described in section 2.2, and the results of the study presented in section 2.3. Finally, I will undertake some discussion of these results and their implications for solar cell technology in sections 2.4 and 2.5.

2.1 Introduction and Theory

2.1.1 Titanium Dioxide

Titanium dioxide is also known as titanium(IV) oxide and also by the less formal name titania. Three allotropes of titania appear naturally; anatase, brookite and rutile. The physical properties of each appear below [72]:

Table 2.1 *Data on the physical properties of the allotropes of titanium(IV) oxide, from the CRC Handbook of Chemistry and Physics. Densities (ρ) and refractive indices (n) may vary between samples by up to ten percent. MP = melting point. Note: Rutile is birefringent with an extraordinary refractive index of 2.9.*

Allotrope	Structure	ρ/g cm^{-3}	MP / °C	n
Anatase	tetragonal	3.9	1560	2.5
Brookite	orthorhombic	4.2		2.6
Rutile	tetragonal	4.2	1843	2.6*

At room temperature and pressure titania is a bright white solid and rutile is the

thermodynamically stable allotrope, with anatase being a long-lived metastable state. For nanometer scale crystallites, Barnard et al [10] found that surface effects begin to affect the bulk crystal structure and the anatase phase can be stabilised. Photoelectrochemical research has therefore focused on nanometer-sized colloids of the anatase allotrope due to its favourable electron diffusion properties [103].

2.1.2 Van Der Waals Attraction

In the absence of any other interactions, there is always an attraction between two surfaces of the same material in a common medium[1]. This attraction arises from forces between induced dipole moments between the two surfaces, and is a short range but strong force on the scale of colloidal radii and Brownian forces. In general the magnitude of the van der Waals force depends on the geometry of the interacting surfaces. For two interacting spheres at small separations, where the colloidal radius is much larger than the inter-colloid separation the potential can be expressed as

$$V_{vdW} = -\frac{A}{6}\left(\frac{2}{s^2-4} + \frac{2}{s^2} + \ln\frac{s^2-4}{s^2}\right) \tag{2.1}$$

where $s = x/a$ is the ratio of the centre to centre separation of colloids x and the colloidal radius a and A is known as the Hamaker constant, a material dependent quantity measuring the strength of the interaction [52]. [2]

Various approaches have been attempted to quantify the magnitude of the Hamaker constant for titania in water. Theoretically, the problem can be approached *ab initio* via a quantum mechanical treatment of the atoms in each surface and in the intervening medium. The result, first derived by Lifschitz [35], is an expression for A which is dependent on the dielectric and optical properties of the materials across all frequencies of interaction. Unfortunately this data can be hard to access for many materials, and so approximations which limit the accuracy and validity of the theoretical results must be used.

[1] For two surfaces of differing materials, the van der Waals force can be attractive or repulsive, depending on the dielectric properties of the materials which are interacting.

[2] Due to the finite speed at which the electric field due to the fluctuating dipole can propagate, van der Waals forces tend to weaken more rapidly beyond separations of about 5 nm to 10 nm. This is known as retardation. Due to this effect A is often qualified as the non-retarded Hamaker constant.

The Hamaker constant can also be calculated from force against surface separation measurements in well defined geometries. The surface force apparatus of Israelachvili [52] and the more modern atomic force microscope both offer the ability to measure extremely small forces and separations accurately. Difficulties arise, however, in obtaining well defined geometries and pure samples.

The best measures made to date of the Hamaker constant for anatase in an aqueous solvent fall in the range $A = 20 \times 10^{-21}\,\mathrm{J}$ to $90 \times 10^{-21}\,\mathrm{J}$, or 5 to 20 kT at room temperature [71]. The theoretical treatment of the Hamaker constant reveals that it depends on the refractive index of the material. It is therefore to be expected that the high refractive index of titania results in stronger van der Waals interactions compared to the (usually polymeric or silica) colloids studied in the colloidal physics literature.

2.1.3 Electrostatic Interactions

Titanium dioxide surfaces, as with most metal oxides [49], are usually terminated with hydroxyl groups, which are sensitive to the pH of their environment. High pH encourages dissociation of a hydrogen ion, while low pH encourages association of a hydrogen ion. In water, for example, the following equilibria hold for metal (M) oxide surfaces:

$$\mathrm{M-OH_2^+ + OH^-} \underset{\text{Low pH}}{\rightleftharpoons} \mathrm{M-OH + H_2O} \underset{\text{High pH}}{\rightleftharpoons} \mathrm{M-O^- + H_3^+O} \qquad (2.2)$$

In general, therefore, a non-negligable charge will be present at the surface of titania colloids. This charge will cause any ions present in the water to migrate towards (or away from, depending on the charge) the colloid surface. The equilibrium distribution of ions around a charged colloid is known as the double layer, as it is known to consist of a strongly bound layer of ions which move with the colloid and a diffuse layer of ions which can be displaced from the colloid by shear. The effect of the ions in the double layer on the motion and arrangement of the colloids can be large and long ranged, and so a theory of the double layer is important in understanding the properties of the colloidal ensemble [31].

Theoretically, the double layer is modelled by combining the Boltzmann and Poisson equations for the distribution of ions away from the surface of the colloid. The derivation is relatively simple, however the resulting Poisson-Boltzmann

equation is insoluble for many applicable surface geometries. The Derjaguin approximation allows the calculation of the potential around a sphere if the potential away from the corresponding planar surface is known. The resulting expression for the potential surrounding a spherical colloid is [71]:

$$V_E = 2\pi\epsilon_0\epsilon_r\psi^2 a \exp(-\kappa h) \qquad \text{for } h > 2a \tag{2.3}$$

where $h = x - 2a$ is the distance of closest approach between the two surfaces, ψ is the surface potential of the colloid, κ is known as the Debye-Hückel parameter, a the colloidal radius and ϵ_0 and ϵ_r the permittivity of free space and relative dielectric constant of the medium, respectively. The Debye-Hückel parameter reflects the activity of the electrolytic ions in solution, and is given by the following expression for monovalent salts:

$$\kappa = \sqrt{\frac{2N_A e^2 C}{\epsilon_r\epsilon_0 kT}} \tag{2.4}$$

N_A is Avogadro's constant, $2C$ is the molar density of ions in solution, k is Boltzmann's constant, T is the absolute temperature and the other terms have been defined previously. κ therefore has units of inverse length, and κ^{-1} is a measure of the extent of the double layer away from the colloid and therefore a measure of the range of the electrostatic potential. To illustrate, the value of κ^{-1} can be evaluated for water at room temperature ($\epsilon_r = 80$, $T = 297\,\mathrm{K}$):

$$\kappa^{-1} = \frac{0.307}{\sqrt{c}} \tag{2.5}$$

where κ^{-1} is evaluated in nanometers and c is now given in moles per litre.

Combining the van der Waals attraction discussed previously with electrostatic repulsion is the basis of the theories of Derjaguin, Landau, Verwey and Overbeek and is known as DLVO theory in honour of these scientists [30, 106]. The principal features of the interaction potential arising from combining V_{vdW} and V_E are a deep van der Waals attractive minimum, known as the primary minimum, a repulsive barrier and at higher salt concentrations a wide secondary minimum. The primary minimum is usually deeper than the thermal energy available to free colloids, and therefore colloids that are trapped in it are irreversibly bonded [67].

This process is known as aggregation. In contrast, the secondary minimum is not usually deep enough to cause irreversible bonding and so bonding in this minimum is known as agglomeration, to differentiate it from aggregation. This distinction between reversible and irreversible bonding is important when discussing gelation in colloidal systems, which is the subject of the next section.

2.1.4 Clustering and Gelation in Colloidal Systems

When we say a material is a gel, we are usually describing a jelly-like material which acts like a solid, in that it can deform elastically, but can also flow under applied stress like a liquid. Investigation of these materials has identified other common properties: they are low density phases with a lack of long-range periodic order like liquids but exhibit yield stresses like a solid. Gels are useful due to this combination of liquid and solid behaviour: material can be applied under stress to cover an appropriate area and it will retain its shape once the stress is removed. Emanuela Zaccarelli [110] has recently published a review of colloidal gelation which aims to describe what gels are and what mechanisms may be behind their formation. The following section is a summary of this work with an emphasis on current theories of colloidal gelation.

Historically, gelation was first studied in the context of chemical gels. Chemical gels are formed of subunits bonded by strongly attractive permanent chemical bonds. As the monomers diffuse in solution and collide with each other they bond irreversibly. The newly formed dimers then diffuse until they collide with more monomers or other dimers, and so on. After sufficient time has passed, all the particles will be part of the same bonded cluster. If this cluster spans the entire sample, this is known as percolation. Percolation results in dramatic changes in the flow properties of the chemical gel and the macroscopic inhibition of diffusion across the sample. This is the original definition of the gelation point of chemical systems.

Zaccarelli continues this line of thought to 'physical gels', systems where the attractive bonds are weaker, and therefore their lifetime is not infinite. The same process of aggregation continues but percolation is no longer a sufficient condition for dynamic arrest, as the percolating network is transient. To understand the source of dynamic arrest in physical gelation we consider colloidal glasses, another system where dynamic arrest is responsible for dramatic changes in flow properties.

In colloidal glasses, dynamic arrest has its origins in the inability of the particles to rearrange to reach the equilibrium state due to the free energy cost of the intermediate rearrangement states. Both the energetic cost of breaking particle bonds and the entropic cost of cooperative rearrangement contribute to free energy required to rearrange particle positions. There are therefore two timescales in the dynamics of the system; we have the bond lifetime and the cooperative rearrangement timescale τ. While the bond lifetime is fixed by the colloidal potential, τ is dependent on volume fraction. If τ is larger than the timescale of the experiment then the system will demonstrate arrested dynamics.

The difference between a glass and a gel is that a gel is a low density phase. In order for dynamic arrest to occur on experimental time scales for low attractive bond strengths (short bond lifetimes) there must be high density regions within the system to prevent the system relaxing to its entropically favoured equilibrium state. For all systems with a purely attractive colloid-colloid potential, two phase separation occurs when a system is quenched into the binodal region of the phase diagram. At this point the sample begins to coarsen microscopically into continuous low and high density phases located at the edges of the binodal region. In the locally high volume fraction phase, τ can dramatically increase to the point at which it exceeds the experimental timescale, leaving the system dynamically arrested at a low total volume fraction — the system has gelled. This is a non-equilibrium route to gelation. The spinodal decomposition process is interrupted by the dynamic arrest of the high density phase and the system drops out of equilibrium. This should be a universal feature of all systems with purely attractive colloidal potentials.

If a long-ranged repulsive part is added to the attractive potential, system wide spinodal decomposition is inhibited by the kinetic barrier this raises to aggregation. It becomes energetically favourable to form finite sized clusters, with the preferred cluster size depending on the strength and range of the repulsion and sample volume fraction. The residual potential between clusters then dictates the cluster dynamics. At high enough volume fraction, the clusters become large enough to form a percolating network and at this point the clusters (as opposed to the particles) will begin to demonstrate dynamic arrest. This is an equilibrium approach to gelation, as the clusters are free to rearrange to approach equilibrium with respect to the particles at all points in the quench until the sample gels.

Finally, if phase separation is further inhibited by the introduction of directional bonding, such that the average coordination number of clusters is small, it may

become possible to quench into a gel state without any phase separation occurring at all. The low coordination number means that saturated networks (which minimise the energetic component of the free energy due to bonding) are sparsely space filling. The saturated networks then interact in a similar way to the space filling equilibrium cluster phase above, with a percolation of networks giving rise to dynamic arrest. As the free energy is still minimised, this is again an equilibrium approach to colloidal gelation.

The microscopic structure in all cases is a tenuous, interconnected network of subunits with void space between them. For gels arising from interrupted spinodal decomposition, the voids are the low density phase; for cluster phase gels, the voids are the space left over after cluster packing and for directionally bonded gels the voids are the spaces between network filaments.

Theoretically the aggregation process can be described by the diffusion limited cluster aggregation (DLCA) model [19, 59, 61, 68], which makes the assumptions that the inter-particle potential is infintely attractive at contact and zero elsewhere and collisions between particles are purely diffusive. The stochastic nature of the collision process results in a microscopic structure which preserves the statistical distribution of particles and voids at all length scales between that of a single subunit and the percolating cluster. The structure of a chemical gel is therefore fractal and analytical approaches have shown that the mass contained within a volume defined by a particular length scales with an exponent less than 3. To provide a concrete example, imagine a cube of material with side a and density ρ. The mass of the cube is $m = \rho a^3$. Now we examine a smaller cube cut from the cube. The ratio of the new mass to the old still scales with the ratio of side lengths with an exponent of 3, e.g.

$$\left(\frac{m'}{m}\right) = \left(\frac{a'}{a}\right)^3 . \tag{2.6}$$

Now consider a cube of a DLCA gel. As the material is inhomogeneously distributed through the volume, the mass of the cube is no longer proportional to a^3. However, the fractal nature of the gel guarantees that it *will* be proportional to some lower power D and in addition, this power law will hold for *any* smaller or larger cube we examine:

$$\left(\frac{m'}{m}\right) = \left(\frac{a'}{a}\right)^D . \tag{2.7}$$

The assumptions of the DLCA system allow the analytical calculation of the fractal dimension and it is found to be $D = 1.75$.

A variant of the same system can be derived to cover interactions where bonds are only formed after many particle or aggregate collisions. This is known as reaction limited cluster aggregation (RLCA). As particles can now diffuse into clusters without bonding at the edges, RLCA results in less sparse structures than DLCA. This is reflected in the higher observed fractal dimensions of RLCA systems ($D \approx 2.0$)

Effect of Gravity on Gelation

Titanium dioxide is very dense with respect to water — the density mismatch $\Delta\rho = 2.9\,\mathrm{g\ cm^{-3}}$. It is expected, therefore that gravitational fields will have an important effect on the system. In general, the effect of gravity on a suspension is to set up a gradient in osmotic pressure through the sample [20]. A well known effect of this is the hydrostatic balance density distribution, the exponential form of which is easily derived from pressure differences with height due to the gravitational energy mgh. In the dilute limit the gravitational height h_g can be defined, which is related to the balance between Brownian motion and the gravitational potential of a colloid:

$$h_g = \frac{kT}{mg} = \frac{3kT}{4\pi\Delta\rho g a^3} \tag{2.8}$$

where here it has been expressed for a spherical colloid of buoyant mass $m = \Delta\rho a^3$. If $h_g < a$ then the osmotic pressure will vary strongly over colloidal length scales and will strongly affect their dynamics. If $h_g > a$ then the effect of gravity on the system is small at a microscopic scale, although macroscopic gradients in density are still present [87].

The effect of gravity on gelation is two-fold. Firstly, when the gravitational length of the cluster becomes smaller than their radius parts of the cluster will experience a higher osmotic pressure. This will cause density gradients within clusters. Equivalently, their sedimentation is enhanced and they fall anisotropically away from the other clusters which are forming, which will peturb both their size and shape away from that anticipated theoretically in the absence of gravity.

Second, if an arrested state can form before too many clusters have sedimented,

gravitation now induces a stress on the newly formed gel network. As gels are sparse, unless bond strengths are very high their yield stress can be quite low. If the yield stress is exceeded the network must rearrange until the stresses on it are balanced. The resulting collapse leads to a compaction of the gel network which is guided in general by both the initial network structure and the flow of solvent away from the compacting regions [48]. These effects are reflected in a variety of time dependent collapse phenomena including the appearance of a sharp interface between settling sediment and supernatant [4] and in weakly attractive gels a variety of delayed collapse behaviours [100]. As these behaviours will have an important impact on the manufacture and processing of electrode materials, it will be important to explore the effect of these features on the colloidal titanium dioxide system.

2.2 Materials and Methods

The colloidal titanium dioxide used for this study was obtained from Nanostructured And Amorphous Materials, Inc. of Houston, USA. The stock code was 5425HT. The manufacturers description claims it is 99 % pure anatase titanium dioxide with an average particle size of 10 nm.

As the titanium dioxide is supplied as a dry powder, it will be necessary to use a dispersion tool to deagglomerate and disperse the particles once they are in solution. Ultrasonic irradiation is a commonly used technique for dispersing colloidal powders in solution. Jiang et al [55] have reported that dispersion of titanium dioxide in water is more effective using probe sonication than bath sonication. I have therefore chosen to use an ultrasonic horn (VCX 500, 500 W maximum power output, Sonics & Materials Inc., Newtown, USA) to deagglomerate all samples using the protocol of 30 s per 10 mL solution at 20 % of maximum tip oscillation amplitude.

A note on pH data: There is an important distinction between the pH values recorded in this chapter and the pH values recorded in chapter 3. In this chapter, the pH of the aqueous solvent is set *before* the titania colloid is mixed in ultrasonically, while in chapter 3 the pH of the suspension is set *after* mixing in the titania colloid, with the pH adjusted iteratively after dispersion until it remains stable. The work in chapter 3 was carried out after the work in this chapter had revealed that the suspension pH was not stable after mixing in the titania colloid, and the protocol was adapted to gain greater control over the suspension pH.

Volume Fraction

One of the most important parameters in any colloidal system is the volume fraction:

$$\phi = \frac{v}{V} \tag{2.9}$$

where v is the volume of the dispersed phase and V is the total volume of the system. As the solid phase in these experiments is provided as a dry powder, the simplest method to measure ϕ is by measuring the weight fraction of titanium dioxide to solvent and converting this to a volume fraction using the literature

values for the densities:

$$\phi = \left(\frac{m_s}{m} \frac{\rho}{\rho_s} + 1 \right)^{-1} \tag{2.10}$$

where m and m_s are the masses of colloid and solvent added and ρ and ρ_s are their densities. As pointed out by Poon et al. [82] in a recent paper, this method does suffer from some drawbacks. It assumes that the properties of the dry particle are the same as those of the wet particle. This means that, for example, the effects of charging (discussed further in the next section) are not included and as such this ϕ is actually a measure of the equivalent hard sphere system. The measured densities of anatase in the literature also have a spread of 3 % to 6 % about the theoretical value, limiting the maximum precision with which ϕ can be known. The density ratio also has a temperature dependent component. Despite these limitations, the practical simplicity of the density fraction approach makes it the most appropriate for an initial study of the titanium dioxide system from a soft matter perspective.

2.2.1 Characterising the Charge/pH Relationship

Zeta Potential and the Henry Equation

In order to understand the phase behaviour of titania colloids it is important to know how the colloidal surface charge varies with solution pH, as discussed earlier. Kosmulski [62] has suggested that the charging properties of anatase titania reported in the literature are contestable as widely varying values have been claimed. It will therefore be necessary to characterise the charging properties of the titania sample used in this study.

Experimentally, the easiest way to access the electrical properties of a colloidal surface is through electrophoretic mobility measurements. Electrophoresis is the movement of particles due to an externally applied electric field. If the velocity imparted to a colloid by an external field is known, the electric potential due to surface charges can be derived using the Henry equation [49]:

$$U_E = \frac{2\epsilon\zeta f(\kappa a)}{3\eta} \tag{2.11}$$

where U_E is the electrophoretic velocity, ζ is the zeta potential of the colloid, $f(\kappa a)$ is known as Henry's function, a is the particle radius and κ, ϵ_0 and ϵ_r have

been defined previously. Some discussion of ζ and $f(\kappa a)$ will now follow.

The zeta potential is the potential at the slip plane within the double layer between the layer of ions strongly bound to the colloidal surface and the diffuse layer of freely moving ions. This is not identical to Ψ, the surface potential, which was used in section 2.1.3 to describe the electrostatic potential around a colloid, but as this is not an easily accessible value it is common to equate the zeta and surface potentials when mapping experimental results onto theoretical energy values.

Henry's function incorporates the effect of the electrical double layer on the colloid's viscosity. Two simple approximations can be taken. In situations where the double layer is much smaller than the colloidal radius ($\kappa a \gg 1$), for example, high dielectric constant media (e.g. water) with moderate electrolyte concentration ($c > 1\,\text{mM}$), $f(\kappa a)$ can be taken to be 1.5. This is known as the Smoluchowski approximation. In the opposite case, where the double layer is much larger than the particle radius ($\kappa a \ll 1$), usually applicable in non-polar solvents with moderate colloidal radii, $f(\kappa a)$ can be taken to be 1.0. This is the Hückel approximation.

U_E can be measured in a variety of ways, either directly through particle tracking in microscopy experiments or more commonly in recent times through indirect optical measurements. The method utilised by the instrument chosen for these experiments (Zetasizer Nano Z, Malvern Instruments, UK) is laser Doppler velocitometry. Briefly, a laser beam is split and one part passed through the sample before the beams are recombined. The resulting interference pattern contains information on the Doppler shift induced in the sample beam by the electrophoretic motion of the colloids. The advantages of this technique are that it rapidly produces information on electrophoretic mobilities and mobility distributions.

pH Dependence of the Zeta Potential

0.001 g of titania were dispersed into 10 mL of deionised water using the above dispersion protocol to provide an initial volume fraction of $\phi = 2.6 \times 10^{-5}$. The pH of the deionised water had been adjusted before mixing to the appropriate value using either 1.00 M hydrochloric acid (1.002 N standard solution, SigmaAldrich) or concentrated acetic acid and a pH meter (Mettler

Toledo SevenEasy pH meter equipped with a Mettler Toledo InLab Expert Pro solid state pH probe). The acetic acid measurement was carried out to see if any qualitative difference was present in the charging curves due to, for example, specific ion absorption onto the titania surface. 1 mL of this sample was then extracted using a micropipette and added to a new vial, to which 9 mL of pH adjusted distilled water was added to effect a 1:9 dilution to a volume fraction of $\phi = 2.6 \times 10^{-6}$. This sample was then sonicated again before loading into the electrophoresis apparatus.

The electrophoretic sample cell (Folded capillary cell, DTS 1060, Malvern Instruments, UK) had been flushed with ethanol and cleaned with deionised water according to the procedure outlined in the user instructions prior to measurement. The sample was sonicated according to the previously discussed protocol and then transferred to the sample cell using a 1 mL disposable plastic syringe. The sample cell was then sealed with plastic stoppers. An electrophoretic measurement was carried out after a five minute equilibiriation period at 25 °C. The automatically determined instrument parameters were a field strength of 148 V and 27 measurements per result.

Zeta potential measurements were then made for varying mass fraction of titania. Two concentration quench routes were investigated. First, samples were made up by the addition of 0.01 g of titania to 10 g of HCl at a pH of 4.5 (before mixing) with more dilute concentrations in the series made up by diluting this sample by 1:3, 1:6 and 1:9 with further pH 4.5 (before mixing) HCl. The mother sample was dispersed via the usual sonication method with the diluted samples being mixed via gentle vortex mixing. The zeta potentials of these samples were measured immediately after mixing. Second, samples were made up directly by adding varying masses of titania to 10 g of HCl and sonicating. Again, the zeta potentials of these samples were measured directly after mixing.

2.2.2 Primary Particle Characterisation by Electron Microscopy

The primary titania particles are expected, from the manufacturers description, are expected to have dimensions under 100 nm. This is below the diffraction limit for the visual spectrum and so it is unlikely that optical microscopy will be useful for characterising the morphological properties of the primary titania

units. Electron microscopy and atomic force microscopy are two alternatives to conventional microscopy which are well suited to visualising objects on the nanometer scale.

The contrast available in electron microscopy depends on the electron density of the material under study compared to the background. Titanium atoms, with an atomic number of 22, will give good contrast against carbon, atomic number 12, the material usually used as an imaging substrate for transmission electron microscopy (TEM). The good conduction properties of anatase titanium dioxide will also help to alleviate charging effects.

Titania samples were prepared by adding a mass of titania powder to 10 mL deionised water equivalent to a volume fraction of $\phi = 0.0026$. The deionised water was adjusted to a pH of 3.1 before the titania was added. The sample was sonicated using the protocol discussed earlier. A single drop of the dispersed sample was deposited onto a gold TEM grid supported by a carbon-coated polymer layer and left to dry in a fume cupboard. After ten minutes, excess fluid was absorbed from the grid by touching it with a piece of filter paper.

Images of the primary particles were obtained using a Zeiss TEM. Representative regions of non-agglomerated particles were imaged. An example image is shown in figure 2.1.

After capture, images were processed by applying a 10 pixel median filter to remove background stippling followed by a binary thresholding using ImageJ [1], a widely available scientific image analysis suite. After filtering (see figure 2.2, the histogram of grey values showed two peaks, one corresponding to particle grey values and another corresponding to background grey values (see figure 2.3. The threshold value was selected at the point between these two peaks. Where a background gradient in grey value made isolation of the clusters difficult, thresholding was carried out individually on segments of the image to preserve particle-background contrast. After thresholding, ellipses were fitted to contiguous thresholded regions by finding fit ellipses which have identical second statistical moments and areas to the thresholded pixels[3]. Figure 2.4 shows a representative image with detected particles highlighted.

[3]This procedure is implemented in ImageJ using the "Analyze Particles" analysis filter, and the statistical procedure is outlined in [29]

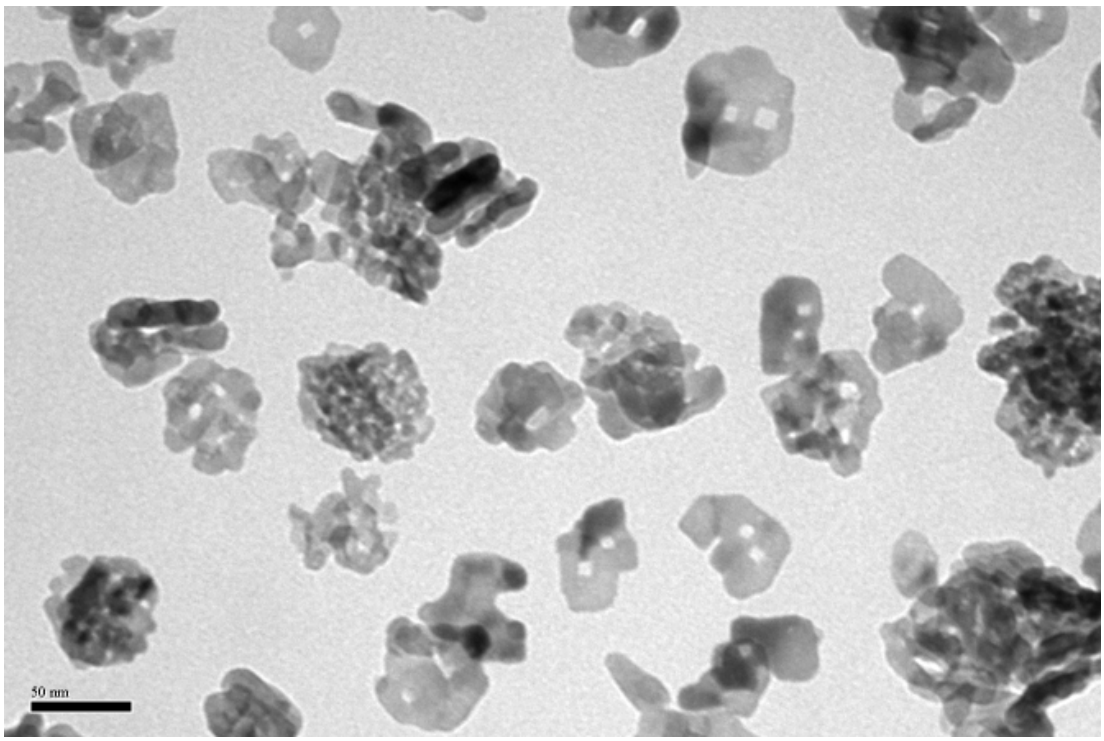

Figure 2.1 *A representative sample of a TEM micrograph of the titanium dioxide nanoparticles*

2.2.3 Measurement of Self-Assembled Clustering

The controlled cohesive forces which drive self-assembled clustering can be weak when compared to the shear forces encountered when handling samples. It is therefore important to be able to analyse the clustering process *in situ*. Light scattering techniques are able to probe the ensemble-averaged structure of materials in solution.

A detailed discussion of dynamic light scattering techniques is undertaken in chapter 4. Briefly, by investigating correlations in the time dependence of the intensity of coherent light scattered from a suspension the size distribution of the suspended scatterers can be inferred. By examining the nature and evolution with time of the inferred scatterer size distribution, information on how titania clusters assemble in dilute aqueous suspension can be obtained.

In parallel with the pH dependence of zeta potential described in section 2.2.1 the pH dependence of cluster size of titania in dilute solution was studied. DLS samples were extracted from the main sample using a disposable 1 mL plastic syringe. The sample was placed in a culture tube (Fisherbrand disposable culture

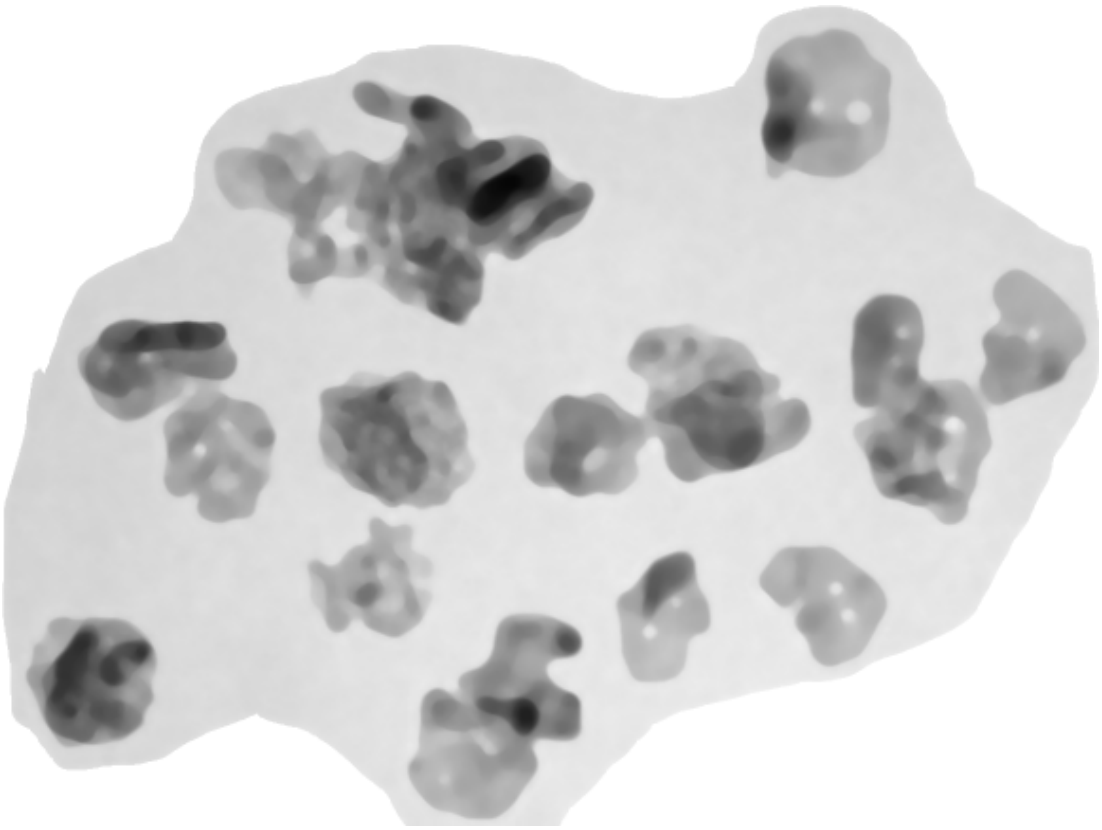

Figure 2.2 *Application of the 10 pixel median filter to the image in figure 2.1*

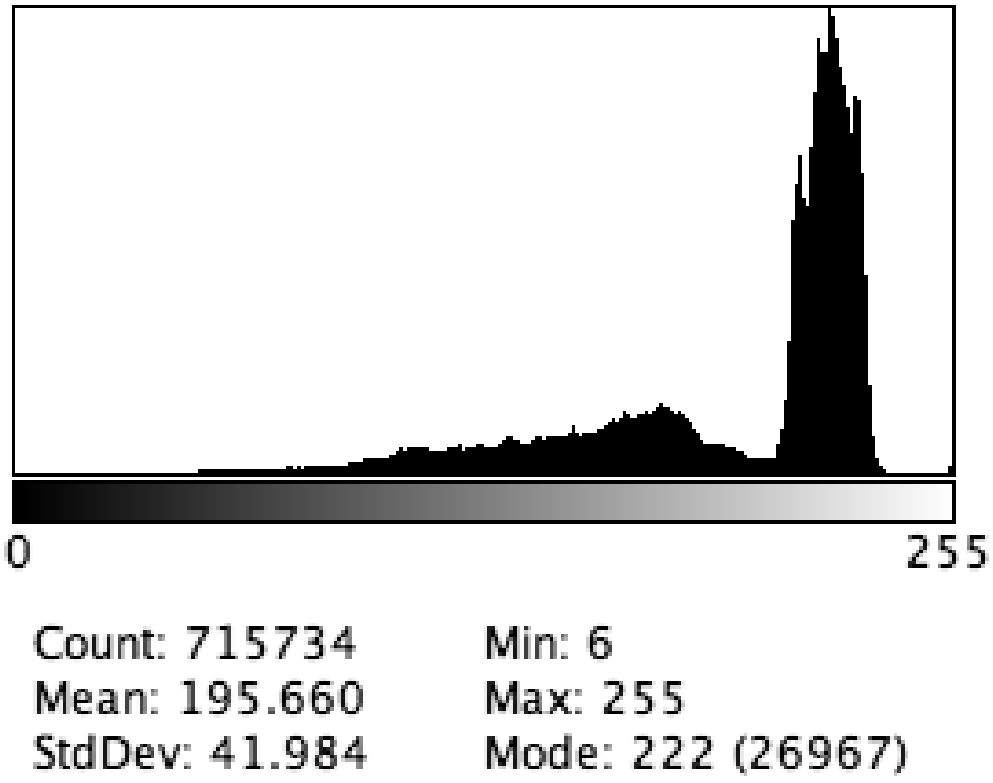

Figure 2.3 *Grey value histogram for the filtered image in figure 2.2*

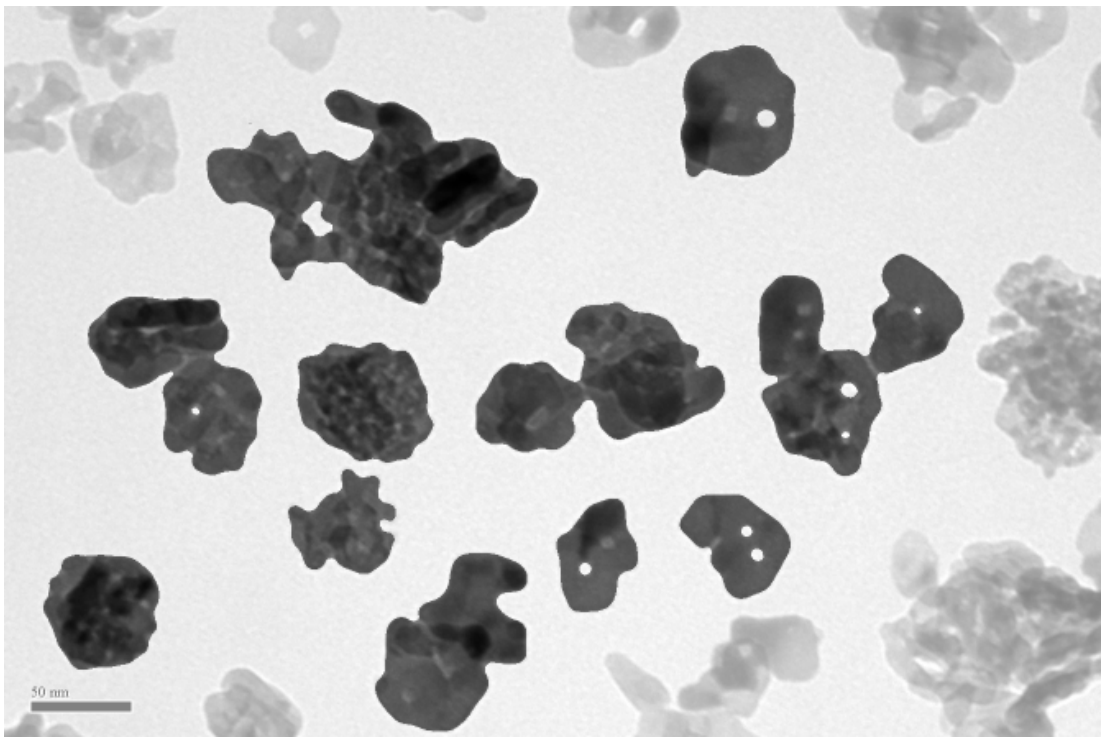

Figure 2.4 *The image in figure 2.1, with detected particle pixels emphasised in dark grey*

tubes, Borosilicate glass 10 mm × 75 mm, Cat. no. 14-961-25) which had been cleaned successively using 10 % Decon solution and deionised water, followed by ethanol and acetone (to successively increase solvent volatility) before being blown dry using a compressed air duster. The sample was placed in a toluene heat bath at 20 °C and allowed to equilibriate for 5 minutes. Measurements were taken with a laser operating at a wavelength of 632.8 nm at a scattering angle of 90°. Each measurement was the average of 3 runs of 10 s each. An ALV/LSE-5004 digital correlator was used to generate the intensity correlation function. Runs with obvious dust contamination were omitted and repeated. Zeta potential measurements were initiated at the same time as DLS measurements. Cluster sizes were calculated by performing a regularised unweighted fit to the correlation data. The timescales were used to calculate hydrodynamic radii through the Stokes-Einstein diffusion relation for a sphere, using a viscosity of $\eta = 0.89$ mPa s.

2.2.4 Towards a Phase Diagram

The effects of varying pH and salt concentration were also evaluated on the macroscopic properties of the suspension by direct observation. Samples with differing volume fraction ϕ (0.025 % to 7.6 % in 6 logarithmically spaced steps), pH (3.10, 3.50 and 4.50 before mixing) and salt concentration (no salt, 3 mM KCl, 3 mM K_2SO_4) were made up by placing the appropriate masses of solids into a vial and adding 10 mL of pH adjusted deionised water, and sonicating via the established procedure. These vials were then imaged as soon as possible after sonication, one day later and then one week later to attempt to capture the steady state behaviour of the suspensions.

2.2.5 Time Lapse Photography of Sample Dynamics

Some samples exhibited rapid sedimentation dynamics. Time-lapse photography was used to capture the behaviour of these samples. Six rectangular glass sample cells (Starna Scientific Type 21 standard rectangular optical glass cell with PTFE stopper, 10 mm × 10 mm × 48 mm) were cleaned in an ultrasonic bath in a solution of 10 % Decon and rinsed with deionised water, ethanol and acetone before drying in an oven at 50 °C. Occasionally after sonication in Decon the cells required manual cleaning with a lint-free cotton bud before rinsing to remove strongly adhered titania.

For each sample composition, 6 vials of 10 mL of suspension were prepared as above. The time at which sonication ceased for each sample was recorded using a stopwatch. A 3.5 mL aliquot of each vial was then loaded into the glass sample cells using a disposable plastic 5 mL syringe. Again a note was made of the time at which loading into the sample cell was completed. Each cell was then sealed using plastic stoppers and plastic film and placed in a bespoke imaging setup consisting of camera (QImaging Micropublisher RTV equipped with a 16 mm television lens) and sample bench with recessed holes mounted inside an incubator. Images of the samples were taken approximately every 1 s for 700 s, after which images were taken approximately every 600 s for a further 60 000 s. Another stopwatch synchronised with the previous was placed in the field of view of the camera to obtain an accurate frame rate calibration.

For the lowest concentrations studied, sedimentation occurred so rapidly that the

above frame rate was not appropriate. In this case, each of the six samples were mixed, loaded and imaged separately at the highest frame rate the camera was capable of (approximately 2.3 frames / second). Due to the low exposure time (6 ms) extra lighting was directed at the sample and stopwatch face to increase contrast. The rapid imaging experiments were also performed outside of the incubator and without sealing the sample cells to minimise loading time. The effects of evaporation should be negligible over the duration of imaging (ca. 160 s).

The time lapse recordings were analysed using the free scientific analysis suite ImageJ [1] with custom edge analysis and seven segment optical character recognition (see appendix C) plugins. See the appendices for a detailed description of their operation. Each region of the image stack corresponding to a sample cell was then extracted and the 'Find Edges' filter applied[4] The custom edge detector plugin was then used to extract the pixel positions of the base of the sample cell, the sediment/supernatant interface and the base of the fluid meniscus from each image.

2.2.6 Characterisation by DLS of Stable Suspensions

Some of the samples prepared for observation in section 2.2.4 appeared stable and no sharp supernatant/sediment interface became visible over extended periods of time. DLS measurements were performed on the (transparent) supernatant of the pH 3.1 (before mixing), 0.01 g sample three months after mixing. Measurements were taken as described in section 2.2.3. Three measurements were taken at each scattering angle between 30° and 150° in 20° steps.

To probe the evolution of the short term state of stable suspensions, light scattering measurements were undertaken on samples with $\phi = 0.025\,\%$ and $0.08\,\%$ at a pH of 3.50 (before mixing). 10 mL vials of sample were prepared as above in section 2.2.3. Measurements were taken each day, for five days beginning with the day of sample preparation. Dilution quenched samples were prepared by extracting a small amount from the top of the sample using a glass Pasteur pipette and adding one drop of sample to a culture tube (prepared as above in section 2.2.3) filled with distilled water. 2.5 mL of sample was then extracted using a plastic syringe and the process repeated with a new culture tube.

[4]The 'Find Edges' filter uses a Sobel operator to detect sharp changes in pixel intensity across an image. See `http://imagejdocu.tudor.lu/doku.php?id=gui:process:find_edges` for details (May 2011).

This was repeated until four fractionations of each sample had been prepared. Measurements were taken as soon as possible after dilution quenching using the same scattering and correlation setup as in section 2.2.3. Each measurement was a 10 s run at scattering angles of 40°, 60°, 80°, 100°, 120° and 140°.

2.2.7 Rheology of Non-Sedimenting Suspensions

At higher volume fractions samples became markedly more viscous and displayed limited sedimentation. The rheological response of these samples was investigated using a stress-controlled rheometer (Anton Paar AR-2000) with a cone and plate geometry (60 mm, 2° cone with a 60 µm truncation gap, Anton Paar). A solvent trap was used with the geometry to prevent sample drying. A diagram is presented in figure 2.5. All test procedures except where explicitly stated began with a preshear of 1000 s^{-1} for 30 s to deagglomerate the sample to a reproduceable state.

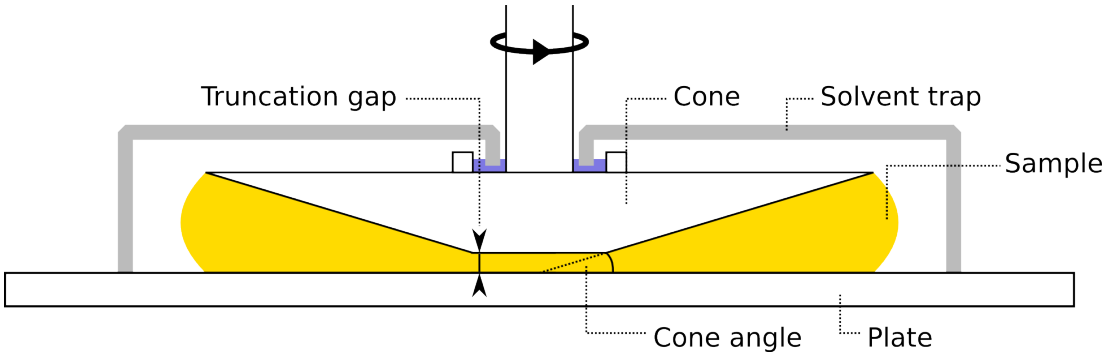

Figure 2.5 *Diagram of a cone-plate geometry as used for the rheological experiments detailed in section 2.2.7. The rheometer applies a set stress to the cone and measures its displacement. The displacement of the cone is affected by the rheological response of the sample. In a shear-controlled experiment, a feedback loop is applied to the stress setpoint to attain the desired rate of displacement.*

2.3 Results

2.3.1 pH Dependence of the Zeta Potential

Calculation of the zeta potential from the measured electrophoretic mobility requires a value for the Henry parameter $f(\kappa a)$. Given a typical primary unit size of 20 nm and an ionic strength of 1 mM, κa was evaluated as $\sqrt{0.001}/0.307 \times 20 \approx 2$. As this is a minimum value for a this implies that the Smoluchowski approximation is most valid and so $f(\kappa a)$ was taken to be 1.5 to determine the zeta potential. The viscosity, dielectric constant and refractive index of water at 25 °C were taken to be $\eta = 0.8872$ mPa s, $\epsilon = 78.5$ and $n = 1.330$. Tables 2.2 and 2.3 give the raw data.

Table 2.2 *Measurements of the mean and deviation of the zeta potential distribution of titania colloids in solutions of hydrochloric acid of varying pH (before mixing).*

pH (before mixing)	$\phi/10^{-5}$	ζ/mV	$\sigma(\zeta)$/mV
3.020(10)	2.3(3)	3.46	4.87
3.500(10)	2.3(3)	−9.04	4.24
4.020(10)	2.1(3)	−25.8	4.08
4.490(10)	2.3(3)	−35.8	4.34
5.000(10)	2.1(3)	−37.1	4.74

Table 2.3 *Measurements of the mean and deviation of the zeta potential distribution of titania colloids in solutions of acetic acid of varying pH (before mixing).*

pH (before mixing)	$\phi/10^{-5}$	ζ/mV	$\sigma(\zeta)$/mV
3.000(10)	2.6(3)	1.12	4.49
3.490(10)	2.8(3)	−8.88	4.86
3.990(10)	2.6(3)	−21.9	3.83
4.490(10)	2.8(3)	−28.4	4.02
5.010(10)	2.6(3)	−25.6	4.17

As noted in the caption to table 2.4, for some of the sample space investigated it proved difficult to obtain repeatable measurements of the zeta potential. For both of these measurements the potential was low. It is likely in these cases that

Table 2.4 *Values of measured zeta potential for varying weight fraction of titania. Data from table 2.2 have been included for comparison. These entries are marked* †*. Some measurements varied considerably between repeats. The average of these measurements is recorded and these data are marked* **.*

pH (before mixing)	ϕ_w $\times 10^{-5}$	Diluted?	ζ mV	
3.1	50	no	30	
	10	no	28	
(3.0)	1	yes	3	†
3.5	50	no	32	
	10	no	18	
	10	yes	9	*
	1	yes	-9	†
4.5	50	no	-12	*
	10	no	-25	
	10	yes	-34	
	1	yes	-36	†

the system was aggregating and sedimenting during measurement, which would affect measured particle mobility and thus may mean these values are unreliable indicators of the true zeta potential.

2.3.2 Primary Particle Characterisation

Fourteen representative TEM images were analysed using the procedure outlined in the methods section. One hundred and eighty-five particles were identified by the process. Figure 2.6 presents a histogram of results. Characteristic lengths were extracted from measured particle areas by finding the equivalent circle radius, e.g. length $= \sqrt{\text{area}/\pi}$

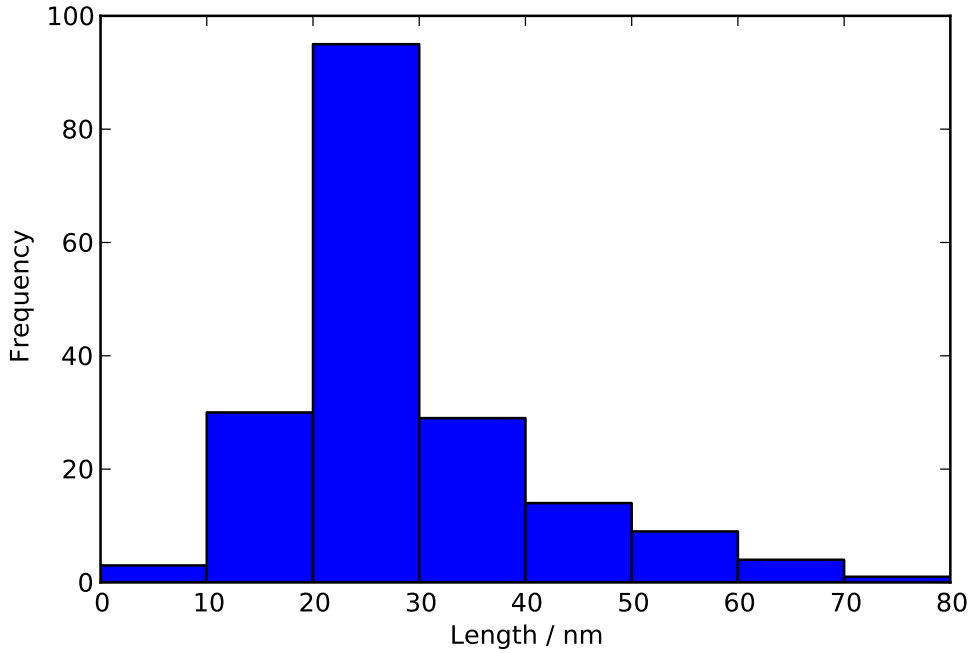

Figure 2.6 *A histogram of calculated characteristic lengths for the 185 particles identified in the TEM micrographs*

The distribution is slightly larger than the manufacturer's stated approximate size of 10 nm, with a peak between 20 nm and 30 nm and a narrow distribution of sizes about that mean. From the TEM images, these primary particles appear to be composite objects due to the appearance of voids in their structure. The 10 nm size referred to by the manufacturer is likely the grain size within these composites. As no averaged measurements this small were recorded, these grains must be irreversibly bonded to each other, either as a side-effect of the particle synthesis or drying processes. The size distribution appears to be skewed towards higher characteristic lengths. This may be an artefact of the image processing, as there is a tendency for clusters which are very close together to be merged into one cluster. The subsequent application of a median filter, which improves contrast

at the expense of systematically increasing thresholded areas, may aggravate this issue, as particles only separated by narrow contrast differences may be joined together after thresholding. Fitting ellipses to falsely joined particle images will then give an erroneously large fitted ellipse, although the scaling of the ellipse by its real area after fitting will alleviate this to some extent.

2.3.3 Measurement of Self Assembled Clustering

The results of the dynamic light scattering measurement, performed simultaneously with the zeta potential measurements from section 2.3.1, are presented in figure 2.7 with the data in tables 2.5 and 2.6.

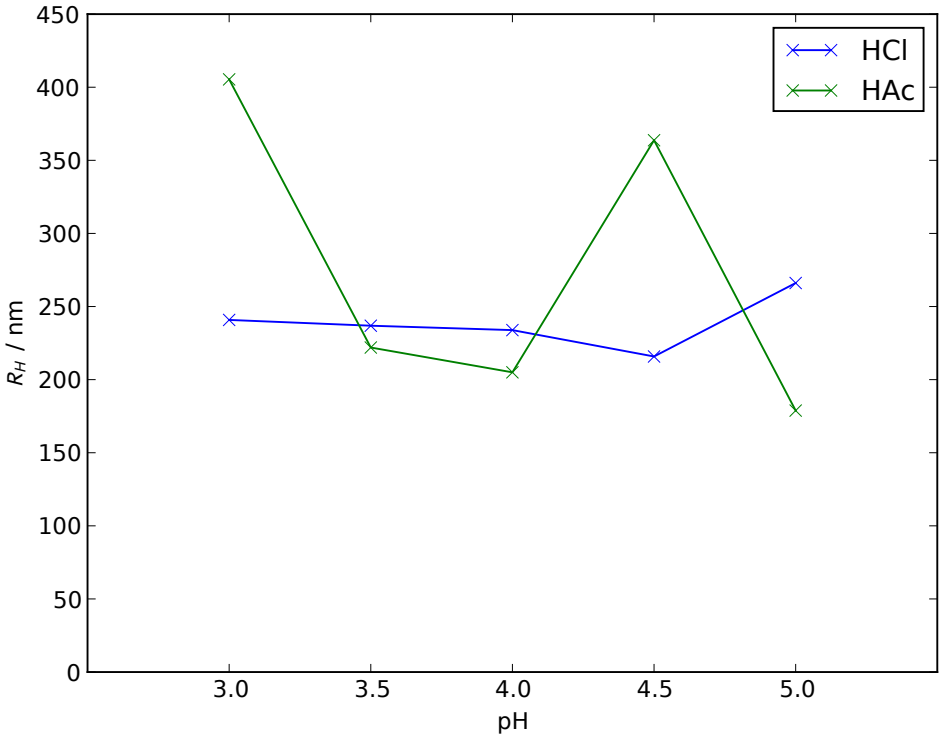

Figure 2.7 *Relationship between pH (before mixing) and cluster radius of gyration, as measured by dynamic light scattering. Volume fractions are given in tables 2.5 and 2.6. Measurements were performed as soon as possible after mixing (within one hour).*

Cluster sizes measured by DLS appear to be largely independent of pre-mixing pH, and therefore independent of zeta potential, across the range of pH studied here. As the standard deviations from the correlator were not recorded for these

Table 2.5 *Measurements of the hydrodynamic radius of titania colloids in solutions of hydrochloric acid of varying pH (before mixing).*

pH (before mixing)	$\phi/10^{-5}$	R_g/nm
3.020(10)	2.3(3)	241
3.500(10)	2.3(3)	237
4.020(10)	2.1(3)	234
4.490(10)	2.3(3)	216
5.000(10)	2.1(3)	266

Table 2.6 *Measurements of the hydrodynamic radius distribution of titania colloids in solutions of acetic acid of varying pH (before mixing).*

pH (before mixing)	$\phi/10^{-5}$	R_g/nm
3.000(10)	2.6(3)	405
3.490(10)	2.8(3)	222
3.990(10)	2.6(3)	205
4.490(10)	2.8(3)	364
5.010(10)	2.6(3)	179

measurements, exact calculations of errors in fitted parameters propagated from the fit are not available. On the basis of measurements where this information is available (see section 2.3.6, data from days 3–5) the error in the radii should be of the order of 2%. No measurable polydispersity was detected. This may be due to the lack of data on the standard deviations of the values of $g^{(2)}(\boldsymbol{q}, \tau)$.

2.3.4 Towards a Phase Diagram

Tables 2.7, 2.8 and 2.9 provide an overview of the observed behaviour of the samples immediately after mixing, the day after mixing and one week after mixing.

ϕ	pH 3.1 (pre-mix)			pH3.5 (pre-mix)			pH 4.5 (pre-mix)		
	None	KCl	K_2SO_4	None	KCl	K_2SO_4	None	KCl	K_2SO_4
0.025 %	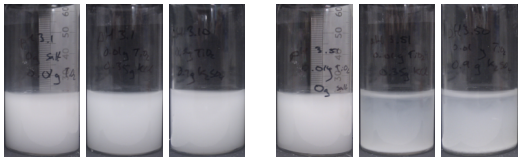								
0.08 %	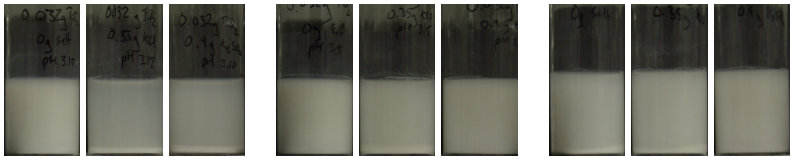								
0.25 %	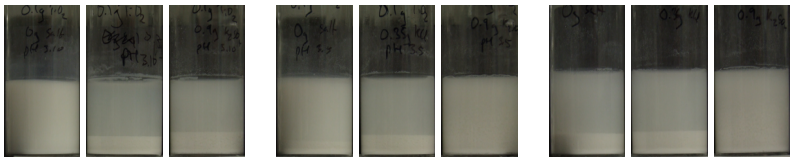								
0.8 %	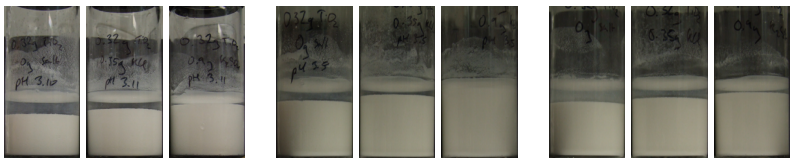								
2.5 %									

Table 2.7 *Photographs of samples of varying volume fraction and pH (before mixing) imaged immediately (ca. 5 minutes) after ultrasonic dispersion. Note that the imaging time post-sonication was not precisely controlled; conclusions over trends in sediment heights for rapidly sedimenting samples, for instance, will not be valid.*

ϕ	pH 3.1 (pre-mix)			pH 3.5 (pre-mix)			pH 4.5 (pre-mix)		
	None	KCl	K_2SO_4	None	KCl	K_2SO_4	None	KCl	K_2SO_4
0.025 %									
0.08 %	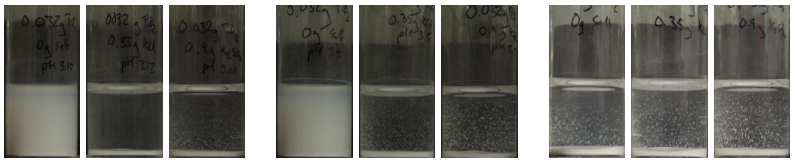								
0.25 %	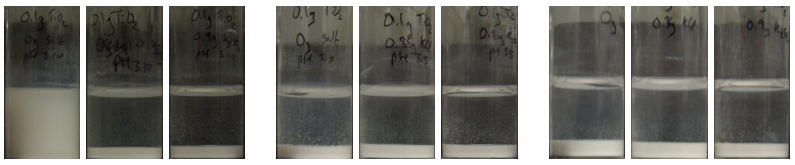								
0.8 %	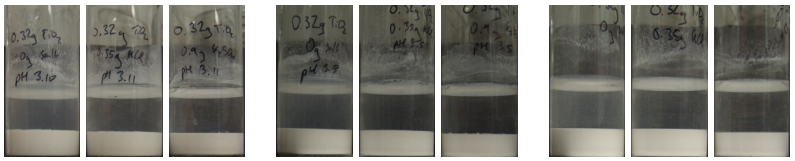								
2.5 %									

Table 2.8 *Photographs of samples of varying volume fraction and pH (before mixing) imaged ca. 16 hours after ultrasonic dispersion.*

ϕ	pH 3.1 (pre-mix)			pH 3.5 (pre-mix)			pH 4.5 (pre-mix)		
	None	KCl	K_2SO_4	None	KCl	K_2SO_4	None	KCl	K_2SO_4
0.025 %	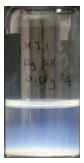			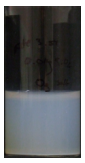					
0.08 %	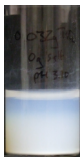								
0.25 %									
0.8 %	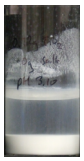	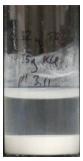							
2.5 %									

Table 2.9 *Photographs of samples of varying volume fraction (before mixing) and pH imaged ca. one week after ultrasonic dispersion.*

Macroscopic observation has revealed three distinct phase behaviours in the charged colloidal titania system:

- At low volume fraction and pre-mix pH, samples remain turbid for extended periods of time. As sedimentation occurs, a transparent supernatant becomes visible with a vivid blue hue which can be attributed to Mie scattering from scattering bodies smaller than the wavelengths of visible light. Figure 2.8 demonstrates this behaviour as observed for the $\phi = 0.025\,\%$, pH (before mixing) = 3.10 sample.

- At intermediate volume fraction, a sharp interface between sediment and supernatant can be identified. The supernatant can be transparent (e.g. $\phi = 0.8\,\%$, pH (before mixing) = 3.10, figure 2.9) or turbid (e.g. $\phi = 0.25\,\%$, pH = 4.50, figure 2.10). The interfacial sedimentation velocity is rapid, with the sediment volume reaching a constant value within hours or minutes. The sediment often has an observable grainy texture.

- At high volume fraction no significant sediment collapse can be observed over periods of days and no grainy texture is visible. Samples appear viscous and demonstrate viscoelastic yielding behaviour.

These behaviours can be summarised diagrammatically, as shown in figure 2.11. Red dots correspond to diffuse, slowly sedimenting samples, blue dots to those samples which display a clear rapidly sedimenting interface and orange dots for those samples which displayed viscous, self-supporting behaviour.

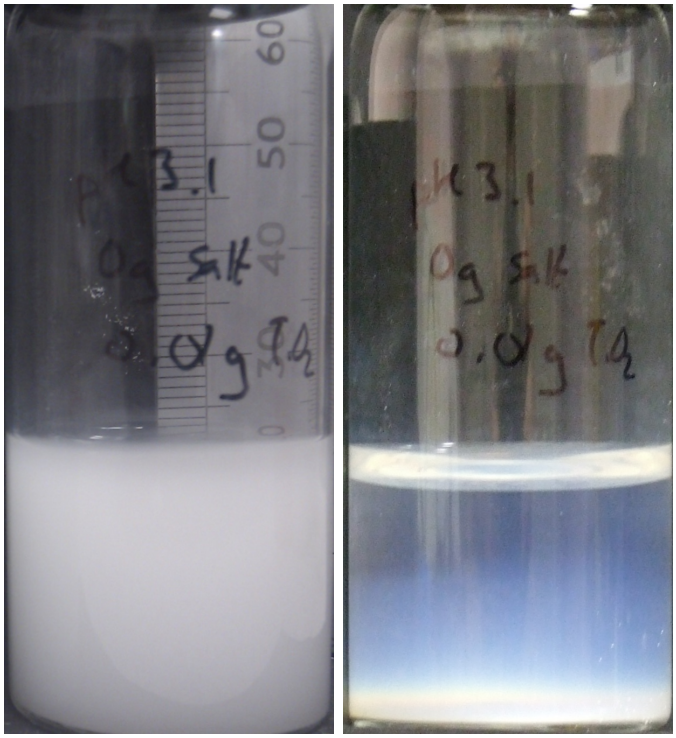

(a) *After mixing* **(b)** *ca. 1 week*

Figure 2.8 *Detailed photographs of the behaviour of the* $\phi = 0.025\,\%$*, pH (before mixing)* $= 3.10$ *sample.*

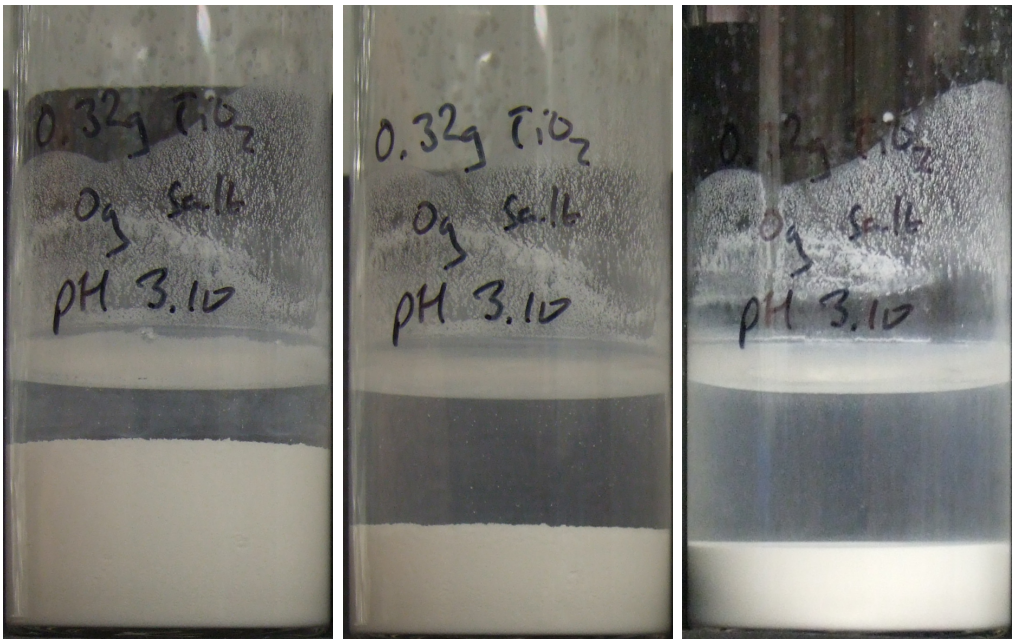

(a) *After mixing* **(b)** *ca. 16 hours* **(c)** *ca. 1 week*

Figure 2.9 *Detailed photographs of the behaviour of the* $\phi = 0.8\,\%$*, pH (before mixing)* $= 3.10$ *sample.*

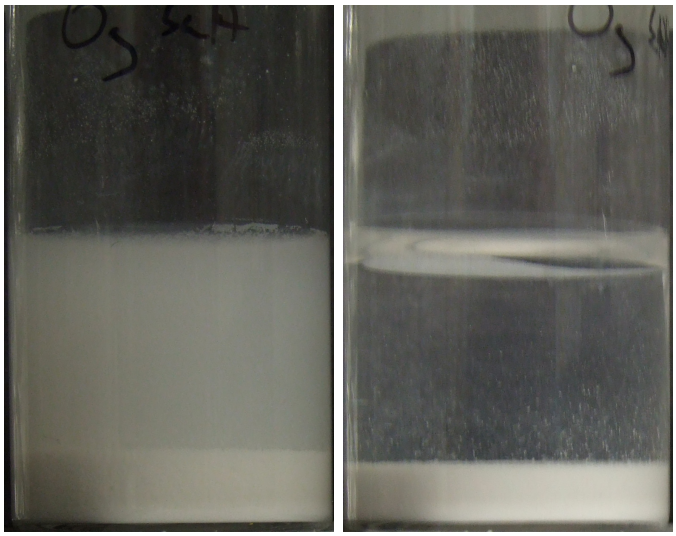

(a) *After mixing* **(b)** *ca. 16 hours*

Figure 2.10 *Detailed photographs of the behaviour of the* $\phi = 0.25\,\%$*, pH (before mixing)* $= 4.50$ *sample.*

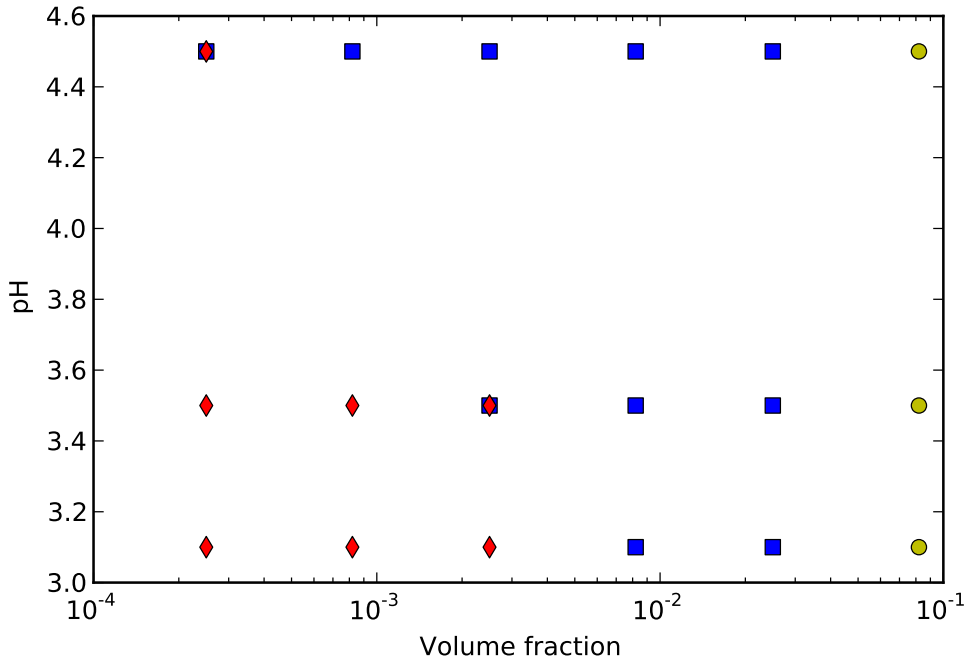

Figure 2.11 *Macroscopic colloidal phase diagram for charged titanium dioxide in water. Red diamonds indicate sedimenting clusters, blue squares indicate poroelastic consolidation and yellow circles denote long-lived free-standing gels.*

Further Observations

During the more detailed examination of sample dynamics which is described in the next section (section 2.3.5) some further observations were made which are relevant to interpreting figure 2.11:

- The $\phi = 0.25\,\%$, pre-mix pH 3.5 samples exhibited a mix of rapid and slow collapse behaviours, as shown in figure 2.12. It is therefore denoted by both red and blue in figure 2.11. During the imaging period (22.5 hours) three of the six samples demonstrated rapid collapse behaviour and three demonstrated slow behaviour. It may be possible that both slow and rapid collapse behaviours are the same behaviour occurring over different timescales. A longer observation period would be necessary to determine if the slowly collapsing sediments eventually exhibit rapid settling behaviour or if they smoothly approach the long time sharp, stationary interface. The rapid sedimentation behaviour occurs simultaneously with the appearance of large titania clusters nucleated on to the sample cell walls.

- The $\phi = 0.025\,\%$, pre-mix pH 4.5 samples displayed a similar mix of rapid and slow sedimentation behaviours as with the $\phi = 0.25\,\%$, pre-mix pH 3.5 samples (see figure 2.13). The slow settling velocity was much faster than in the previous case (compare figures 2.12h and 2.13h). Two of the six samples took significantly longer to sediment than the others. In addition, a 'swirling' motion could be seen in the top of the diffuse supernatant of all samples, both those which sedimented rapidly and those that sedimented slowly. It is possible that this phenomenon may be due to vibrations induced by the fan built into the incubator or a periodic oscillation in the light source within the incubator, a fluorescent tube.

- The $\phi = 0.08\,\%$, pre-mix pH 4.5 samples appear to rapidly aggregate into large clusters, which then sediment rapidly (see figure 2.14). A sharp interface forms at the base of the cell, but the sediment volume is small enough to be obscured by the metal cell holder in these images. As above, sedimentation was observed in the syringe prior to loading. There appears to be a diffuse supernatant left behind which slowly sediments with time; however, this could be due to a thin layer of titania adhered to the glass of the sample cell.

- When tilting consolidating samples through small angles, for short times

after mixing (e.g. ca. 5 minutes for $\phi = 0.8\,\%$, see figure 2.15a) the sedimenting interface remains parallel to the liquid meniscus, implying a fluid-like behaviour. At longer times (2 hours, see figure 2.15b), the sediment does not fully rearrange shape on tilting, implying viscoelastic behaviour.

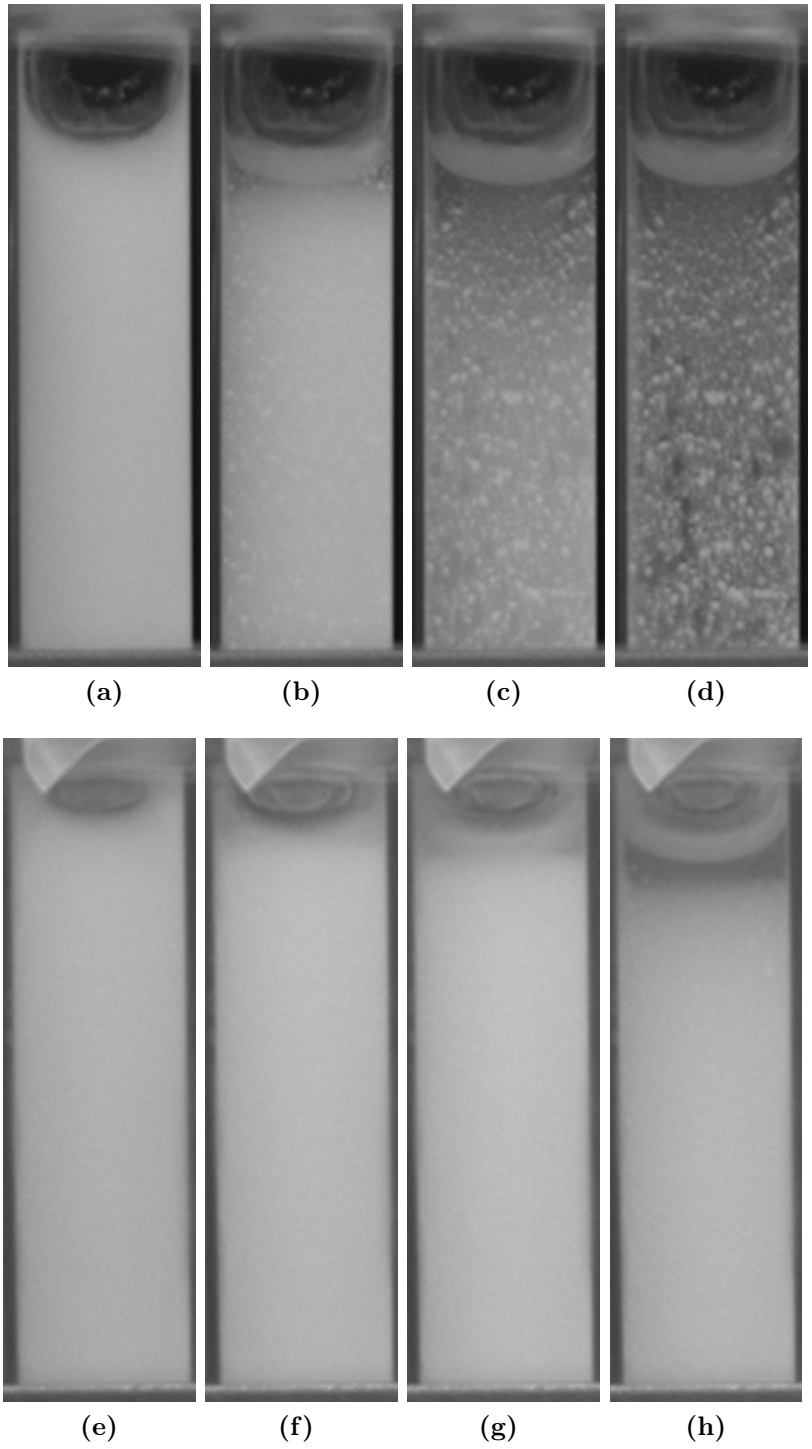

Figure 2.12 *Representative images of the fast and slow sedimentation behaviour of the $\phi = 0.25\,\%$, pre-mix pH 3.5 sample. The times after mixing are approximately 3 minutes (a, e), 2 hours (b, f), 6.5 hours (c, g) and 22.5 hours (d, h) respectively.*

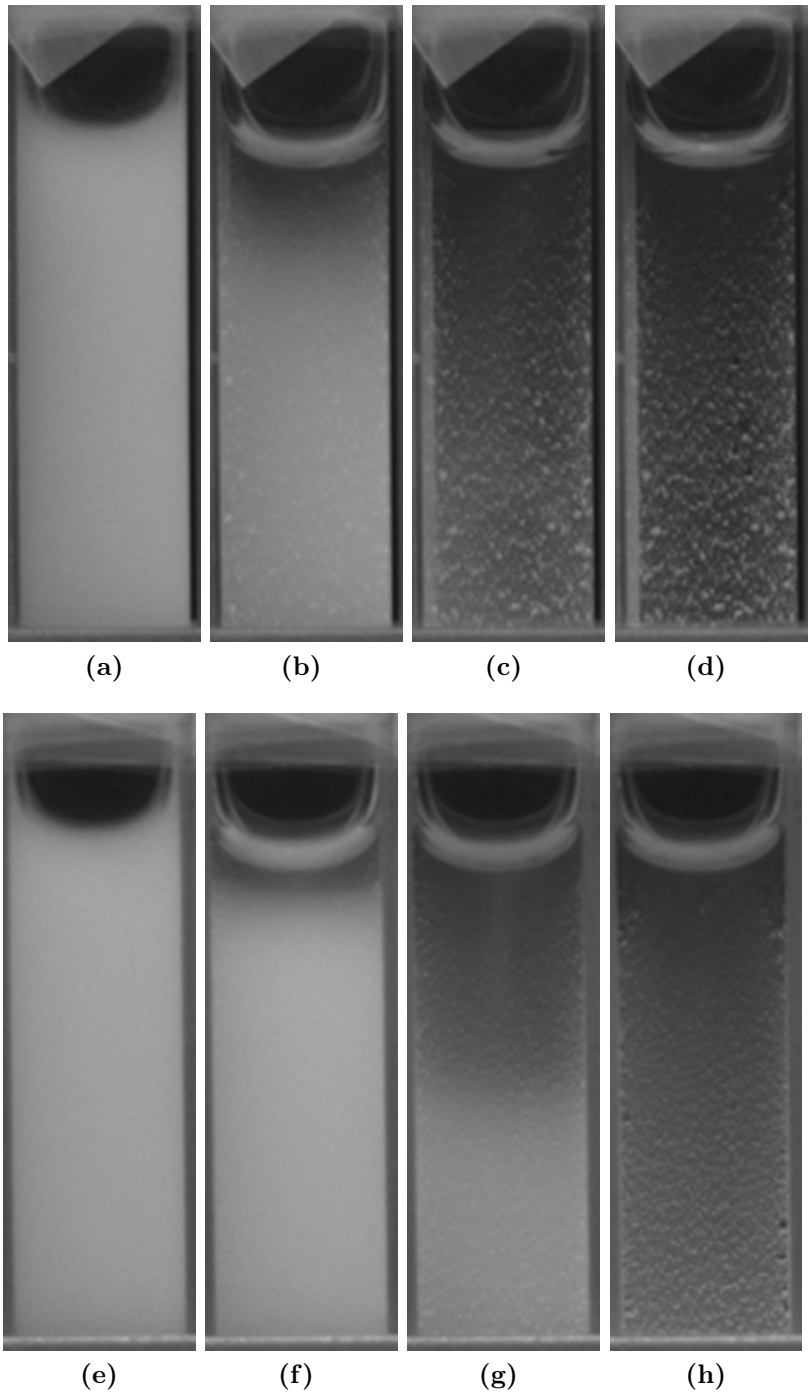

Figure 2.13 *Representative images of the fast and slow sedimentation behaviour of the $\phi = 0.025\,\%$, pre-mix pH 4.5 sample. The times after mixing are approximately 3 minutes (a, e), 2 hours (b, f), 6.5 hours (c, g) and 20.5 hours (d, h) respectively.*

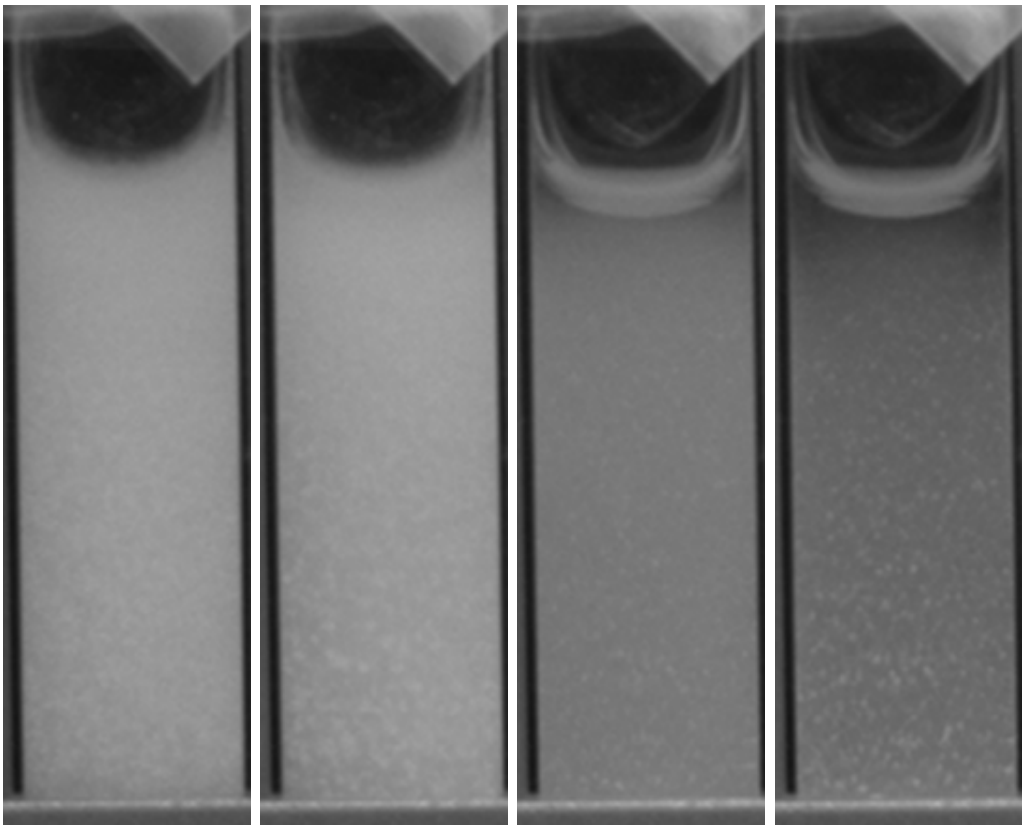

(a) *1 minute* **(b)** *1.5 minutes* **(c)** *30 minutes* **(d)** *1 hour*

Figure 2.14 *Representative images of the sedimentation behaviour of the* $\phi = 0.08\,\%$*, pre-mix pH 4.5 sample*

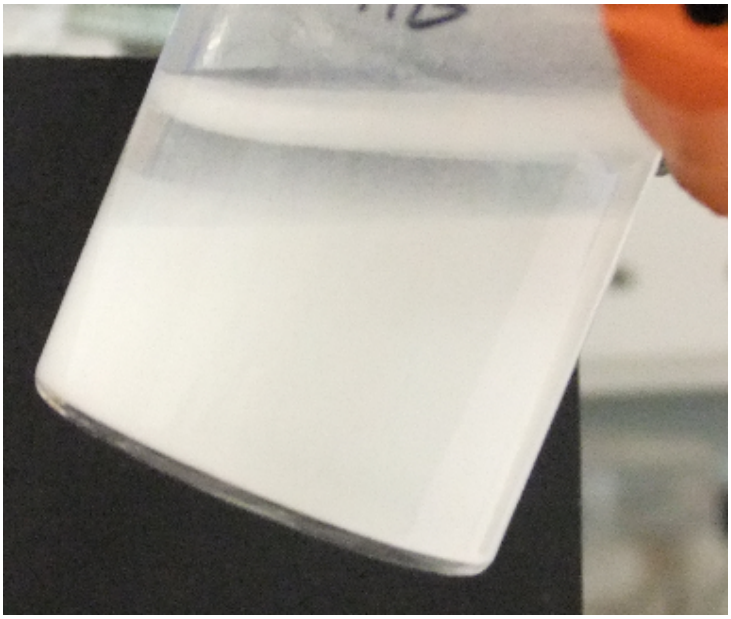

(a) *pre-mix pH 3.10, $\phi = 0.8\,\%$ sample with slight tilt, five minutes after mixing.*

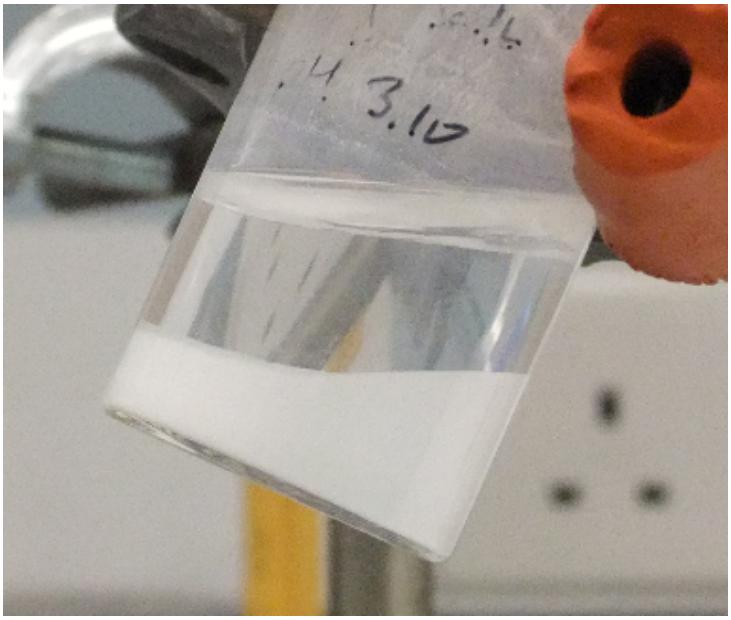

(b) *pre-mix pH 3.10, $\phi = 0.8\,\%$ sample with slight tilt, two hours after mixing*

Figure 2.15 *pre-mix pH 3.10, $\phi = 0.8\,\%$ sample with slight tilt, five minutes and two hours after mixing*

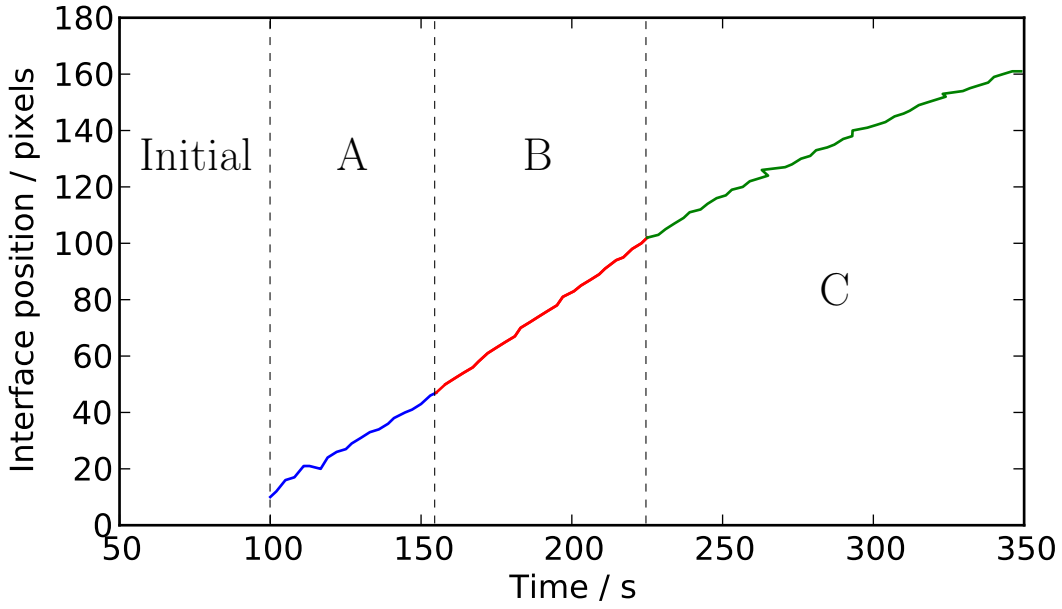

Figure 2.16 *An example sedimentation profile, indicating the four regimes of studied behaviour.*

2.3.5 Time Lapse Photography of Sample Dynamics

Data were collected for all the 'blue dot' points in the phase diagram as well as an additional series of points logarithmically spaced between $\phi = 0.25\,\%$ and $\phi = 4.1\,\%$ at a fixed pH (before mixing) of 4.5. As mentioned earlier (section 2.2.5), the speed of sedimentation for the $\phi = 0.25\,\%$ samples was high enough that special precautions had to be taken to ensure the sediment interface was appropriately imaged.

In general every curve had a similar shape, exemplified by figure 2.16. There is an initial time during which the sediment is not visible. During this time, the sample gels and the edges of the meniscus drain of material. At a certain time τ_A it becomes possible to resolve the sediment/supernatant interface from the supernatant/air interface. For a short period after the sediment interface can be resolved, the collapse velocity is linear in time (A). At a time τ_{AB} the velocity changes discontinuously but remains constant (B). At longer times, the velocity begins to decay to zero as the sediment approaches its final state (C). At some time τ_f the velocity tends to zero and the sediment attains a final volume fraction ϕ_f. Example images at times τ_A and τ_{AB} are shown in figure 2.17.

For each curve, the gradient of part A was found by least-squares fitting. The

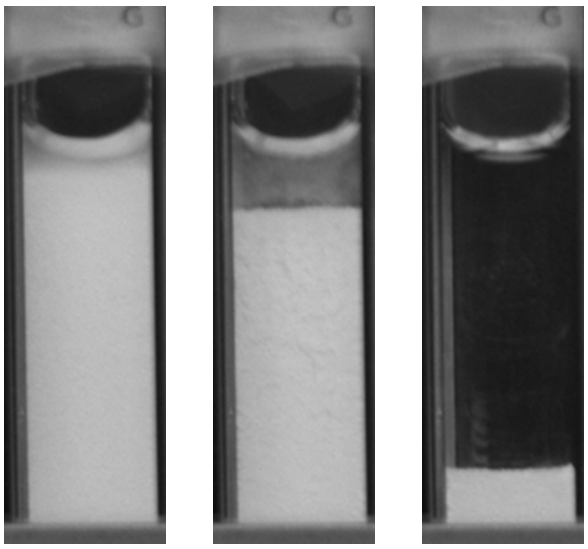

(a) τ_A **(b)** τ_{AB} **(c)** τ_f

Figure 2.17 *Example images of the state of a sample at the transitions between the periods of interest*

end of regime A was found by finding the number of points which minimised χ^2 for a linear fit starting with the earliest data points available. An example of the residuals after fitting the first part of the curve can be seen in figure 2.18. The final sediment volume fraction ϕ_f was also extracted by assuming that the supernatant contained a negligible mass of titania and finding ϕ_f from the ratio of sediment height to initial sediment height (see equation 2.12). This assumption is validated by noting titania suspensions are visibly turbid down to volume fractions as low as 1×10^{-5}.

$$\phi_f = \frac{h_0}{h_f}\,\phi \tag{2.12}$$

Data for every sample can be found in appendix B. A summary giving the mean and standard deviation of the appropriate values is given in tables 2.10 and 2.11.

It can be seen from table 2.10 that pH (before mixing) has no effect on the initial sedimentation velocity v_A. The secondary sedimentation velocity v_B is the same within error for samples with pre-mix pH 3.1 or 3.5, but lower for pre-mix pH 4.5, indicating that charging the colloids results in a decrease in v_B. A corresponding increase in τ_{AB} can also be identified. Pre-mix pH appears to have no effect on the final sediment height h_f and therefore no effect on the calculated final sediment volume fraction ϕ_f. As discussed earlier and further in chapter 3, this may be due to controlling suspension pH by modifying solvent pH before, rather

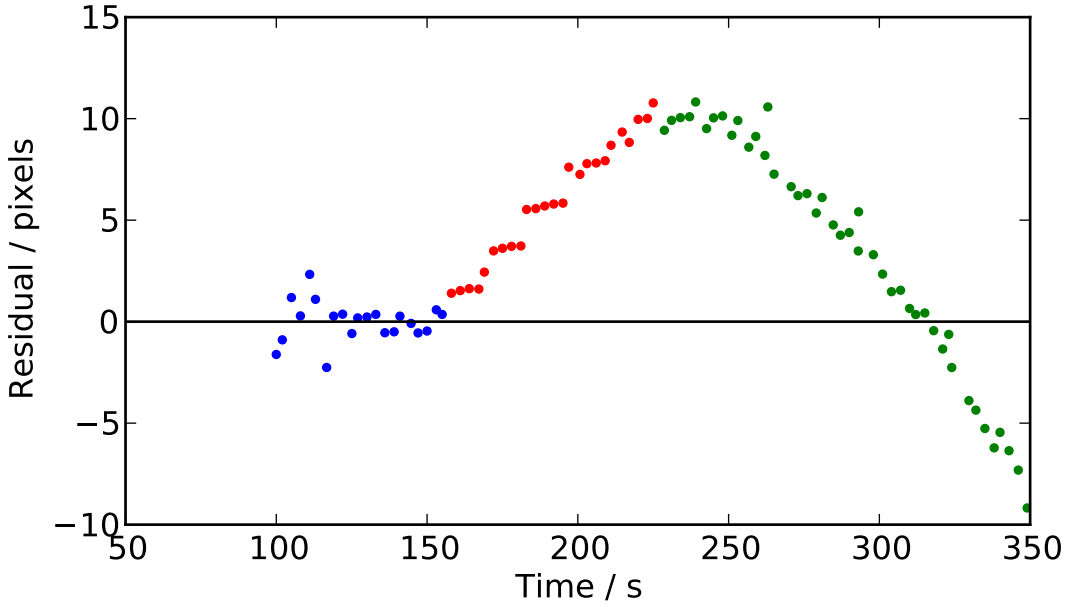

Figure 2.18 *Residuals of the example data set after a linear fit to the first twenty data points (regime B).*

Table 2.10 *Mean and standard error of extracted parameters for samples of varying pre-mix pH in appendix B.*

ϕ %	pH (pre-mix)	v_A µm s^{-1}	v_B µm s^{-1}	τ_{AB} 10^3 s	h_{AB} mm	h_f mm	ϕ_f %
0.8	3.1	22.6(3)	29.0(16)	0.3(3)	28.4(6)	11.1(4)	2.41(3)
	3.5	26(2)	26(2)	0.35(2)	27.6(9)	11.43(13)	2.35(1)
	4.5	22.8(16)	16.9(10)	0.5(4)	25.1(7)	11.8(2)	2.37(6)
2.5	[1] 3.1	1.44(7)	1.33(4)	2.34(8)	33.1(2)	25.0(3)	3.49(2)
	[1] 3.5	1.41(2)	1.29(3)	2.34(8)	33.3(3)		
	4.5	1.37(2)	1.17(3)	2.70(8)	31.2(5)	24.4(4)	3.40(2)

[1] These results do not have clearly defined ends to the initial linear period and so v_B and therefore τ_{AB} may not be accurately identified in these cases.

than after, mixing. Due to the increase in net titania surface area with increasing volume fraction of titania and assuming a given pH results in a constant amount of titania surface becoming charged, the effective charge per unit colloid area will be reduced as volume fraction is increased.

Table 2.11 *Mean and standard deviation of extracted parameters for samples of varying ϕ at a fixed pre-mix pH of 4.50 in appendix B.*

ϕ %	v_A µm s^{-1}	v_B µm s^{-1}	τ_{AB} 10^3 s	h_{AB} mm	h_f mm	ϕ_f %
0.25	230(30)	370(30)	0.052(2)	40(2)		
0.6	44(3)	60(6)	0.126(12)	32.9(8)	10.01(12)	2.23(2)
0.8	22.8(7)	16.9(5)	0.50(16)	25.1(3)	11.8(7)	2.37(3)
1.2	9.38(18)	8.7(3)	0.47(4)	32.6(3)	15.56(19)	2.67(2)
1.7	3.9(4)	4.4(3)	0.68(8)	33.4(5)		
2.5	1.37(2)	1.17(3)	2.70(9)	31.2(5)	24.4(4)	3.40(3)
3.2	0.58(7)	0.41(7)	5.4(9)	33.3(8)	31(2)	3.7(3)
3.9	0.15(2)	0.10(2)	12.0(11)	34.4(5)	33.2(4)	4.14(2)
4.3 [1]	0.06	0.02	19.2	34.2	33.5	4.53

[1] Most $\phi = 4.3\,\%$ samples did not sediment within the resolution of the imaging apparatus over a period of three days. This value represents the maximum recorded initial velocity and as such is an upper bound on the sedimentation velocity. This value was excluded from fitting.

Table 2.11 displays the dependence of the fitted parameters on volume fraction at a fixed pre-mix pH of 4.5, which should correspond to the low charge regime. v_A appears to display power law dependence on volume fraction (see figure 2.19). This is not unexpected as v_A can be related to the flow of solvent through the fractal structure of the gel (see discussion section 2.4). A non-linear fit to an empirical relation of the form $v_A = A\phi^B + C$ was performed. The fitted parameters were $A = 8 \times 10^{-10}$, $B = -2.13$ and $C = -7 \times 10^{-7}$. The quality of the fit was good, with a reduced χ^2 of 1.47. Fitting a power law without an additional constant yielded a much worse fit ($\chi^2 = 49$). Rearranging the equation indicates that $\phi = 0.04$ when $v_A = 0$, indicating the suspension develops a yield stress sufficient to resist gravitational compaction at this volume fraction.

The v_B velocities also appear to demonstrate a power law dependence with volume fraction (see figure 2.20) which is very similar to the v_A power law. The fitted parameters were $A = 3.5 \times 10^{-10}$, $B = -2.29$ and $C = -4.73 \times 10^{-7}$ with a reduced $\chi^2 = 17$. The poor goodness-of-fit parameter may be due to systematic uncertainties introduced into the measurement from the occasionally ill-defined

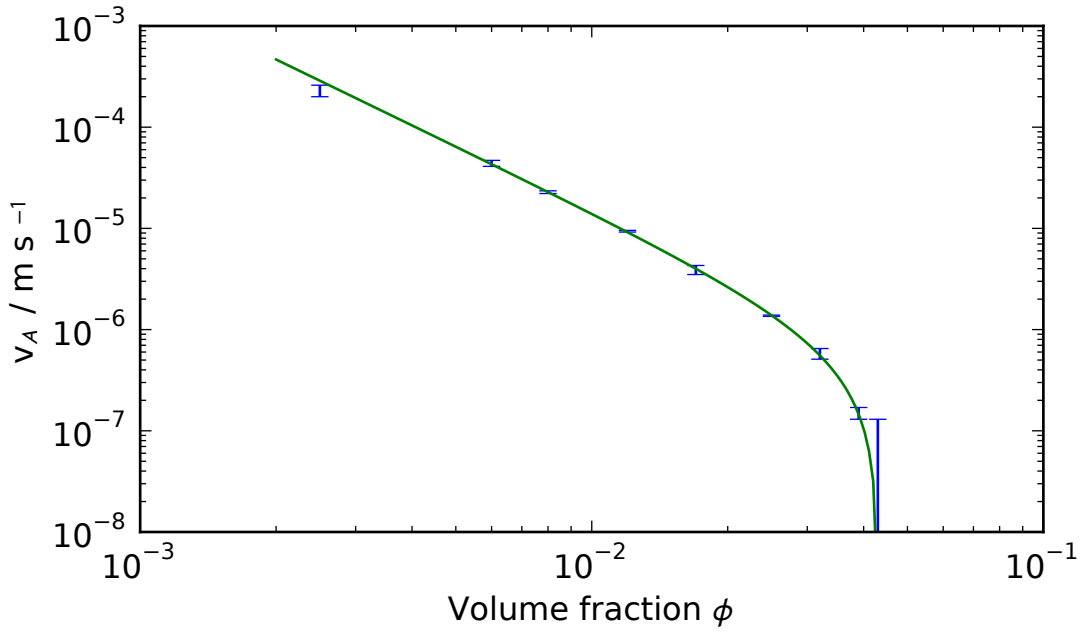

Figure 2.19 *A log-log plot of volume fraction versus initial sedimentation velocity v_A at pre-mix pH 4.50 (values from table 2.11).*

transition from period A to period B.

The volume fraction of the sediment at long times, ϕ_f, appears to follow a linear relationship with initial volume fraction (see figure 2.21). The results of the fit $\phi_f = A\phi + B$ were $A = 0.59$ and $B = 0.02$ with a χ^2 of 8. The larger goodness-of-fit value found here may be due to the statistical errors used in the analysis becoming of the same order of magnitude as the instrumental errors arising from the finite pixel size of the CCD camera used. Both of these errors are of the order of 1% of ϕ_f.

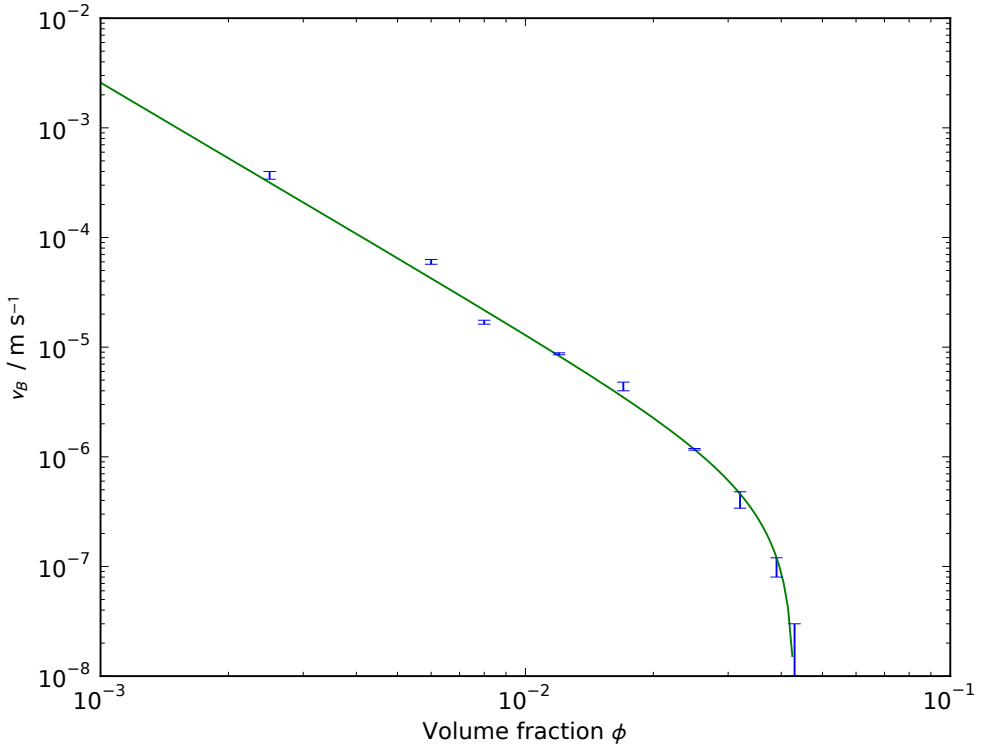

Figure 2.20 *A log-log plot of volume fraction versus secondary sedimentation velocity v_B at pre-mix pH 4.50 (values from table 2.11).*

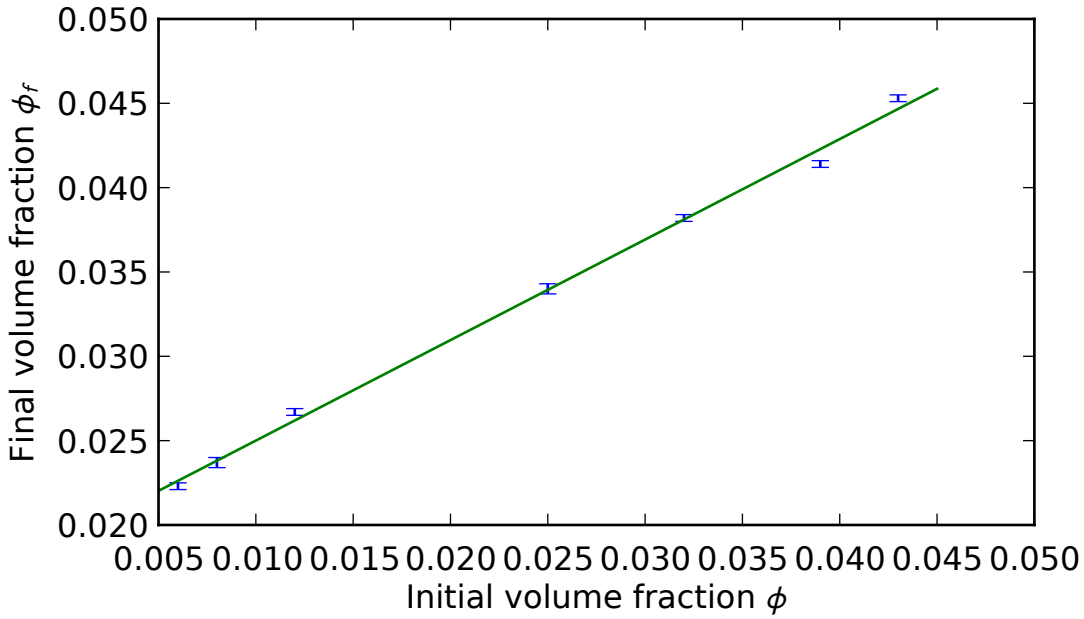

Figure 2.21 *A plot of volume fraction versus final volume fraction ϕ_f at pre-mix pH 4.50 (values from table 2.11).*

2.3.6 Characterisation by DLS of Stable Suspensions

The raw correlation functions for the $\phi = 0.025\%$, pH 3.1 (before mixing) sample are presented in figure 2.22. $g^{(2)}(\boldsymbol{q}, \tau)$ is plotted against $q^2 t$ to collapse the expected dependence from Brownian motion of $g^{(2)}(\boldsymbol{q}, \tau)$ on the square of the scattering vector. Each run of the ALV-5000 correlator in a multi-run experiment appears to incorrectly normalise the calculated $g^{(2)}(\boldsymbol{q}, \tau)$, resulting in the y-intercept of $g^{(2)}(\boldsymbol{q}, \tau)$ for the second and third runs to be double and triple that of the first run, respectively. This should not affect the fitting process other than to artificially increase the fitted value of the coherence. The recorded $g^{(2)}(\boldsymbol{q}, \tau)$ at low scattering angle (30°) also seems to differ significantly from other measurements.

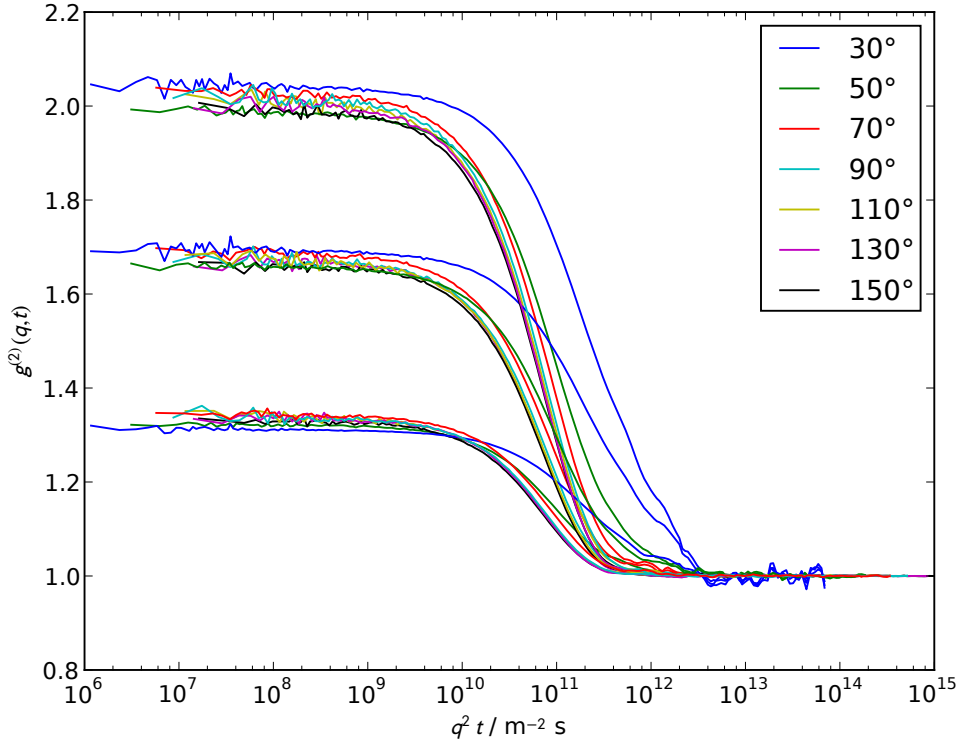

Figure 2.22 *Raw DLS data for supernatant of the $\phi = 0.025\%$, pH 3.1 (before mixing) suspension.*

The data in figure 2.22 were fitted via a second order non-linear fit as described in chapter 4. The results against scattering vector are presented in figure 2.23. Although fit errors could not be estimated due to the absence of error data for $g^{(2)}(\boldsymbol{q}, \tau)$, an indication of the error can be seen in the spread of fitted results at each angle, as each measurement at a single angle was identical. The fitted hydrodynamic radius and polydispersity index are constant at high q (high

scattering angle) and increasing at low q, as can be expected from the raw data. The increase begins when $qR_H \approx 1$. The fitted polydispersity index is above 0.4 for $q < 0.01\,\mathrm{nm}^{-1}$, which indicates that systematic deviations from the fitting procedure may be present in parameter estimates below this threshold.

The DLS data for the time resolved measurements, described in section 2.2.6, of $\phi = 0.025\,\%$ and $0.08\,\%$, pre-mix pH 3.5 samples are presented in figures 2.24 to 2.27. Two samples were prepared at each concentration. From the raw data it was noted that the fourth fraction of the $\phi = 0.08\,\%$ sample on days 1 and 2 display very broad decorrelation curves. These broad curves are attributed to accidental disturbance of large agglomerated clusters which will have rapidly sedimented to the bottom of the vial.

The data were fitted to an intensity auto-correlation function expanded through the method of moments to second order as described in chapter 4 ("Dynamic Light Scattering"). Fitted parameters are tabulated in appendix A. Instrument-provided values for the error in the measurement of $g^{(2)} - 1$ were only available for days 3 – 5 of measurement and therefore errors estimated from the fit are not available for days 1 and 2. As systematic error becomes significant using this analysis for systems with a polydispersity μ_2 (defined as the variance of the size distribution) greater than 0.4, results with a fitted $\mu_2 > 0.4$ have been excluded from the analysis below.

The mean radius of gyration as a function of sample age is given in figures 2.24 and 2.25. Both samples are included for the first two fractions to demonstrate result repeatability. Fit errors were estimated to be ca. 2% for days 3, 4 and 5. Exact fit error estimates are not available for days 1 and 2 as the error in the measured $g^{(2)}(\boldsymbol{q}, \tau)$ was not recorded, but should be similar due to an identical experimental protocol.

All samples show a decrease in measured hydrodynamic radius over three days from ca. 250 nm on day 1 to ca. 100 nm by day 3. The measured size distribution is reasonably reproducible for the top two measured fractions with the exception of the second repeat (red points) of the 0.08% sample on day two. The bottom two fractions exhibit greater variability, although the trend established by the top fractions is still present. In general there is an uneven distribution of outliers with more measurements of unusually high radii than unusually low. This may be due to large agglomerates being disturbed during sample loading. As the intensity from a spherical scattering increases as the sixth power of its radius the effect of

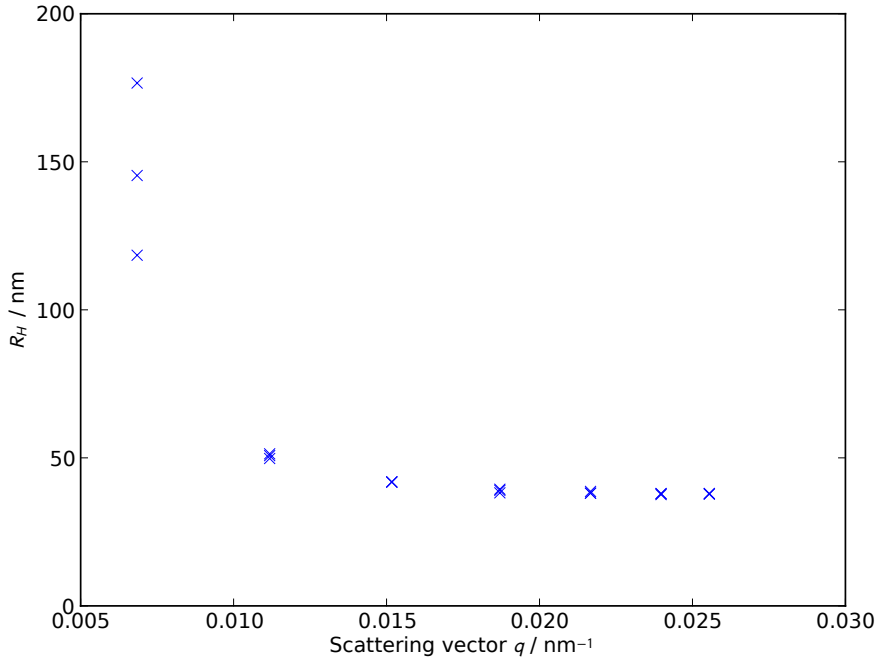

(a) *Fitted hydrodynamic radius for $\phi = 0.025\%$, pH 3.1 (before mixing) sample against scattering vector*

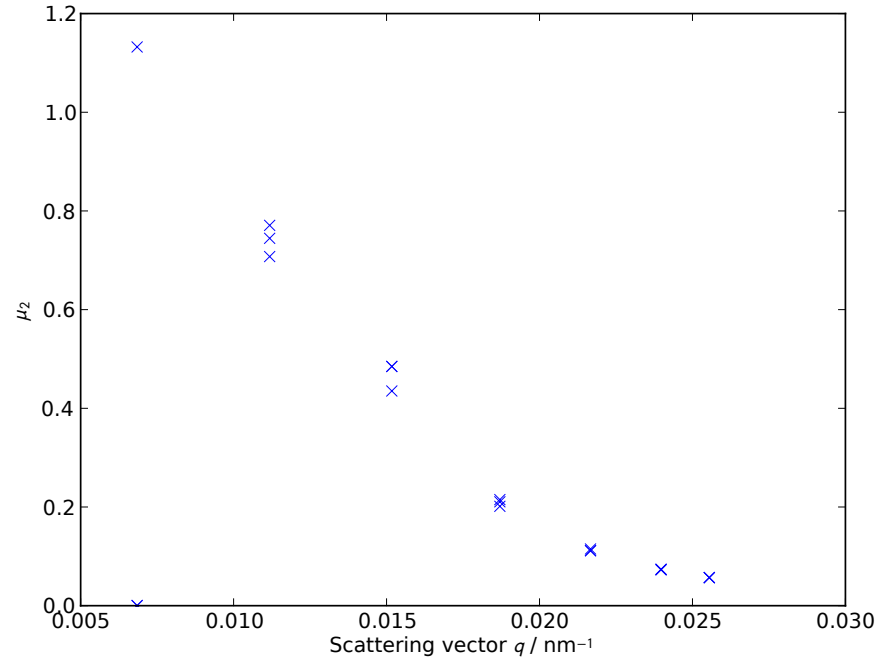

(b) *Fitted polydispersity index for $\phi = 0.025\%$, pH 3.1 (before mixing) sample against scattering vector*

Figure 2.23 *Fitted parameters for the $\phi = 0.025\%$, pH 3.1 (before mixing) sample.*

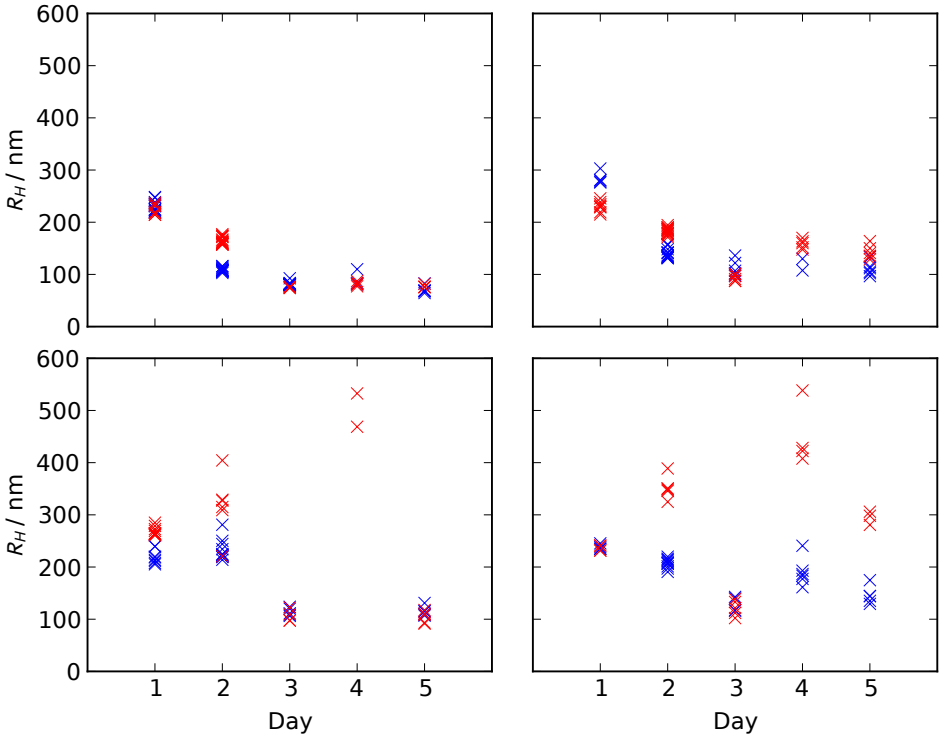

Figure 2.24 *Fitted effective hydrodynamic radii of gyration versus time of measurement for $\phi = 0.025\,\%$, pH 3.5 (before mixing) samples. Red and blue denote the two sample repeats tested. Top,* 2.5 mL, 5.0 mL *and* 7.5 mL *fractions are presented top left, top right, bottom left and bottom right respectively.*

a few large scatterers may affect the fitted value. As the fitting procedure is also not optimised for heterogeneous size distributions, this may also affect the fitted hydrodynamic radius.

The fitted polydispersity index as a function of sample age is given in figures 2.26 and 2.27. Estimated fit errors are ca. 15% for each data point. As above, fits with $\mu_2 > 0.4$ have been omitted due to the effect of systematic errors from the fitting process. Fitted polydispersities fluctuate strongly between measurements, although most are still within 2σ of the mean.

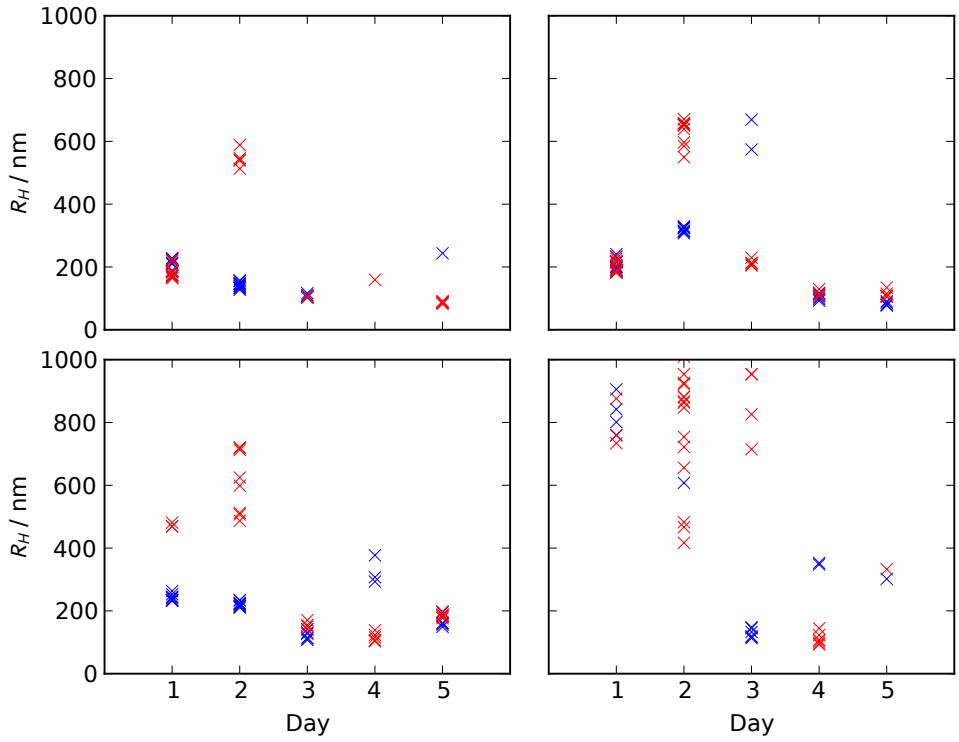

Figure 2.25 *Summary of fitted effective radii of gyration versus time of measurement, for* $\phi = 0.08\,\%$*, pH 3.5 (before mixing) samples. Red and blue denote the two sample repeats tested. Top,* $2.5\,\mathrm{mL}$*,* $5.0\,\mathrm{mL}$ *and* $7.5\,\mathrm{mL}$ *fractions are presented top left, top right, bottom left and bottom right respectively.*

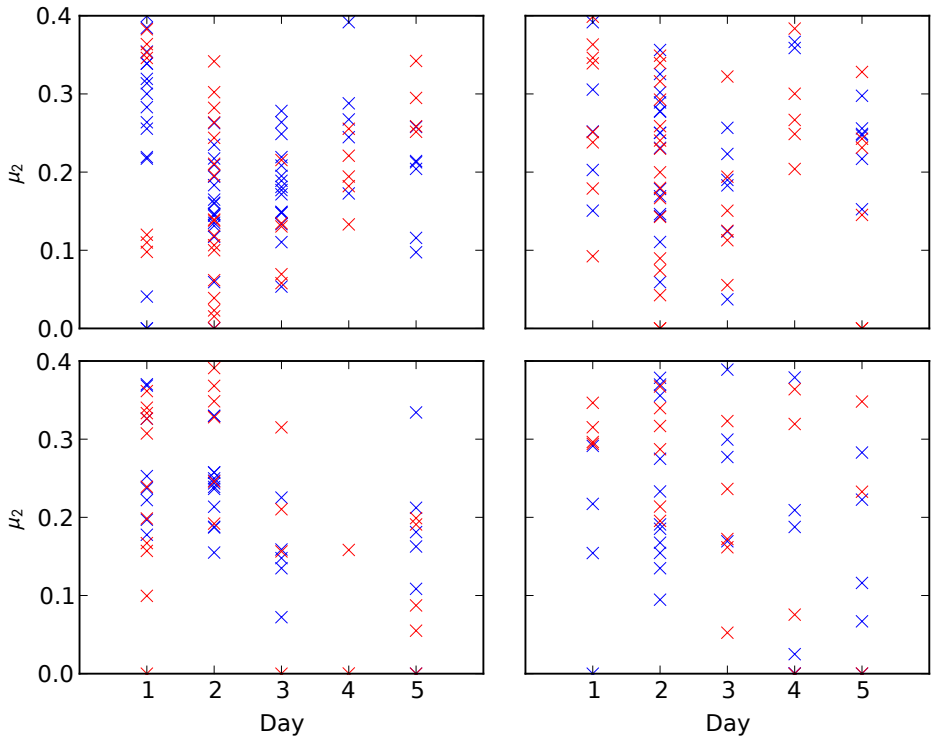

Figure 2.26 *Fitted polydispersity versus time of measurement, for* $\phi = 0.025\,\%$*, pH 3.5 (before mixing)samples. Red and blue denote the two sample repeats tested. Top,* 2.5 mL*,* 5.0 mL *and* 7.5 mL *fractions are presented top left, top right, bottom left and bottom right respectively.*

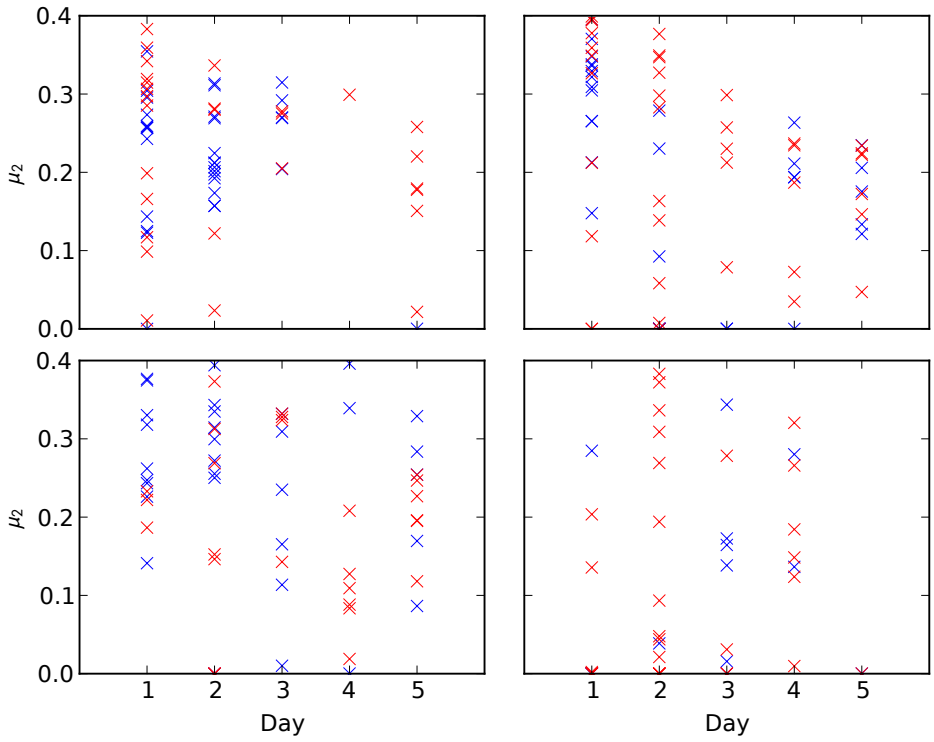

Figure 2.27 *Summary of fitted polydispersity versus time of measurement, for* $\phi = 0.08\,\%$*, pH 3.5 (before mixing) samples. Red and blue denote the two sample repeats tested. Top,* $2.5\,\mathrm{mL}$*,* $5.0\,\mathrm{mL}$ *and* $7.5\,\mathrm{mL}$ *fractions are presented top left, top right, bottom left and bottom right respectively.*

2.3.7 Rheology of Non-Sedimenting Suspensions

As a simple test of the nature of the non-sedimenting suspensions ($\phi \geq 7.6\,\%$) samples were prepared in the standard way at a pre-mix pH of 4.5 and either with no salt or 3 mM KCl or K_2SO_4. They were then transferred to a sealed cuvette inside an incubator using a plastic disposable syringe. The temperature was maintained at 25 °C by the incubator, with the temperature calibration achieved using a glass thermometer placed inside the cabinet. Photographs were taken of the samples while upright. The samples were then gently laid on their side (lying perpendicular to gravity) and left in the incubator before being imaged again after eight days.

The images are presented in figure 2.28. None of the samples displayed any significant flow over eight days. Milky liquid appeared to collect at the lower edge of the sample with no salt. The sample with KCl appeared to demonstrate some heterogeneity at the interface which may be related to some slip of the material downward. The K_2SO_4 sample also appeared to demonstrate a similar behaviour. Confirmation of the nature of this change is difficult due to the opaque nature of the titania gel.

A steady state flow curve is a plot of material viscosity as a function of shear rate after a steady flow has been established. The flow curve for $\phi = 7.6\,\%$, pre-mix pH 3.1 and pre-mix pH 4.5 samples is presented in figure 2.29. It demonstrates the apparent shear thinning nature of titanium dioxide suspensions. Pre-mix solvent pH seems to have little effect on the flow properties. When the shear rate is above $20\,s^{-1}$ and below $0.2\,s^{-1}$ viscosity appears to show a power law dependence on shear rate with an exponent of approximately -0.8. In between these values there appears to be a plateau region in the viscosity although the onset and magnitude of the plateau is not well defined between different samples. It is likely that the plateau region is due to inhomogeneous response of the sample e.g. slip at the geometry surface or shear banding behaviour, due to the combination of the irreproducibility of the flow curve within the region and the well-defined transition from reproducible to irreproducible behaviour.

Slip is an important consideration when interpreting rheological data for particulate suspensions [22], especially when the magnitude of the relative viscosity[5] is large. From figure 2.29 it can be seen that this is indeed the case for titanium dioxide

[5]The relative viscosity η_r is defined as the ratio of the apparent suspension viscosity to the viscosity of the solvent.

(a) *No salt, before*

(b) *No salt, after*

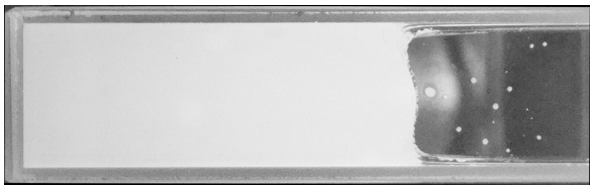

(c) *KCl, before*

(d) *KCl, after*

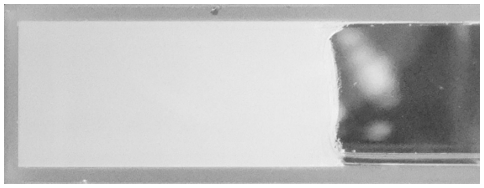

(e) K_2SO_4, *before*

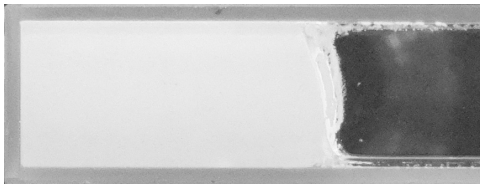

(f) K_2SO_4, *after*

Figure 2.28 *Observation of self-supporting behaviour of* $\phi = 7.6\,\%$ *samples at a pre-mix pH of 4.5. Note that the before images have been rotated from the vertical to the horizontal to allow better comparison with the after images.*

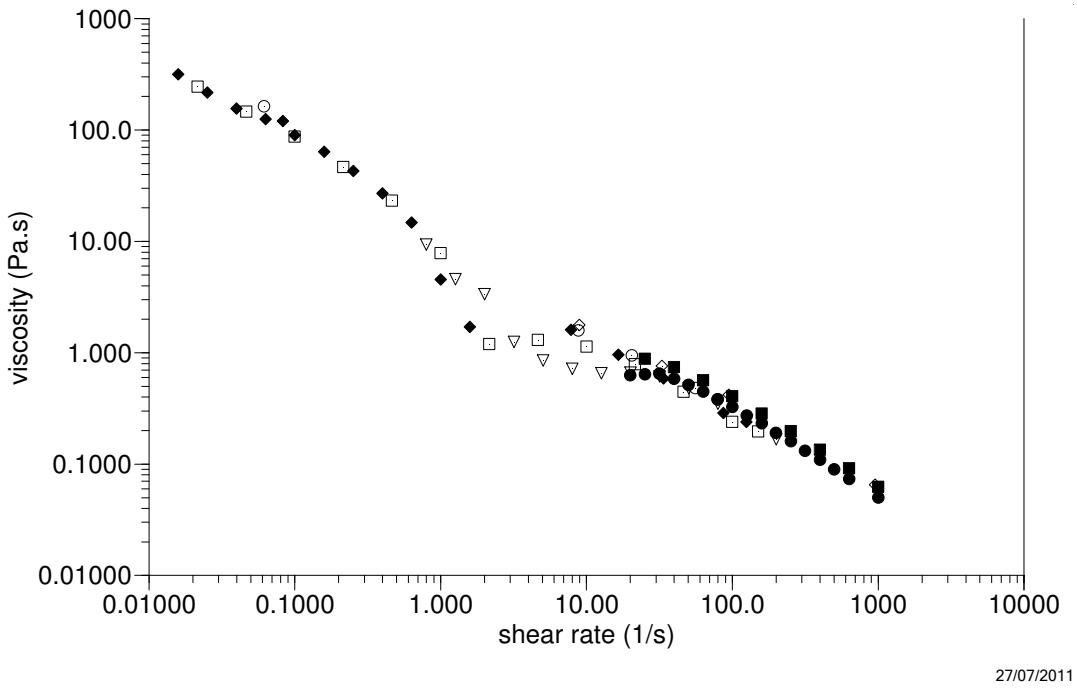

Figure 2.29 *The steady state flow curve for $\phi = 7.6\,\%$ suspensions at high shear rates. The open symbols are pre-mix pH 3.1 samples and the closed symbols are pre-mix pH 4.5 samples. Note values below a shear rate of about $20\,\mathrm{s}^{-1}$ may not be reliable (see text). The filled circles and squares are consecutive measurements (with preshear) of the same sample.*

suspensions. Slip is especially prevalent when the roughness of the geometry used for the experiment is less than the size of a particle radius. Although smoothly machined tools were used in these experiments, it must also be noted that the expected particle size is extremely small (ca. 30 nm) which may act towards mitigating slip effects given that the machined aluminium is unlikely to have nanometer scale smoothness. Finally, it also needs to be noted that Buscall also found a time dependence in the slip behaviour which was attributed to the bonding process between suspension and rheometer tool [21]. Due to the short waiting times after preshear in these experiments, wall slip may well be an important uncontrolled factor.

It was found that conditioning preshear rates between $200\,\mathrm{s}^{-1}$ and $1000\,\mathrm{s}^{-1}$ did not significantly affect the flow curve. Experiments with preshear rates of $5000\,\mathrm{s}^{-1}$ and $8000\,\mathrm{s}^{-1}$ were performed to produce flow curves for extremely high shear. These curves (not shown) resulted in similar shear thinning behaviour but at lower viscosities. The interpretation of these data is difficult as samples appeared to foam or displayed an over layer of solvent when examined after unloading.

As the rheometer is a stress controlled instrument, attempts were made to perform both shear rate sweeps (achieved through a rapid feedback system built into the rheometer) and shear stress sweeps. It was noted during shear stress sweeps that samples did not exhibit any detectable shear until the applied shear stress exceeded approximately 10 Pa. Therefore the data presented in figure 2.29 relate to the properties of the yielded material, not the material in its nascent state.

The properties of the unyielded state can be probed by oscillatory rheometry at low strain magnitudes. Figure 2.30 presents the sample response under an applied sinusoidal strain of amplitude 0.1% and frequencies between 0.01 Hz and 10 Hz. The sample response is solid-like ($G' > G''$) and frequency independent in the range of frequencies studied. The values of the moduli G' and G'' can vary up to 30 % between identical samples and up to 10 % during single frequency sweep (up and down). The varying of the moduli during sweeps on the same sample is a likely indicator that slip is a possible issue [22].

The viscoelastic response of the yielded state can be probed using oscillatory rheometry at larger strain amplitudes. The relaxation moduli are plotted as a function of strain amplitude in figure 2.31. Initially the sample did not yield within the resolution of the instrument. As soon as a threshold stress of about 10 Pa was exceeded, the sample underwent a rapid change from a solid-like to

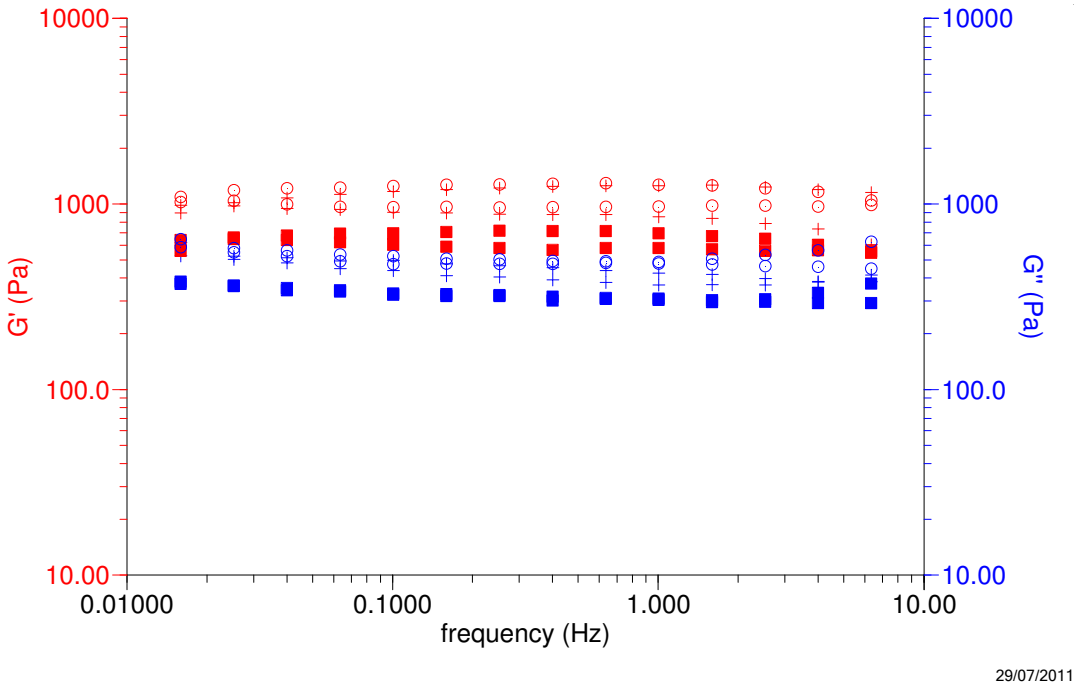

Figure 2.30 *Relaxation moduli against frequency calculated from the oscillatory response of three* $\phi = 7.6\,\%$*, pre-mix pH 3.1 samples. The experimental protocol was a preshear of* $1000\,\mathrm{s}^{-1}$ *for 30 s followed by an oscillatory shear of amplitude 0.1 % across a frequency sweep of* 100 Hz *to* 0.01 Hz *and back up to* 100 Hz*. The first part of the initial sweep (from* 100 Hz *to* 10 Hz*) demonstrated increased values of recorded moduli, which were not replicated on the return sweep or in sweeps with a waiting time of 30 s after preshear. They are attributed to artefacts arising from the preshear and this frequency range is not included in the plot.*

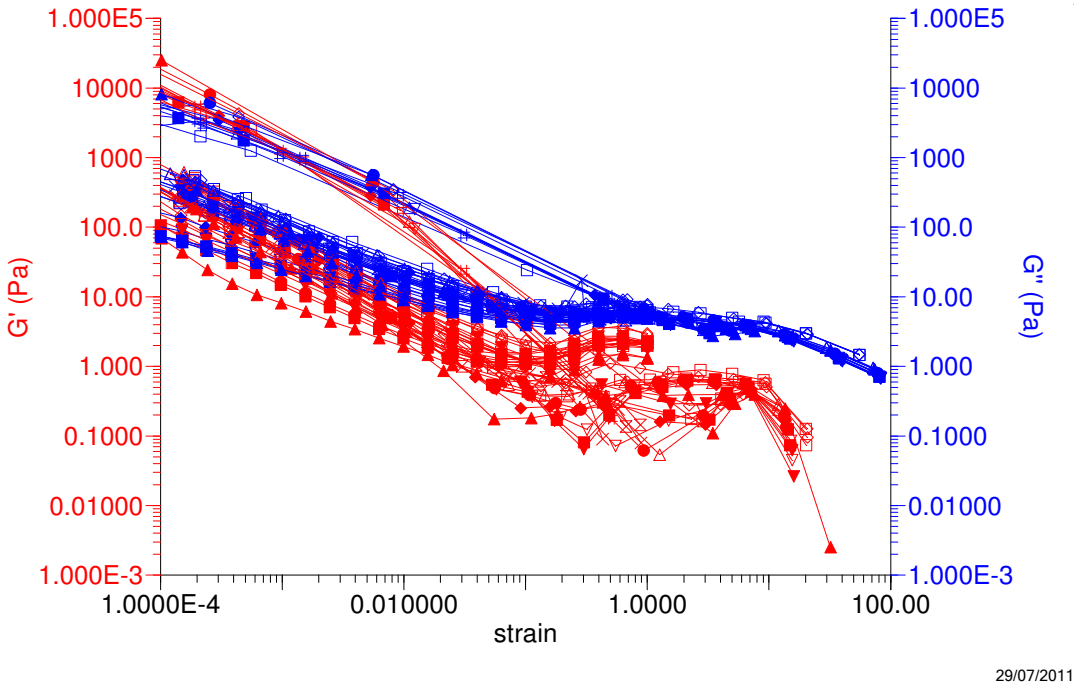

Figure 2.31 *Non-linear oscillatory measurements of the rheological response of several $\phi = 7.6\,\%$, pre-mix pH 3.1 samples. The experimental protocol was a preshear of $1000\,\mathrm{s}^{-1}$ for 30 s, followed by stress-controlled sweep up and down from 0.1 Pa to 100 Pa and a strain controlled sweep up and down from 1×10^{-4} to 1. The initial high modulus branch of the curve is part of the first stress controlled sweep. After yielding, samples showed reproduceable liquid-like behaviour during the downward stress sweep and both strain-controlled sweeps.*

a liquid-like ($G' < G''$) state. This is reflected in the high value moduli branch of the sample response curve, which begins at high values of the modulus (ca. 1×10^4 Pa) and rapidly joins the liquid-like branch, which displays values of the moduli between 1 Pa and 100 Pa. The response of the high modulus branch appears to be solid-like, but as it is likely that these data points only represent transient, non-equilibrium states the sample passes through when becoming liquid-like. The linear oscillatory measurements in figure 2.30 agree in order of magnitude of the high branch storage and loss moduli at the appropriate strain of 1×10^{-3}.

To investigate the time dependent response of samples, with a view to forming a comparison with the work on viscosity bifurcation by Bonn et al [28], a series of experiments were performed where a certain shear stress was applied and the time-dependent viscosity recorded. The results are presented in figure 2.32. It can be seen that below a threshold stress the viscosity diverges to a value beyond the

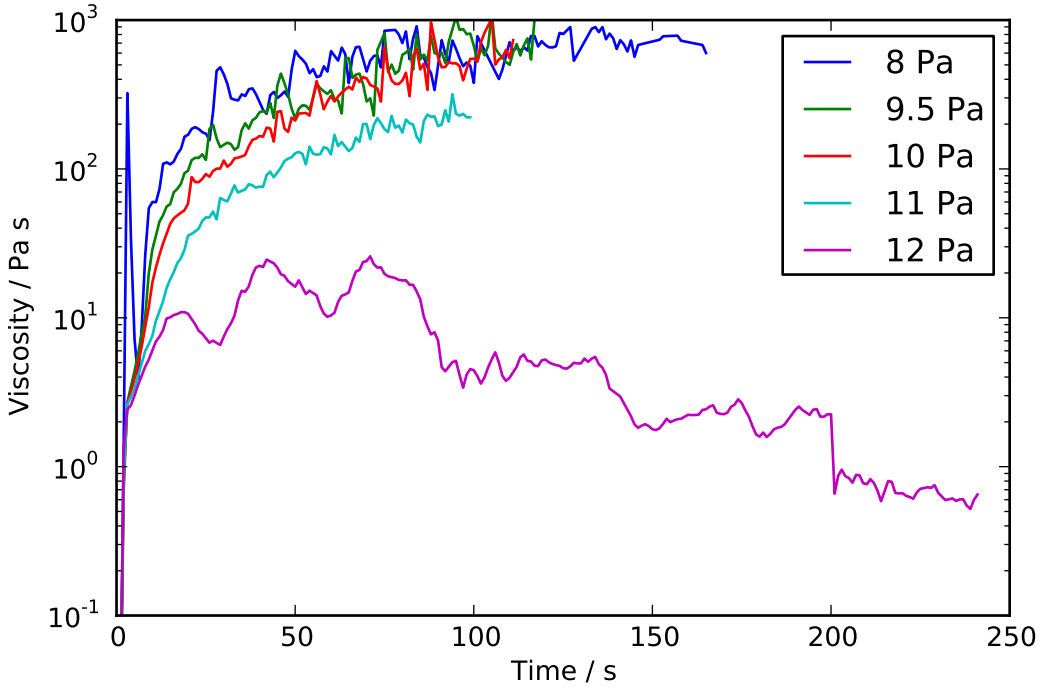

Figure 2.32 *A semi-log plot of viscosity against time after preshearing for premix pH 4.5 titania suspensions at various applied stresses. For low stress the suspension solidifies with the viscosity increasing dramatically with time until reaching the detection threshold of the instrument. For higher stress the viscosity initially rises before decaying slowly.*

resolution of the instrument. Above this threshold a constant viscosity is found, although a steady state is not reached within the duration of the experiment.

2.4 Discussion

2.4.1 Role of pH in Colloid Charging

The long-time stable behaviour of low volume fraction samples described in section 2.3.4 implies that the system is charged at a pH of 3.1 or 3.5 before mixing. This is corroborated by the sensitivity of these samples to ionic strength, with the addition of salts causing the sample dispersion to become unstable. The results of the direct zeta measurements at higher concentration samples ($\phi_w = 1 \times 10^{-4}$, section 2.3.1) support the observed behaviour. However, no dependence on pre-mix pH or ionic strength was noted in the consolidation behaviour or rheological properties of suspensions. This implies that either the zeta potential of the colloids or the ionic strength has an unknown volume fraction dependence or that charging does not significantly affect the consolidation dynamics of the suspensions.

The pH insensitivity of high ϕ rheological properties and intermediate ϕ consolidation dynamics is surprising as it would be expected that the effect of the zeta potential of the colloids would enter both through the bond strength contribution to network elasticity and the effect of the long range repulsions on the hydrodynamics. As discussed further in chapter 3, it is likely that this is due to choosing to fix the solvent pH before mixing rather than after. Reasonably high volume fractions were used to study the sedimentation behaviour, enough to shift the suspension pH close to the isoelectric point regardless of initial solvent pH. The studied suspensions therefore will have had similar and low surface potentials. The zeta potential curve measured is therefore only technically valid in the dilute limit, and higher volume fraction results should be interpreted as being in the weakly charged limit.

There appears to be a small variation in the measured radius of the titania clusters in suspension for varying pre-mix pH and dilution protocols. The hydrodynamic radius, at large q, of the supernatant of the pH 3.1 (before mixing), $\phi = 0.025\%$ sample reported in figure 2.23 is 40 nm. Light scattering intensities vary with the sixth power of the radius of the scattering object. The observed radius may therefore be larger due to contributions from particle dimers or other small oligomers weighting the evaluated correlation rate. In addition, if a degree of aggregation is present in the system, the shape of the aggregated object will affect

its diffusion coefficient, thus affecting the inferred radius. DLS results have been shown to report radii which are larger than radii observed from TEM [32]. Both TEM and DLS results are larger than the manufacturers stated size. This could be due to irreversible aggregation of individual grains during the manufacturing process. Often peak broadening from small angle x-ray scattering (SAXS) is used to infer nanoparticle radius during manufacturing, however this will only measure grain sizes, not agglomerate sizes. Therefore, DLS is reporting the maximum redispersible particle size, which is larger than the measured grain size.

The top fractions of the supernatants of the suspensions used for the time-resolved DLS study, after five days of sedimentation, all yielded hydrodynamic radii of approximately 100 nm. This size increase can be attributed to the slight reduction in charging noted from zeta potential measurements without dilution due to the change of pre-mix pH from 3.1 to 3.5. The radii measured from the DLS measurements which were carried out in parallel with the zeta potential measurements with dilution (figure 2.7) are even larger, approximately 250 nm, and independent of pre-mix pH. This is consistent with the zeta potential data with dilution for pre-mix pHs less than 4 (e.g. close to the experimentally determined isoelectric point, see table 2.4), as the clusters in these suspensions will be neutrally charged and therefore prone to aggregation, but it is not clear why there is no reduction in observed size above a pre-mix pH of 4 as colloidal charging becomes more significant.

2.4.2 Consolidation of Titanium Dioxide Suspensions

It is apparent that at the highest volume fractions studied, the suspensions exhibit gel-like behaviour at long times. The basic tilt testing of suspensions (including tilt testing of consolidated suspensions) combined with the linear oscillatory rheology indicate that the material is solid-like although consolidated volume fractions are still very small.

The response of the consolidating systems under gravitational stress provides, indirectly, information about the structure and interactions in the sediment on the microscopic scale. The primary evidence produced in this study is the power law scaling relation of initial sedimentation velocity with volume fraction. The fluid-like response of the system before consolidation is complete plus the divergent decrease in sedimentation velocity indicates that samples transition from a fluid state to a low density arrested state during consolidation.

The initial sedimentation velocities are much higher than the expected sedimentation velocity in the dilute limit for the primary particles (calculated from a balance of gravitational and drag forces) identified in section 2.3.2:

$$\frac{v_s}{v_0} = v_A \frac{6\pi\eta a}{mg} = \frac{v_A}{4\,\mathrm{nm}\ /\mathrm{s}} = 40 \text{ to } 58\,000 \tag{2.13}$$

This indicates that a large degree of aggregation is occurring. In order to separate out the effect of cluster aggregation from other effects on the sedimentation velocity, an equivalent to v_0 for the cluster aggregates is required.

Allain et al. [4] discussed a scaling approach to the analysis applicable to the fractal nature of DLCA clusters. Starting from the same force balance equation as Buscall and White, they derive a scaling relation for the velocity of sedimentation using the theoretical scaling relations for cluster size and modelling the gel point as a random packing of fractal clusters. The expected scaling relation is $v_A \propto \phi^{\frac{1-D}{3-D}}$ where D is the fractal dimension of the clusters. Note that this argument does not explain the observed divergence in v_A for higher volume fractions as cluster-cluster interactions are modelled as hard spheres.

The calculated fractal dimension using the above argument and the measured exponent $B = -2.13$ is $D = 2.36$. This is larger than the theoretical values of fractal dimension for both DLCA ($D = 1.8$) and RLCA ($D = 2.0$) in the dilute limit. Several factors could contribute to the fractal dimension being higher than expected. Flow-induced rearrangement could increase the fractal dimension if bond strengths are weaker than the shear stresses imposed by the fluid flow. Fractal dimensions as high as 2.5 have been observed for fractal clusters undergoing rearrangement due to high shear rates [88].

In order to investigate the divergence of v_A at higher ϕ, it is useful to plot v_A normalised by the expected sedimentation velocity of a fractal system where aggregates are modelled as effective hard spheres, here denoted by v_0^{eff}. Figure 2.33 presents v_A/v_0^{eff} against ϕ, where $v_A/v_0^{\mathrm{eff}} = A\phi^B$ and A and B are the power law amplitude and exponent obtained from fitting. If the system could truly be modelled as effectively rescaled hard spheres, this quantity would always be one. Deviations from one indicate the effect of inter-cluster interactions or a breakdown of the fractal structure of the aggregates. It can be seen that the ratio does indeed deviate from one for higher volume fraction. What follows is a short discussion of possible interactions which give rise to this phenomenon.

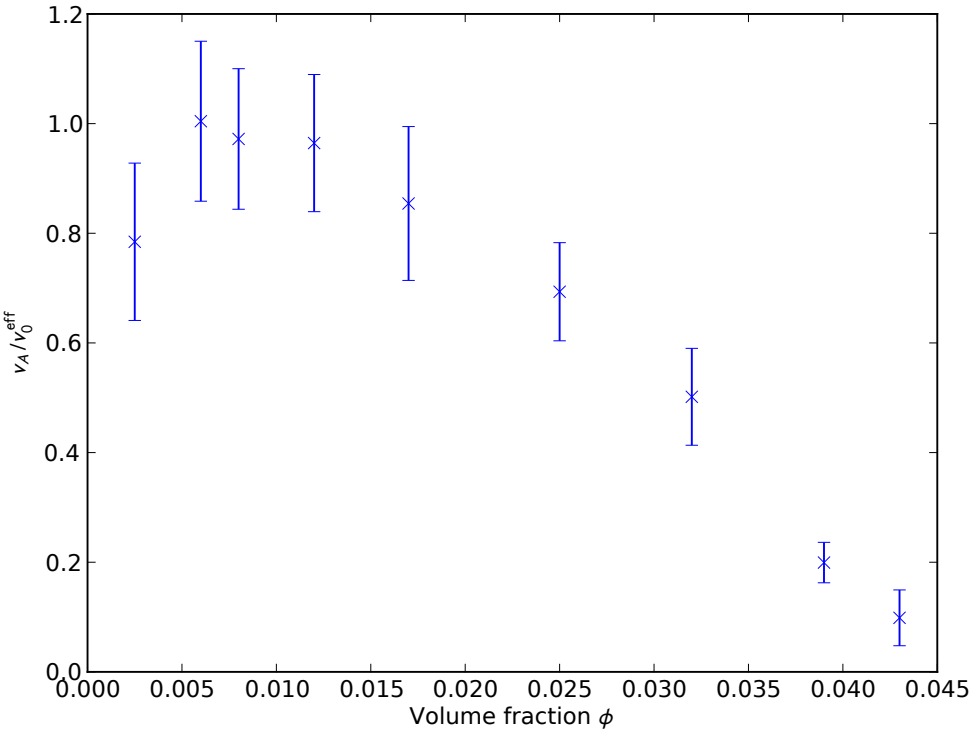

Figure 2.33 *A graph of v_A/v_0^{eff} against ϕ, where $v_A/v_0^{\text{eff}} = A\phi^B$ and A and B are the power law amplitude and exponent obtained from fitting.*

It has been shown [31] that the sedimentation velocity of charged hard spheres displays a divergent term in $\phi^{1/3}$ due to the ordering imposed on the spheres by long-ranged repulsive interactions:

$$\frac{v_A}{v_0^{\text{eff}}} = \left[1 - \frac{2}{3}C\phi^{1/3} + O(\phi^{2/3})\right]. \tag{2.14}$$

Although the errors in the measured data are large, v_A/v_0^{eff} appears to be a concave function, indicating that the dominant correction must scale as $\phi^n, n > 1$. This rules out electrostatic ordering as the dominant correction to the sedimentation velocity.

In anticipation of the gelled system exhibiting some form of space filling network, it is useful to examine the effect of network elasticity on the sedimentation velocity. Buscall and White [23] discussed the consolidation of irreversibly and reversibly aggregated networks. Assuming an irreversibly gelled sample which provides a load bearing network, they derived the following equation (equation 3.21 in the paper) for the initial rate of sedimentation:

$$v_A = -\frac{\Delta\rho g V K(\phi_0)}{\zeta_d}\left[1 - \frac{P_y(\phi_0)}{\Delta\rho g \phi_0 H_0}\right] \tag{2.15}$$

where ζ_d is the hydrodynamic drag coefficient, V is the volume of a particle in the network, $K(\phi_0)$ is a dimensionless quantity giving the effect of the porous network on fluid flow at the initial volume fraction ϕ_0, $P_y(\phi_0)$ is the compressive yield stress of the network and H_0 is the initial height of the gelled column.

The first term outside the brackets is equivalent to v_0^{eff}. From this it can be seen that the dominant contribution to the initial sedimentation velocity should scale with $P_y(\phi_0)/\phi_0$. For fractally aggregated clusters in a gel, the yield stress of the gel is expected to scale as $\sigma_y \propto \phi^{2/(3-D)}$ [109], which results in a scaling for $P_y(\phi_0)/\phi_0 \propto \phi^{(D-1)/(3-D)}$. Using the fractal dimension calculated from the power law exponent in the analysis by Allain, this results in a $\phi^{2.13}$ correction, which is consistent with the concave behaviour recorded. The evidence therefore suggests that the studied sedimentation occurs due to aggregation of primary units into fractal clusters, and that as volume fraction is increased a cluster network forms resulting in an elastic response to gravitational deformation of the gel network. Eventually observable sedimentation ceases as the yield stress becomes sufficient to counter gravitational consolidation.

2.4.3 Rheology of Gelled Titania Suspensions

The titania suspensions exhibit many features previously identified in fractally aggregated systems. The frequency independence of the small shear oscillatory rheology has been theoretically predicted for space-filling networks [73] and experimentally verfied in gelled, density matched aqueous dispersions of polystyrene latex with diameter 20 nm [39].

The high shear rate shear thinning behaviour has been noted by several authors in aggregated colloidal systems previously [25, 94, 105, 109]. To summarise: power law shear thinning persists for fractal gels of widely varying volume fraction, from below the gel point to very concentrated (c.a. 56 % at least). The exponent of the power law depends on the fractal dimension of the clusters [25, 109] and therefore also the strength of the flocculating attraction [105] which affects the cluster fractal dimension through its effect on aggregation kinetics. Reported exponents range from 0.3 to 0.5 for strongly flocculated systems at moderate (up to 20 %) volume fraction, with the exponent increasing to 0.8 for weakly flocculated systems at moderate volume fractions or strongly flocculated systems at high volume fractions (ca. 50 %). Interestingly, the exponent for the titania system is 0.8, even though the rheology is performed at low volume fractions and strong inter-particle attractions are expected.

2.5 Conclusions

Through the studies performed in this chapter, several practical points are raised which are important for future studies of the titania system:

- To ensure surface charging is a significant effect on suspension properties, the pH of the suspension should be adjusted to the desired value after mixing. This informed the experimental protocol used in later work (see chapter 3).
- For volume fractions lower than 5×10^{-5}, dynamic light scattering is a useful probe of aggregate size in the solution environment.
- Near the point of zero charge, gelation is observed for $\phi > 0.082\%$. In a moderately charged state (pH 3.1 or 3.5 before mixing) gelation is observed for $\phi > 0.82\%$.

- Spontaneous collapse of the gel under gravity is seen for $\phi < 8.2\%$. Free-standing gels are seen for $\phi \geq 8.2\%$. The initial collapse rate exhibits power law behaviour away from the free-standing gel point. This is linked to the fractal structure of the collapsing aggregates, and indicates an aggregate fractal dimension of either 1.72 or 2.36 dependent on if network yielding or solvent flow is the principal opposition to gravitational compaction.

- The yield stress of free-standing gels, as identified as the onset of detectable shear, was found to be in the region of 10 Pa to 12 Pa.

The expected electrostatic stabilisation of suspensions at higher volume fractions with decreasing pre-mix pH was not observed, as evidenced by a transition from stabilised behaviour at low volume fraction to unstable behaviour (aggregation) at higher volume fractions. This indicates that simple control of colloid surface charge by measurement of solvent pH *before* mixing is not possible. Later research (see chapter 3) found that measuring pH *after* mixing high concentration suspensions yielded dramatic changes of suspension behaviour with pH, more in line with expectations from the theory of electrostatic stabilisation.

The fractal structures noted here will have important implications for diffusive electron transport in the mesoporous layers of sensitised solar cells if such structures persist in films after drying. Differing fractal dimension will result in larger/smaller pore spaces, which will have an effect both on the volume of 'dead space' in a cell, where light absorbing material is too far from a heterojunction to prevent exciton recombination, and the efficacy with which hole-conducting materials can be back-filled into the network. The structure of drying films and the effect of measuring pH after mixing are discussed in chapter 3.

In addition, the presence of cluster phases in suspension raises the possibility of designing a cell in which they form the central structure. Appropriately large stable clusters could be chemically treated with wet sintering agents such as titanium tetrachloride (see chapter 5) and then cast onto a substrate to form a porous layer with two pore sizes; large inter-cluster pores to facilitate effective infiltration of a hole-transport medium after sintering and fractally distributed nanoscopic pores to enable efficient exciton collection.

Chapter 3

Drying and Cracking of Titania Films

3.1 Introduction

Thin colloidal films, with thicknesses in the range of 10 µm to 500 µm are of technological interest in the areas of energy materials, sensors and catalysis. As with larger ceramic bodies, the manufacture of these materials is complicated by various failure modes activated by strong capillary forces induced in the material during drying. This chapter focuses on one such failure mode, quasi-2D cracking in the plane of the film, and the nature in which these cracks propagate in charge-stabilised, additive-free colloidal titania films.

The fundamental thermodynamic basis of fracture in solid materials was outlined by Griffith in 1920, and a thorough critique of this work is given in 'Fracture of Brittle Solids' by Lawn [69]. Briefly, Griffith's contribution was to place the physics of fracture on a firm foundation by expressing the problem in terms of energy transfer between surface and bulk energy during crack formation and modelling this as a reversible thermodynamic process.

Consider a small nucleated crack in a solid under uniform tension. The tension is acting to pull the crack further apart, therefore an increase in crack length will result in a reduction in system energy due to the relaxation of the stress in the solid. Balancing this is the increase in solid surface area on crack extension and associated free energy penalty. Evaluating the first and second derivatives of the

sum of these energies using the theories of linear elasticity to model the stress shows that an unstable thermodynamic equilibrium exists with respect to small perturbations of crack length. Crack extension is suppressed until crack length exceeds a critical value, beyond which cracks will propagate across the extent of the solid. This concept underlies modern understanding of fracture in systems as diverse as steels, glass, natural stone and ceramics.

Several research areas contribute to current understanding of the drying and cracking of colloidal films. Much work has focussed on the drying of latex suspensions [14, 70, 89], which demonstrate behaviour related to the deformable nature of the particles. Aqueous suspensions of inorganic oxides such as alumina and silica [45, 71] have also been the focus of work in the area of applied ceramic processing technology. Recent academic interest in the area has also related this work to space dividing hierarchical pattern formation in starch solutions [15] and ordered crack pattern formation in confined geometries [3, 5, 9, 33, 34]. The nature of the pattern formation in cracking colloidal films appears to have universal properties which have been observed in a number of other diverse systems including urban road networks [13] and leaf venation patterns [12].

Previous studies on the drying and cracking of charge-stabilised colloidal films have focussed on modifying the range of the interaction using salt screening effects [45]. The inclusion of salt in the study complicates the interpretation of the final stages of drying (including cracking phenomena) due to salt precipitation and bridging effects. In addition, Guo and Lewis concentrated on how the compressive rheology of the suspension determines the tensile stress evolved in the colloidal film during drying, and did not provide any description of cracking phenomena beyond a determination of critical cracking thickness and how this varied with suspension stability.

This study aims to investigate the effect of modifying the strength, rather than the range, of the stabilising electrostatic repulsion in aqueous solutions of titanium dioxide colloid. By modifying the pH of the suspension, the zeta potential of the suspended colloids can be modified with minimal perturbation of the screening length (between pH 3 and 4, the theoretical screening length roughly triples from 10 nm to 30 nm). Titanium dioxide deposited by tape casting was chosen as a material due to its technological importance in soft energy systems. The previous chapter, on titanium dioxide suspension stability and phase behaviour, will inform the work in this chapter.

3.2 Methods and Materials

Suspensions for casting were prepared by placing 3.2 g of titanium dioxide powder (Nanostructured and Amorphous Materials, 10 nm average particle size) into a vial with 10.0 g of distilled water. This mixture was gently stirred and then agitated with an ultrasonic probe (Vibrasound) for 30 s at 20 % oscillation amplitude. After agitation the mixture was a highly viscous, opaque white paste. The pH of the mixture was then adjusted using either 1 M or 0.1 M hydrochloric acid and a pH meter. The mixture was stirred while the acid was added and the mass of the vial and contents measured before and after mixing to obtain a rough estimate of the mass of acid added. The mixture was then sonicated again and the pH measured once more after sonication.

A note about pH values: This method differs from that used to make up suspensions in the phase behaviour chapter of this thesis (chapter 2) where the pH of the solvent used to suspend the titania was set before mixing and not adjusted afterwards. It was found, after the work for the phase behaviour chapter had been completed, that the pH of titania suspensions with volume fractions of several percent changed quite dramatically after mixing. In general the pH would be shifted upwards from that of the initial solvent pH, towards the isoelectric point of titania.

Altering the pH of the suspensions after mixing, as described above, resulted in dramatic changes in suspension viscosity for the higher volume fractions studied in this chapter. The repulsive part of the DVLO potential (see section 2.1.3, chapter 2) depends on the surface charge of the colloids, while the chemical equilibrium between charged and uncharged titania surface groups only depends on hydrogen ion concentration. It is therefore expected that increasing the mass (and therefore surface area) of titania in suspension while holding the initial pH (and therefore hydrogen ion concentration) constant will result in a lower surface charge density for a given solvent pH. A lower surface charge density will affect the inter-colloid potential and therefore the viscosity of the suspension. The decision to switch to fixing pH after mixing was taken for this chapter to maximise the effect of modifying the inter-colloid potential on drying behaviour.

3.2.1 Drop-casting

A plastic 5 mL Luer lock syringe (Braun Injekt) was filled with suspension. It was locked into a syringe pump (New Era Pump Systems Inc., model NE-1010) and attached, via a Luer lock converter, to a ca. 15 cm length of plastic tubing, which in turn was attached to a 5 µL glass micropipette (SupraCaps). The suspension/glass contact angle was increased to prevent the suspension from creeping up the outside of the capillary during deposition. This was achieved by placing the micropipettes into a hexane solution of dichlorodimethylsilane (3:1 mass ratio) for 15 minutes. A diagram of this setup is presented in figure 3.1.

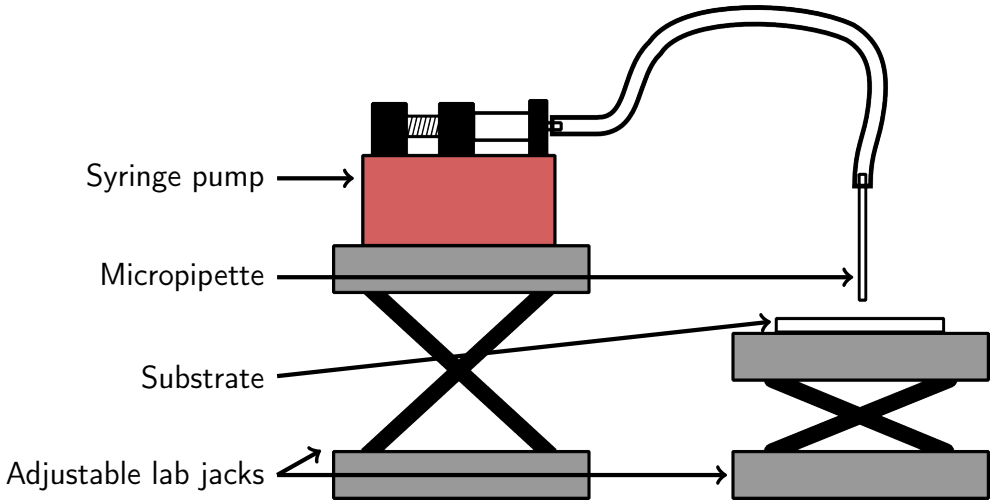

Figure 3.1 *Equipment setup for drop casting experiments. The syringe pump is loaded with a* 5 mL *disposable plastic syringe loaded with casting suspension. The tip of the micropipette is treated with DCDMS in hexane for at least 15 minutes to increase the contact angle between the aqueous suspension and the glass. The lab jack on which the substrate rests is levelled prior to deposition.*

Microscope slides were used as deposition substrates, and were cleaned in 10 % Decon solution for 15 minutes under ultrasonic agitation, followed by thorough rinses with distilled water, ethanol and acetone. After the acetone rinse, the surface was carefully dried with optical tissue by pulling the drying front across the slide. This reduces the chance of large dust deposits forming as the acetone dries.

Prior to deposition, the equipment was flushed with suspension. The deposition procedure itself consisted of pumping 3 µL of suspension to form a pendant drop at the tip of the micropipette and slowly bringing a levelled stage with the substrate on it up to the drop. In this way, controlled volumes of suspension can be

deposited. Five droplets were dispensed onto each substrate. The droplets of suspension were then left to dry in ambient conditions, a process which usually was complete in 2-3 hours, before being imaged.

3.2.2 Tape-casting

Microscope slides were rinsed thoroughly with water, ethanol and acetone. After the acetone rinse the slides were dried by pulling the drying front across the slide using a piece of optical tissue to reduce the level of dust contamination of the surface. A casting mould was formed by affixing three layers of Kapton tape (3M, silicone adhesive, 70 µm average thickness) to the slide. A plastic 1 mL syringe was used to dispense a small quantity of paste onto the slide, and this was spread over the entire slide using a PTFE doctor blade. Excess paste was absorbed after being pushed off the end of the slide with paper towel.

The cast tapes were then transferred rapidly to a precision balance (Sartorius Extend series) equipped with datalogging equipment (see figure 3.3). The Kapton tape moulds were not removed during the drying process. The temperature and humidity of the environment inside the balance enclosure was monitored during drying and recorded at the start and end of the drying process. The temperature did not vary more than 1 ℃ between start and end of drying for all samples and was typically between 20 ℃ and 24 ℃. The humidity increased very modestly by two or three percentage points of relative humidity, with the ambient initial humidity varying from 32 % to 37 % between samples.

The first two post-mix pH 3 tapes cast onto smooth substrates dried inhomogenously due to the combination of a tilt in the drying stage and the low viscosity of the post-mix pH 3 suspension. These results were excluded from analysis. After more careful levelling, the third post-mix pH 3 tape dried homogeneously. The post-mix pH 4 tape cast onto a smooth substrate was also dried on the stage before the tilt was corrected, but did not display inhomogeneous drying behaviour, presumably due to its higher viscosity, and so was included in analysis

Once the films had dried, they were imaged using a CCD camera (qImaging MicroPublisher) both in ambient light (reflection imaging) and with strong backlighting (transmission imaging). The Kapton tape moulds were then removed carefully. Some damage occurred to the edge of the ceramic tape during removal of the mould, especially for tapes cast from lower pH suspensions. This had no

visible effect on the parts of the film which were still well bonded to the slide. The tapes were then profiled with a DekTak profilometer (Veeco Instruments) using a scan range of 1 cm (horizontal) × 131 µm (vertical). The slide was marked with 5 mm graduations to allow co-location of images with profiles, and to spatially calibrate the images. In the text these graduations are denoted as positions 1 – 10. The doctor-blade was passed along the slide from before position 10 to a point 10 mm after position 1.

The low magnification (×5) microscopy images were processed in ImageJ [1]. Several overlapping images were combined into a mosaic using the MosaicJ [104] plugin for ImageJ into a continuous image with dimensions of approximately 7×5 mm and a resolution of 1.12 px μm^{-1}. A Gaussian blurring operation with a sigma of 2 pixels and a median blur with a sigma of 5 pixels were applied to reduce pixel noise while preserving the edges of crack domains. A rolling ball algorithm is then used to remove the grey domains to allow thresholding of crack regions. Individual spurs are then noted in the processed image and these regions are imaged at a higher magnification (×50) to identify if cracks are connected at both ends and thus divide one region into two. The processed image was then modified to reflect this information using hand drawn lines. In the post-mix pH 3 sample, 83 suspect spurs were identified, with 35 identified as true junctions under high magnification and 11 remaining ambiguous (37 were therefore non-terminating cracks). For the post-mix pH 4 sample there were 65 suspect spurs, of which 15 were true junctions, 6 were ambiguous and therefore 44 were non-terminating cracks. The number of crack junctions requiring modification was therefore small compared to the number of junctions imaged. All contiguous regions were then labelled and their calibrated areas measured. It should be noted that at ×50 magnification, cracks smaller than 1 µm will not be resolved.

Junction positions and angles in the microscopy mosaics were automatically measured using a combination of processing of the thresholded image in ImageJ and analysis using Python scripts. The process is summarised in figure 3.2. The thresholded image was first cleared of artefacts by filling of the crack domain regions labelled above and the inverse selection, resulting in a binary image without point defects. The image was then skeletonised in ImageJ and then pruned via morphological thinning with appropriate kernels [36] in Scientific Python. A binary hit or miss transform was then applied with a kernels to identify all eight-connected three way junctions in the skeletonised image. The result of the hit or miss transform was then used to identify all junctions in the

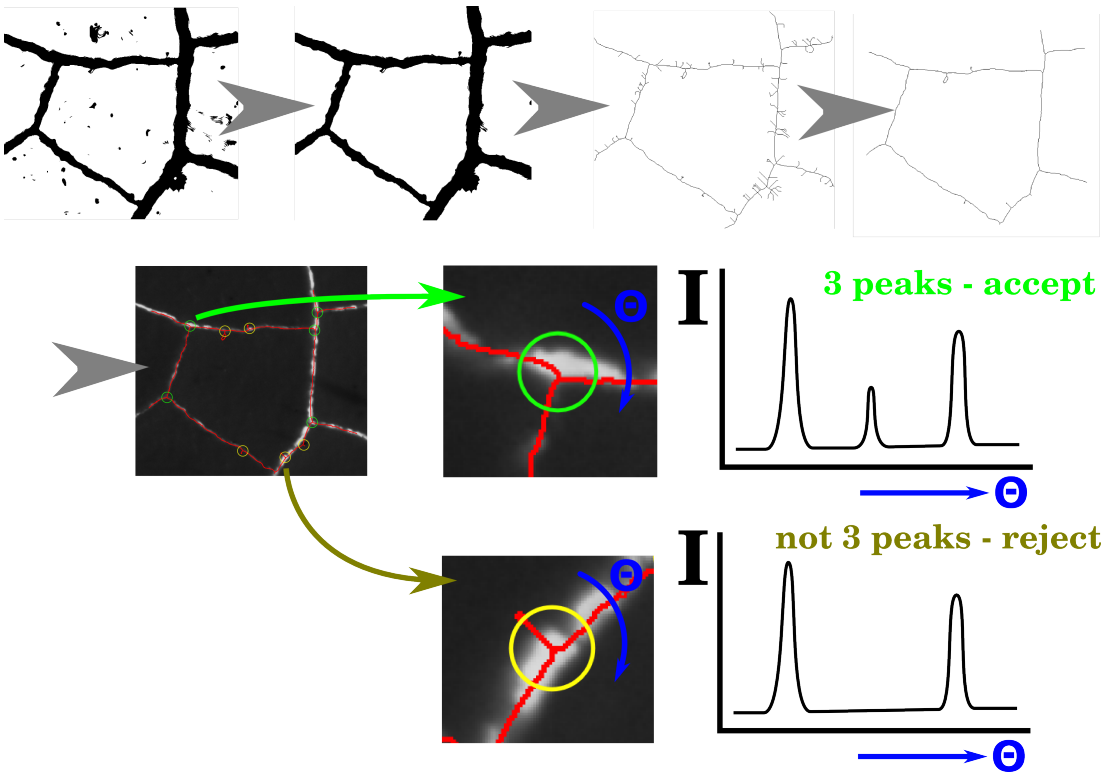

Figure 3.2 *Summary of the crack identification process. 1: artefact removal. 2: skeletonisation. 3: pruning. 4: Identification of valid junctions and fitting of intensity in original image as a function of polar angle.*

original (unskeletonised but filtered) image. Crack directions were then identified by fitting a linear sum of three Lorentzian distributions with a floating baseline to a circular intensity profile about each junction point. The radius of the circular profile was chosen to be 30 px (equivalent to 34 µm) such that false positives in identified junctions (due to small spurs remaining after skeletonisation) were excluded from analysis. The circular profile was chosen to be small enough compared to the width of the cracks that identified cracks were essentially straight from the centre of the junction to the point where they intersect the profile.

The dynamics of crack development were followed using the datalogging balance and time series of images, matching the two for each sample by tying measurements to the computers internal clock. This allows attribution of the effect of various events during drying (such as the first and last appearance of cracks) to changes in the rate of evaporation of solvent in the tape. The rate of mass loss was derived from the mass data by a finite difference method:

$$\frac{\mathrm{d}}{\mathrm{d}t}m(t) \approx \frac{m(t+\Delta t) - m(t-\Delta t)}{2\Delta t}$$

where $\Delta t = 90\,\mathrm{s}$ was chosen as the interval over which $m(t)$ changed appreciably. Smaller values of Δt increased the noise in the signal, while larger values introduced systematic errors through smoothing of rapid changes in the rate.

Rough substrates were produced by grinding one surface of a microscope slide in silicon nitride (Carborundum) powder for ten minutes. The same cleaning protocol as with the smooth substrates was used. This resulted in a surface roughness with a maximum peak to trough height of the order of $20\,\mu\mathrm{m}$.

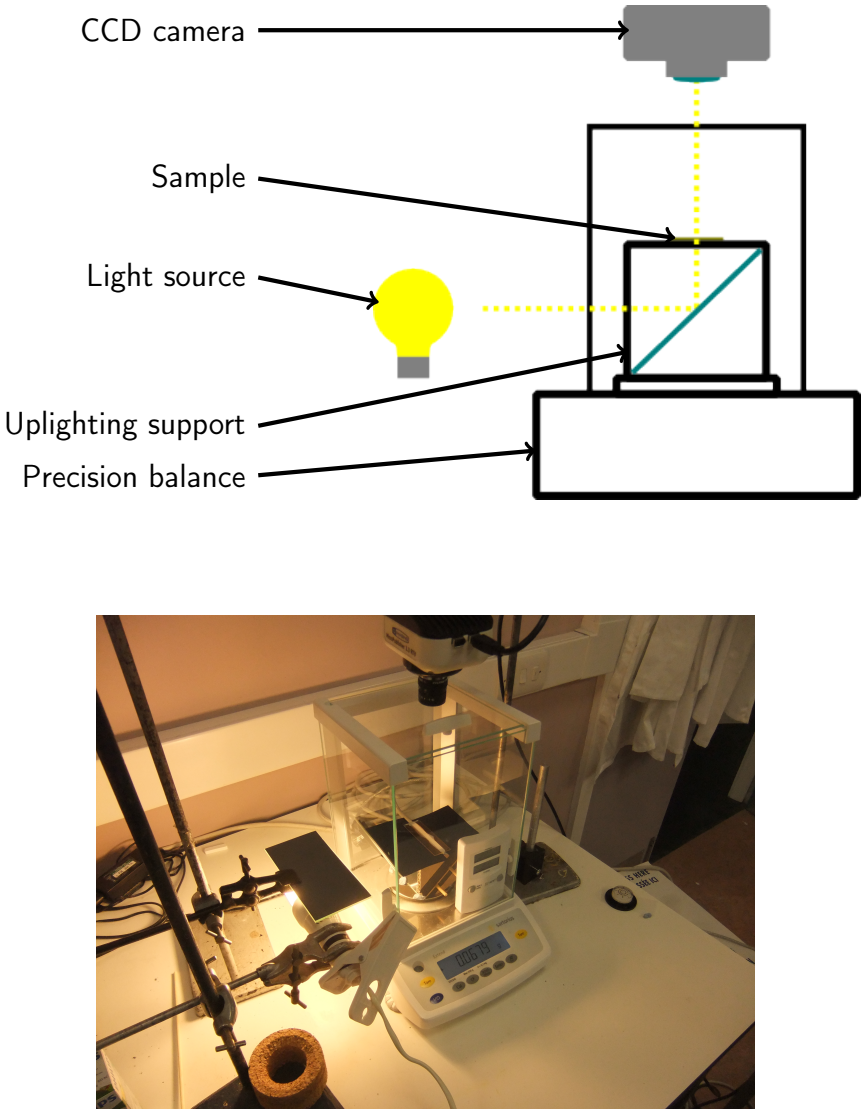

Figure 3.3 *Diagram and photograph of apparatus used for simultaneous imaging and weighing of drying samples. The sample rests on a support which contains a mirror angled at 45°, allowing bright uplighting of the sample by the light source. A fluorescent energy saving bulb was used (Phillips Genie 1145 Lumen) to minimise heating of the balance enclosure by the bulb. The balance is connected via a RS232-USB adapter to a computer which is also recording images from the CCD camera.*

3.3 Results

3.3.1 Drop-casting

Transmission images of droplets cast are presented in figure 3.4. Profiles of the green bodies[1], obtained by profilometry, are presented in figure 3.5. As the post-mix pH increases, the drop characters change:

- At post-mix pH 2, a coffee-ring like deposit forms, with a smooth film in the centre and a cracked edge region. The profilometer traces indicate that the cracked regions are substantially thicker than the centre film region, although delamination effects could be responsible for some of the recorded height.
- At post-mix pH 3, a uniformly cracked film is deposited with no optical evidence of a special edge region. Cracks appear to be random in direction. The profilometer trace indicates the green body thickness is substantially increased and therefore is substantially less dense than the pH 2 deposit.
- At post-mix pH 4, a central deposit is present, surrounded by cracks and a grainy edge of the green body. The central body resembles a heap of sand, as can be seen in profile on a larger volume droplet (the top-down view of the larger drop volume sample is qualitatively identical to that of the smaller volume droplet).

3.3.2 Tape-casting

Some preliminary trials of the tape-casting process were performed to identify the minimal thickness (or critical cracking thickness, CCT) below which films did not display evidence of cracking. Tapes were cast using one, two and three layers of Kapton tape (70 µm, 140 µm and 210 µm spacer thickness, respectively) and a post-mix pH 4 paste. Green bodies cast with one layer of tape displayed no cracking. Tapes cast with two layers displayed mixed domains of cracked and uncracked tape. Tapes cast with three layers consistently displayed cracking

[1]The term 'green body' refers to a ceramic object cast from solution after the solvent has been extracted but before firing/sintering

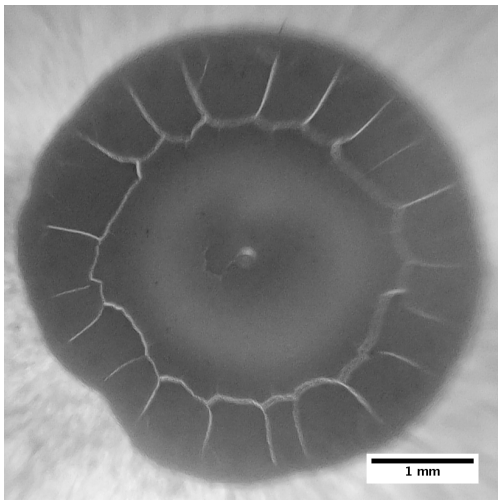

(a) *pH 2 droplet*

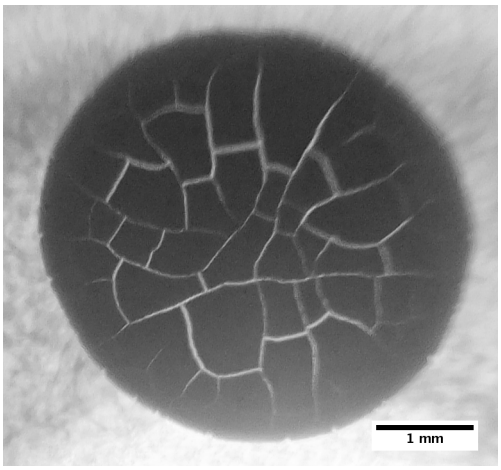

(b) *pH 3 droplet*

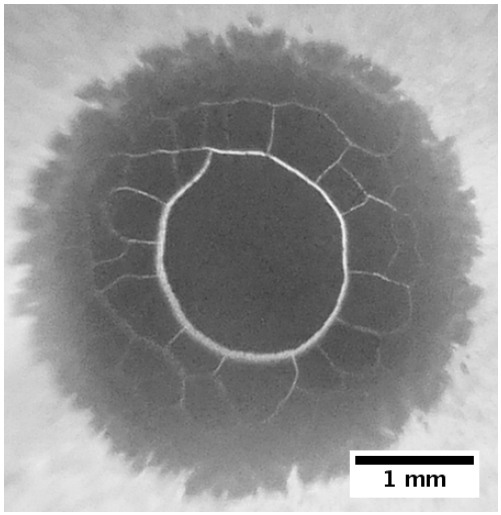

(c) *pH 4 droplet*

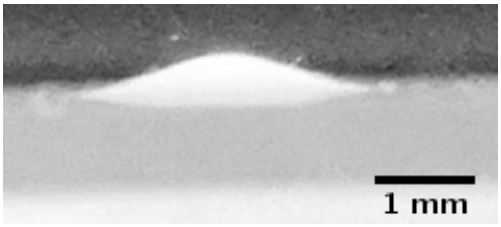

(d) *Profile of* 9 µL*, pH 4 droplet*

Figure 3.4 *Images of drop-cast green bodies of varying post-mix pH. Drop volumes were all* 3 µL*, except where otherwise noted.*

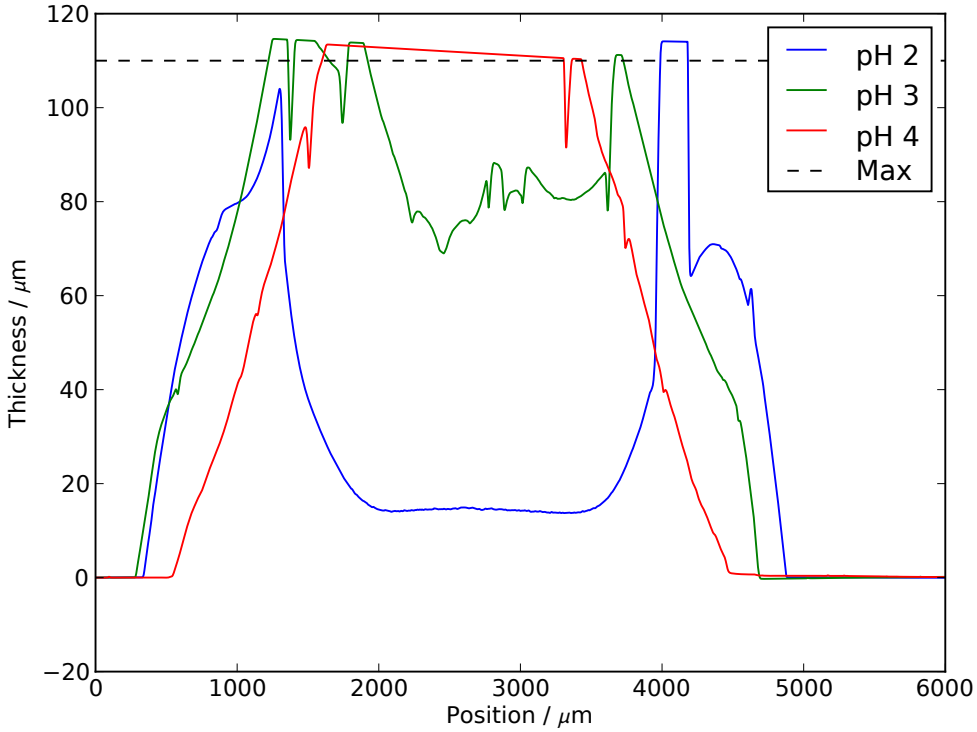

Figure 3.5 *Profilometer traces of green bodies of varying post-mix pH. The profilometer has a maximum deflection measurement of* 130 µm. *The trace is corrected for stage tilt by applying a first order plane fit, taking the glass substrate away from the green body to be flat. This results in a lower maximum measurable deviation, as indicated by the dashed line on the plot.*

behaviour. Spacers formed from three layers of Kapton tape were therefore chosen to ensure that cast films were above the critical cracking thickness.

The following data sets were then collected using the methods detailed above:

1. Photographs of ceramic tapes cast from five suspensions ranging in post-mix pH from 3.00 to 4.00 in 0.25 pH unit steps. Profilometry traces were gathered for post-mix pH 3.00 and pH 4.00 tapes at two positions along the tape.

2. Low magnification microscopy images of crack regions near the first profilometry positions on the post-mix pH 3.00 and 4.00 tapes.

3. Time lapse photographic series of the drying of three post-mix pH 3 and one post-mix pH 4 tape cast from the same suspensions with simultaneous recording of tape mass. The suspensions were sonicated before deposition in order to redisperse the mixture to the same state as the previous samples. Profilometry traces were recorded for ten positions along the pH 4 tape, but profilometry measurements could not be performed on the pH 3 tape due to delamination of the film from the substrate.

4. Time lapse photographic series of the drying of a post-mix pH 3 tape and a post-mix pH 4 tape cast onto roughened substrates with simultaneous recording of tape mass. Ten profiles were recorded from the pH 4 tape but, as above, the pH 3 tape delaminated when profiles were attempted.

Transmission images of ceramic tapes cast with post-mix pHs between 3 and 4 in 0.25 unit steps (dataset 1) are presented in figure 3.6. The most distinctive feature is the prominent parallel cracks stretching from left to right in the pH 3.00 tape, and its contrast with the random crack pattern in the pH 4.00 tape. Successive generations of crack also display a reduction of intensity, due to narrower clefts in the film. As the pH is increased, there is a smooth change in the persistence length of crack lines, from lines which maintain straight paths across the tape (from left to right) from pH 3.00 to 3.50 to cracks which rapidly bend, often resulting in crack termination at the edges of the tape, for pH 3.75 and pH 4.00.

Thickness measurements from profilometer traces across the post-mix pH 3 to 4 transition region (dataset 1) are summarised in table 3.1. The final film appears to be thicker within the transition region (defined above as the region where samples display a heterogeneous mix of ordered and disordered crack trajectories) than at

Sample	Position / mm	Thickness / µm
pH 3.00-1	1	57 – 71
	5	75 – 88
pH 3.25-1	1	80 – >102
pH 3.25-2	1	88 – >102
pH 3.50	1	>102
pH 3.75-1	5	89 – >102
	9	76 – 91
pH 4.00-1	1	74 – 84
	5	78 – 94
	9	76 – 90

Table 3.1 *Table of film thicknesses estimated from profilometry measurements (dataset 1). Measurements give minimum and maximum film thicknesses, excluding any peaks at the edges of the film and those arising from delaminated segments of the dried film.*

pH 3.00 or 4.00. This is reflected in the larger domain sizes in the transmission photographs (figures 3.6b, 3.6c and 3.6d) for these samples. The scaling of domain area with film thickness is discussed further below.

The accompanying profilometer traces to the photographs (dataset 1) for profilometer position 1 are presented in figure 3.7. Each profile displays a similar average thickness of about 60 to 70 µm and a smoothly varying asymmetry across the film of approximately 10% of the mean thickness. The cracks between domains are clearly visible as the sharp discontinuities in the thickness sample. Disregarding the crack discontinuities, the post-mix pH 4 film is flatter and rougher across individual crack domains with the post-mix pH 3 film domains consisting of smooth but curved surfaces. By looking at the samples, it can be seen that individual domains in the post-mix pH 3 sample are curved, and this is attributed to delamination of the titania domains from the substrate in a similar manner to that observed by Lazarus and Pauchard [70].

Scaled versions of the assembled microscopy mosaics (dataset 2) are presented in figure 3.8. The change in persistence length noted in dataset 1 is also clear here at higher magnification. Slight mismatches in contrast can be seen between mosaic strips; this is attributed to varying background light during imaging. The contrast between cracks and domains is sufficient that the filtering procedures used to isolate crack domains were able to cope with the differences. A thin scoring line can be seen in the centre of the post-mix pH 4 mosaic and is attributed to light damage to the film from the profilometer tip.

pH (after mixing)	Mean α	Std. deviation α
3.00	3.5(3)	0.85(8)
4.00	5.6(5)	1.43(13)

Table 3.2 *Estimated parameters and errors of the distribution of α in post-mix pH 3 and post-mix pH 4 samples.*

A histogram of the crack domain areas from the low magnification microscopy images (dataset 2)is presented in figure 3.9a. According to Lazarus and Pauchard [70], the square root of the crack domain area should be proportional to the thickness of the domain[2]. By combining the measured thickness profile data with the measured domain areas, it should be possible to study the effect of changing the pH on domain size accounting for the variable thicknesses of the samples.

As the profilometer produces a line trace, it is necessary to use an interpolation scheme to calculate the thickness each domain area should be normalised by. The traces were first smoothed to remove the crack discontinuities by fitting a fourth order polynomial to each (dashed lines in figure 3.7). The mean thickness of these profiles was then used to normalise all measured crack areas. The maximum error introduced in this scheme, as defined as the ratio of the standard deviation of the polynomial to its mean, is 9%. The results of this analysis are presented in figure 3.9b. The histogram data are well fitted by a Gaussian distribution of α (dashed lines in figure 3.9b), with both the mean and variance of the distributions dependent on post-mix pH. The statistical error in the parameters of the distributions was estimated to be about 1% by bootstrap sampling and therefore small compared to the uncertainty in the thickness of the film. The results of the distribution analysis are presented in table 3.2. On increasing the post-mix pH from 3 to 4 (and therefore destabilising the suspension) the mean domain α value and the scatter of domain values about the mean increase by 60%, from 3.5 to 5.6 and 0.85 to 1.43 respectively.

More complicated interpolation schemes, such as matching the exact form of the polynomial to the y coordinate of the centre of mass of crack domains across the film, were considered. These schemes would introduce new sources of systematic error and significantly complicate the analysis, and initial attempts indicated that the basic form of the results remained unchanged.

[2]The paper itself refers to the quantity $\alpha = \sqrt{\text{Area/Thickness}}$. This is not dimensionally consistent, and the values from other studies referenced are more consistent with the dimensionally correct definition of $\alpha = \sqrt{\text{Area}}/\text{Thickness}$. I will therefore use the latter definition in my study.

The angles between cracks were also measured (dataset 2), and a histogram of results is presented in figure 3.10. As only two of the three angles can be independent in a Euclidian geometry, only the smallest two angles between cracks at a junction were counted. The distribution appears monomodal and is centered at 100°, with a half width at half maximum of 18°. There does not appear to be any variation between samples of different pH (see discussion section for further comment on these results).

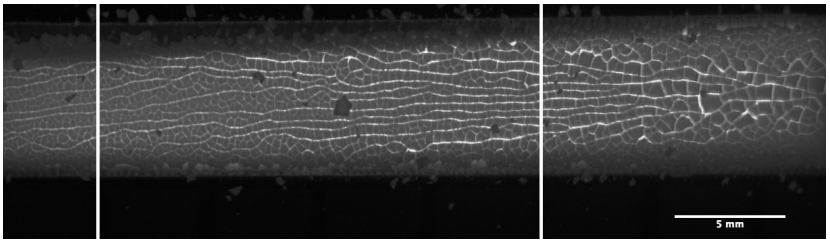

(a) *pH 3.00 (after mixing)*

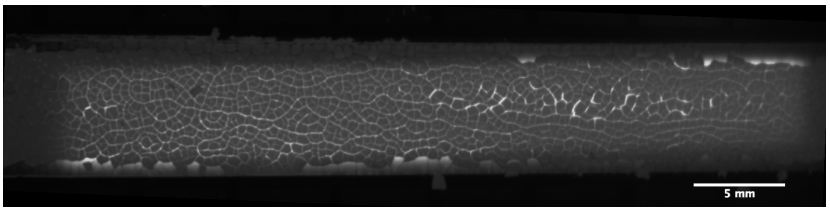

(b) *pH 3.25 (after mixing)*

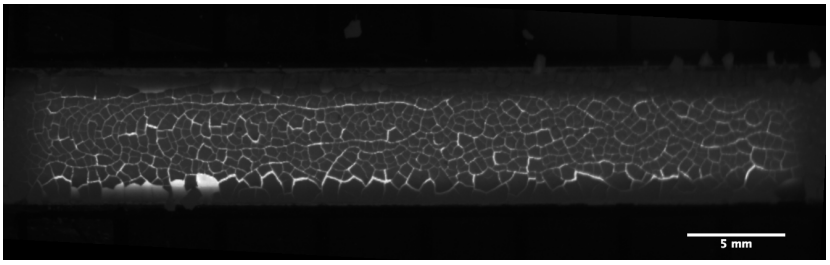

(c) *pH 3.50 (after mixing)*

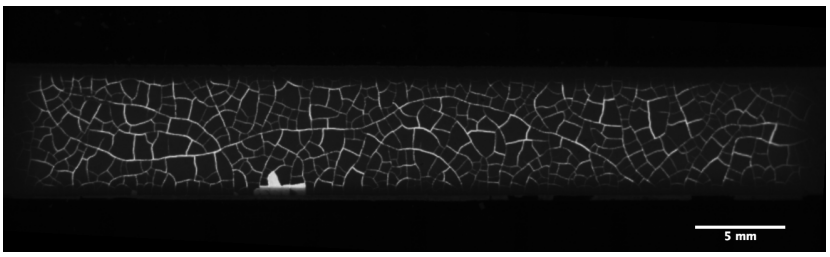

(d) *pH 3.75 (after mixing)*

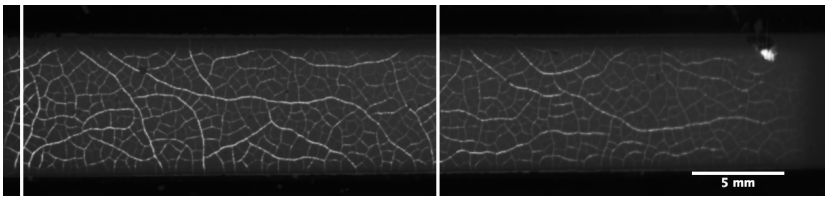

(e) *pH 4.00 (after mixing)*

Figure 3.6 *Transmission images of films formed with suspensions with post-mix pH between 3.00 and 4.00 in 0.25 unit steps. The white lines for pH 3.00 and 4.00 films indicate where profilometer traces were taken at positions 1 and 5 and are* 25 mm *apart. The profilometer traces for the pH 4.00 film at these points are presented in figure 3.7.*

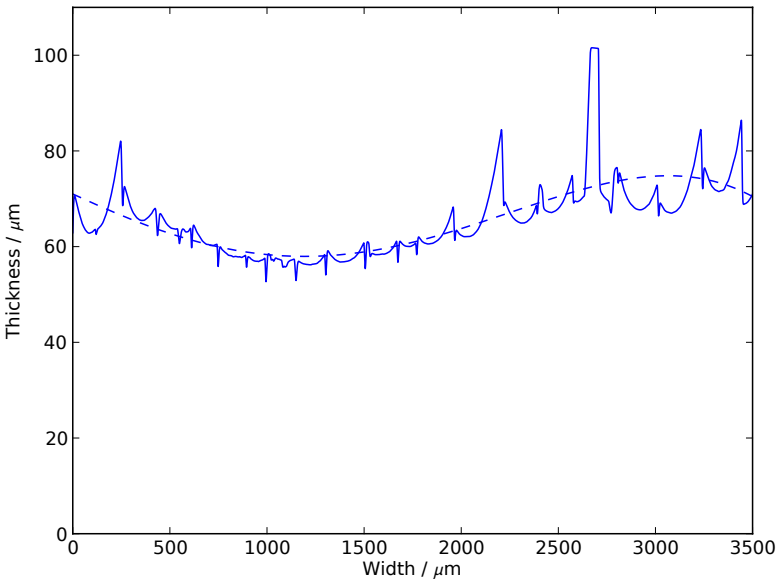

(a) *pH 3.00 (after mixing)*

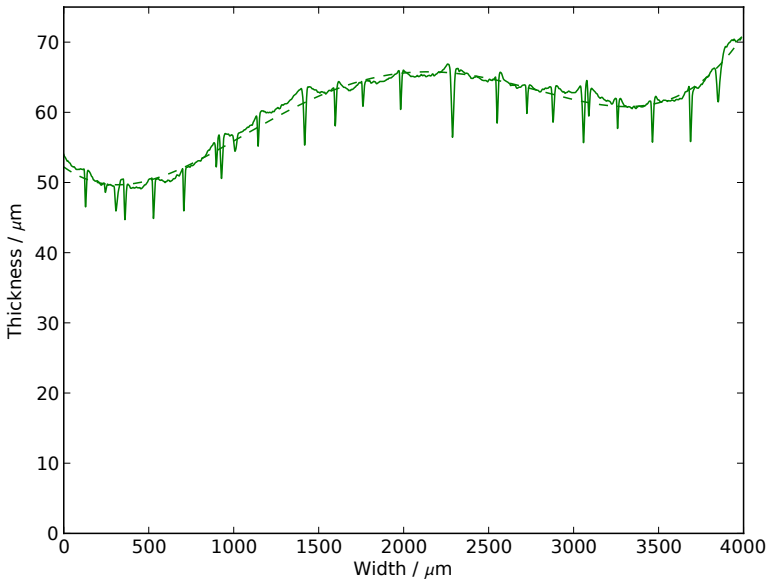

(b) *pH 4.00 (after mixing)*

Figure 3.7 *Dektak profilometer traces for the post-mix pH 3.00 and 4.00 tapes imaged in figure 3.6 (dataset 1). Note the flat top to the extreme peak in the pH 3.00 profile is an artefact due to the profilometer reaching its maximum measurement deflection. The dashed lines indicate the fourth order polynomial fits to the data used to determine the average thickness.*

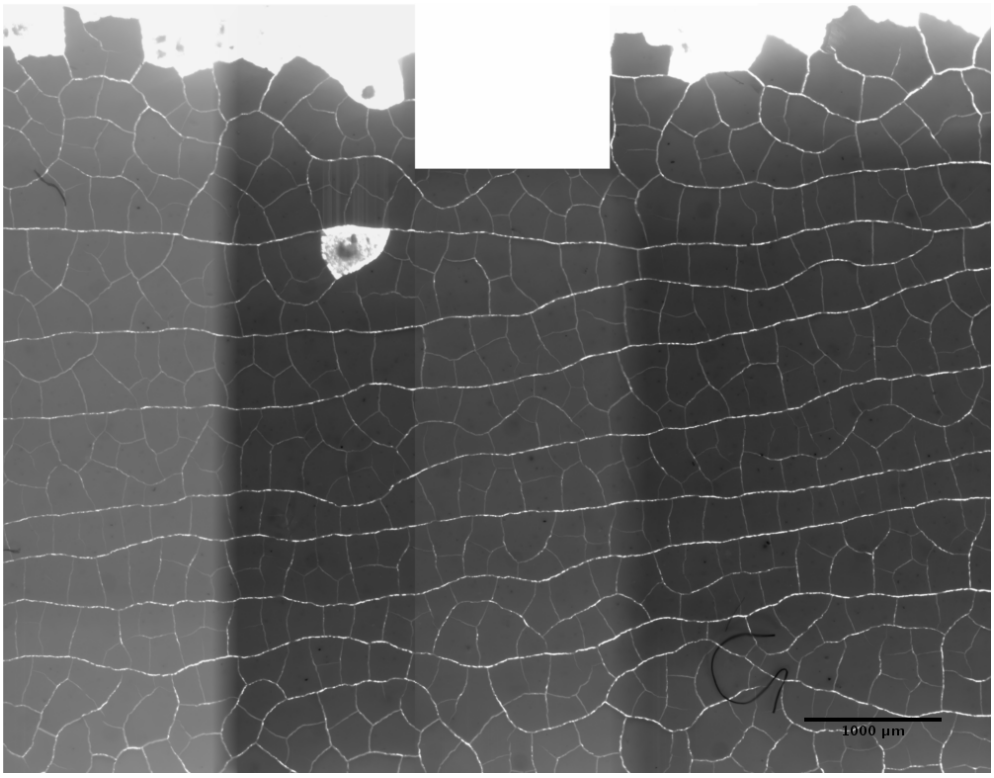

(a) *Post-mix pH 3 sample*

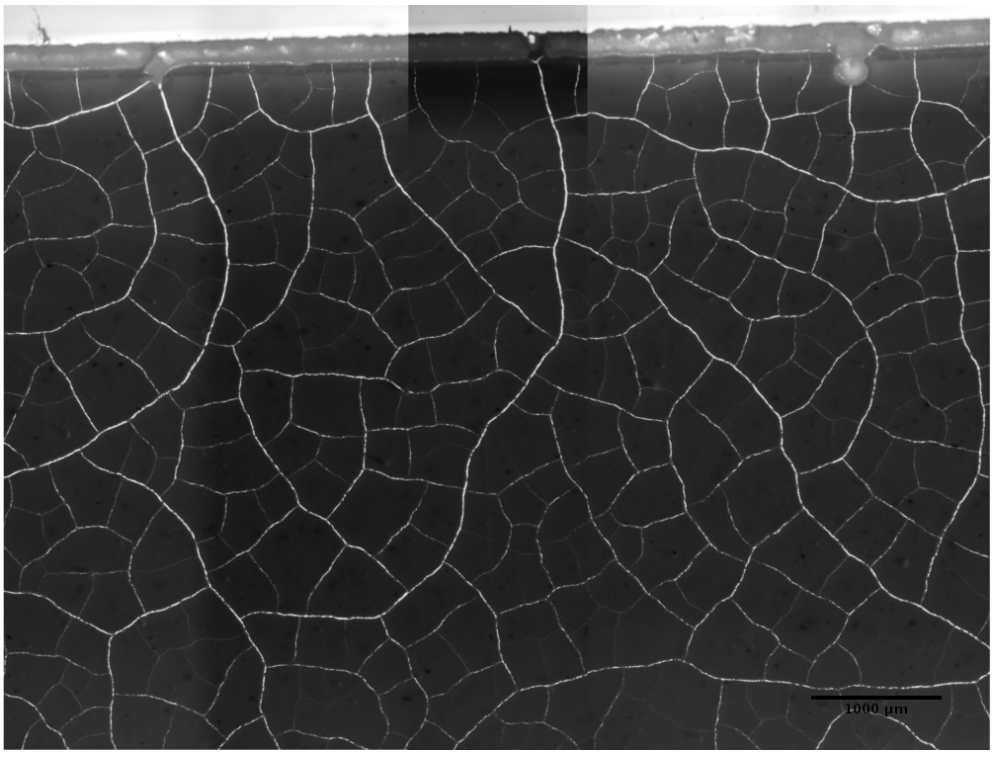

(b) *Post-mix pH 4 sample*

Figure 3.8 *Scaled versions of the microscopy mosaics (dataset 2). The scale bars are* 1000 µm. *The profilometer trace was taken in the centre of each of the images.*

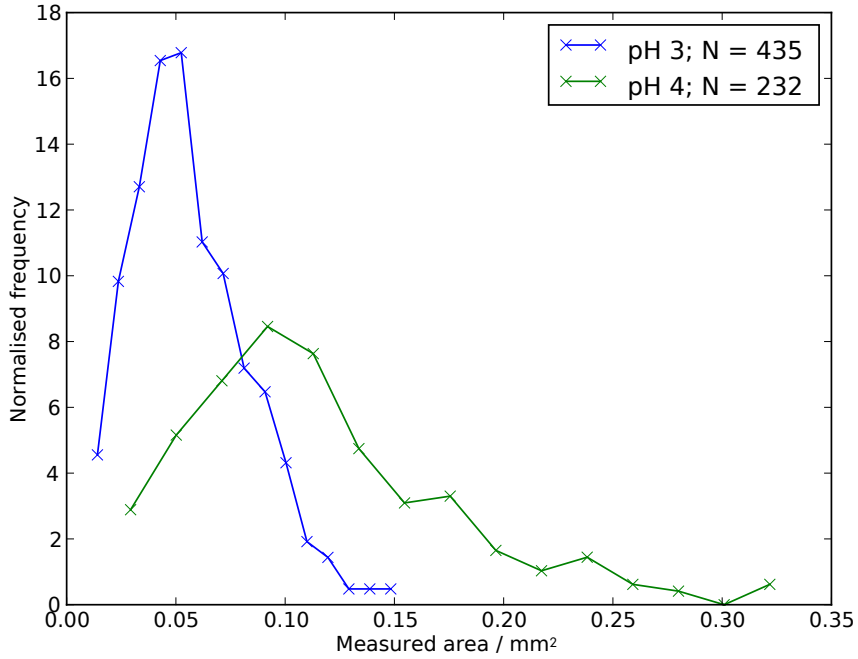

(a) *Normalised frequency versus crack domain area.*

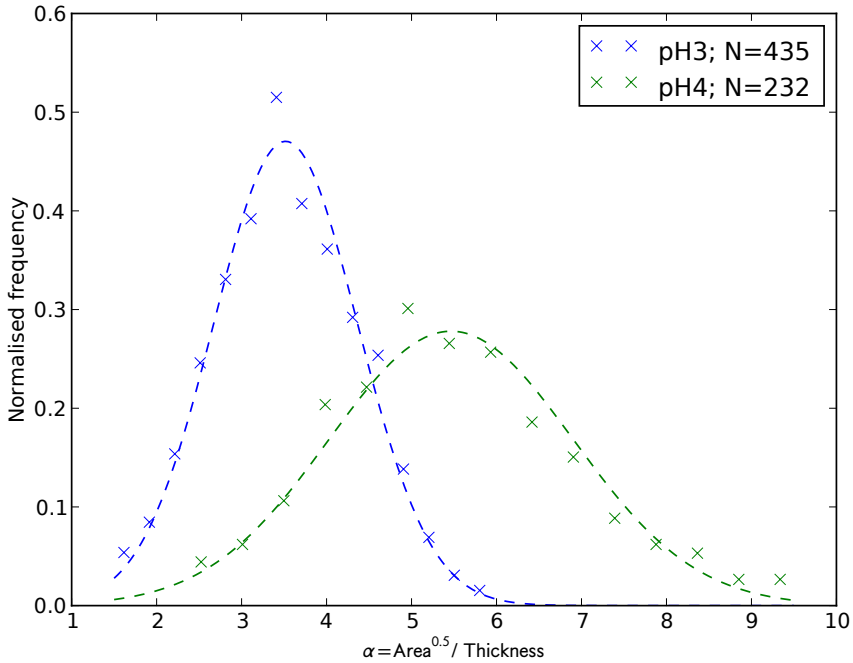

(b) *Normalised frequency versus calculated α.*

Figure 3.9 *Fifteen bin normalised histograms of the crack domain area and calculated α for post-mix pH 3 (blue) and post-mix 4 (green) tapes (dataset 2).*

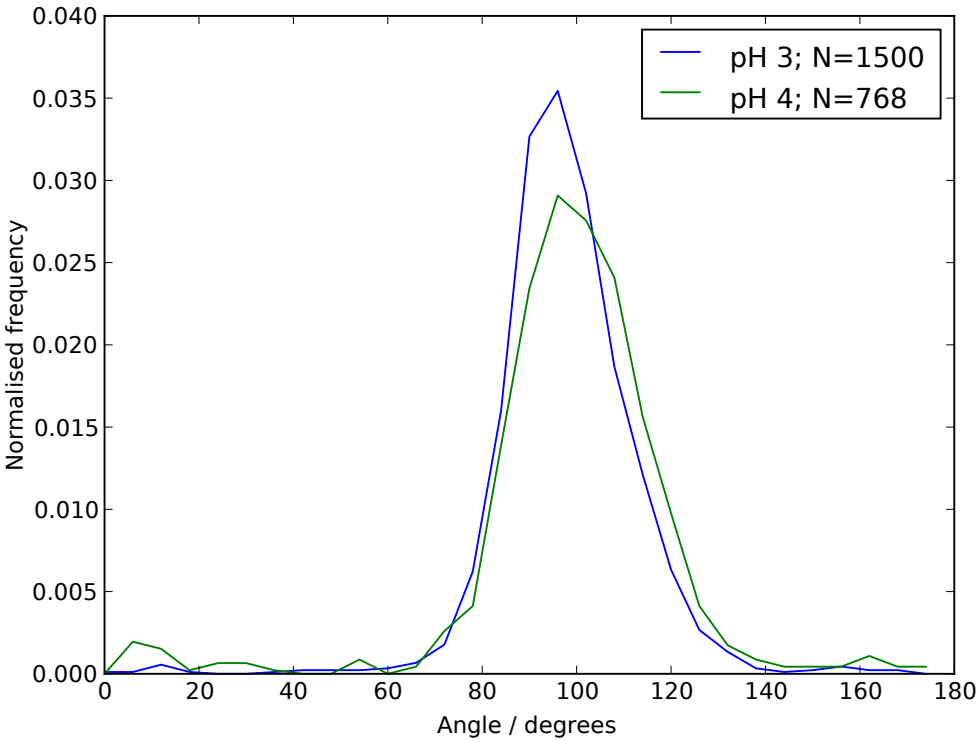

Figure 3.10 *Histogram of the two lowest angles at crack junctions for post-mix pH 3 and 4 samples, as measured from microscopy images (dataset 2).*

The results of the dynamic imaging measurements (dataset 3) are presented in figures 3.11 and 3.12. The film is initially homogenous, with a slowly increasing transmission intensity as water in the film evaporates freely. A visible drying front sweeps across the film. At the time denoted 'Cracking starts', cracks can be observed, following the previously observed drying front. At the point denoted 'Drying stops', the drying front disappears into one edge of the tape. Shortly afterwards, at 'Cracking stops', the crack pattern ceases to develop further and no more cracks are seen to form for the rest of the observation. After this point, the intensity of the crack pattern is observed to fade until the point denoted 'Dimming stops', beyond which there is no further observed visual change in the sample. The same behaviour is also observed in the samples cast onto roughened substrates.

A graph of mean pixel intensity for representative 3×3 pixel cracked and uncracked regions is presented in figure 3.13. The initial thinning of the film can be seen for early times in the rise of transmitted intensity. As the drying front passes, the film becomes suddenly brighter, most likely due to another thinning of the film. As a crack forms in the region under measurement, the two intensity traces diverge, with the crack region getting much brighter and the uncracked region becoming slightly darker. As the 'dimming' front passes, the crack region becomes darker and the uncracked region becomes slightly brighter. After this point the intensities remain constant.

The measurement of film mass with time for samples on a smooth substrate are presented in figure 3.14 (dataset 3). The mass loss curves for the films deposited on rough substrates are presented in figure 3.15 (dataset 4). Both datasets share similar features; initially, the rate of mass loss is either moderately increasing with time (post-mix pH 3 samples) or constant with time (post-mix pH 4 samples). A sharp decrease in the rate of mass loss[3] appears correlated with the appearance of cracking in the sample. The rate of mass loss continues to decrease after visible cracking has finished until a new plateau value is reached at $-10\,\mu g\ s^{-1}$. The rate of mass loss then smoothly reduces to zero in the long time limit.

To highlight the similarities , the early time curves for both datasets are presented together in figure 3.16. It can be seen that the initial film mass for the smooth post-mix pH 4 sample is lower than for the other samples and that the rate curve is considerably offset to earlier times from the trend established by the other

[3]Note that on the graphs, loss of mass is defined to be be negative, therefore this appears as a peak

three datasets. The most likely explanation for this feature is a larger amount of pressure being applied to the spreading tool during application of post-mix pH 3 suspension to the smooth substrate, resulting in a thinner wet film being cast. The variation in film thickness does not contradict this theory, with the final thickness of the post-mix pH 4 film on a smooth substrate being approximately 75% of that of the post-mix pH 3 film, which matches the difference in initial film mass between the samples.

The long time drying behaviour was captured for samples deposited on a roughened substrate only (dataset 4) and is presented in figure 3.17. Some unusual behaviour is recorded. At $t \approx 35\,000\,\mathrm{s}$, the mass of the post-mix pH 3 sample begins increasing slightly, before it continues to decrease again. At $t \approx 55\,000\,\mathrm{s}$ the rate of mass loss in the post-mix pH 4 sample discontinuously increases, with the film mass dropping by approximately 10 mg before the rate stabilises and becomes slightly positive until the end of the recorded data.

By calculating the initial mass fraction of titania in each suspension and assuming the deposited film initially has the same concentration the quantity of solid titania deposited can be calculated. This equates to $m_{initial} = 0.0468\,\mathrm{g}$ for the post-mix pH 3 suspension and $m_{initial} = 0.0424\,\mathrm{g}$ for the post-mix pH 4 suspension. This raises some doubts over the long time absolute mass data for the post-mix pH 4 film on a rough substrate, for which $m_{final} = 0.0052\,\mathrm{g}$, indicating that some titania has been lost from the substrate during drying or that the scales are subject to long time drift. Even assuming the plateau value at $t \approx 55\,000\,\mathrm{s}$ is the true final mass (and ignoring the final drop as an artefact) this results in $m_{final} = 0.0146\,\mathrm{g}$, which again indicates that some titania has been lost. The final post-mix pH 3 film mass of 0.0517 g appears more reasonable. As titania is hydrophilic, the effect of the wetting of the titania powder and film by atmospheric moisture should be considered.

An estimate of the final volume fraction of the film can be derived from the final titania mass and the literature value of its density. The volume of the post-mix pH 3 film on a rough substrate is approximately $7.55\,\mathrm{cm} \times 0.7\,\mathrm{cm} \times 0.007\,\mathrm{cm}$, assuming the thickness of the post-mix pH 3 film deposited on the roughened substrate is similar to the thickness of the post-mix pH 3 film deposited on the smooth substrate. The final volume fraction is then $\phi_f = (m_{TiO2}/\rho_{TiO2})/V_{tape} = 0.36$.

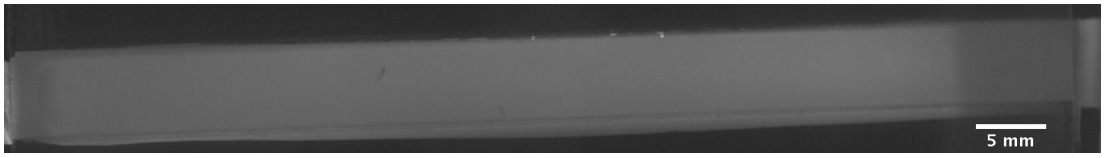

(a) *After spreading: homogeneous film*

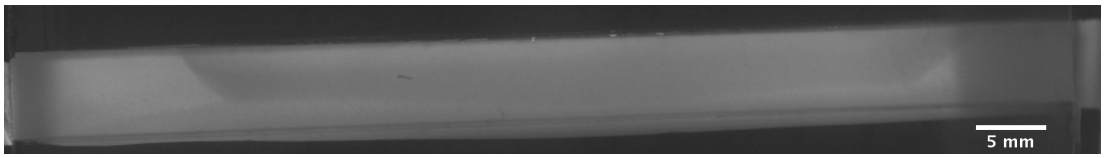

(b) *Drying front moving across film*

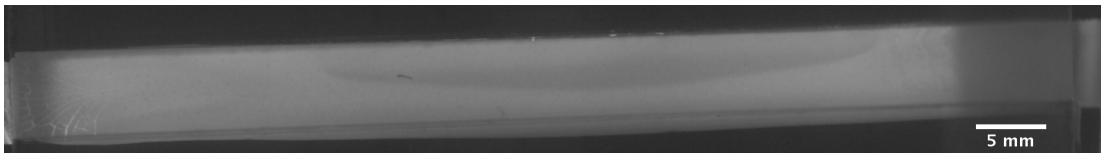

(c) *Cracking starts*

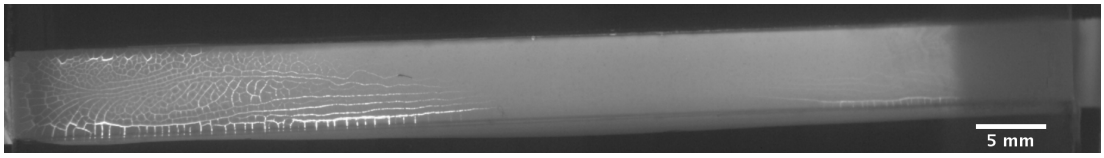

(d) *Drying ends*

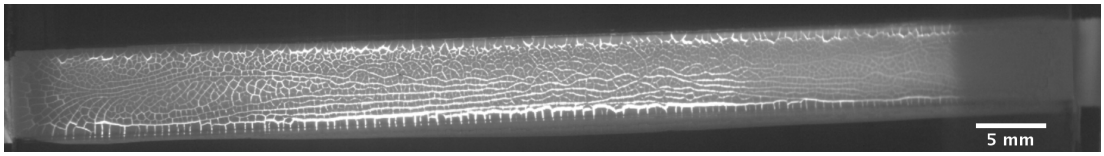

(e) *Cracking ends*

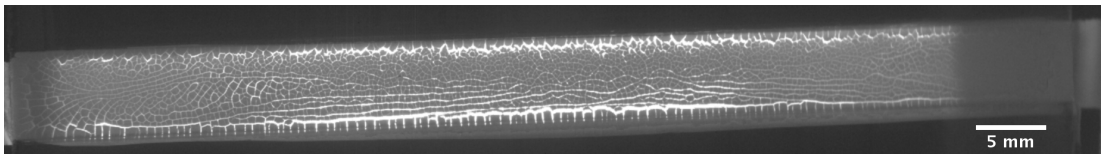

(f) *Dimming ends*

Figure 3.11 *Example drying dynamics for a post-mix pH 3 film (dataset 3).*

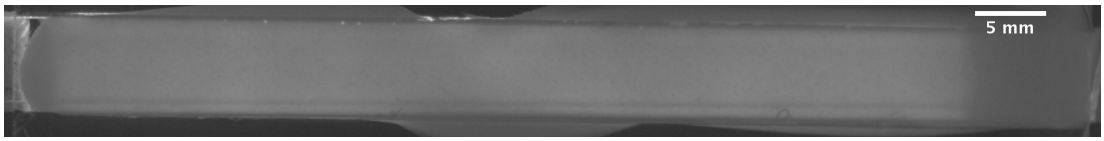

(a) *After spreading: homogeneous film*

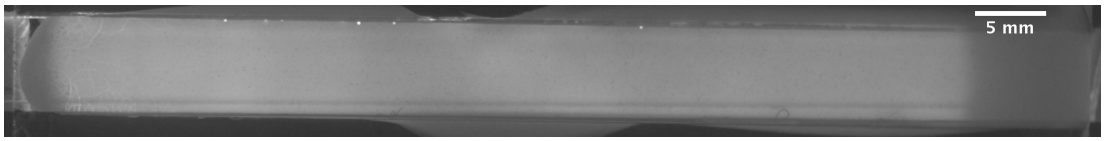

(b) *Cracking starts*

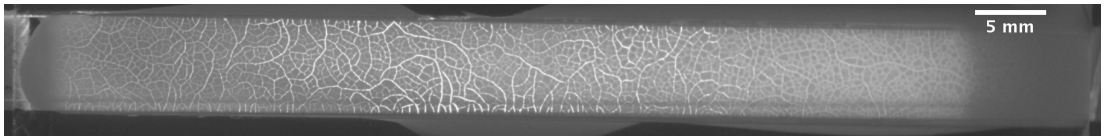

(c) *Cracking stops*

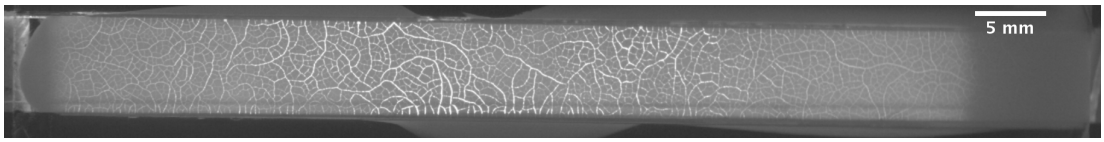

(d) *Dimming stops*

Figure 3.12 *Example drying dynamics for a post-mix pH 4 film (dataset 3).*

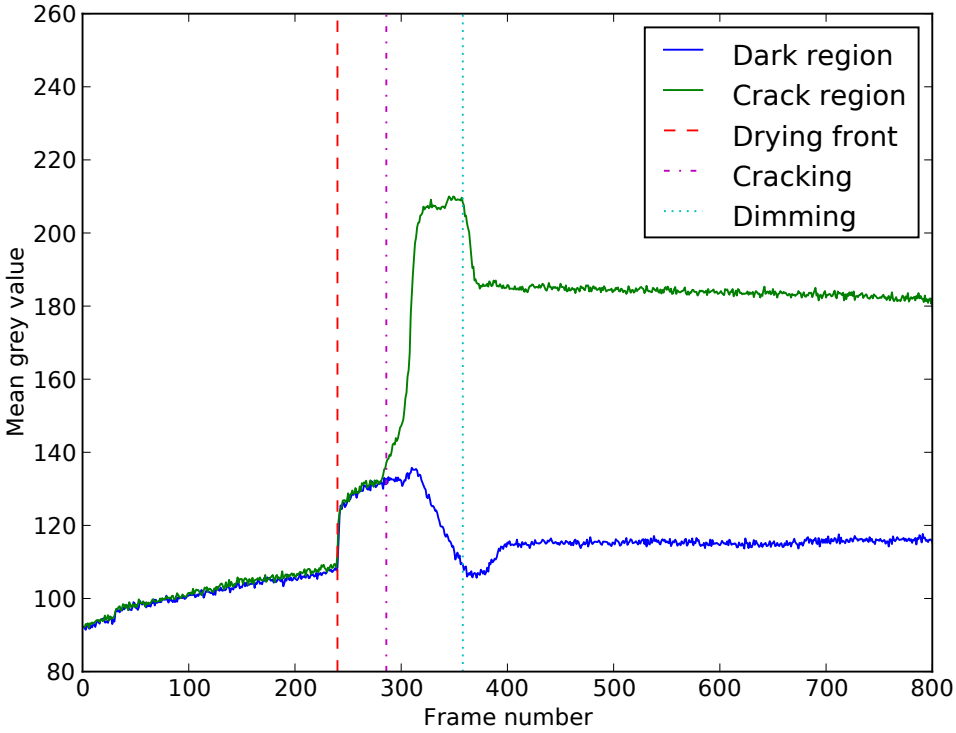

Figure 3.13 *Mean grey value versus time for representative* 3×3 *pixel regions from cracked and uncracked regions of the roughened post-mix pH 3 sample (dataset 4). Similar intensity profiles are seen for other samples exhibiting dimming behaviour. Times at which drying fronts, crack regions and dimming fronts pass across the studied regions are noted with vertical lines.*

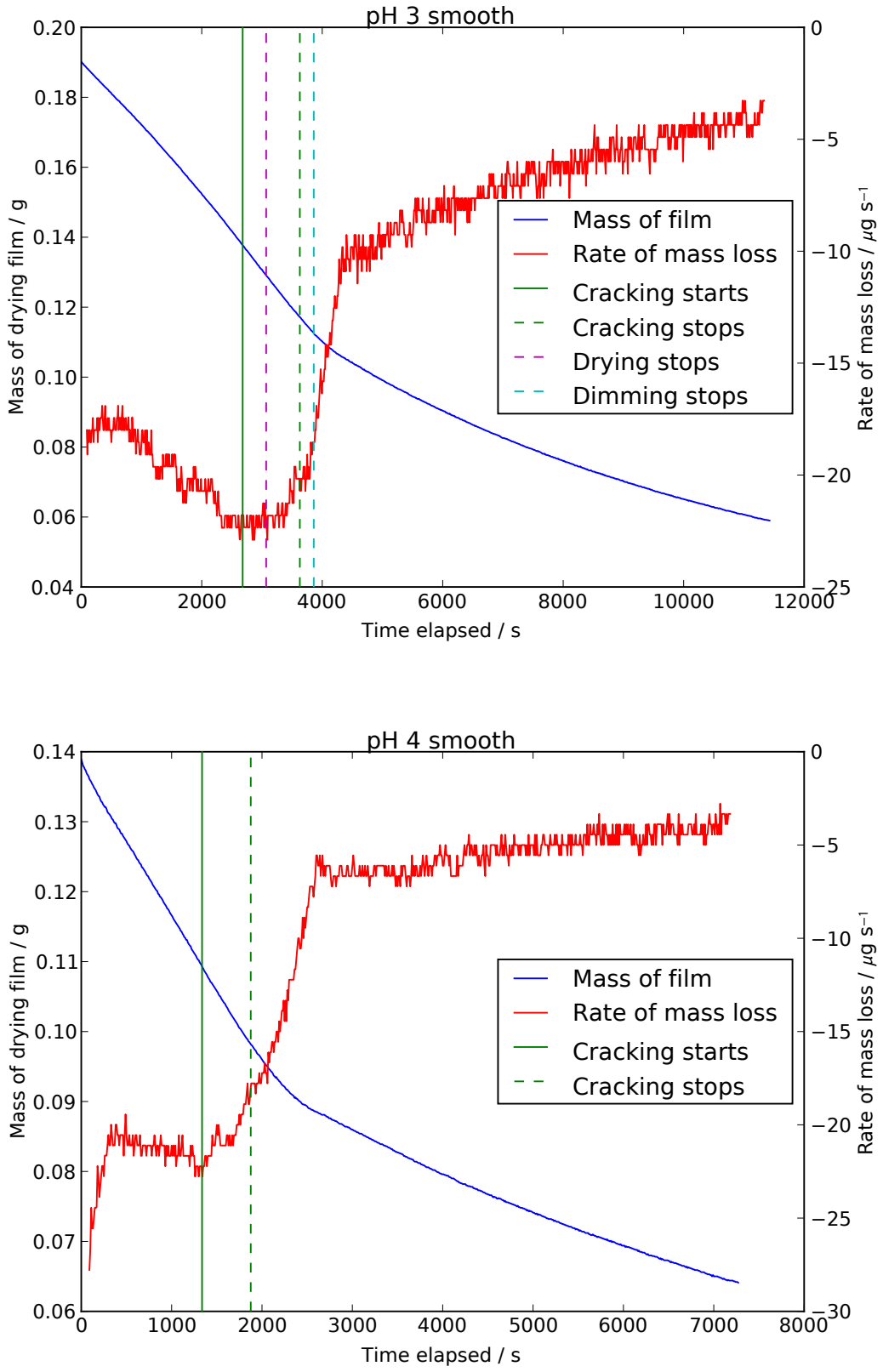

Figure 3.14 *Calculated rate of mass loss for a post-mix pH 3 sample on a smooth substrate (dataset 3), with times of interest marked.*

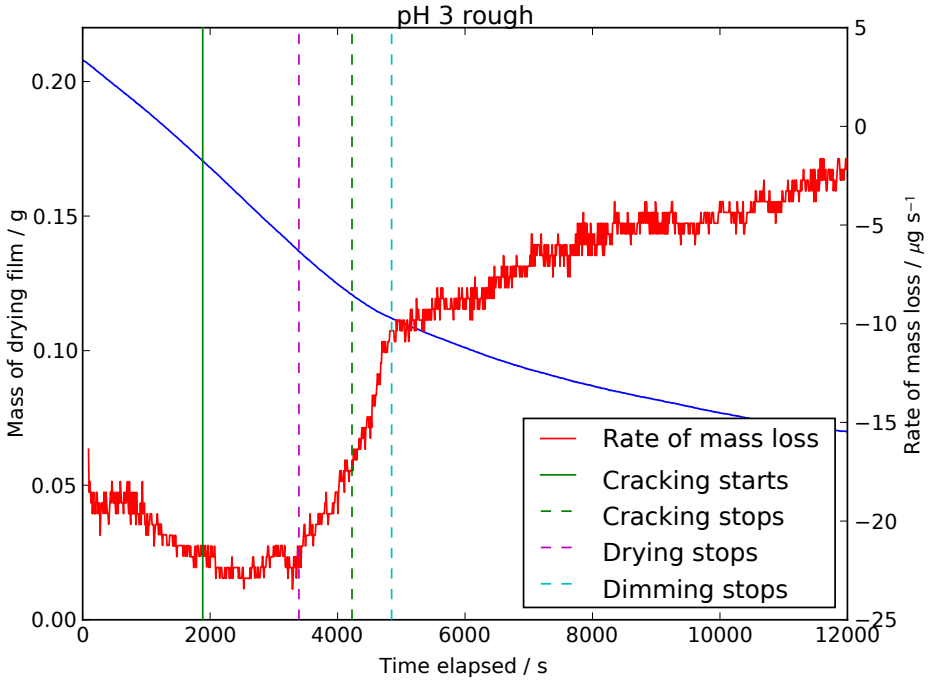

(a) *Post-mix pH 3 film deposited on a rough substrate*

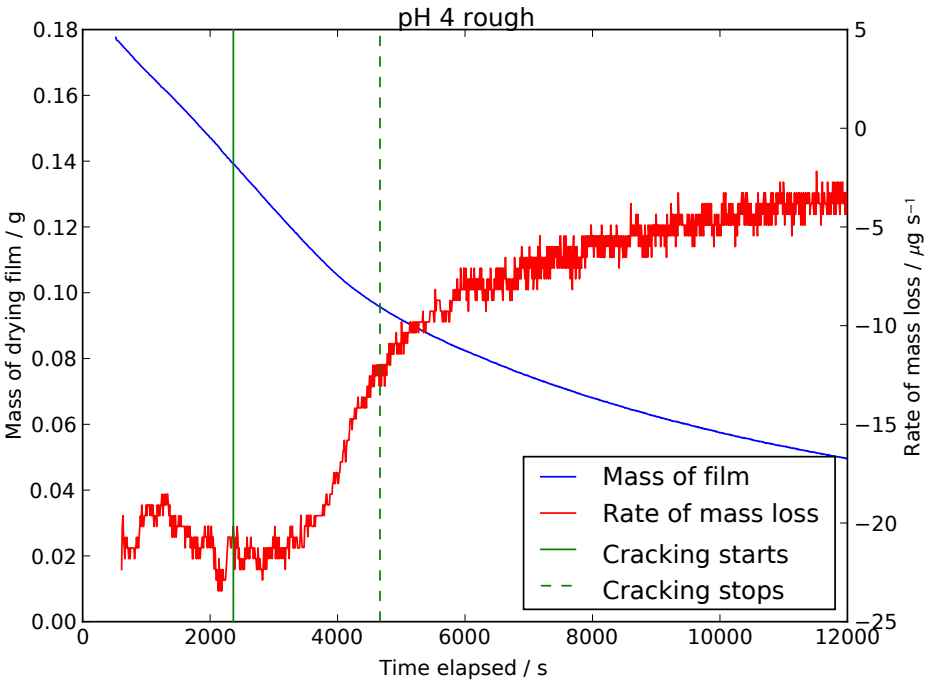

(b) *Post-mix pH 4 film deposited on a rough substrate*

Figure 3.15 *Film mass and calculated rate of mass loss of post-mix pH 3 and 4 films deposited on a roughened substrate.*

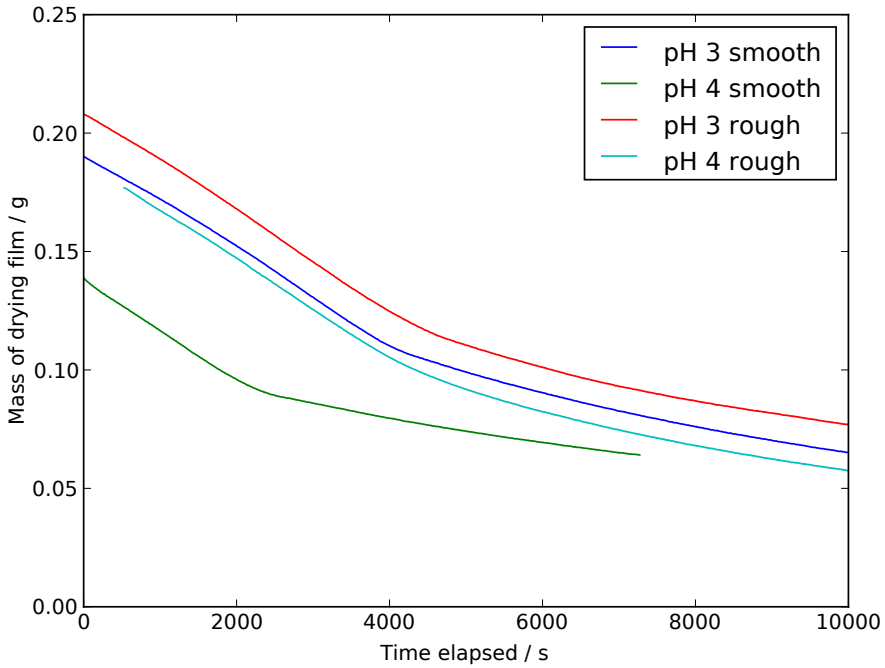

(a) *Mass of drying film versus time.*

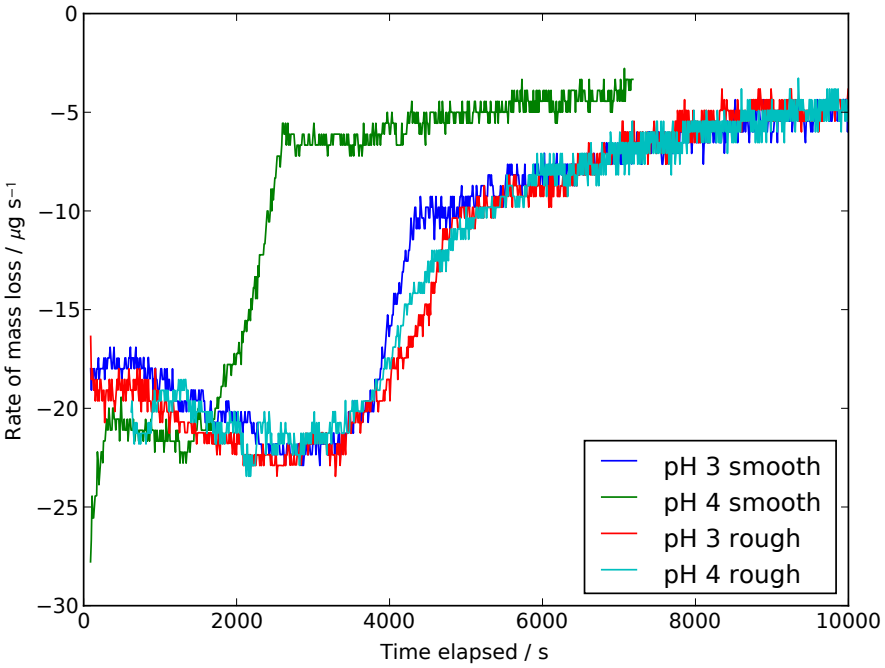

(b) *Evaporation rate versus time.*

Figure 3.16 *Mass of drying film and evaporation rate versus time for films deposited on rough and smooth substrates (datasets 3 and 4).*

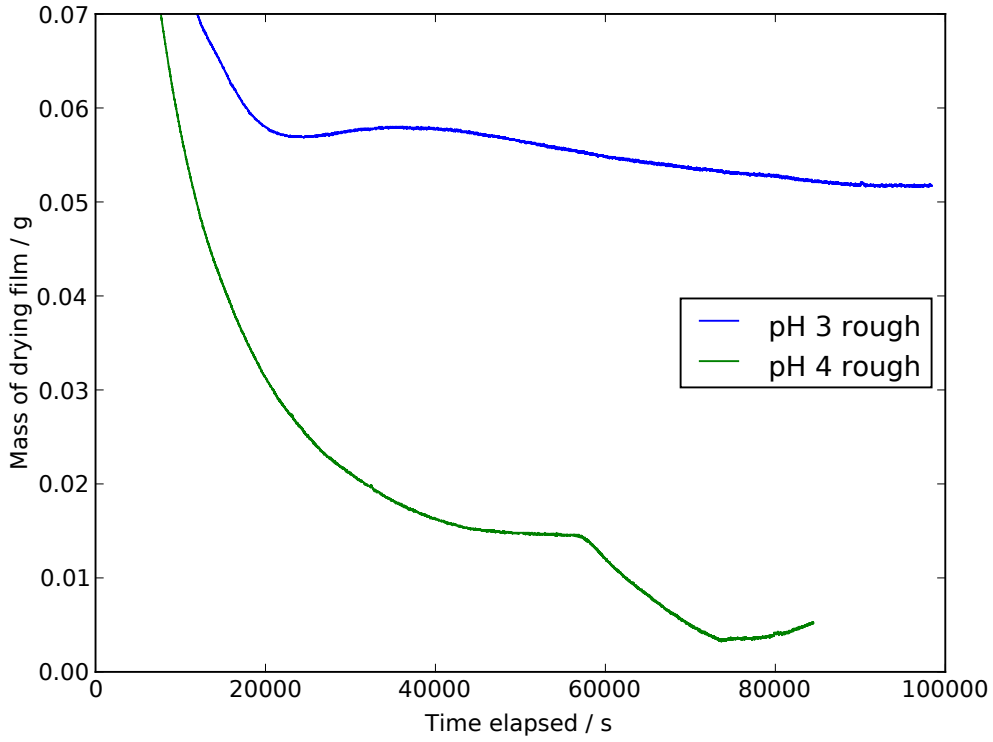

Figure 3.17 *Mass of drying film in the long time limit for films deposited on roughened substrates.*

3.4 Discussion

This study is the first to focus on the effect of systematic variation of the strength (rather than the range) of the inter-colloid potential on the drying of thin films of colloidal suspension. The advantage of this approach is that no salt is introduced into the suspension, reducing the effect on drying of residual salt precipitation seen in studies such as that done by Guo and Lewis [45]. This is important for scientists seeking to form additive-free suspensions for casting of tailored ceramic materials, such as in the area of photoelectrochemical solar cells.

3.4.1 Drying of Titania Droplets

The drop-casting results illustrate the changes in the drying process induced by raising the pH of the casting suspension after mixing. The pH 2 sample demonstrates the well-known coffee ring effect, where excess evaporative flux at the edges of the drying droplet induces convective currents in the wet suspension, causing migration and deposition of material preferentially at the edge of the droplet. The final thickness of the centre of the droplet is below the critical cracking thickness of the suspension, and is therefore smooth and without visible flaws, while the outer edges are cracked due to the thickness of the film at these points. This is clear evidence of the effect of the charge stabilisation of the titania colloids in a pH 2 environment.

In a pH 3 environment, flocculation is sufficiently favoured to drastically increase the viscosity of the suspension, inhibiting the flow of free colloid to the edge of the film. The profilometer trace indicates that there is still some preferential deposition of material at the edge of the film, but the uniform nature of the crack pattern indicates that the thickness gradients are not large enough to perturb the balance of forces during fracture. This indicates that the suspension is not gelled strongly enough to prevent the droplet from spreading uniformly.

The pH 4 suspension appears to demonstrate gel-like behaviour, with attractive inter-colloid forces large enough to prevent the droplet from spreading from its initial state after deposition. The central region is a desiccated gel with a yield stress sufficient to resist deformation by gravity and drying forces. Around the edge are deposits of macroscopic fragments of gel, presumably from solvent which has leaked out of the gel in a similar fashion to that observed in the tilt tests in

the previous chapter.

3.4.2 Crack Propagation Phenomena

In general, current understanding of the drying process is applicable to both post-mix pH 3 and 4 films and is well described by the review of Lewis [71], the important points of which are described here. As water evaporates from the fluid, colloid becomes concentrated at the air/water interface. The colloids pack locally until the response of the colloid structure at the interface (e.g. either the volume-fraction dependent osmotic pressure for dispersed samples or the network compressive yield stress for aggregated samples) is able to resist the compression placed upon the surface by capillary forces. At this point the fluid undergoes a transition to a solid-like state, becoming an elastic slab on the surface of the substrate. Water continues to evaporate from the slab as the super-saturated fluid phase retreats.

Evaporation continues at the same rate as before from the pores present at the surface of this saturated volume. Capillary forces at the nanometer sized meniscii resist the retreat of the water/air interface into the porous tape volume and the loss of fluid due to evaporation begins to reduce the pressure within the remaining fluid below that of the surrounding atmosphere. This causes water to flow toward the drying surface from both larger pores at the drying surface [27, 71] and the super-saturated volume behind. The remaining pressure difference across the interface acts to compress the film. Adhesion anchors the bottom of the tape against compression, resulting in the film being placed under tensile stress in the plane of the substrate. Cracks begin to propagate from microscopic surface defects once the bulk elastic energy arising from the tensile stress is greater than the surface energy required to create a crack [69]. The crack continues to propagate until the bulk/surface energy balance is restored through bulk relaxation or viscous dissipation of energy by water in the porous network [34].

The post-mix pH 3 sample exhibits directional ordering in the first generation of propagating cracks. Similar results were also noted by Shorlin et al [93] in their studies of directional drying imposed by gas currents above the drying sample. Various theories have been proposed to describe why the cracks are aligned perpendicular to the drying front and the origin of the regular spacing between them. Allain and Limat [5] propose a superposition with time of the initial

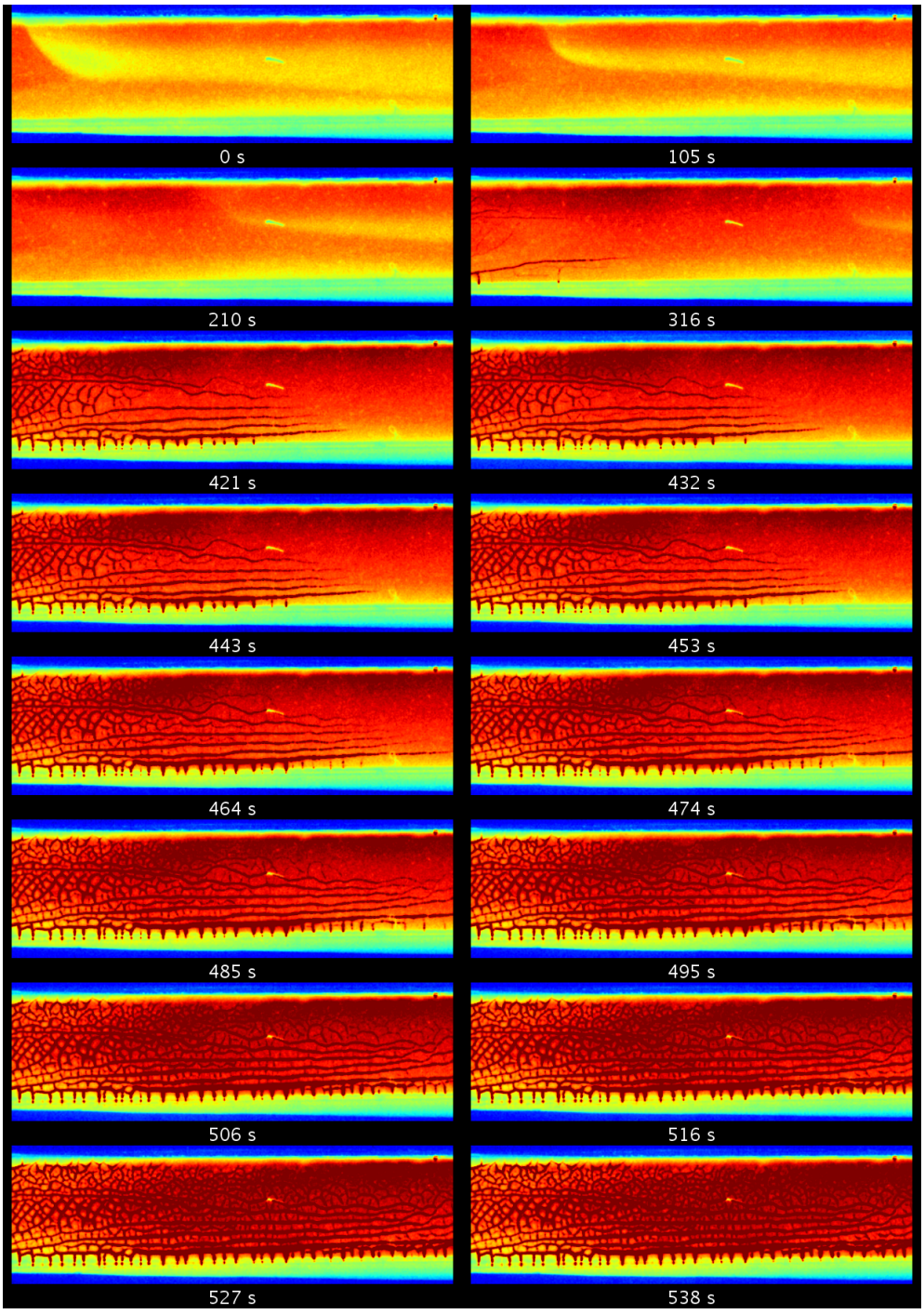

Figure 3.18 *A montage of false colour images of the drying behaviour of a post-mix pH 3 sample. The first four images are separated by* 100 s *intervals, while the last twelve are separated by* 10 s *intervals. Initially, a drying front recedes across the film, followed by cracks perpendicular to this front and a final phase where secondary cracking occurs between existing parallel cracks.*

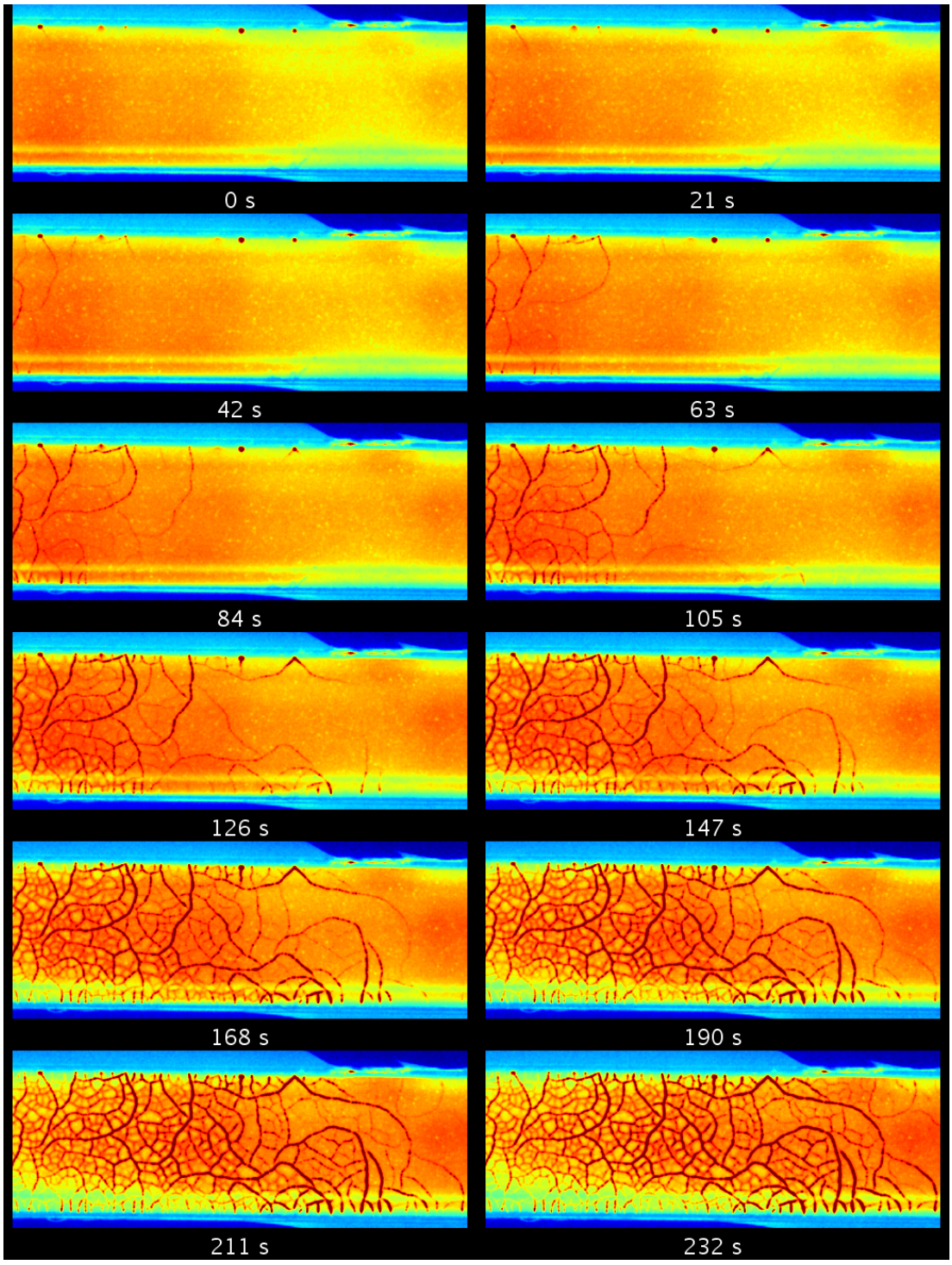

Figure 3.19 *A false colour montage of images from the drying of a post-mix pH 4 sample. In contrast to the post-mix pH 3 sample, no drying front is observed. Cracks nucleate initially from defects at the film edge and travel rapidly across the film until quenched by another crack or another defect site. This initial nucleation travels from left to right. As time proceeds, new cracks nucleate from the initial cracks until the crack network is stable.*

stress relaxation caused by opening a crack with an imposed stress due to water evaporation from the new crack, resulting in a well-defined stress maximum in a direction parallel to the drying front. The next crack will therefore preferentially nucleate at a well defined distance from the first. Adda-Bedia and Amar [3] propose that the regular fracturing can be explained purely by the geometry in which the tensile stress is applied to the layer, although their model depends on a three layer sandwich structure, while the drying tape described here does not have a stress applying top layer. It seems likely therefore that the directional crack propagation observed in this study is due to moisture gradients in the drying film rather than drying geometry considerations.

The flocculated post-mix pH 4 samples yielded different cracking dynamics, as can be seen in the false colour montage in figure 3.19. No initial drying front is observed. Initial cracks nucleate at defects at points on the edge of the film and travel rapidly until quenched by the edge of the film or another crack. A wave of initial cracks spread in this manner from left to right across the tape. In this case, due to the viscosity of the tape, it is unlikely that droplet asymmetry due to an unlevelled stage breaks the symmetry of the drying process. It must therefore be caused by the spreading process.

The two striking differences between the post-mix pH 4 and post-mix pH 3 early crack propagation phenomena are that the pH 3 film results in a more ordered network which forms rather slowly, while the pH 4 film has large direction fluctuations occurring during a rapid propagation process. Bohn et al (2005) [15] have observed that in relatively thick (1 mm to 10 mm) films of starch, a decrease in the thickness of the film resulted in an increase in initial crack direction fluctuation. They attribute this to the ratio of film thickness to the length of the crack domain which is being bisected by the crack (the entire sample in the initial case). They model the tensile stress distribution in the drying film using linear elasticity with adhesion at the substrate and demonstrate that as the ratio of crack domain size to layer thickness decreases, the distribution of tensile stress at the centre of the domain switches from a broad plateau to a well defined peak. Without a well defined spatial peak in the stress distribution, the formation of initial cracks is controlled by film inhomogeneity e.g. the macroscopic capillary pressure gradient due to directional drying in the case of the pH 3 film and point defects in the case of the pH 4 film. The different initial crack patterns observed arise due to different mechanisms driving the quenching of the tensile stress field in the vicinity of the crack tip, consistent with the observations of Goehring et al

in their study on oscillating crack patterns [40].

Further generations of cracking occur in a new tensile stress field which incorporates the stress relaxation of the previous generations of cracks. As domain sizes get progressively smaller, the stress distribution within domains switches from a plateau to a peak, before the residual stress finally drops below the threshold for crack propagation.

The final crack pattern, from which our measurements of the distribution of α are derived, is principally determined in this later, deterministic stage of cracking. A doubling in both mean and deviation of α is observed as the pH of the drying film after mixing is switched from 3 to 4. There are two possible causes for this increase; the change in the material properties of the film due to the alteration of the inter-colloid potential and/or the effect of the difference in initial crack geometry on allowed quench routes for later generations of cracking.

Due to the generational nature of cracking, the initial crack distribution in the film strongly affects future crack development. As discussed earlier, post-mix pH 3 films demonstrate significantly different initial crack patterns to post-mix pH 4 films due to a switch from gradient following crack propagation, which is spatially ordered, to defect hopping which is spatially disordered.

In post-mix pH 3 films, domain subdivision occurs between equally spaced parallel initial cracks, while in post-mix pH 4 films the same process has to occur between non-parallel domains. Due to the competition between stress relaxation near an existing crack, which causes cracks to terminate at other cracks at a right angle, and the minimisation of free energy by reducing domain areas to a certain minimum area, differing degrees of geometrical frustration could occur between samples, causing both a broadening of the distribution of α and an increase in its mean. However, it would be expected that there would be a skew in the distribution of α, reflecting the spectrum of metastable frustrated states the system is frozen in on the way to a fully relaxed state. The observed distribution of α is symmetric about the mean in both cases, indicating this effect, if it exists, is small.

Modifying the pH will cause changes in the material properties of the film through a modification of the inter-colloid potential, as evidenced by the large rheological differences between post-mix pH 3 and 4 suspensions. A larger α implies larger domain areas for a given thickness and therefore less exposed crack area per unit area of film. This implies, by the bulk/surface energy balance argument of

Griffiths [69], that less energy is stored in the bulk during fracture, and therefore the film must either be under a lower tensile stress or more energy is dissipated by viscous forces and plastic deformation in the film during crack propagation. In the work by Guo and Lewis [45], drying silica films with similar thicknesses experienced much higher maximum stresses when deposited in a dispersed state than when in a flocculated state. It is therefore likely that the shift to higher α at post-mix pH 4 is due to the film experiencing lower tensile stress during drying.

The measurement of the distribution of crack angles in the film indicates that most are close to right-angled junctions. These primarily form when a new crack nucleates or terminates at an older crack, due to the existing gradient in tensile stress near the crack. If new cracks primarily nucleated out of pristine film, a peak at 120° would be expected, as this would maximise the relaxation of tensile stress in the film at that point. This has been observed for films close to the critical cracking thickness by Lazarus and Pauchard [70] and Shorlin et al [93]. The evidence in this study therefore supports a generational view of crack formation in a high stress field.

The offset from 90° angles towards larger angles reflects that the older crack appears to bend toward the new crack. There does appear to be some evidence for this in the microscopy images in figure 3.8, however, it is possible that the offset is due to the effect of soft edges at the junction on the skeletonisation procedure. Rounded junction edges can cause the procedure to offset the measured centre of the junction towards the offshoot, as can be seen in figure 3.20. The effect of an offset of the junction centre toward the junction offshoot is an overestimation of the lowest two angles, which reflects the offset seen in the measured angle data. A similar offsets observed in leaf venation patterns by Bohn et al [12], in an automated process which utilises skeletonisation procedures, but not in the study of alumina by Shorlin et al [93] where the angle measurement process is not stated explicitly.

Assuming that this effect is not an artefact of the image analysis process, Bohn et al attribute this to network reorganisation *after* a leaf vein has formed [13]. It is difficult to envisage a similar mechanism in the colloidal film system by which a domain can expand after cracking has occurred; the critereon of strong film adhesion to the substrate would seem to forbid it. Delamination of the film after cracking is observed in post-mix pH 3 films and could contribute to the angle offset through the same image processing artefact as outlined above. However, no delamination is observed visually in post-mix pH 4 films and the angle offset

(a) *Test image* **(b)** *After skeletonisation*

Figure 3.20 *Example illustrating the offset in junction centre estimated by skeletonising a smoothly rounded right-angled junction.*

is still present. Therefore it seems more likely that the bond angle is locked in at the point where a new crack nucleates. The offset toward obtuse angles indicates that cracks preferentially nucleate from convex sections of a parent crack. This matches observations made by Goehring et al [40] in their study on oscillating crack formation in directionally drying films, although they do not pursue the nature of the secondary cracking in their report.

3.4.3 Drying Behaviour

Three periods can be identified from the mass loss curves in both samples: an initial rate period with a moderate increase in evaporation rate and two falling rate periods, which is similar to what has been observed by Lewis [71] although the initial regime is usually constant in evaporation rate. While the shape of the curve of rate of mass loss is similar between samples, there is a time offset from other samples for the post-mix pH 3 film on a smooth substrate. As the initial film mass is lower for this film, it seems likely that a difference in the initial wet film conformation before drying is responsible for this change.

The constant rate period is the time during which the evaporation of water is not restricted by the processes occurring within the film. All films appear to display a increase in the rate (about 10% to 20% of average drying rate) over the first 3000 s. It is not clear what process could cause this increase. Sedimentation processes could decrease the concentration of colloid at the water-air interface, therefore increasing the available interfacial area for evaporation. A naive calculation of the Stokes sedimentation velocity indicates that sedimentation over distances equivalent to a particle radius occur on the timescale of seconds for 100 nm spheres. Without more detailed information on the structure of the colloidal

clusters within the suspension the significant corrections to the drift velocity arising from particle roughness and porosity cannot be included. It seems unlikely that these corrections can account for the three orders of magnitude discrepancy in the timescale of the observed process.

One process which could occur over the pertinent time scale is changes in particle wettability due to irradiation by visible light. Films of titania colloid cast onto a surface have been shown to exhibit a photoresponsive contact angle, with a change from 0° to about 30° observed over about 25 minutes under visible light and an equivalent reverse process observed under UV light [101]. As the drying of films has rarely been studied using titania as the colloidal phase, this could explain the discrepancy between the constant rate period reported by Lewis and the moderate increase in rate reported here. The increase of the contact angle with time causes a reduction in the negative capillary pressure within the fluid phase at surface pores. This would result in an enhancement of the evaporation rate with time until the negative pressure can no longer be sustained within the film (see first falling rate period, below).

The cracking process begins during the constant rate period and initially does not significantly affect the evaporation rate. This indicates that capillary redistribution of fluid within the film occurs at a rate large enough to replenish liquid at the film surface as it evaporates [71]. This supports evidence presented by Dufresne et al that crack edges remain wet during the cracking process [34].

The rapid fall in evaporation rate (first falling rate period) after cracking is due to the retreat of fluid into the pores of the solid crack domains once the film is no longer able to crack. Due to the preferential drainage of large pores in the network during the constant rate period [71] only nanoscopic pores will still be wet at this stage. The geometric limit to pore size is approximately $0.1a$, which for the particles in this study is of the order of 3 nm. With the size of a water molecule being approximately 0.5 nm, these small pores present a significant hindrance to vapour diffusion (Knudsen diffusion) once the meniscus has retreated a short distance into the pore, and therefore there is a sharp drop in evaporation rate [34]. This can only occur when the capillary forces at the fluid meniscus can no longer balance the negative pressure due to evaporation, which can be determined geometrically to be $P_{max} = 2\gamma/r_p$, with γ being the surface tension and r_p the pore radius. With evaporation curtailed, the rise in capillary pressure for later times is restricted and therefore the tensile stress in the film drops. This correlates with the end of cracking in the film. As this occurs at the length scale of the

individual colloids, inter-colloid interactions are not important and therefore both pH 3 and 4 films exhibit this behaviour.

The second falling rate period, which has a slower drop in mass loss rate to zero, is attributed by Lewis to a change in water droplet conformation from tube filling to pendant droplet within the porous network. The resulting increase in evaporating surface area and porous network connectivity is enough to slow the rate at which evaporation diminishes. This can only be a favourable conformation change at low water concentrations within the network. The 'dimming' behaviour observed is therefore probably related to an increase in optical interfaces, as titania/water/titania interfaces de-wet and become titania/air/water/titania interfaces. The higher prevalence of optical interfaces results in greater scattering, resulting in a reduction of intensity reaching the camera.

The final film mass (see figure 3.17 and accompanying text in the results section) for the post-mix pH 3 sample on a rough substrate indicates a loosely packed film is formed with a volume fraction lower than that of close packing, although this estimate is reliant on assumptions about the thickness of the tape (which was only measured in two regions). This, combined with the low viscosity of the pH 3 suspension, would be consistent with the presence of a stable colloidal cluster phase.

A higher degree of delamination is observed in post-mix pH 3 samples than in post-mix pH 4 samples. Delamination may be exacerbated by various factors, including increased drying after the sizes of the crack domains have reached their final value and the adhesive interactions of the ceramic tape with the substrate. Once cracking is energetically forbidden, delamination is the only route to relaxing the tension within the film. As the stable films experience higher stresses than the flocculated films, a higher degree of delamination is to be expected.

3.5 Conclusions

A study of cracking in thin films of colloidal titania has been presented in which, for the first time, the strength (rather than the range) of the stabilising electrostatic potential between colloids has been varied. Two principal effects have been noted. Firstly, the driving force for crack propagation changes from gradient-following to defect-hopping as the suspension pH after mixing is increased from

3 to 4. As defects are isotropically spread throughout the film while drying gradients are non-isotropic, this results in a spatially ordered drying pattern for pH 3 films and a disordered pattern for pH 4 films. Second, the switch from a pH 3 to a pH 4 film increases the characteristic ratio of crack domain area to film thickness α. This was related to a lowering of the maximum stress experienced by the film during drying.

The evidence supports a drying process as outlined by Lewis [71]. A reduction of the intensity of light transmitted through cracks in the film is observed as a distinct process after cracking has completed and is attributed to the redistribution of moisture through the film during the final stages of the drying process. An interesting increase in evaporation rate with time during the initial drying phase has been reported where previous studies have found this period to be constant in evaporation rate. The final volume fraction recorded for post-mix pH 3 films is consistent with a sparse packing of colloids and combined with the low measured viscosity of the suspension provides further evidence for a stable cluster phase for post-mix pH 3 suspensions.

Chapter 4

Dynamic Light Scattering

4.1 Introduction

The interaction of light and matter is a commonly used tool in science to measure the properties of materials. Dynamic light scattering (DLS, also referred to as photon correlation spectroscopy) [83] measures the fluctuations in intensity of a scattered light field and relates these fluctuations to the properties of the scatterers, for instance their size. With modern equipment, DLS data are easy to gather. The difficulty lies in reducing the measured fluctuation data to parameters of interest in non-ideal systems where simplifying assumptions cannot be made.

The equipment required for a dynamic light scattering experiment is very similar to that used for a static scattering experiment, and often rigs are constructed so that both measurements can be carried out simultaneously. A diagram is presented in figure 4.1. The sample is illuminated with a coherent light source (e.g. a laser) and the intensity scattered at a particular angle measured using a photodetector mounted on a goniometer. The time-averaged scattered intensity is related to the shape of the scatterers and how they are arranged in space. For example, for a static structure such as a crystalline solid, the intensity pattern is a series of Bragg peaks as a result of the coherent interference of scattered light from the periodic structure. This type of measurement is the domain of static light scattering. The information about the scatterers is encoded into the phase shift of the scattered electric field. It can be shown that this phase shift is proportional to $-\boldsymbol{q} \cdot \boldsymbol{r}$, with the scattering vector $\boldsymbol{q}$ encoding the geometry of the

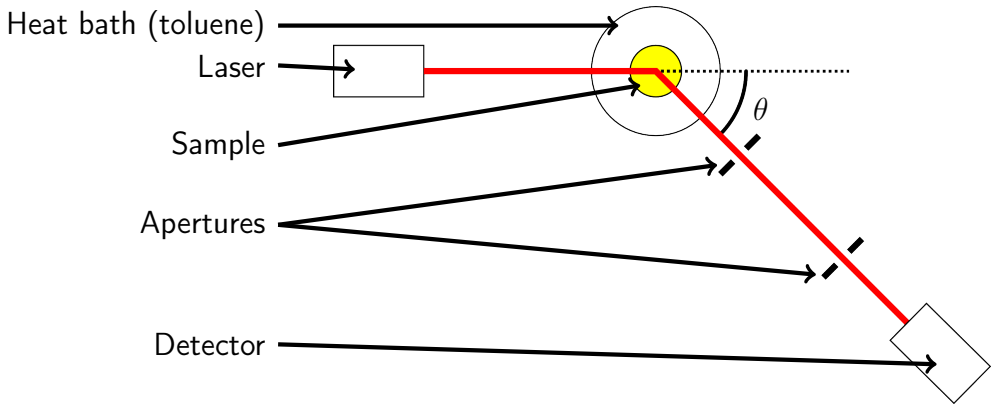

Figure 4.1 *Diagram of apparatus used for light scattering, after [83]. The apertures are used to ensure that only light from one diffraction speckle is collected by the detector.*

problem:

$$q \equiv |\boldsymbol{q}| = \frac{4\pi n}{\lambda} \sin \frac{\theta}{2} \tag{4.1}$$

where λ/n is the wavelength of the incident light inside the scattering medium. Note that the scattering vector has dimensions of inverse length. It is instructive to briefly diverge into the technique of sizing colloids using this static scattering information. The average scattered intensity from a collection of identical scatterers can be split into two quantities, the form factor of the scatterers $P(q)$ and the structure factor $S(q)$:

$$I(q) \propto P(q)S(q) \tag{4.2}$$

The structure factor records the effect of spatial correlations between scatterers on scattered intensity. In the case of disordered and dilute scatterers spatial correlations are negligable and the structure factor conveys no information, e.g. $S(q) = 1$. The form factor is related to the shape of the scatterers. In general it will have a complex form, but in the limit where the scatterers are much smaller than the wavelength of the probing light ($qR_g << 1$, where R_g is the radius of gyration of the scatterers) it can be shown that it takes the Guinier form [44]:

$$\ln P(q) = 1 - (R_g^2/3)q^2 \tag{4.3}$$

This form places a minimum limit on the size of the particle which can be probed

using static light scattering techniques. As identified from electron micrographs, the colloidal scatterers in this study have radii on the order of 10 nm. The magnitude of the scattering vector for a laser with a wavelength of 632.8 nm (typical He-Ne red emission band) for a 90° scattering angle (which maximises $\sin\theta/2$) is $1.4 \times 10^7\,\mathrm{m}^{-1}$. The product $R_g^2 q^2$ is therefore of the order of 0.01 and the reduction in scattered intensity will be so small that it will be indistinguishable from noise. The signal will be further degraded by the effect of any polydispersity in scatterer size on the recorded form factor.

It can be seen from the above that static light scattering techniques are not useful for studying nanometer scale systems (unless the wavelength of the probe can be reduced, for example by using x-rays or neutrons as probes). DLS does not suffer from the same difficulty, as instead of considering the perturbation in space of a probing wave by a scatterer, it considers the perturbation in time. This is limited only by the time response of the apparatus (e.g. the dead time of the photodetector, frequency of probe oscillation) which with modern photodetectors and correlation hardware allows measurement down to a resolution of a few nanometers.

The normalised intensity correlation function is measured by calculating the expectation of the product of measured intensity at two times separated by a lag time, τ:

$$g^{(2)}(\boldsymbol{q},\tau) = \frac{\langle I(\boldsymbol{q},0)I(\boldsymbol{q},\tau)\rangle}{\langle I(\boldsymbol{q})\rangle^2} \tag{4.4}$$

In order to calculate the effect of the scatterer dynamics on the scattered phase of a coherent light field, we will need to consider field correlations, rather than the measured intensity correlations. Defining $E_S(\boldsymbol{q},t)$ as the scattered electric field at scattering vector $\boldsymbol{q}$ and time t we have:

$$\langle I(\boldsymbol{q},0)I(\boldsymbol{q},\tau)\rangle = \langle I(\boldsymbol{q})\rangle^2 \left[1 + \langle E_S(\boldsymbol{q},0)E_S^*(\boldsymbol{q},\tau)\rangle^2\right] \tag{4.5}$$

Defining the normalised field correlation function $g^{(1)}(\boldsymbol{q},\tau)$ (also referred to as $f(\boldsymbol{q},t)$ in the literature):

$$g^{(1)}(\boldsymbol{q},\tau) \equiv \frac{\langle E_S(\boldsymbol{q},0)E_S^*(\boldsymbol{q},\tau)\rangle}{\langle I(\boldsymbol{q})\rangle} \tag{4.6}$$

$$\implies g^{(2)}(\boldsymbol{q},\tau) = 1 + \left[g^{(1)}(\boldsymbol{q},\tau)\right]^2 \tag{4.7}$$

In practice, the non-ideal nature of laser sources introduces a degree of decoherence

during scattering. This is reflected in an empirical coherence factor β:

$$g^{(2)}(\boldsymbol{q},\tau) = 1 + \beta\left[g^{(1)}(\boldsymbol{q},\tau)\right]^2 \tag{4.8}$$

The above equation is known as the Siegert relation. By measuring $g^{(2)}(\boldsymbol{q},\tau)$ we can calculate $g^{(1)}(\boldsymbol{q},\tau)$ and thus extract information about the time correlations in the dynamics of the scatterers from the time-dependence of the scattered intensity.

The scattered field from N particles at scattering vector q is equal to the sum of N spherical waves centred at each particle, with each wave phase shifted by the appropriate amount. Given the positions of the centres of the particles at time zero, $\boldsymbol{R}$, and their subsequent displacements at later times $\boldsymbol{r}_i(\tau)$, the scattered field is therefore:

$$E_S(\boldsymbol{q},\tau) = -E_0\frac{\exp\left[i(kR-\omega t)\right]}{R}\sum_{j=1}^{N} b_j(\boldsymbol{q},t)\exp\left[-i\boldsymbol{q}\cdot\boldsymbol{r}_j(\tau)\right] \tag{4.9}$$

The scattering amplitudes, $b_j(\boldsymbol{q},\tau)$, weight each field contribution by how effectively the light is scattered by particle j. They depend on the fluctuations in the refractive index field ρ caused by the particles:

$$b_j(\boldsymbol{q},\tau) = \int_{V_j}\Delta\rho(\boldsymbol{r},\tau)\exp(-i\boldsymbol{q}\cdot\boldsymbol{r})d^3r \tag{4.10}$$

This gives a final form for $g^{(1)}(\boldsymbol{q},\tau)$:

$$g^{(1)}(\boldsymbol{q},\tau) = \frac{\sum_j\sum_k\langle b_j(\boldsymbol{q},0)b_j^*(\boldsymbol{q},\tau)\exp\left\{-i\boldsymbol{q}\cdot[\boldsymbol{r}_j(0)-\boldsymbol{r}_k(\tau)]\right\}\rangle}{\sum_j\sum_k\langle b_j(\boldsymbol{q})b_j^*(\boldsymbol{q})\exp\left\{-i\boldsymbol{q}\cdot[\boldsymbol{r}_j(0)-\boldsymbol{r}_k(0)]\right\}\rangle} \tag{4.11}$$

The first assumption made in a DLS data reduction to extract e.g. the size of the particles is that the sample is dilute. This allows us to neglect multiple scattering events e.g. the fields scattered by points within other particles $k \neq j$ do not need to be considered when calculating the field scattered by points within particle j. This allows a collapse of the multiple summations into one. Denoting the displacement of particle j in time τ as $\Delta\boldsymbol{r}(\tau) = \boldsymbol{r}(0) - \boldsymbol{r}(\tau)$:

$$g^{(1)}(\boldsymbol{q},\tau) = \frac{\sum_j b_j^2(q)\langle\exp\left\{-i\boldsymbol{q}\cdot[\Delta\boldsymbol{r}_j(\tau)]\right\}\rangle}{\sum_j b_j^2(q)} \tag{4.12}$$

For colloidal particles undergoing Brownian motion, $\Delta\boldsymbol{r}$ has a three dimensional

Gaussian probability distribution and the expectation value can be analytically obtained:

$$\langle \exp\{-i\boldsymbol{q}\cdot[\Delta\boldsymbol{r}(\tau)]\}\rangle = \exp\left(-D_0\, q^2\, \tau\right) \tag{4.13}$$

Usually, the next assumption made is that all the particles are identical i.e. that the sample is monodisperse. This collapses the scattering amplitudes and leaves:

$$g^{(1)}(\boldsymbol{q},\tau) = \exp\left(-D_0\, q^2\, \tau\right) \tag{4.14}$$

Thus the observed intensity correlation function is a single exponential decay with a rate $\Gamma = D_0 q^2$. By fitting the observed $g^{(2)}(\boldsymbol{q},\tau)$ to the above expression via the Siegert relation, a hydrodynamic radius can be extracted using an appropriate form for D_0, for example the Stokes-Einstein relation $D_0 = k_B T/6\pi\eta R_H$. The data reduction is simple in this case and can be performed using a linear regression of $\ln\sqrt{g^{(2)}(\boldsymbol{q},\tau)-1.0}$ vs $q^2\tau$.

Relaxing the assumption of identical scatterers is necessary to address polydisperse samples. To do this, the single rate Γ is replaced by an integral over a distribution of rates, $G(\Gamma)$, which also includes the scattering amplitudes of each rate component:

$$g^{(1)}(\boldsymbol{q},\tau) = \int G(\Gamma)\exp\left(-\Gamma\tau\right) d\Gamma \tag{4.15}$$

In this case, direct extraction of the rate distribution $G(\Gamma)$ (which encodes the size distribution) is an inverse Laplace transform of the intensity correlation function. With non-zero noise in the intensity correlation function, this is what is known as an ill-defined problem. Even a small amount of noise in $g^{(2)}(\boldsymbol{q},\tau)$ will result in the inverse transform being intractable. This can be seen graphically by noting that a smooth sum of exponentials looks similar to a single exponential about the mean of the series of exponentials.

The inverse Laplace transform can be avoided by exploiting the narrow distribution of rates about the mean rate $\bar{\Gamma} = \int G(\Gamma)\Gamma d\Gamma$. Expressing the argument of the integral as the difference from the mean decay rate and expanding the exponential

as a power series:

$$g^{(1)}(\boldsymbol{q},\tau) = \exp\left(-\bar{\Gamma}\tau\right) \int G(\Gamma) \exp\left(-(\Gamma-\bar{\Gamma})\tau\right) d\Gamma \tag{4.16}$$

$$= \exp\left(-\bar{\Gamma}\tau\right) \int G(\Gamma) \left[1 - (\Gamma-\bar{\Gamma})\tau + \frac{1}{2!}(\Gamma-\bar{\Gamma})^2\tau^2 + \cdots\right] d\Gamma \tag{4.17}$$

$$= \exp\left(-\bar{\Gamma}\tau\right) \left[1 + \frac{1}{2!}\mu_2(\bar{\Gamma}\tau)^2 - \frac{1}{3!}\mu_3(\bar{\Gamma}\tau)^3 + \cdots\right] \tag{4.18}$$

where μ_n are the normalised moments about the mean:

$$\mu_n = \frac{1}{\bar{\Gamma}^n} \int G(\Gamma)(\Gamma-\bar{\Gamma})^n d\Gamma \tag{4.19}$$

Expanding about the mean to obtain parameters of the probability distribution in this way is known as the method of moments [83, 84]. As with a monodisperse fit, taking the logarithm of $\sqrt{1-g^{(2)}(\boldsymbol{q},\tau)}$ and fitting using linear least-squares techniques is the established method [51] for extracting the polydispersity index (defined as the ratio of the variance — the second moment about the mean — to the mean of the size distribution) from dynamic light scattering data. However, this method results in a divergence at long lag times due to the truncation required to linearise the logarithm of the series. As much of the information about the higher moments of the distribution is only explicit at longer lag times, this method can only reliably resolve the second and third moments for small polydispersities.

The advent of cheap modern computing has made non-linear fitting techniques viable for everyday use. There has been some recent interest in testing the improvements non-linear fitting techniques may bring to interpreting scattering data from polydisperse samples. Frisken [38] first experimentally investigated the advantages of non-linear fitting via the method of moments and reported promising improvements in fit quality. However, without exact knowledge of the properties of the scatterer size distribution doubts remain over the effect of systematic deviations on the fit. Hassan and Kulshreshtha [46] began work on fitting simulated data via non-linear second order fits using the methods of moments. They were able to confirm that the non-linear technique improved estimates of distribution mean and variance but did not discuss how systematic errors in fit parameters varied with polydispersity or if higher order expansions improved fit quality. This chapter will discuss the fitting of simulated data using non-linear techniques and the application of the insights gained to real polydisperse samples of titania suspensions.

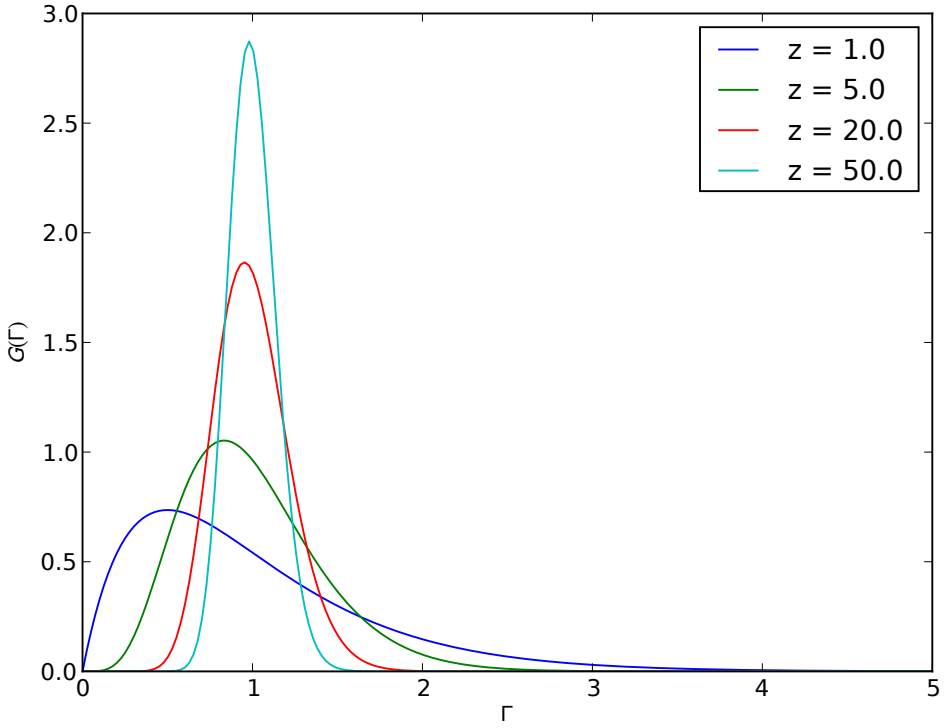

Figure 4.2 *The Schultz distribution for* $\bar{\Gamma} = 1.0$ *and various values of* z*. Lower values of* z *have higher width and skewness.*

4.2 Methods and Materials

4.2.1 Simulation Strategy

In order to simulate $g^{(1)}(\boldsymbol{q}, \tau)$ data, an appropriate form for the distribution of decay rates $G(\Gamma)$ needs to be chosen. One popular choice is the Schultz distribution [63], due to its similarity to real particle size distributions and its analytic tractability:

$$G(\Gamma) = \frac{1}{\bar{\Gamma}} \frac{(z+1)^{z+1}}{z!} \left(\frac{\Gamma}{\bar{\Gamma}}\right)^{z} \exp\left[-\frac{\Gamma}{\bar{\Gamma}}(z+1)\right] \tag{4.20}$$

Here z is a parameter quantifying the width of the distribution. The Schultz distribution is plotted for various values of z in figure 4.2. From equation 4.15, the field correlation function can be explicitly calculated for a Schultz distributed

size distribution of scatterers:

$$g^{(1)}(\boldsymbol{q},\tau) = \left[1 + \frac{\bar{\Gamma}\tau}{z+1}\right]^{-(z+1)} \tag{4.21}$$

It is also useful to evaluate the normalised moments about the mean of the Schultz distribution. The normalised second moment is equivalent to the variance of the distribution, and can be shown to be:

$$\mu_2 \equiv \sigma^2 = \frac{\bar{\Gamma}^2}{z+1} \tag{4.22}$$

One convenient property of the Schultz distribution is that the higher moments can be expressed in terms of the variance. The higher moments are:

$$\mu_3 = 2\sigma^4 / \bar{\Gamma} \tag{4.23}$$

$$\mu_4 = 3\sigma^4 + 6\sigma^2 / \bar{\Gamma}^2 \tag{4.24}$$

Simulated $g^{(1)}(\boldsymbol{q},\tau)$ curves were generated by evaluating equation 4.21 for N_τ logarithmically spaced lag times between τ_{min} and τ_{max}. $g^{(2)}(\boldsymbol{q},\tau)$ data were calculated from these values via the Siegert relation (equation 4.8) with β being the simulated coherence factor. Each point was then multiplied by a random number drawn from a Gaussian distribution with a mean of 1.0 and standard deviation of σ_{g2}. The simulation was implemented in Python [85] (using the 2.6.6 interpreter and the IPython interactive python shell [81]), using the Scientific Python (0.9.0) and Numeric Python (1.6.1) [56] libraries.

These free parameters are summarised in table 4.1. For simplicity, β and $\bar{\Gamma}$ were chosen to be 1.0. This scaling should not affect the generalisation of results to real experimental data as long as appropriate care is taken to include the effect of floating point precision on calculations involving exponentials. As the effect of the polydispersity on the fitting was the phenomenon of interest, the simulated β and $\bar{\Gamma}$ were held constant while the simulated σ was varied. To generate realistic $g^{(2)}(\boldsymbol{q},\tau)$ data, an estimate of the noise in the signal needs to be made. Typical photon coincidence rates in $\langle I(0)I(\tau)\rangle$ are of the order of $10^6\,\mathrm{s}^{-1}$. Therefore the error in $g^{(1)}(\boldsymbol{q},\tau)$ will be of the order of $1/\sqrt{10^6} = 10^{-3}$. Minimum and maximum simulated τ of 1×10^{-2} and 1×10^2 were chosen to ensure an adequate level of data on the decorrelation. In some cases, a high τ cutoff $g^{(2)}_{cut}$ was implemented by discarding data (before fitting) for which $g^{(2)}(\boldsymbol{q},\tau) - 1.0 < g^{(2)}_{cut}$.

Parameter	Value	Description
β	1.0	Simulated coherence parameter
$\bar{\Gamma}$	1.0	Simulated mean decay rate
σ	*varies*	Second moment of the Schultz distribution
σ_{g2}	0.001	Standard deviation of the Gaussian noise applied to the simulated intensity correlation function
τ_{min}	0.01	Shortest correlation time simulated
τ_{max}	100	Longest correlation time simulated
N_τ	150	Number of correlation time points simulated (logarithmically spaced)

Table 4.1 *Table of free parameters for the simulation of a $g^{(2)}(\boldsymbol{q},\tau)$ dataset.*

Linear fitting to simulated data was performed using a linear least-squares method [11] with a bespoke Python implementation. The data were fitted to a variable order polynomial in τ using the expression:

$$\ln\left[\sqrt{g^{(2)}(\boldsymbol{q},\tau)-1.0}\right] = \frac{1}{2}\ln(\beta) - \bar{\Gamma}\tau + \frac{\mu_2\bar{\Gamma}^2}{2!}\tau^2 - \frac{\mu_3\bar{\Gamma}^3}{3!}\tau^3 + \cdots \tag{4.25}$$

$$= A - B\tau + C\tau^2 - D\tau^3 + \cdots \tag{4.26}$$

Each coefficient was allowed to vary independently and then distribution parameters were extracted via the appropriate combination of coefficients.

Non-linear fitting was accomplished using the pyminuit [74] Python bindings for the minuit optimisation suite [53]. The data were fitted to:

$$g^{(2)}(\boldsymbol{q},\tau) = B + \beta\left\{\exp\left(\bar{\Gamma}\tau\right)\left[1 + \frac{1}{2!}M_2\tau^2 - \frac{1}{3!}M_3\tau^3 + \cdots\right]\right\}^2 \tag{4.27}$$

where B is a baseline which can be allowed to vary or be set to 1.0 and M_n are the *unnormalised* moments about the mean e.g. $M_n = \bar{\Gamma}^n\mu_n$. Parameters β, $\bar{\Gamma}$, M_n and B (if fitting with a variable baseline) were allowed to vary. B, β, $\bar{\Gamma}$ and M_n (for even n) were constrained to be positive during fitting. In the results which follow, the simulated $\bar{\Gamma}$ was always set to 1.0. In this case, $M_n = \mu_n$.

An example of a non-linear fit to simulated data is given in figure 4.3. The data were drawn from a Schultz distribution with $\bar{\Gamma} = 1.0$ and $\sigma = 0.4$, noise parameter $\sigma_{g2} = 0.001$ and $\beta = 1.0$. Non-linear fitting was performed on the

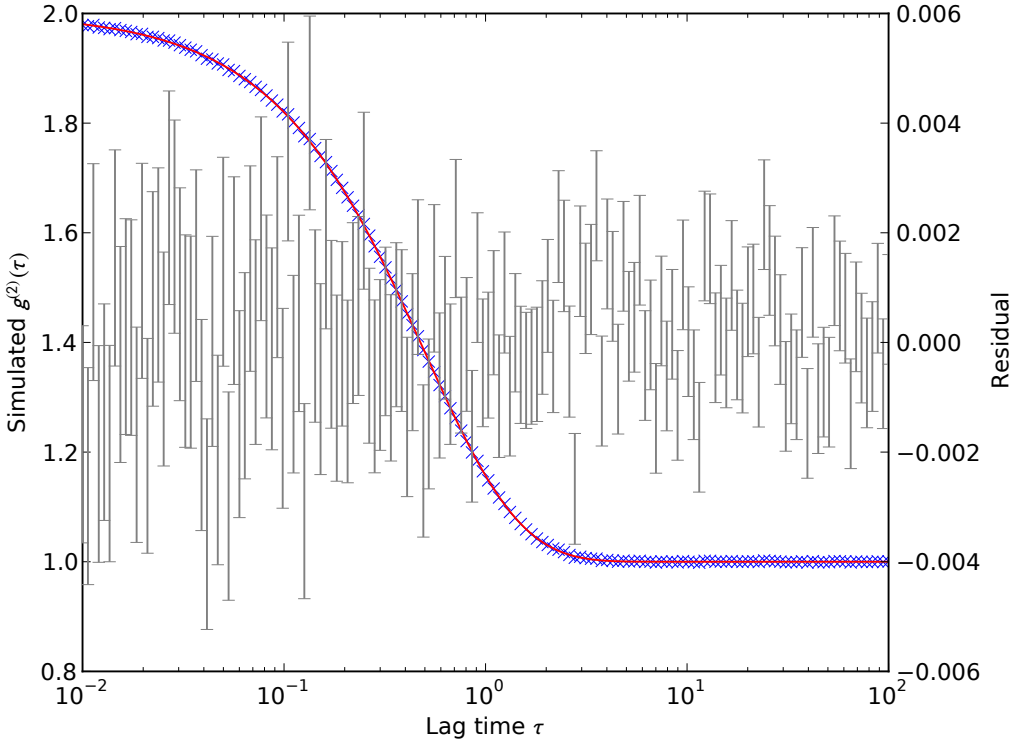

Figure 4.3 *Example fit of a polydisperse $g^{(2)}(\boldsymbol{q}, \tau)$ (for $\sigma = 0.4$) via a second order non-linear fit. The simulated data are marked with $\times$, the red line is the fitted curve and the residuals are presented in grey.*

data with a second order fit. The initial parameter values were $\beta = 1.0$, $\bar{\Gamma} = 1.0$ and $M_2 = 0.0$. The fitted parameters were $\beta_{fit} = 1.0003(4)$, $\bar{\Gamma} = 1.0014(18)$ and $M_2^{fit} = 0.156(4)$, which corresponds to a $\sigma_{fit} = 0.40(2)$.

4.3 Results of Simulation

4.3.1 Stability of Non-Linear Fits

The iterative nature of non-linear fitting demands that an initial guess of parameter values be made as a starting point for the algorithm. A corresponding trade-off ensues between algorithm convergence speed and algorithm stability. A less thorough search of the parameter space results in convergence in a smaller number of steps at the risk of converging to a local minimum if the initial parameter values are chosen wrongly.

The stability of the Minuit algorithm was tested by simulating data for a monodisperse decay rate and fitting a series of these data with either a first or second order non-linear fit without a variable baseline. The Minuit suite itself reports a failure if convergence occurs above an estimate of the global minimum. Failure rates were recorded over fits made to 20 independently generated sets of $g^{(2)}(\boldsymbol{q}, \tau)$ data. This was then repeated for second order fits to a Schultz $g^{(2)}(\boldsymbol{q}, \tau)$ with a σ of 0.4.

Monodisperse Distribution, First Order Fit

Initially a non-linear first order expansion was fit to the data with varying initial parameter values. Figure 4.4 plots the average failure rate (ratio of data sets for which the fit did not converge to total data sets generated) for varying start values of β, the fitted coherence factor, and Γ, the fitted decay rate.

- Varying β above 1.0 does not affect the fit failure rate and that the initial value of Γ is constrained to values below $1000\Gamma_{true}$.
- There does not appear to be a lower bound to Γ.
- Some isolated points in initial parameter space below the stability threshold also appear to be highly unstable (e.g. $\beta = 3$, $\Gamma = 90$).

Monodisperse Distribution, Second Order Fit

Results for the stability of non-linear fits using a second order expansion are presented in figure 4.5. This plot exhibits similar features to that for the first order fit:

- An upper stability boundary in $\bar{\Gamma}$, shifted down to $100\Gamma_{true}$ and broadened in comparison to the first order fit result
- The appearance of islands of instability at about $\Gamma = 0.01$
- It is also apparent that the fit is not very sensitive to the initial value of the un-normalised second moment M_2

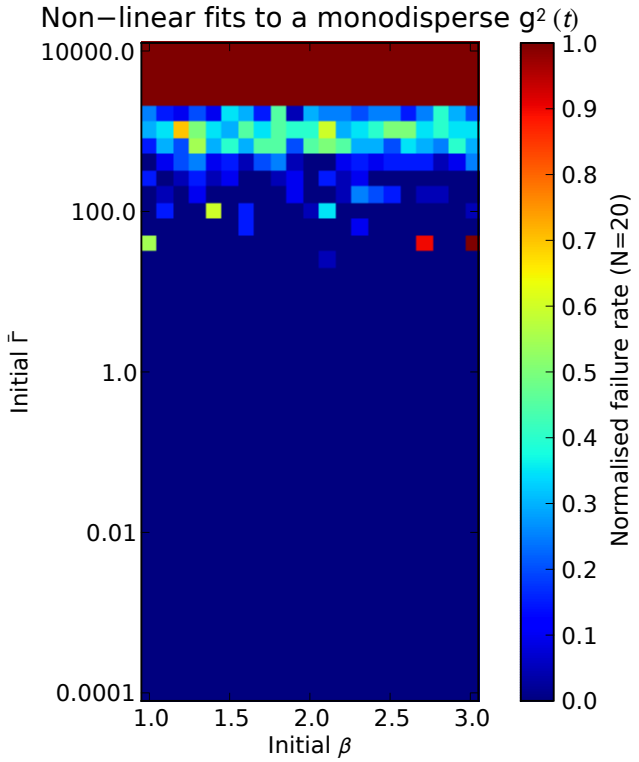

Figure 4.4 *Failure rates for first order fits to a simulated monodisperse distribution with noise*

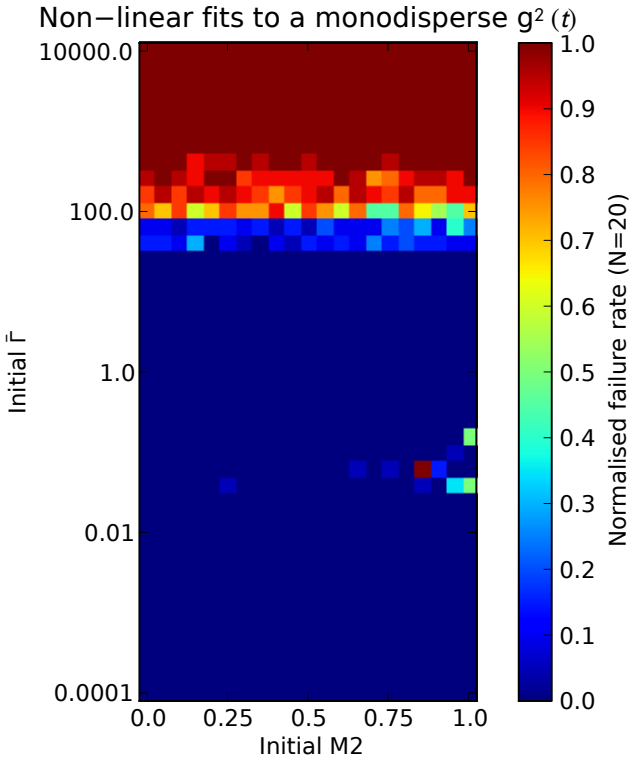

Figure 4.5 *Failure rates for second order fits to a simulated monodisperse distribution*

Schultz Distribution, Second Order Fit

The failure rates for a range of $\beta_{initial}$ and $\bar{\Gamma}_{initial}$ for representative values of $M_2^{initial}$ are presented in figure 4.6. Again, features similar to those in the failure rate graphs are present:

- A lack of $\beta_{initial}$ dependence.
- An upper bound of stability in $\bar{\Gamma}_{initial}$ at about 100 and no apparent lower bound.
- A band of instability in $\bar{\Gamma}_{initial}$ at about 0.025 which broadens as $M_2^{initial}$ is increased. This band is still present even when $M_2^{initial}$ is close to the true value.
- Aside from near the stability limits, most fitted values converge to within one standard error of the true value.

Using this information, initial parameter estimates in the following sections were set as follows: $\beta_{initial} = 1.0$, $\bar{\Gamma}_{initial} = 1.0$, $M_n^{initial} = 0.0$.

4.3.2 Effect of Varying σ and β on Fit

When fitting correlation functions using the method of moments, systematic errors can be introduced into the resulting parameter estimates due to a truncation of the power series representation of the underlying decay rate distribution. Using simulated data, these systematic effects can be studied in terms of the deviation of the fit estimate of a parameter from the underlying simulated value. The effect on the fit of varying the simulated polydispersity (σ) and coherence (β) on third order fits was investigated using the parameters in table 4.2.

The systematic deviation of fit parameters as a function of σ is presented in figures 4.7 and 4.8 for linear and non-linear fits of order 3 and 4 respectively. Each of the twenty datasets was fitted by the appropriate algorithm to extract parameter estimates P for each of the fit parameters and estimated errors in those estimates ΔP. The figures plot the deviation $(\bar{P} - P_{true})/\overline{\Delta P}$ against σ_{true} where $\bar{P}$ is the mean parameter estimate averaged over the twenty fits performed for each value of σ_{true} and $\overline{\Delta P}$ is the standard deviation of the parameter estimates across the

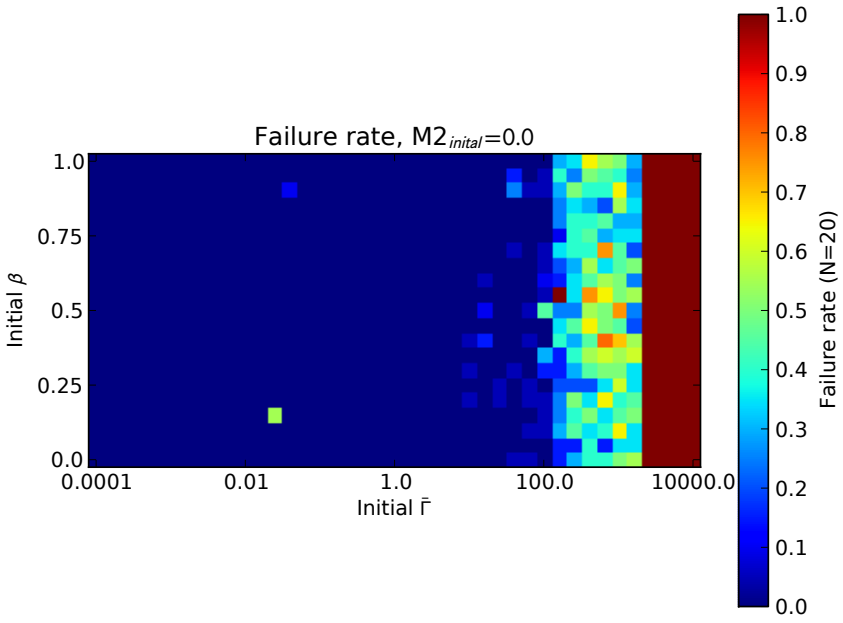

(a) *Failure rates for* $M_2^{initial} = 0.0$

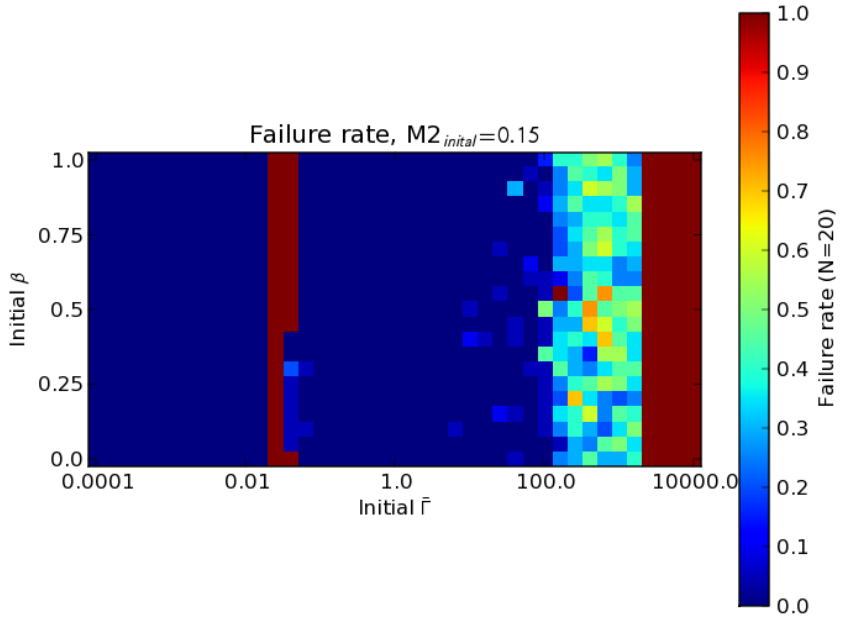

(b) *Failure rates for* $M_2^{initial} = 0.15\,(= \sigma^2)$

Figure 4.6 *Failure rates for a range of* $\beta_{initial}$ *and* $\bar{\Gamma}_{initial}$ *for representative values of* $M_2^{initial}$

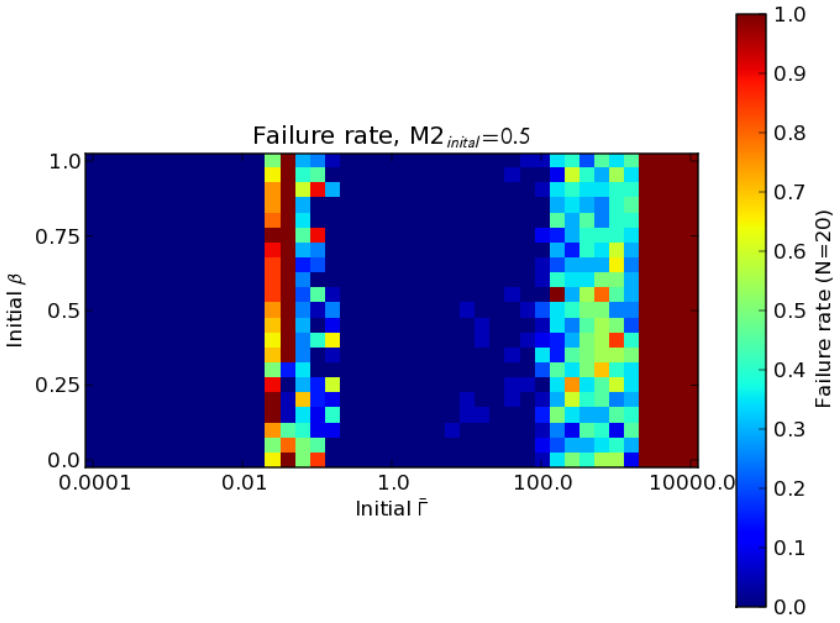

(c) *Failure rates for* $M_2^{initial} = 0.5$

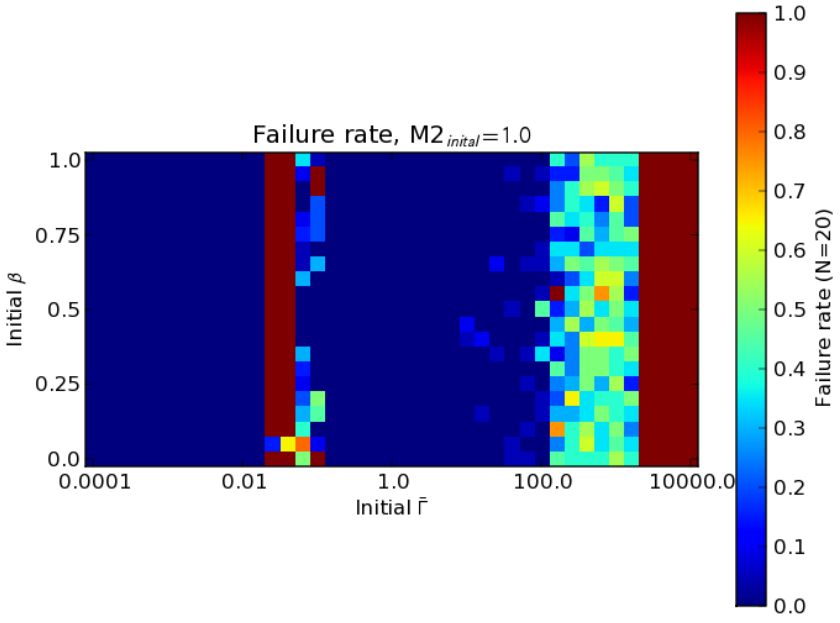

(d) *Failure rates for* $M_2^{initial} = 1.0$

Figure 4.6 *(Continued) Failure rates for a range of* $\beta_{initial}$ *and* $\bar{\Gamma}_{initial}$ *for representative values of* $M_2^{initial}$

Parameter	Value	Description
β	0.02 – 1.0 or 1.0	Coherence factor of the simulated Schultz distribution. Held at 1.0 while polydispersity was varied
σ	0.02 – 1.0 or 0.6	Second moment of the simulated Schultz distribution. Held at 0.6 while coherence was varied
N	20	Number of independently generated samples of $g^{(2)}(\boldsymbol{q}, \tau)$ which were fitted

Table 4.2 *Table of experimental variables for fits to variable polydispersity and coherence datasets*

same twenty fits. P_{true} is the true value of P arising from the simulated Schultz distribution i.e. $M_3^{true} = 2\sigma^4$ (see equation 4.23). It was found that the errors estimated from individual fits by extrapolation along the χ^2 surface matched the sample standard deviations very closely e.g. $\Delta P \approx \overline{\Delta P}$. All fits tended to underestimate the true value of each parameter.

Linear fits only capture β and $\bar{\Gamma}$ without serious systematic error for a broad range of σ. M_2 and M_3 parameters exhibit systematic errors greater than $\approx 2\sigma_{fit}$ for $\sigma > 0.2$ in third order fits. Fourth order linear fits capture M_2 and M_3 for $\sigma < 0.4$. Surprisingly, M_2 estimates suffer from worse systematic error than M_3 estimates for both orders.

Non-linear fits at high σ result in less systematic error than linear fits for parameters M_2 and M_3 but more in β and $\bar{\Gamma}$. In contrast to linear fits, the systematic error in M_2 is less than the systematic error in M_3. Setting $g_{cut}^{(2)} = 0.1$ during third order non-linear fitting resulted in less systematic error at high σ in low order parameters, with the highest order parameter being unchanged. For fourth order non-linear fits, the systematic error was reduced for all parameters at high σ. Switching from third to fourth order fits reduces the systematic error in low order parameters at the expense of adding a new high order parameter with a large degree of systematic deviation.

The results for systematic deviation of fit parameters as a function of β is presented in figures 4.9 and 4.10. In all cases, increasing beta resulted in an increasing underestimate of β. As opposed to the abrupt transition threshold behaviour seen for varying σ, deviation values smoothly increase in a linear fashion to those reflecting the underlying polydispersity, as measured above.

Again, non-linear fits with a cutoff performed better than linear and non-linear fits without a cutoff, with a lower slope of deviation from the true simulated values.

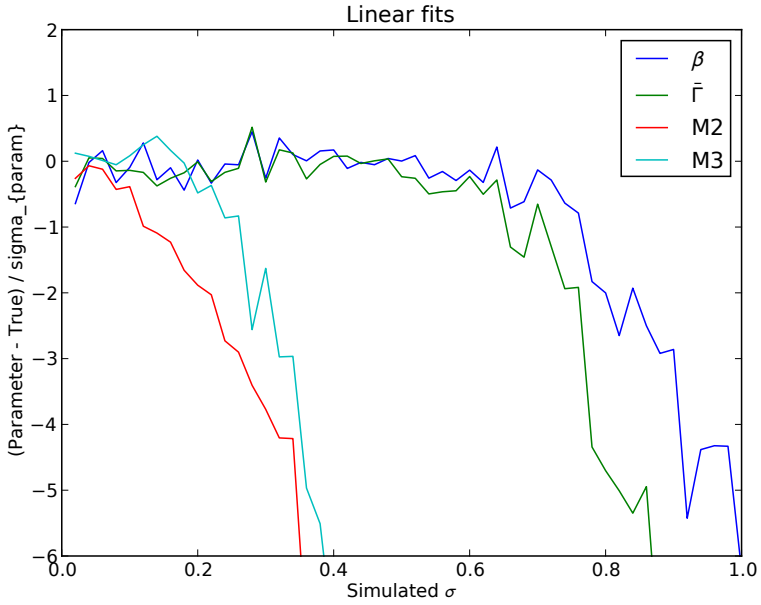

(a) *Linear fits, order 3*

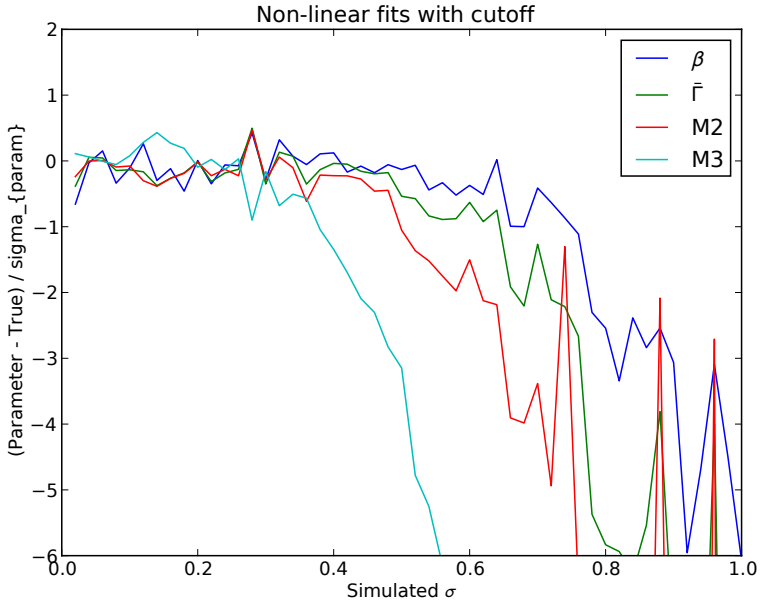

(b) *Nonlinear fits with* $g^{(2)}_{cut} = 0.1$*, order 3*

Figure 4.7 *Systematic deviations of fitted parameters for* third order *linear and non-linear fits. Twenty datasets were fitted with initial* β_{fit} *and* $\bar{\Gamma}_{fit}$ *equal to one and* M_2 *and* M_3 *equal to zero. The plotted data are the mean of the fitted parameters minus its true value, scaled by the standard deviation of the fitted parameters versus the true simulated polydispersity of the distribution,* σ*.*

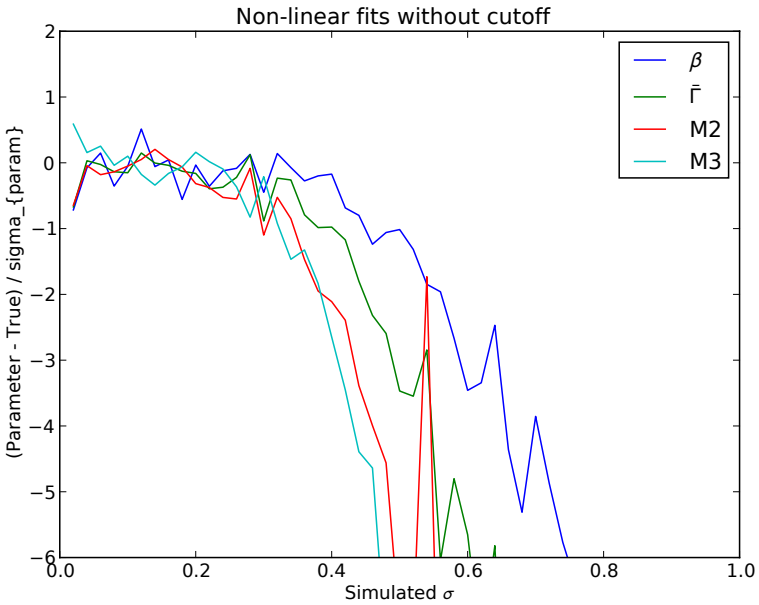

(c) *Nonlinear fits with no cutoff, order 3*

Figure 4.7 (Continued) *Systematic deviations of fitted parameters for* third order *linear and non-linear fits. Twenty datasets were fitted with initial* β_{fit} *and* $\bar{\Gamma}_{fit}$ *equal to one and* M_2 *and* M_3 *equal to zero. The plotted data are the mean of the fitted parameters minus its true value, scaled by the standard deviation of the fitted parameters versus the true simulated polydispersity of the distribution,* σ*.*

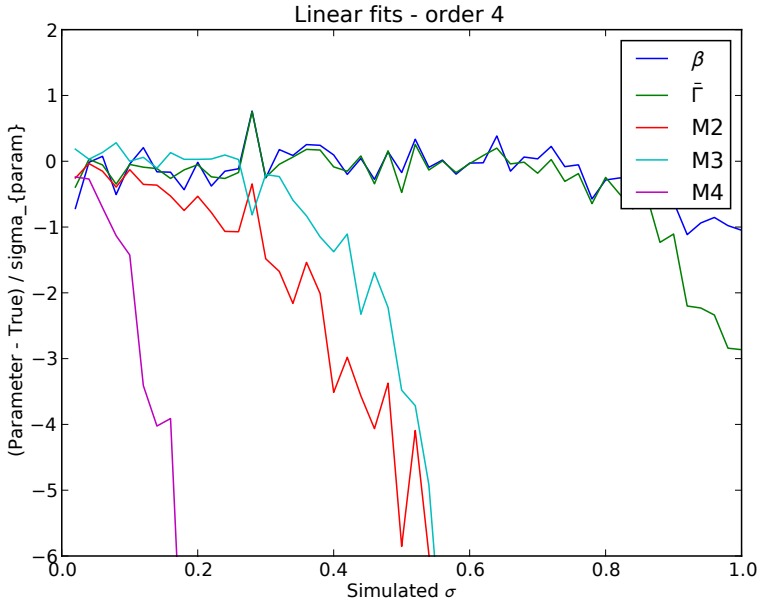

(a) *Linear fits, order 4*

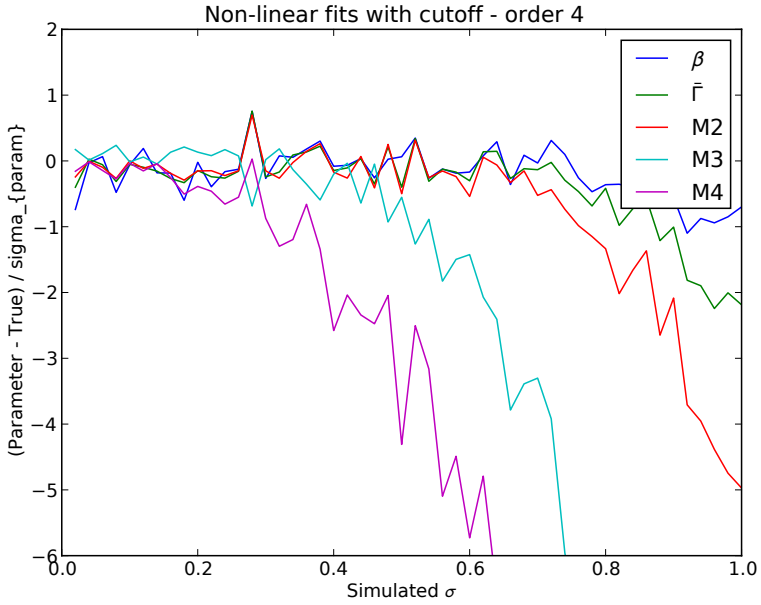

(b) *Nonlinear fits with* $g_{cut}^{(2)} = 0.1$*, order 4*

Figure 4.8 *Systematic deviations of fitted parameters for* fourth order *linear and non-linear fits. Twenty datasets were fitted with initial* β_{fit} *and* $\bar{\Gamma}_{fit}$ *equal to one and* M_2*,* M_3 *and* M_4 *equal to zero. The plotted data are the mean of the fitted parameters minus its true value, scaled by the standard deviation of the fitted parameters versus the true simulated polydispersity of the distribution,* σ*.*

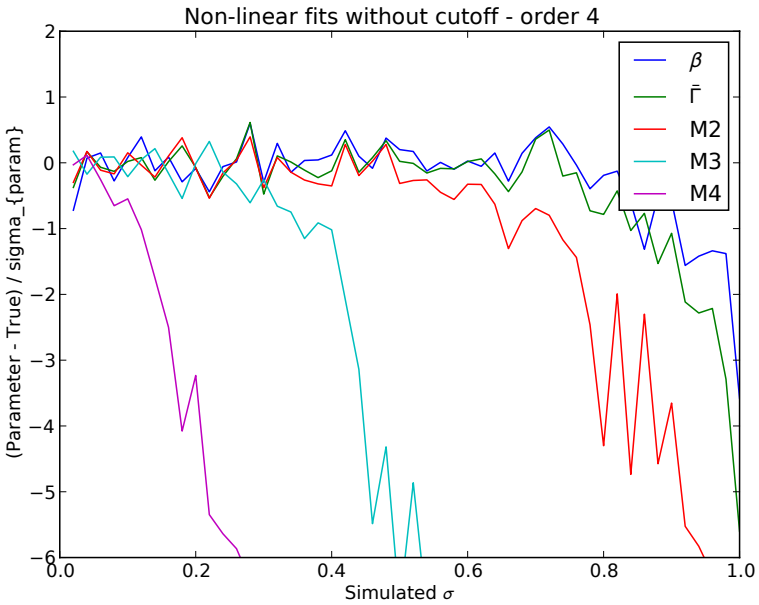

(c) *Nonlinear fits with no cutoff, order 4*

Figure 4.8 (Continued) *Systematic deviations of fitted parameters for* fourth order *linear and non-linear fits. Twenty datasets were fitted with initial* β_{fit} *and* $\bar{\Gamma}_{fit}$ *equal to one and* M_2*,* M_3 *and* M_4 *equal to zero. The plotted data are the mean of the fitted parameters minus its true value, scaled by the standard deviation of the fitted parameters versus the true simulated polydispersity of the distribution,* σ*.*

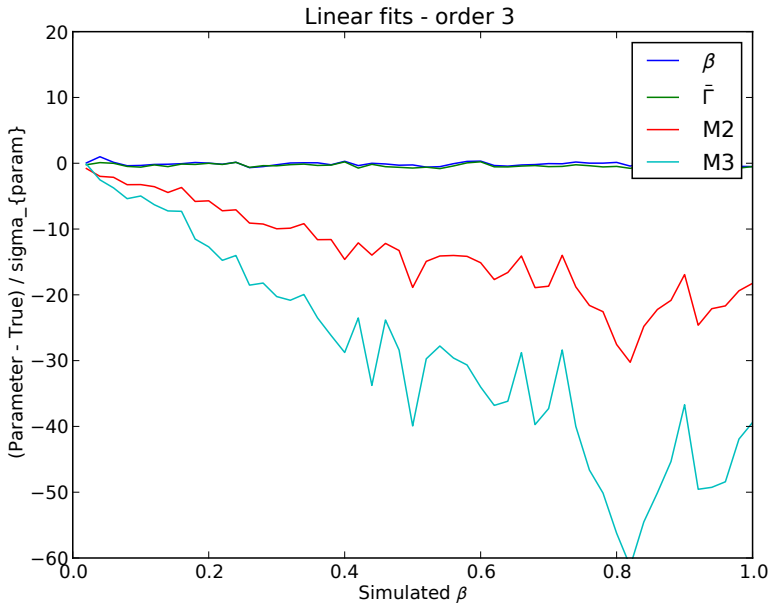

(a) *Linear fits, order 3*

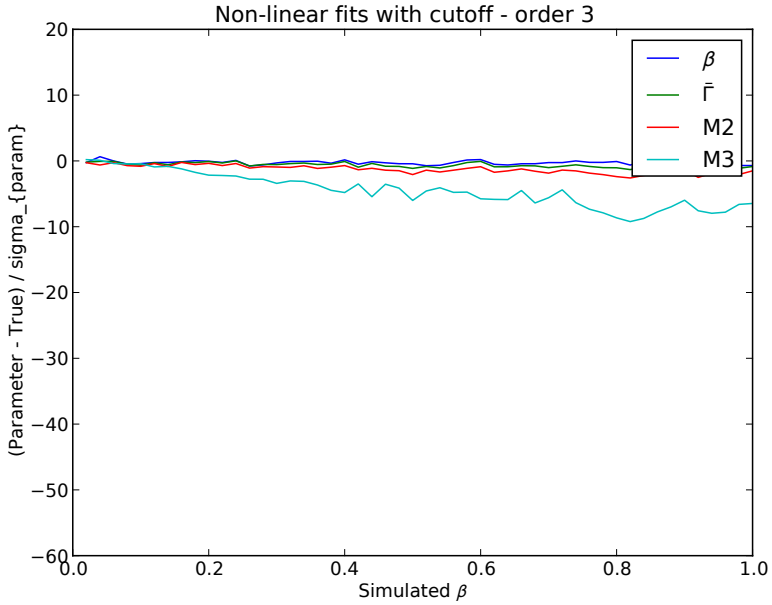

(b) *Nonlinear fits with* $g^{(2)}_{cut} = 0.1$*, order 3*

Figure 4.9 *Systematic deviations of fitted parameters for* third order *linear and non-linear fits. Twenty datasets were fitted with initial* $\bar{\Gamma}_{fit}$ *equal to one and* M_2 *and* M_3 *equal to zero. Initial* β_{fit} *was set to the true value. The plotted data are the mean of the fitted parameters minus its true value, scaled by the standard deviation of the fitted parameters versus the simulated coherence of the distribution,* β*.*

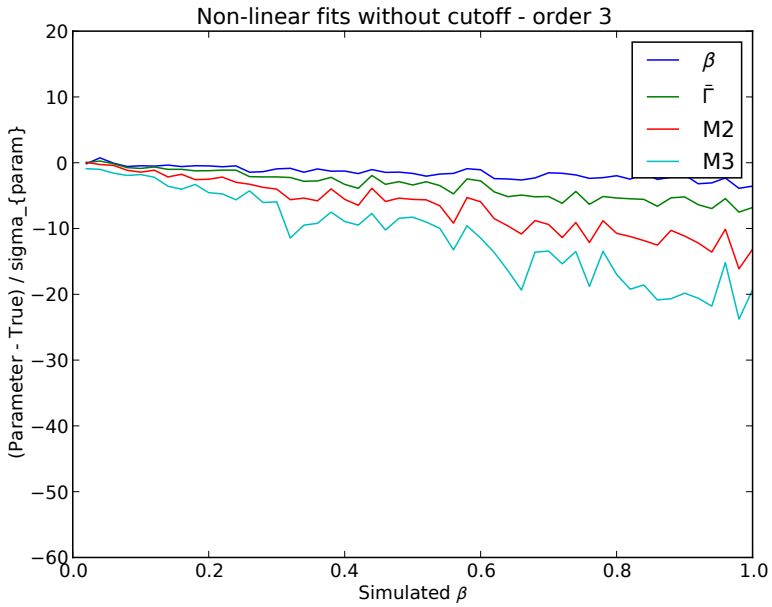

(c) *Nonlinear fits with no cutoff, order 3*

Figure 4.9 (Continued) *Systematic deviations of fitted parameters for* third order *linear and non-linear fits. Twenty datasets were fitted with initial* $\bar{\Gamma}_{fit}$ *equal to one and* M_2 *and* M_3 *equal to zero. Initial* β_{fit} *was set to the true value. The plotted data are the mean of the fitted parameters minus its true value, scaled by the standard deviation of the fitted parameters versus the simulated coherence of the distribution,* β*.*

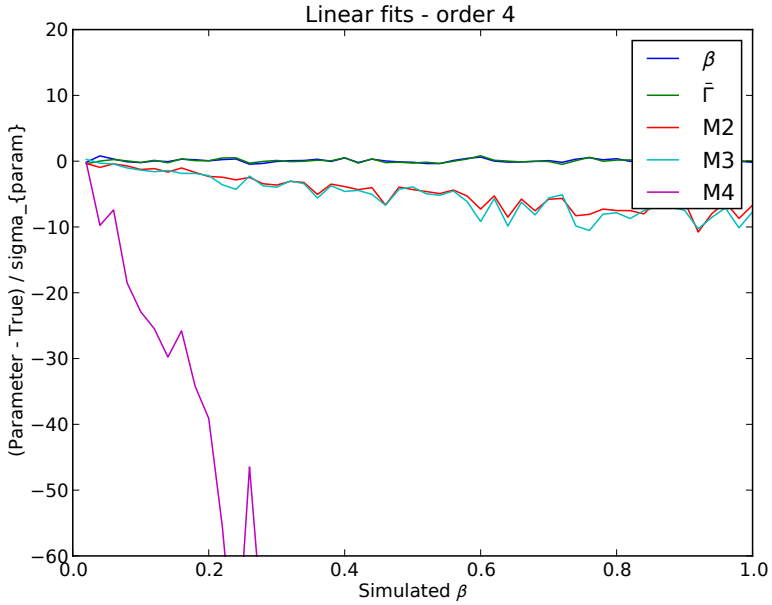

(a) *Linear fits, order 4*

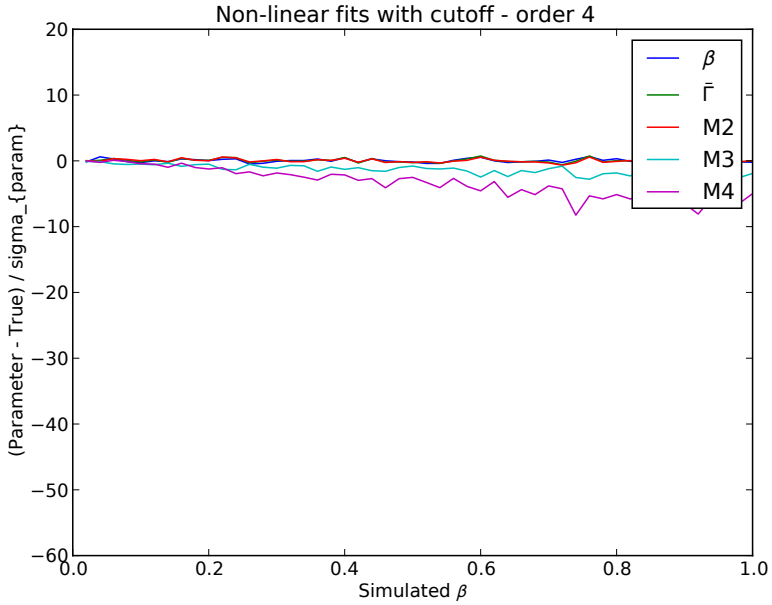

(b) *Nonlinear fits with* $g^{(2)}_{cut} = 0.1$*, order 4*

Figure 4.10 *Systematic deviations of fitted parameters for* fourth order *linear and non-linear fits. Twenty datasets were fitted with initial* $\bar{\Gamma}_{fit}$ *equal to one and* M_2*,* M_3 *and* M_4 *equal to zero. Initial* β_{fit} *was set to the true value. The plotted data are the mean of the fitted parameters minus its true value, scaled by the standard deviation of the fitted parameters versus the simulated coherence of the distribution,* β*.*

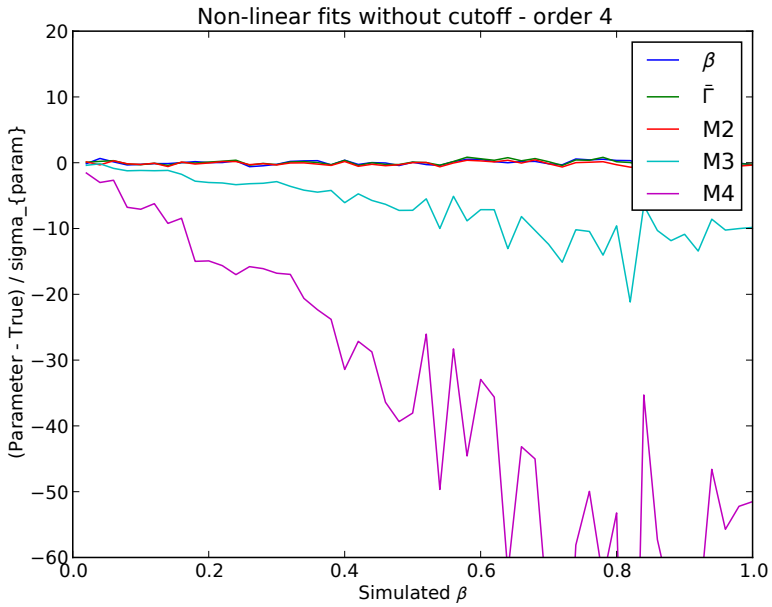

(c) *Nonlinear fits with no cutoff, order 4*

Figure 4.10 (Continued) *Systematic deviations of fitted parameters for* fourth order *linear and non-linear fits. Twenty datasets were fitted with initial* $\bar{\Gamma}_{fit}$ *equal to one and* M_2*,* M_3 *and* M_4 *equal to zero. Initial* β_{fit} *was set to the true value. The plotted data are the mean of the fitted parameters minus its true value, scaled by the standard deviation of the fitted parameters versus the simulated coherence of the distribution,* β*.*

4.3.3 Number of Terms in a Fit for Variable σ

In general one needs to specify the number of terms to use when fitting data. What order of fit to choose may not be easily guessed when fitting real experimental data. In this section the effect of altering the second moment of the simulated correlation data on the resulting systematic errors in the fitted distribution is studied. A comparison of the performance of linear and non-linear fits is also made.

Simulated data are generated from a Schultz distribution with a varying second moment. These data are then fitted with linear and non-linear fits with expansions via the method of moments from first to third order without a variable baseline. The variables used for fits in this experiment are summarised in table 4.3. When performing linear fits, $g^{(2)}_{cut}$ was set to 0.1 e.g. a maximum correlation time of 10 % of the initial value of $g^{(2)}(\boldsymbol{q}, \tau)$ was chosen. Non-linear fits were performed across the whole range of correlation data available.

Parameter	Value	Description
σ	0.0 – 1.0	Second moment of the Schultz distribution

Table 4.3 *Table of experimental variables for variable order fits to Schultz distributions*

The results for fitted β and $\bar{\Gamma}$ are presented in figures 4.11, 4.12 and 4.13. The linear fits behave as expected, with decreasing high σ systematic error for higher order fits. The non-linear fits perform worse than the linear fit for first and third order, but better for second order fits.

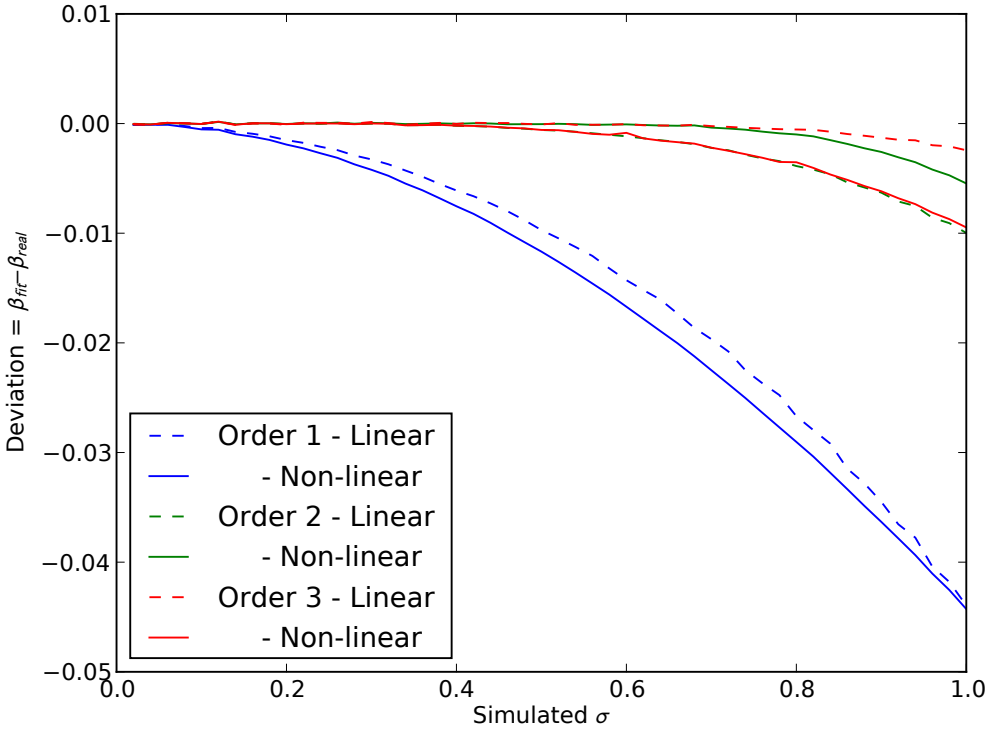

Figure 4.11 *Systematic deviation of fitted β from the underlying simulated value for linear and non-linear fits of increasing order against increasing simulated polydispersity.*

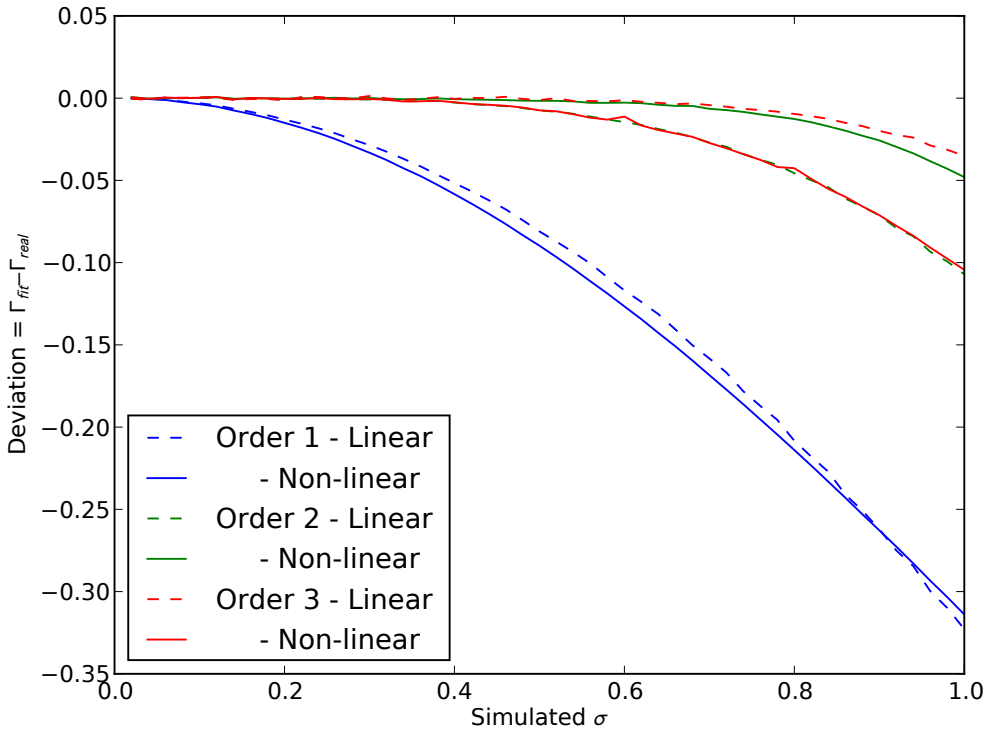

Figure 4.12 *Systematic deviation of fitted $\bar{\Gamma}$ from the underlying simulated value for linear and non-linear fits of increasing order against increasing simulated polydispersity.*

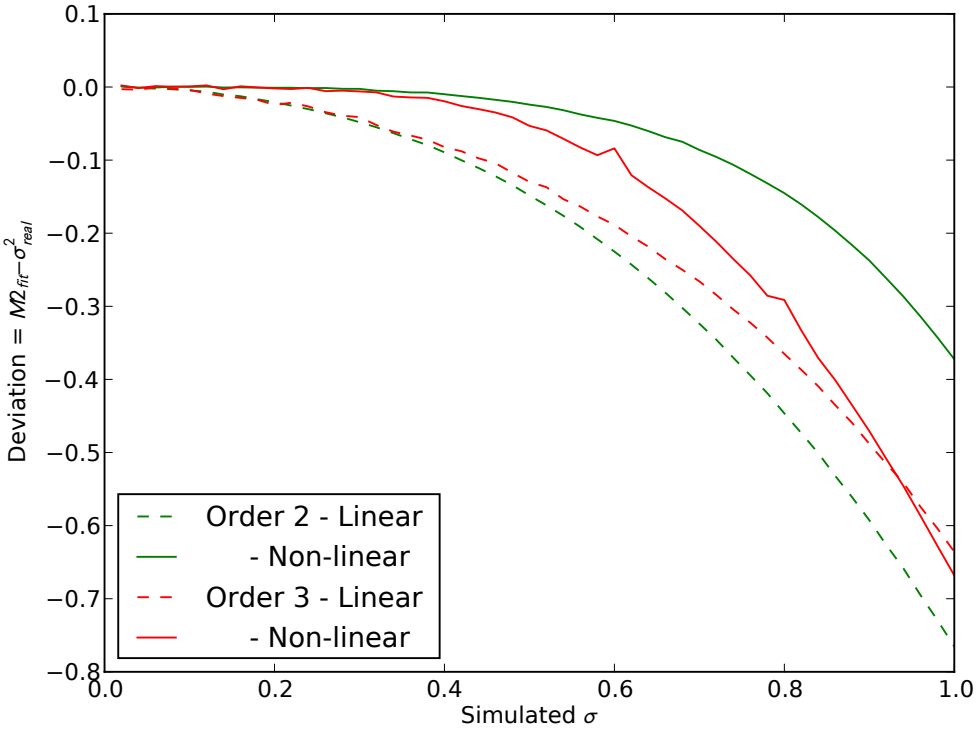

Figure 4.13 *Systematic deviation of fitted M_2 from the underlying simulated value for linear and non-linear fits of increasing order against increasing simulated polydispersity.*

4.3.4 Effect of Maximum Correlation Time

The effect of varying the maximum sampled correlation time was studied by generating $g^{(2)}(\boldsymbol{q},\tau)$ data over time intervals of increasing duration and studying the systematic deviations of the fit. The parameters used to generate $g^{(2)}(\boldsymbol{q},\tau)$ data from a Schultz distribution of decay rates is summarised in table 4.4. Fits were performed to these data using second order linear and non-linear fits. The linear fits had $g^{(2)}_{cut}$ set to 0.1 e.g. a cutoff when $g^{(2)}(\boldsymbol{q},\tau)$ had dropped to 10 % of its initial value.

Parameter	Value	Description
σ	0.6	Second moment of the Schultz distribution
τ_{max}	0.1 – 100	Longest correlation time in fit

Table 4.4 *Table of experimental variables for fits to varying maximum correlation time*

The results are presented in figures 4.14, 4.15 and 4.16. Initially, linear and non-linear fits perform equally. The lack of correlation data over enough of the initial decorrelation limits the precision of the fit. The linear fit begins to systematically deviate from the true value at $\tau_{max} = 5 \times 10^{-1}$. At this point $g^{(2)}(\boldsymbol{q},\tau)$ has not yet fallen below the 10% cutoff value. The non-linear fit also begins to deviate, although with less magnitude. At $\tau_{max} = 1$, the linear fit stabilises while the non-linear fit recovers. For the linear fit, this τ_{max} represents the point at which the 10% cutoff value begins to take effect.

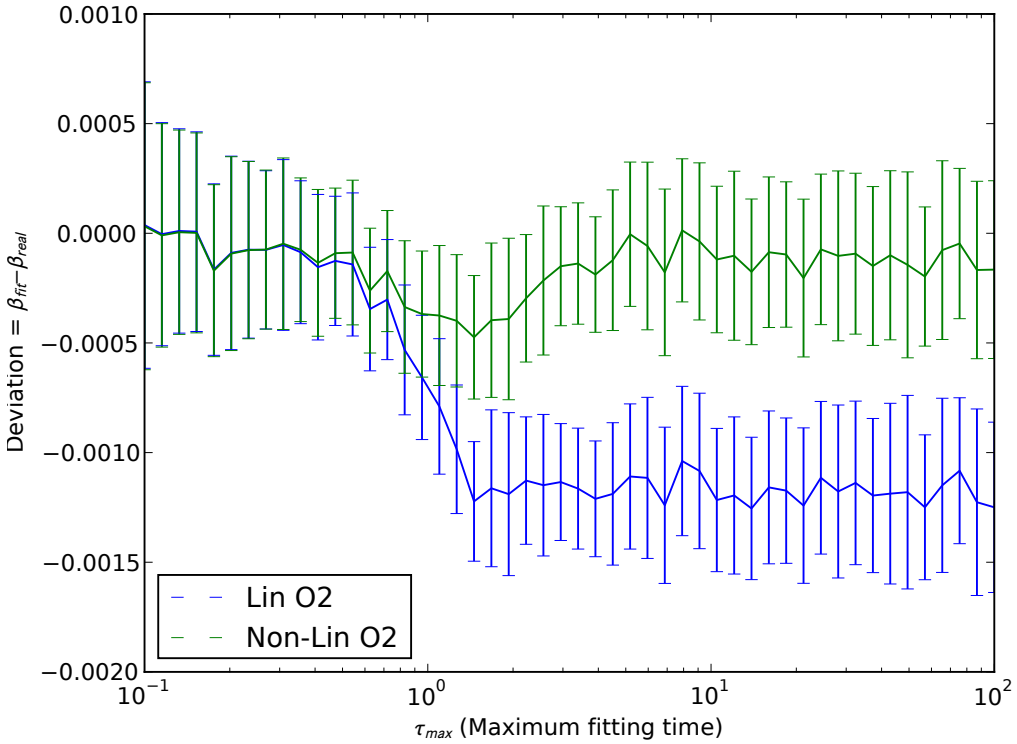

Figure 4.14 *Variation of the systematic deviation of fitted β from simulated data for variable maximum fitted correlation time.*

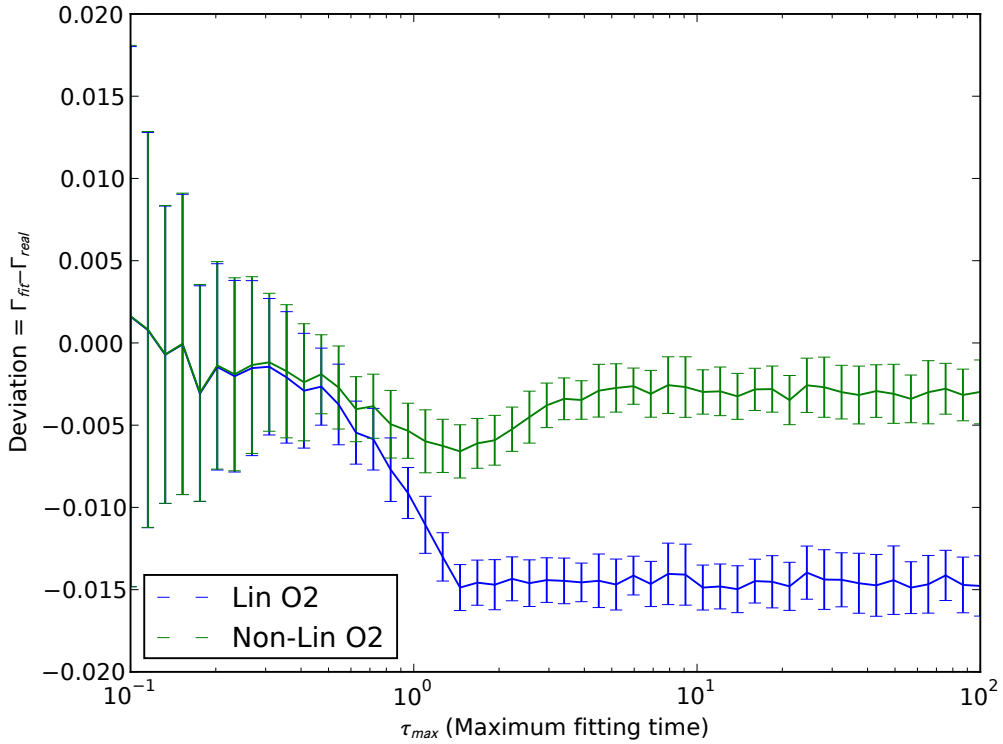

Figure 4.15 *Variation of the systematic deviation of fitted* Γ *from simulated data for variable maximum fitted correlation time.*

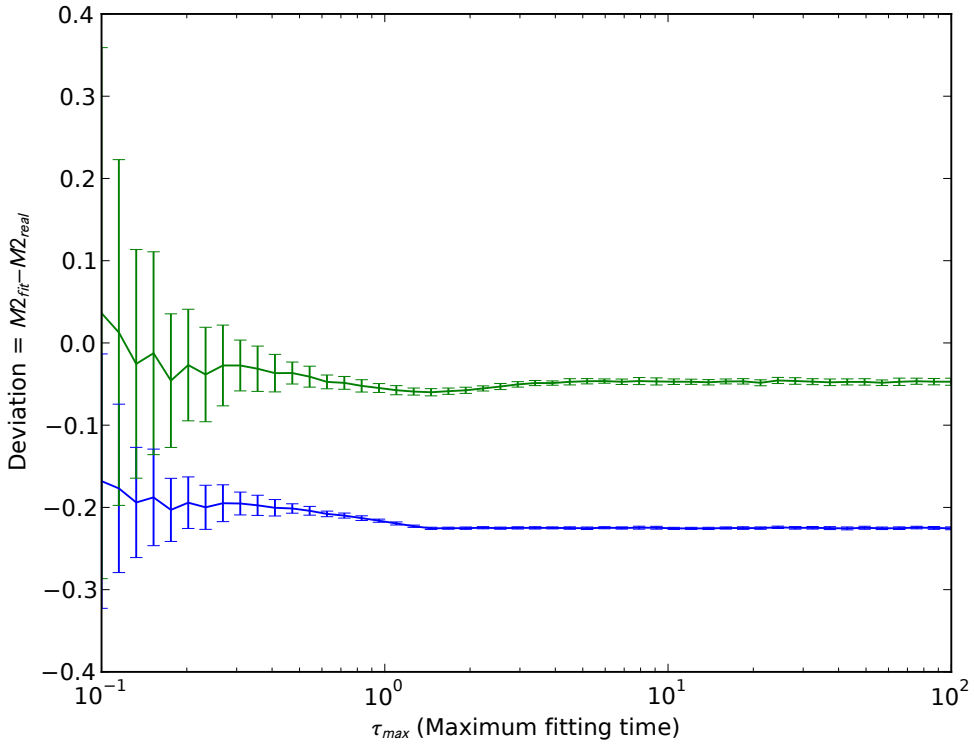

Figure 4.16 *Variation of the systematic deviation of fitted M_2 from simulated data for variable maximum fitted correlation time.*

4.3.5 Effect of Simulated Noise on Fits

The effect of varying the amount of noise in the simulated data was studied by applying linear and non-linear first order fits with $g^{(2)}_{cut}$ set to $1.0 + 0.1\beta$ and data generated using the parameters in table 4.5.

Parameter	Value	Description
σ_{g2}	0.001 – 0.01	Standard deviation of the Gaussian noise applied to the simulated intensity correlation function
σ	0.6	Second moment of the Schultz distribution
N	50	Number of independent datasets fitted

Table 4.5 *Table of experimental variables for fits to varying noise levels*

The results are presented in figures 4.17 and 4.18. Two sets of error bars are presented: the standard deviation of the deviations averaged over the 50 generated datasets and the mean estimated error reported from fitting. It can be seen that the estimated errors are very similar to the true sample standard deviations. The noise appears to have no deleterious effect of the range studied and only increases the uncertainty in the fit estimate. Note however that the systematic error is still present. Figure 4.19 presents similar data for third order fits. A similar trend of increasing fit parameter variability with noise parameter can be noted for all the fit parameters.

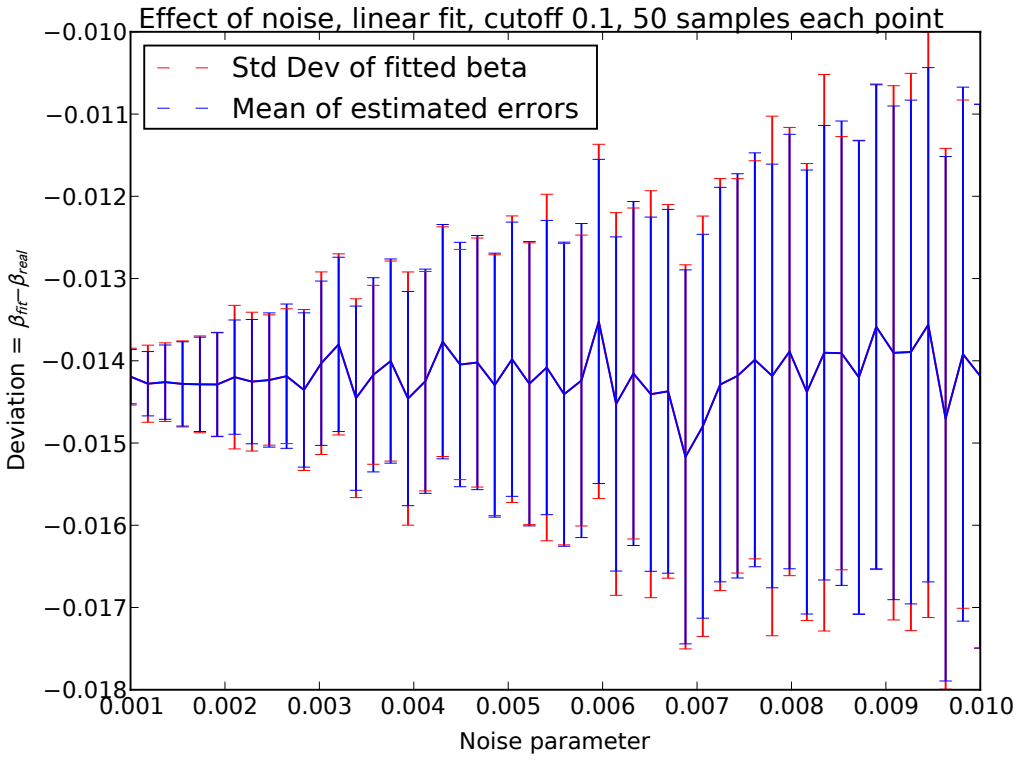

Figure 4.17 *Effect of varying noise on fit estimates for linear first order fit. Red error bars are the standard deviation of the fifty fit parameter residuals and blue error bars are the mean of the estimated errors in the fit parameters from the fit.*

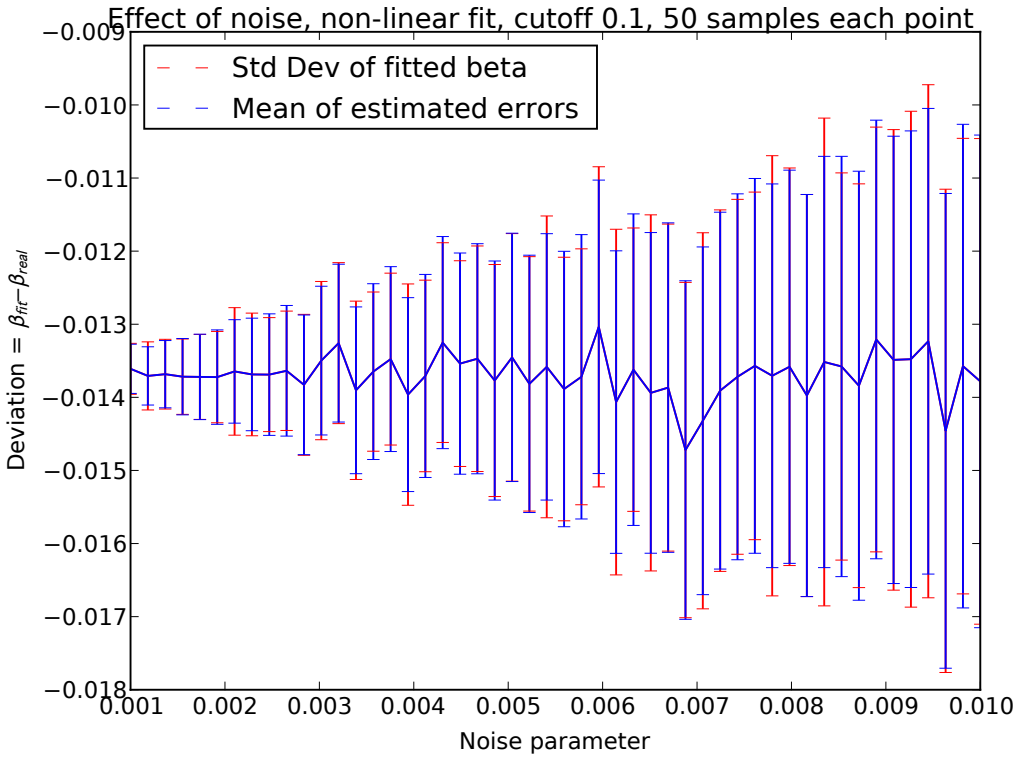

Figure 4.18 *Effect of varying noise on fit estimates for non-linear first order fit. Red error bars are the standard deviation of the fifty fit parameter residuals and blue error bars are the mean of the estimated errors in the fit parameters from the fit.*

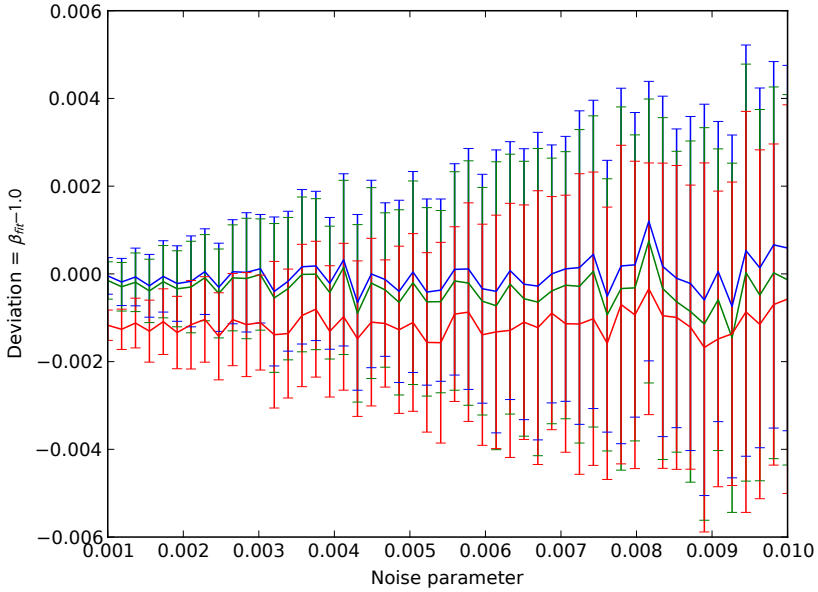

(a) *Variation of fitted β with σ*

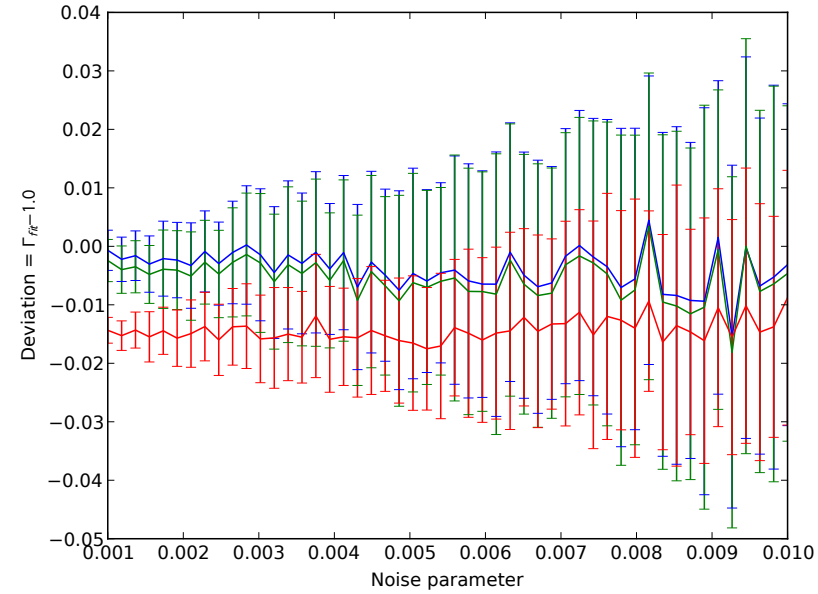

(b) *Variation of fitted Γ with σ*

Figure 4.19 *Systematic deviations of fitted parameters with noise parameter for **third order fits**. Linear and non-linear fits with $g^{(2)}_{cut} = 1.0 + 0.1\beta$ are blue and green respectively, non-linear fits without a cutoff are red. Error bars are the standard deviation of the fit parameter deviations for 50 independently generated $g^{(2)}(\boldsymbol{q}, \tau)$ curves.*

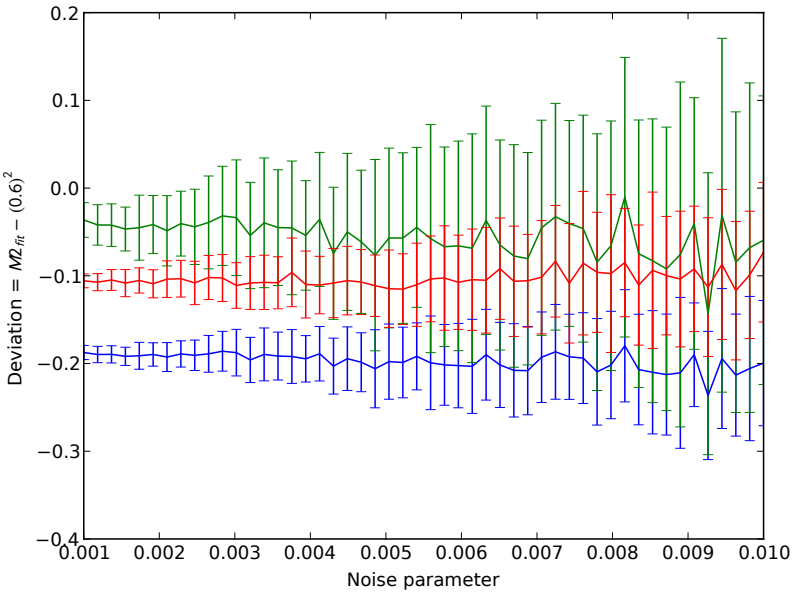

(c) *Variation of fitted M_2 with σ*

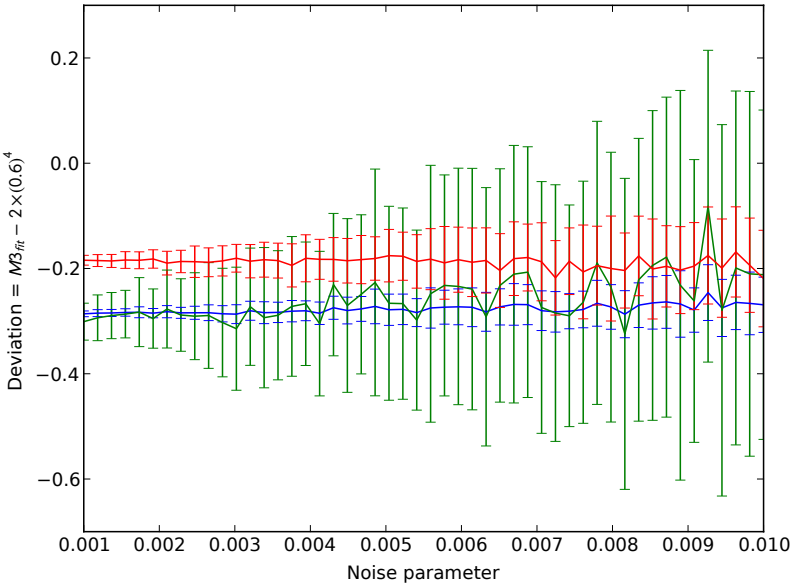

(d) *Variation of fitted M_3 with σ*

Figure 4.19 (continued) *Systematic deviations of fitted parameters with noise parameter for **third order fits**. Linear and non-linear fits with a $g^{(2)}_{cut} = 1.0 + 0.1\beta$ are blue and green respectively, non-linear fits without a cutoff are red. Error bars are the standard deviation of the fit parameter deviations for 50 independently generated $g^{(2)}(\boldsymbol{q}, \tau)$ curves.*

4.4 Discussion

This work is the first to systematically apply a non-linear fitting procedure via the method of moments to polydisperse $g^{(2)}(\boldsymbol{q},\tau)$ data where the precise values of the moments of the underlying distribution are known. It is therefore useful to derive conclusions from this data over the range of values in which the non-linear method is stable and gives accurate estimates of the distribution of decay rates within the polydisperse $g^{(2)}(\boldsymbol{q},\tau)$.

The stability plots in figures 4.4, 4.5 and 4.6 indicate that the non-linear fitting routine utilised is robust to inaccurate initial estimates of parameter values. In general, the highest convergence rates are seen for initial estimates of zero polydispersity and no trend in systematic error is seen for fits where the initial parameter estimates are zero. As a rule of thumb therefore, it is recommended in the first instance to perform the non-linear fits with initial estimates of $M_n = 0$. To reduce the number of iterations required for convergence, a linear fit can be used to obtain parameter estimates which are correct within an order of magnitude (see figure 4.13), which can then be further improved by non-linear fitting. Also important to note in these figures is that all fits converged to the same minimum, indicating the absence of problematic local χ^2 minima.

From the systematic deviation of parameter estimates with simulated σ (figures 4.7 and 4.8) it can be seen that the non-linear fits always yield an improvement in the estimate of M_2 for all but the very lowest values of polydispersity, especially for third order fits. The upper limit for extracting results free of systematic error in all parameters is about $\sigma < 0.4$ for non-linear fits. Estimates of β and $\bar{\Gamma}$ can be reliably obtained even for high polydispersity for all of the fits undertaken here.

In general, reducing the simulated coherence reduces the normalised systematic deviation of the parameter estimates (figures 4.9 and 4.10) if $g^{(2)}_{cut}$ is scaled appropriately so that the total number of datapoints fitted does not change. This is due to an increase in the size of the uncertainty of the parameter estimates (as the ratio of the difference of the $g^{(2)}(\boldsymbol{q},\tau)$ signal to its baseline and the noise in the data approaches one) rather than a reduction in the systematic deviation. It is perhaps to be expected that coherence does not play a major role in influencing the quality of the fit, as it only appears as a linear term in the fitted equation.

The plots demonstrating the change in systematic parameter error with increasing

order of fit (figures 4.11, 4.12 and 4.13) are consistent with the earlier plots of the effect of σ on parameter estimates (figures 4.7 and 4.8) in that the linear fit outperforms the non-linear fit without a cutoff for estimating β and $\bar{\Gamma}$. The order-of-fit plots add to these plots by demonstrating the fit behaviour at lower orders. The non-linear fit appears to perform better than the linear fit at order two than it does at order three, and worse than the linear fit for order one. The improvement in quality of the non-linear fit with no cutoff for order two over the linear fit may be explained by the ability of the non-linear fit to include higher orders of t when fitting M_2. The linear fit estimates parameters from the power law expansion of $\ln \sqrt{g^{(1)}(\boldsymbol{q},\tau) - 1.0}$:

$$\ln \sqrt{g^{(1)}(\boldsymbol{q},\tau) - 1.0} = 0.5 \ln \beta - \bar{\Gamma} t + 0.5 M_2 t^2 + \cdots \tag{4.28}$$

The non-linear fit operates on a series of powers of $\beta \exp(-2\bar{\Gamma}t) t^n$:

$$g^{(2)}(\boldsymbol{q},\tau) = 1.0 + \beta \left[\exp(\bar{\Gamma} t) \left\{ 1 + 0.5\, M_2 t^2 \right\} \right]^2 \tag{4.29}$$

$$= 1.0 + \beta \exp(-2\bar{\Gamma} t) \left\{ 1 + M_2 t^2 + (M_2)^2\, t^4 \right\} \tag{4.30}$$

Each power of $\beta \exp(-2\bar{\Gamma}t) t^n$ affects the shape of the function for higher values of t, as can be seen in figure 4.20. For a second order fit, the non-linear expression includes a t^4 correction which the linear expression does not. For higher order fits, odd powers of t enter into the expansion with coefficients which mix different moments of the distribution, e.g. the coefficient of t^5 for a third order fit is $M_2 M_3/3$. This is likely to be deleterious to the fitting procedure as it will introduce correlations between fitted parameters. Without an adequate parameterisation for higher order fits, it is therefore unlikely that major improvements wil be obtained through non-linear fitting.

Figure 4.20 is also useful for interpreting the maximum lag time data in section 4.3.4. The onset of deviations from the true simulated value occurs at around $t = 5 \times 10^{-1}$. This is where the t^3 correction, which is not present in the order two fits performed, begins to attain a significant value. The linear fit begins to deviate at the same time, as would be expected (since a t^3 correction is also missing from the linear fit expression). The linear fit would continue to deviate were it not for the $g^{(2)}(\boldsymbol{q},\tau)$ cutoff which freezes out the effect of higher order corrections. At $t = 1$, the non-linear fit begins to recover as the t^4 correction becomes important and stabilises as it is attenuated by the exponential envelope, locking in the residual systematic error due to the missing higher order moments

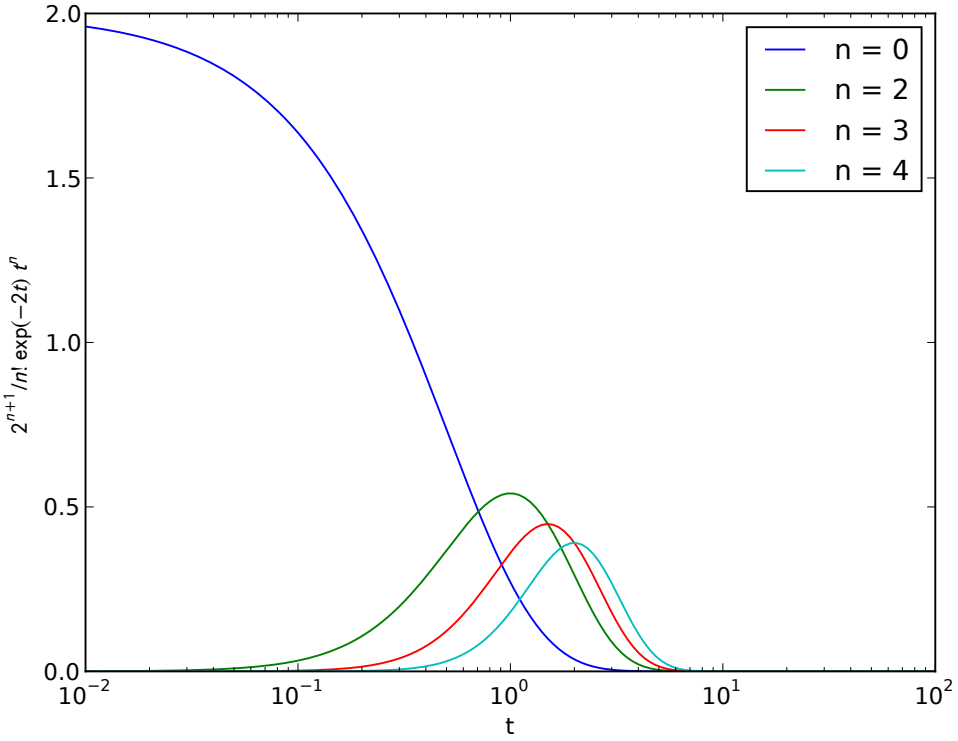

Figure 4.20 *A plot of the function* $\exp(-2t)t^n$ *for varying values of* n.

in the series.

The introduction of higher noise in the analysed $g^{(2)}(\boldsymbol{q}, \tau)$ signal does not appear to have any deleterious effect on any of the fit strategies studied here beyond the expected increase in the random variation of fit estimates. This data also confirms that estimates of fit errors about the χ^2 minimum are similar to the standard deviation of fit estimates about their mean, implying that the χ^2 hypersurface is appropriately hyperbolic about the minimum. This means that error estimates obtained from single fits can be used as an appropriate indicator of the precision of the estimated parameter, even though systematic errors need to be taken into account after this.

4.5 Conclusions

In general, it is apparent that shifting from linear to non-linear fitting via the method of moments is an incremental improvement in fitting to dynamic DLS data. The primary advantage is that the limit in polydispersity of fits free of

systematic bias is shifted higher, from $\sigma < 0.2$ to $\sigma < 0.4$. The non-linear fitting algorithm is robust and converges to the correct values for fit parameters. Past the $\sigma = 0.4$ threshold, the non-linear fit begins to systematically diverge from the true simulated values of the distribution parameters due to the increasing importance of higher order corrections to $g^{(2)}(\boldsymbol{q}, \tau)$.

In order to provide a quick reference to the conlcusions of this chapter, the main points are reiterated in boxes 1, 2 and 3 below.

Scattering Vector, q: The scattering vector encodes the scattering geometry used i.e. definition of scattering angle θ (in this case angular deviation from incident light in the plane formed normal to z) and the wavelength of light in scattering medium λ/n (in an aqueous suspension, n is the refractive index of water).

$$q = \frac{4\pi n}{\lambda} \sin \frac{\theta}{2}$$

Field Correlation Function, $g^{(1)}(\boldsymbol{q}, \tau)$: The field correlation function $g^{(1)}(\boldsymbol{q}, \tau)$ describes the temporal correlation in the scattered electric field E_S over a correlation time τ.

$$g^{(1)}(\boldsymbol{q}, \tau) = \frac{\langle E_S(\boldsymbol{q}, 0) E_S^*(\boldsymbol{q}, \tau) \rangle}{\langle I(\boldsymbol{q}) \rangle}$$

where the angle brackets denote an average over time.

Intensity Correlation Function, $g^{(2)}(\boldsymbol{q}, \tau)$: The intensity correlation function is what can be measured experimentally, as photodetectors measure intensities, not electric fields.

$$g^{(2)}(\boldsymbol{q}, \tau) = \frac{\langle I(\boldsymbol{q}, 0) I(\boldsymbol{q}, \tau) \rangle}{\langle I(\boldsymbol{q}) \rangle^2}$$

Siegert Relation: The Siegert relation is an approximation which allows the field correlation function $g^{(1)}(\boldsymbol{q}, \tau)$ to be estimated from the intensity correlation function, $g^{(2)}(\boldsymbol{q}, \tau)$. It introduces the empirical coherence factor, β.

$$g^{(2)}(\boldsymbol{q}, \tau) = 1 + \beta \left[g^{(1)}(\boldsymbol{q}, \tau) \right]^2$$

Monodisperse Spheres: With the assumptions that the scatterers are identical spheres diffusing via Brownian motion, the field correlation function can be analytically calculated.

$$g^{(1)}(\boldsymbol{q}, \tau) = \exp\left(-D_0 q^2 \tau\right)$$

where the diffusion coefficient $D_0 = k_B T / 6\pi\eta R_H$. Using the Siegert relation, experimental measurements of $g^{(2)}(\boldsymbol{q}, \tau)$ vs τ can be used together with measurements of suspension temperature T and solvent viscosity η to estimate the hydrodynamic radius R_H.

Box 1 *Important terms and conventions used to describe the theoretical aspects of measuring hydrodynamic radii via dynamic light scattering.*

Polydisperse $g^{(1)}(\boldsymbol{q},\tau)$: In order to relax the assumption that all scatterers are identical, it is necessary to model the field correlation function $g^{(1)}(\boldsymbol{q},\tau)$ as a sum of individual decorrelation rates Γ multiplied by the distribution of these distribution rates $G(\Gamma)$.

$$g^{(1)}(\boldsymbol{q},\tau) = \int G(\Gamma)\exp(-\Gamma\tau)d\Gamma$$

In the case of spherical Brownian scatterers, the decorrelation rate can be matched to a diffusion coefficient as in the monodisperse case: $\Gamma = D_0 q^2$.

Method of Moments: The above can be expanded to a form which is easily fitted via the method of moments:

$$\begin{aligned} g^{(1)}(\boldsymbol{q},\tau) &= \exp\left(-\bar{\Gamma}\tau\right)\int G(\Gamma)\exp\left(-(\Gamma-\bar{\Gamma})\tau\right)d\Gamma \\ &= \exp\left(-\bar{\Gamma}\tau\right)\left[1+\frac{1}{2!}\mu_2(\bar{\Gamma}\tau)^2-\frac{1}{3!}\mu_3(\bar{\Gamma}\tau)^3+\cdots\right] \end{aligned}$$

where μ_n are formally known as the normalised moments about the mean of the distribution $G(\Gamma)$:

$$\mu_n = \frac{1}{\bar{\Gamma}^n}\int G(\Gamma)(\Gamma-\bar{\Gamma})^n d\Gamma$$

Note that the second moment about the mean is equal to the variance of the distribution over its mean.

Schultz Distribution: The Schultz distribution is a convenient choice for $G(\Gamma)$ as analytical results for $g^{(1)}(\boldsymbol{q},\tau)$ and μ_n are easily obtained. The parameter z is related to the mean $\bar{\Gamma}$ and variance σ^2 of the distribution via $z = \bar{\Gamma}^2/\sigma^2 - 1$.

$$G(\Gamma) = \frac{1}{\bar{\Gamma}}\frac{(z+1)^{z+1}}{z!}\left(\frac{\Gamma}{\bar{\Gamma}}\right)^z \exp\left[-\frac{\Gamma}{\bar{\Gamma}}(z+1)\right]$$

$$\langle\Gamma^n\rangle = \frac{1}{\bar{\Gamma}^n}\sigma^{2n}\prod_{i=0}^{n-1}\left(\frac{\bar{\Gamma}^2}{\sigma^2}+i\right)$$

Box 2 *Theory of fitting and simulating polydisperse dynamic light scattering data.*

- A linear fit can be performed to extract the variance of the distribution $G(\Gamma)$ by fitting $\ln\left[\sqrt{g^{(2)}(\boldsymbol{q},\tau)-1.0}\right]$ vs τ data to a second or third order polynomial in τ. The fitted coefficients will be the un-normalised moments of the distribution $G(\Gamma)$ and will need to be multiplied by the appropriate power of $\bar{\Gamma}$.

$$\begin{aligned}\ln\left[\sqrt{g^{(2)}(\boldsymbol{q},\tau)-1.0}\right] &= \frac{1}{2}\ln(\beta) - \bar{\Gamma}\tau + \frac{\mu_2\bar{\Gamma}^2}{2!}\tau^2 - \frac{\mu_3\bar{\Gamma}^3}{3!}\tau^3 + \cdots \\ &= A - B\tau + C\tau^2 - D\tau^3 + \cdots\end{aligned}$$

- A non-linear fit can be performed to $g^{(2)}(\boldsymbol{q},\tau)$ vs τ data without transformation. Non-linear fitting also allows the inclusion of a variable baseline B in the fit.

$$g^{(2)}(\boldsymbol{q},\tau) = B + \beta\left\{\exp\left(\bar{\Gamma}\tau\right)\left[1 + \frac{1}{2!}M_2\tau^2 - \frac{1}{3!}M_3\tau^3 + \cdots\right]\right\}^2$$

  Non-linear fitting achieves improvements in the accuracy of the fitted second moment over linear fitting, except for extremely low polydispersity.

- When performing linear fits, often a cutoff in τ is used such that no $g^{(2)}(\boldsymbol{q},\tau)$ data is fitted after $g^{(2)}(\boldsymbol{q},\tau)$ drops below 10% of its starting value. This prevents systematic deviations from high τ data. It is recommended to apply a 10% cutoff when performing non-linear fits as well, as high τ data can cause systematic deviations due to missing contributions from higher order terms in τ.

- Non-linear fits require initial estimates of fit parameters. These initial values can either be set to zero or estimated by performing an initial linear fit and using the resulting values.

- The upper limit on the underlying standard deviation of $G(\Gamma)$ to avoid systematic errors in the fitted parameters is $\sigma < 0.4$. Above this limit systematic errors dominate in estimates of fit parameters. Low coherence does not significantly affect the quality of fit for linear or non-linear fits.

- It is important to have good data on the uncertainties of $g^{(2)}(\boldsymbol{q},\tau)$, as high fitted polydispersities can indicate that a higher order polynomial in τ needs to be fitted.

Box 3 *Fitting polydisperse $g^{(2)}(\boldsymbol{q},\tau)$ data via the method of moments using linear and non-linear techniques.*

- Care needs to be taken when interpreting distribution moments. A broad but monomodal distribution can exhibit a similar variance to a distribution containing two sharply peaked monodisperse components. Examining $g^{(2)}(\boldsymbol{q},\tau)$ vs $\ln(\tau)$ can accentuate multimodal distributions, due to the appearance of multiple plateaux.
- Second order fits are usually sufficient to extract the maximum information available from a dataset. Third and higher order fits can increase the estimated uncertainty in fit parameters and introduce systematic errors due to the introduction of correlations between fitted parameters.

Box 3 (Continued) *Fitting polydisperse $g^{(2)}(\boldsymbol{q},\tau)$ data via the method of moments using linear and non-linear techniques.*

Chapter 5

Design and Fabrication of TiO_2:P3HT Solar Cells

5.1 Introduction

5.1.1 Conventions and Terminology in Solar Cell Research

This section is intended to present a basic overview of the concepts and terminology of solar cell technology for those who are not already familiar with it. Although concentrating primarily on traditional silicon and inorganic thin film cells, 'The Physics of Solar Cells' by Jenny Nelson [76] provides a good introduction to many of the concepts involved in solar cell research. The important points for any discussion of solar cell technology are summarised here.

The performance of a solar cell is defined by three properties; short circuit current density J_{sc}, open circuit voltage V_{oc} and fill factor FF. J_{sc} and V_{oc} are self-explanatory. J_{sc} is primarily influenced by the kinetics of electrons within the cell, while V_{oc} is primarily determined by the energetics[1] of the cell. The fill factor of a cell is the ratio of the maximum power output of the cell to the power available if the cell were able to sustain a short current at its open circuit voltage:

$$\mathrm{FF} = \frac{J_{max}V_{max}}{J_{sc}V_{oc}}. \tag{5.1}$$

[1] A more precise definition would be the variation of chemical potential, or Fermi level, across a cell.

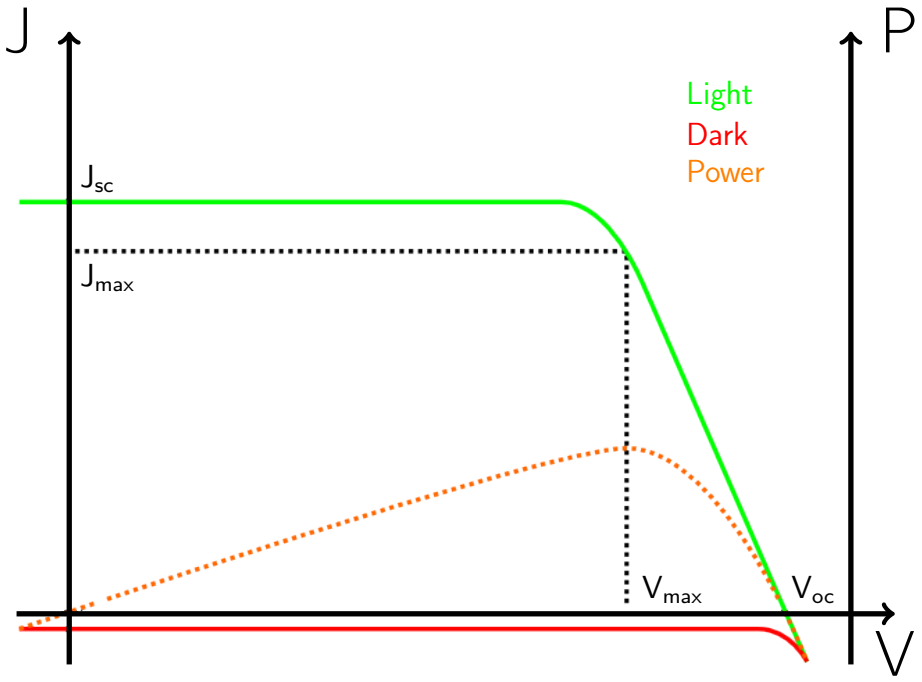

Figure 5.1 *Cartoon of an ideal IV curve, highlighting important characterisation parameters for solar cells. The green and red curves are the current density J for a given cell bias V in the light and dark respectively. The orange dashed curve is the electrical power per unit area ($P = J_{light}V$) yielded by the cell in the light, illustrating the maximum power point (J_{max}, V_{max}).*

The maximum conversion efficiency of a cell is equal to the ratio of maximum electric power output to incident solar radiometric power and can therefore be expressed in terms of the above quantities:

$$\eta = \frac{J_{sc} V_{oc}\,\mathrm{FF}}{P_{solar}}. \tag{5.2}$$

A cartoon of a JV curve with these features illustrated is presented in figure 5.1.

The incident solar power density P_{solar} is in reality a function of many variables, such as elevation angle of the sun (dependent on latitude and season), atmospheric composition and local weather conditions. To enable useful comparison of results, a standard spectrum known as Air Mass 1.5 [6] has been developed. This represents the solar irradiation reaching the Earths surface after attenuation by the atmosphere when the Sun is at an angle of elevation of 42°. At this angle, the optical path length of the Sun's light is one and a half times that of the path length if the Sun were directly overhead.

A standard area power density of $1000\,\mathrm{W\,m^{-2}}$ (also known as 1 Sun) also forms

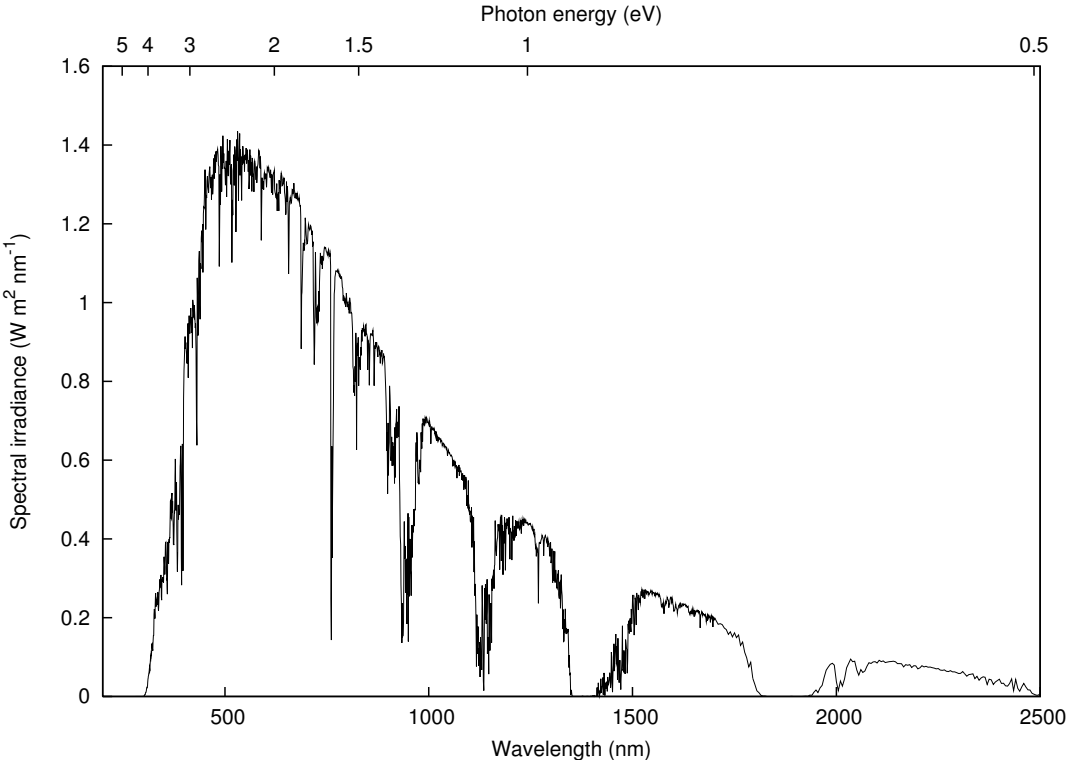

Figure 5.2 *The AM1.5 solar reference spectrum [6]. Note that much of the radiation is in the infrared.*

part of the standard. It should be noted that this figure is chosen for convenience; real solar irradiances vary from 100–300 $\mathrm{W\,m^{-2}}$ according to seasonal and daily shifts in Sun position and average cloud cover. The spectrum is presented in Figure 5.2. All efficiencies should be reported with respect to this reference standard, but in reality due to the costs of obtaining appropriate filters and light sources authors often report efficiencies under monochromatic illumination at a stated (non-standard) irradiance.

Experimentally, the performance of a solar cell is measured by recording the current output from the device under a range of applied bias. An example current vs voltage (IV) curve is presented in Figure 5.3. The response of a perfect photovoltaic system can be modelled as the combination of a current source and a diode. The diode maintains a potential difference between the output terminals for a given load while the current source provides current.

Often there will be power losses within the cell, for instance due to resistive losses through the cell body and short circuits due to manufacturing flaws. These can be modelled using the parasitic series and shunt resistances R_s and R_{sh}. A circuit

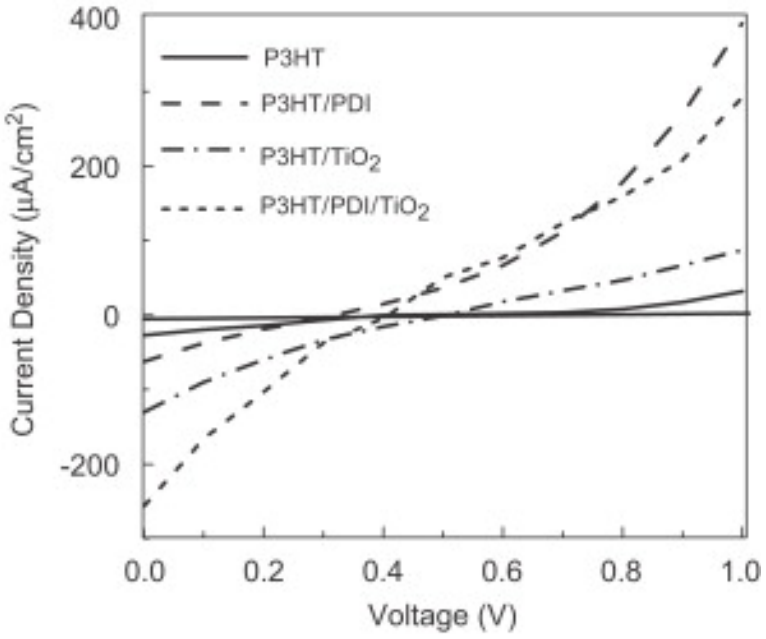

Figure 5.3 *An example of a current-voltage curve for a TiO_2/P3HT solar cell, from [107]. In this paper, photo-induced current was defined to be negative, which is opposite to the convention used in this thesis. The four curves illustrate the photovoltaic effect of TiO_2 P3HT, PDI (a dye) and blends of the three components.*

diagram of this model is presented in Figure 5.4. High series resistance and/or low shunt resistance cause power losses within the cell and therefore reduce the maximum power output and hence the fill factor of the cell. Recombination of electrons and holes within the device can also result in low observed photocurrents and this has been identified as a major issue limiting the efficiency of research cells [76].

The above conventions are used in all solar cell research, both for conventional silicon cells and the new designs described in this report. Modern silicon and thin-film semiconductor cells are now able to approach the theoretical efficiency limits (ca. 25%) established from thermodynamic principles. In order to achieve a reduction in cost per Watt, a shift to new, cheaper materials with less stringent processing requirements is being investigated by the solar cell research community. Fundamentally this reflects a change from transporting charge carriers within cells under majority conditions, which requires stringently pure materials, to transporting carriers under minority conditions. Some of these new designs investigate the advantages offered by solution processable materials and hence researched performed by the complex fluids community is now becoming

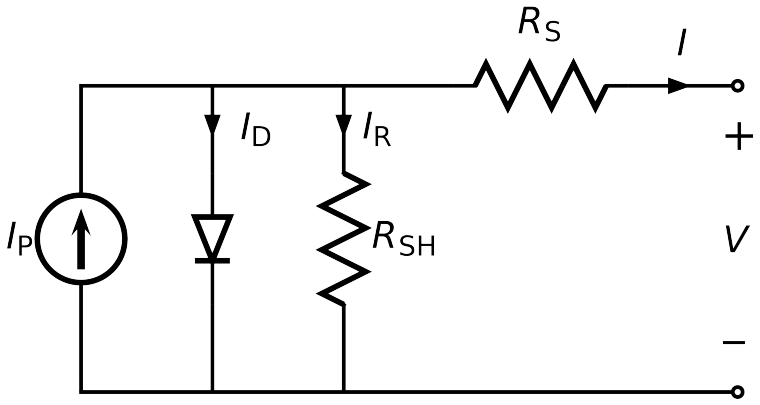

Figure 5.4 *An equivalent circuit diagram for modelling I-V characteristics of a solar cell.*

applicable to this technology area.

5.1.2 Soft Matter Photovoltaic Systems

Advances in the synthesis of conducting and semi-conducting polymers and colloidal inorganic semiconductors (quantum dots) have enabled the solution-based fabrication of electrooptical devices, such as LEDs and photovoltaic cells. Two approaches have special relevance to soft matter physicists due to their solution-based fabrication procedure and the importance of solution structure to their efficiency: solid-state dye sensitised solar cells and bulk heterojunction solar cells.

Solid-State Dye Sensitised Solar Cells (SDSC)

Dye sensitised solar cells operate via a principle that was originally discovered by Tang [102] and harnessed into a viable solar cell design by Grätzel and O'Regan [78]. A colloidal suspension of nanometer sized inorganic semiconductor (titanium dioxide in the original study) is dried out into a thin porous film on a conductive substrate which is then fired to improve its adhesion and particle connectivity. This mesoporous layer is then treated with a monolayer of a light-absorbing material, usually a chemical dye. The cell is completed by introducing a liquid electrolyte into the porous film. During operation, the light absorbing material

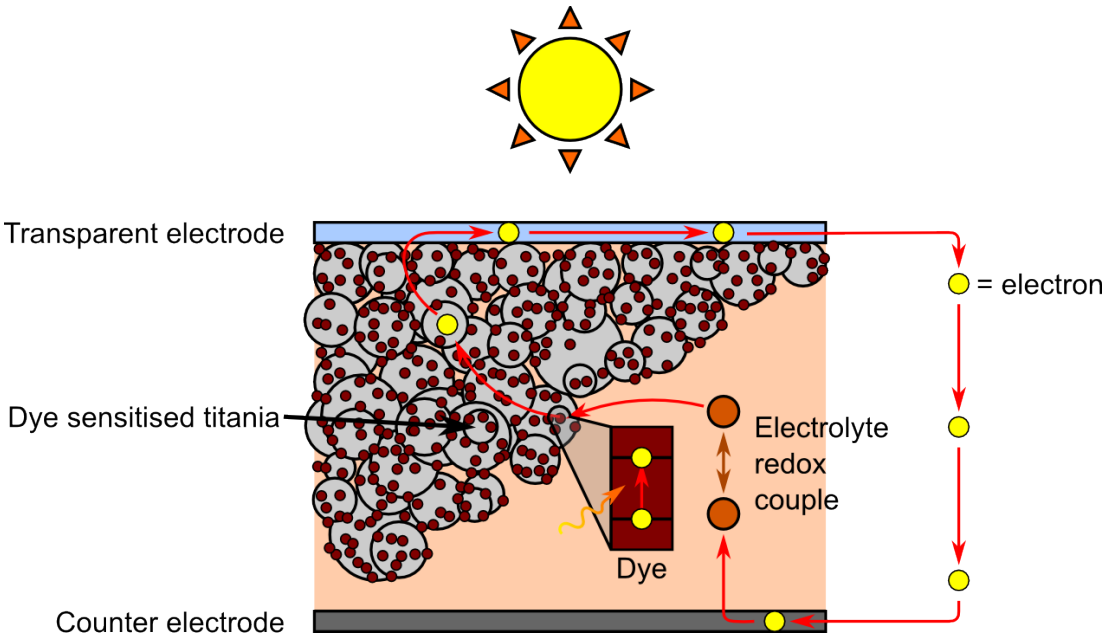

Figure 5.5 *Cartoon of the operation of the DSSC, indicating the path of electrons through the device. Adapted from* `http://www.energyer.com/Know_How/dye-sensitized-solar-cell.html` *(Sep 2012).*

absorbs a photon to produce an excited electron. The electron is injected into the porous layer and diffuses to the conductive boundary, where work can be performed with it. The dye is regenerated by the liquid electrolyte, which in turn is regenerated at the opposite conductive boundary, completing an electrical circuit. A cartoon of this process is presented in figure 5.5.

Use of a liquid electrolyte is necessary to ensure good electrical contact at the microscopic heterojunction after backfilling the tortuous porous network. The high surface area of the porous network is required to ensure a high amount of dye is present per unit area, as the dye layer is usually electrically insulating and designed so electrons can be efficiently injected into a physically adjacent material. However, liquid electrolytes have engineering drawbacks due to evaporation and leakage. There is a strong interest in replacing the liquid electrolyte with a solid hole transport layer which can be introduced into the porous film by solution processing, e.g. a solution of conductive polymer. Aside from the synthetic challenges in producing such materials, the ability to introduce the bulky polymer molecules into the porous layer relies on adequate structuring. As has been demonstrated in earlier chapters, the structure of the suspension used to cast the porous layer affects the resulting dried structure. More generally, the structure of the deposited porous layer determines the length of the route charge-carriers must diffuse in order to reach external electrodes and thus the likelihood that

recombination will occur.

Snaith et al have recently shown that adequate infiltration of the hole transporting component into the porous network is important for solid-state cell efficiencies [2, 96, 98]. It is expected that structuring the mesoporous layer will have implications for cell efficiency [26]. One aim of this study is therefore to try and find a structure-property relationship between the porous layer structure and efficiency in solid-state cells.

Bulk Heterojunction Solar Cells (BHJ)

It is also possible to form cells from blends of nanoparticles and polymers, or from a blend of two conducting polymers. In this case, one or both of the layers act as an optical absorber. Upon absorption, excitons diffuse to the interface between phases where the gradient in local chemical potential is sufficient to dissociate the exciton into its respective charges. This is an important difference to the mechanism in SDSCs where the exciton is physically separated by electron injection into the electron transport layer. Excitons have a limited lifetime before the bound hole and electron recombine. Therefore only excitons within one exciton diffusion length (defined as the distance an exciton can diffuse in its lifetime) of an interface will be able to dissociate; the exciton diffusion length is therefore the optimal domain size in a BHJ cell.

In this type of cell, the morphology of the interface has a large impact on device efficiency. Only excitons that manage to diffuse to an interface before radiative recombination can contribute to I_{sc}. Due to the low electron and hole mobilities of typical constituents of these cells, these diffusion lengths are on the order of a few nanometers and charge carriers are susceptible to recombination before reaching an electrode. Therefore, a highly rough interface is required to maximise the useful absorption of the cell and donor and acceptor phases need to be well connected and continuous. Isolated pockets of either phase will be unable to transport charge carriers, restricting I_{sc}.

The most widely studied BHJ cells are dispersions of polymeric regioregular poly(3-hexylthiophene) (P3HT) and the fullerene derivative [6,6]-phenyl-C_{61}-butyric acid methyl ester (PCBM) in a common solvent and their structures are presented in Figure 5.6. P3HT acts as the donor and PCBM as the acceptor. P3HT is an effective donor as it has a small bandgap (and thus can absorb

more long wavelength photons) and a relatively high electron mobility (10^{-4} – $10^{-1}\,\mathrm{cm^2\,V^{-1}\,s^{-1}}$). In addition, the morphology of the P3HT:PCBM blend seems to be sensitive to solvent and processing conditions, allowing optimisation. The current success of PCBM as acceptor is not well understood, but may be due to the high electron affinity and mobilities [8].

(a) *P3HT* **(b)** *PCBM*

Figure 5.6 *The structures of P3HT and PCBM, from [90]*

As with polymers for SDSCs, there is currently great interest in synthesising new materials with greater mobilities and more favourably spaced energy levels to improve cell performance. FF and V_{oc} are both mostly determined by the energetics of these materials. This project is more concerned with how the arrangement of the interface and the nature of the blending and solvent evaporation processes affect cell performance. The microscopic morphology of the blend film has important implications for exciton dissociation and charge-carrier transport [24]. By combining knowledge from previous chapters of the supracolloidal structure of aggregates in titania suspensions with fabricated test cells, it is hoped some connection between film structure and cell performance can be obtained.

5.2 Methods and Materials

This section reports the various construction techniques used to fabricate test cells and the characterisation methods applied to determine their performance properties. Cells are usually fabricated in a sequential layer structure, with each layer being deposited on the one below. A schematic of the different layers which will be discussed is presented in figure 5.7. The energy levels (work functions for the alumininum electrodes, conduction bands for the anatase nanoparticles, highest occupied molecular orbital (HOMO) level for P3HT) for the two cell designs discussed below are presented in figure 5.8. Each subsection will detail the methods used to deposit the layers.

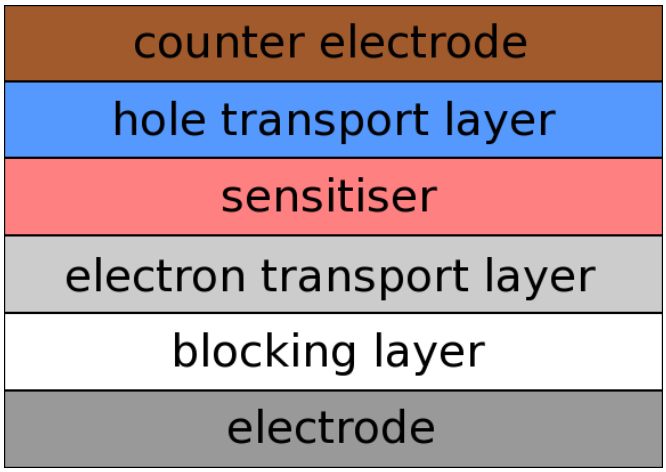

Figure 5.7 *Schematic of the layer structure of the photoelectrochemical test cells constructed.*

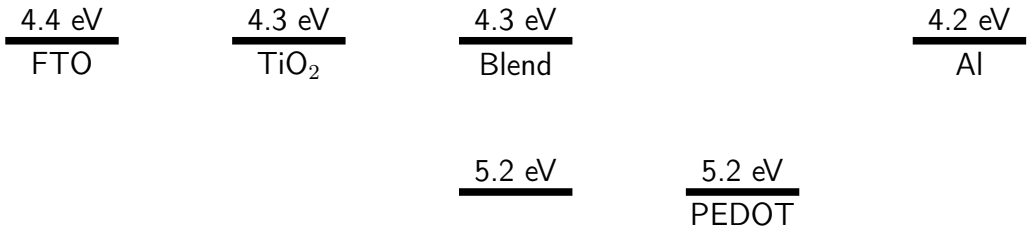

(a) *BHJ-type cell energy level diagram*

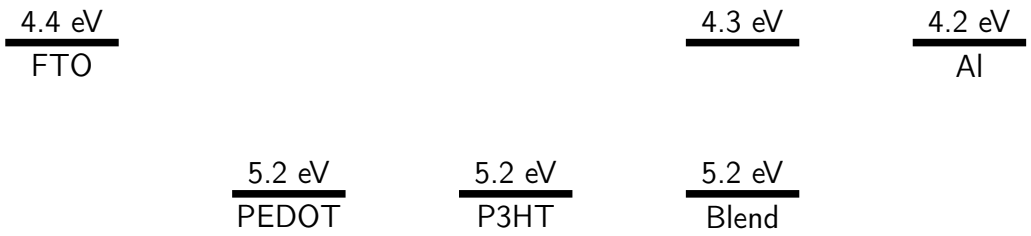

(b) *SDSC-type cell energy level diagram*

Figure 5.8 *Energy level schematic of BHJ and SDSC design patterns*

5.2.1 Electrode

The electrode chosen was fluorine doped tin oxide (FTO) deposited on 1 mm thick plate glass by vapour deposition (TCO10-10, Solaronix SA, Switzerland). FTO is transparent across most of the solar spectrum, chemically stable, offers a high conductivity to transparency ratio and is easily etched [7, 18]. The work function of FTO is 4.4 eV [7]. A large sheet was cut into 4 cm × 3 cm pieces using a glass saw. These pieces were washed successively for 10 minutes under ultrasonic bath agitation in a 10% Decon solution, distilled water, ethanol, twice with isopropanol and finally twice with ethanol.

The FTO was then etched for 1 minute using a bath of 1 mol dm^{-3} HCl to which zinc pellets (ca. 1 mm in diameter) were added as per Bradshaw and Hughes [18]. Electrical insulating tape was used to mask off the central area, leaving 0.5 cm of either both long edges or both short edges unmasked, depending on whether eight 6 mm diameter or four 10 mm cells were required. The substrates were then washed with tap water to remove excess acid and wiped gently to remove excess etched FTO. The masking tape was then removed and the substrates washed again with 10% Decon solution, distilled water, ethanol, isopropanol and finally ethanol before being stored immersed in ethanol to reduce dust contamination. In some cases, substrates were scored on the reverse glass side with a diamond pen before storage to allow one large substrate supporting several test cells to be divided to allow each cell to be tested separately.

5.2.2 TiO_2 Blocking Layer

The addition of a thin, dense layer of titania between the porous titania layer and the FTO electrode has been shown to improve device performance [58, 79], presumably by avoiding parasitic losses through a low device series resistance. Two methods for depositing this dense layer were investigated: a crude form of chemical vapour deposition via the methods described by Fitzgibbons et al [37] and Hardee and Bard [66] and spray pyrolysis of a titanium dioxide precursor as per Kavan and Grätzel [60].

A diagram of the equipment used for chemical vapour deposition is presented in figure 5.9. Briefly, dry nitrogen is used as a carrier gas to combine water and tetraisopropyl titanate (TIP, Purum, Sigma Aldrich) vapour above the substrate,

which was heated to 150 °C. The TIP is hydrolysed rapidly by the water vapour at the hot substrate to form titanium dioxide.

The equipment was left to reach a steady state for 20 minutes before deposition. A substrate was then placed under the deposition nozzle for 10 minutes. By observing the advance of red and green circular white-light interference fringes across the substrate an estimate of the film thickness at the centre of the film could be made, using literature values for the refractive index of pure anatase. White light passes through the titania film and is reflected from the air-titania interface and then with a phase change of π at the glass-titania interface. This results in constructive interference when the layer thickness is equal to $(2n + 1)/(4\lambda/n)$ where λ is the wavelength of the light in vacuum and n is the refractive index of titania. In general two green ($\lambda \approx 510\,\mathrm{nm}$) interference fringes could been seen in the deposited films. This implies a film thickness of approximately 150 nm to 200 nm in agreement with Fitzgibbons [37].

The tubing and especially the nozzle were prone to becoming clogged due to material condensing and needed to be cleaned after a few treatment cycles. The presence of rings (rather than one flat colour) indicates a gradient in material thickness around the central region. Given that the nozzle aperture is smaller than the coated substrate, it is expected that a cap-like film is formed on the substrate. In this case the estimated thickness of the film is accurate only for the central region.

A more common approach encountered in the solar cell literature to blocking layer deposition was proposed by Kavan and Grätzel [60] and involves the spray pyrolysis of a titania precursor. A $0.2\,\mathrm{mol\,dm^{-3}}$ solution of di-isopropoxy titanium bis(acetyleacetonate) in isopropanol (Sigma Aldrich) was loaded into a hand atomiser (Fisher Scientific). Substrates were heated to 450 °C on a hot plate and then treated with three squirts of the atomiser every 10 s for 2 minutes. Electrode contacts on the substrates were covered with glass microscope slides during coating. This method produced a coating without visible defects. This method was found to be much more practical than the CVD method and was used to construct all the cells in this study.

In some cases the substrate was 'chemically sintered' with titanium tetrachloride to improve the electrical characteristics of the layer. A $40\,\mathrm{mmol\,dm^{-3}}$ aqueous solution of titanium tetrachloride/tetrahydrofuran complex (Sigma Aldrich) was prepared and heated to 70 °C. The substrate was then immersed in this solution

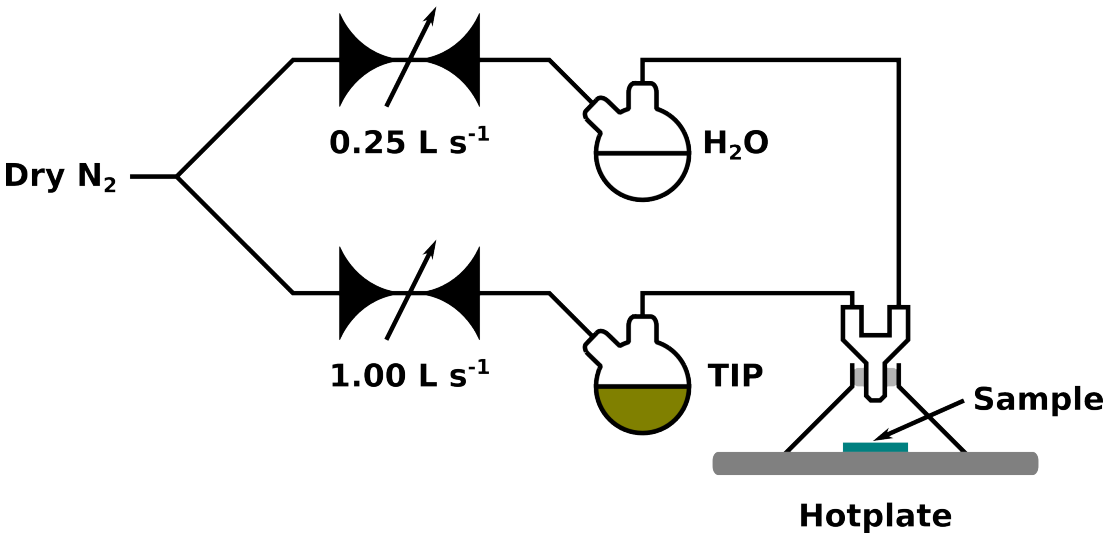

Figure 5.9 *Apparatus used for chemical vapour deposition. Dry nitrogen was split between two lines. After each line had passed through a flow meter, the carrier gas was passed through round bottomed flasks containing distilled water (flow rate* $0.25\,\mathrm{L\,s^{-1}}$*) and tetraisopropyl titanate (TIP, flow rate* $1.00\,\mathrm{L\,s^{-1}}$*) respectively, with the liquid reagents being held at* $75\,^{\circ}\mathrm{C}$ *by immersion of the flask in an oil bath. The two gas lines were then combined in a nozzle above the substrate, which was held at* $150\,^{\circ}\mathrm{C}$ *using a hotplate. A glass funnel was used to exclude drafts from the deposition area.*

for 30 minutes before being washed with distilled water.

5.2.3 Quantum Dot Sensitisation

The bare TiO_2 layer was sensitised by the attachment of lead sulphide quantum dots (fluorescence peak at 850 nm, Evident Technologies) via 3-mercaptopropanoic acid (3MPA) [43, 50]. 3MPA is an aliphatic molecule with a thiol group (which binds to the quantum dot) and a carboxylic acid group (which binds to the titania surface). A $1\,\mathrm{mol\,dm^{-3}}$ solution of 3MPA in acetonitrile was prepared and the substrate immersed in it overnight. The substrate was then removed and washed with pure acetonitrile before being immersed in a toluene solution of the PbS dots overnight. The substrates were then removed and washed with toluene before further processing steps took place.

5.2.4 Hole Transport Layer

A thin layer of regioregular poly-3-hexylthiophene (P3HT, Sigma Aldrich) was spun onto the sensitised layer. Kapton tape (3M) was used to mask off the FTO electrode contact region. P3HT has a high solubility in chloroform, so the spincasting solvent was chosen to be chloroform. P3HT is sensitive to light and oxygen, so mixed solutions were stored in the dark and under a nitrogen atmosphere. A few drops of $10\,\mathrm{mgmL^{-1}}$ of P3HT solution we deposited on the substrate before spinning at 300 RPM for 6 s, 1000 RPM for 2 s and then 2000 RPM for 60 s. The spun film was then annealed on a hotplate in air for 10 minutes at 150 °C to promote an increase in P3HT conductivity via enhanced crystallisation.

To complement the highest occupied molecular orbital (HOMO) of P3HT at $-5.1\,\mathrm{eV}$ [90, 92] an electrode material with good hole transport properties is required. Poly(3,4-ethylenedioxythiophene)-poly(styrenesulfonate) (PEDOT:PSS) is a high-conductivity water-soluble polymer often used as an anti-static coating and is often used as a hole transport material in polymer/nanoparticle cells [91]. PEDOT:PSS (1.4% wt aqueous dispersion, conductive grade, Sigma Aldrich) was applied to the substrate using a syringe fitted with a 0.45 µm Millex HA syringe filter and then spun for 10 s at 500 RPM and 60 s at 6000 RPM. After coating the substrate was then annealed on a hotplate for 10 minutes at 150 °C.

5.2.5 P3HT/TiO_2 Blend Layer

In some cases a blend of titanium dioxide particles and P3HT was used as an active layer instead of a quantum dot sensitisation treatment. The blend was formed from a 40%/60% (after Kwong et al [65] and [16]) mix of P3HT/TiO_2 in chloroform at an overall concentration of $10\,\mathrm{mgmL^{-1}}$ [65]. The titania used in the blend layer had been treated so that its surface was hydrophobic (T805, Evonik). The titania was initially added to the chloroform and then sonicated using an ultrasonic probe (see chapter 2) for 30 s at 20% amplitude. The P3HT was then added and the mixture left in a sealed and light impermeable vial to mix gently through rolling for at least three days. This blend was then applied to the substrate using a glass Pasteur pipette before being spun for 3 s/300 RPM, 5 s/1000 RPM, 60 s/2000 RPM. A small amount of glass wool was added to the neck of the pipette to filter out large aggregates. As above, immediately after

spin-coating the film was annealed on a hotplate for 10 minutes at 150 °C.

5.2.6 Counter Electrode

The back contact electrode was applied using vacuum evaporation deposition apparatus. Aluminium wire was evaporated at low pressure and condensed on the substrate. The deposited metal was patterned by means of an aluminium contact mask to form opaque metal electrodes. The mask designs are presented in figure 5.10. Conductive silver paint (RS Electronics) was then applied to the aluminium and FTO contact regions to ensure a good electrical connection to characterisation equipment.

5.2.7 Characterisation

An example image of completed cells is presented in figure 5.11. Cells were characterised using a potentiostat and an arc lamp fitted with an AM1.5 filter with the assistance of the Robertson group of the School of Chemistry at the University of Edinburgh. Before commencing measurement, the incident light intensity was calibrated to $1000\,\mathrm{W\,m^{-2}}$ using a hand held light meter. The potentiostat working electrode was connected to the electrode of the cell and the potentiostat counter electrode was connected to the counter electrode of the cell. The potentiostat reference electrode was connected to the working electrode. A linear potential sweep from $-1\,\mathrm{V}$ to $1\,\mathrm{V}$ at $0.01\,\mathrm{V\,s^{-1}}$ was performed and the current across the cell electrodes measured. Occasionally smaller voltage ranges were investigated when it was clear the open circuit voltage was small.

An example IV trace is presented in figure 5.12. The short circuit current density J_{sc} and the open circuit voltage V_{oc} can be read off as the x- and y-intercepts of the figure. The fill factor, FF, was in general close to 0.25 for all devices (e.g. IV curves were linear throughout the power generating region. When a more accurate value for the fill factor was required, the maximum power point was estimated from the gathered data and the fill factor estimated from its definition by taking the ratio of $J_{sc}V_{oc}$ and the power at the estimated maximum power point.

The above procedures are crude by the standards of state of the art characterisation procedures [95], for example a measurement of the wavelength-dependent external

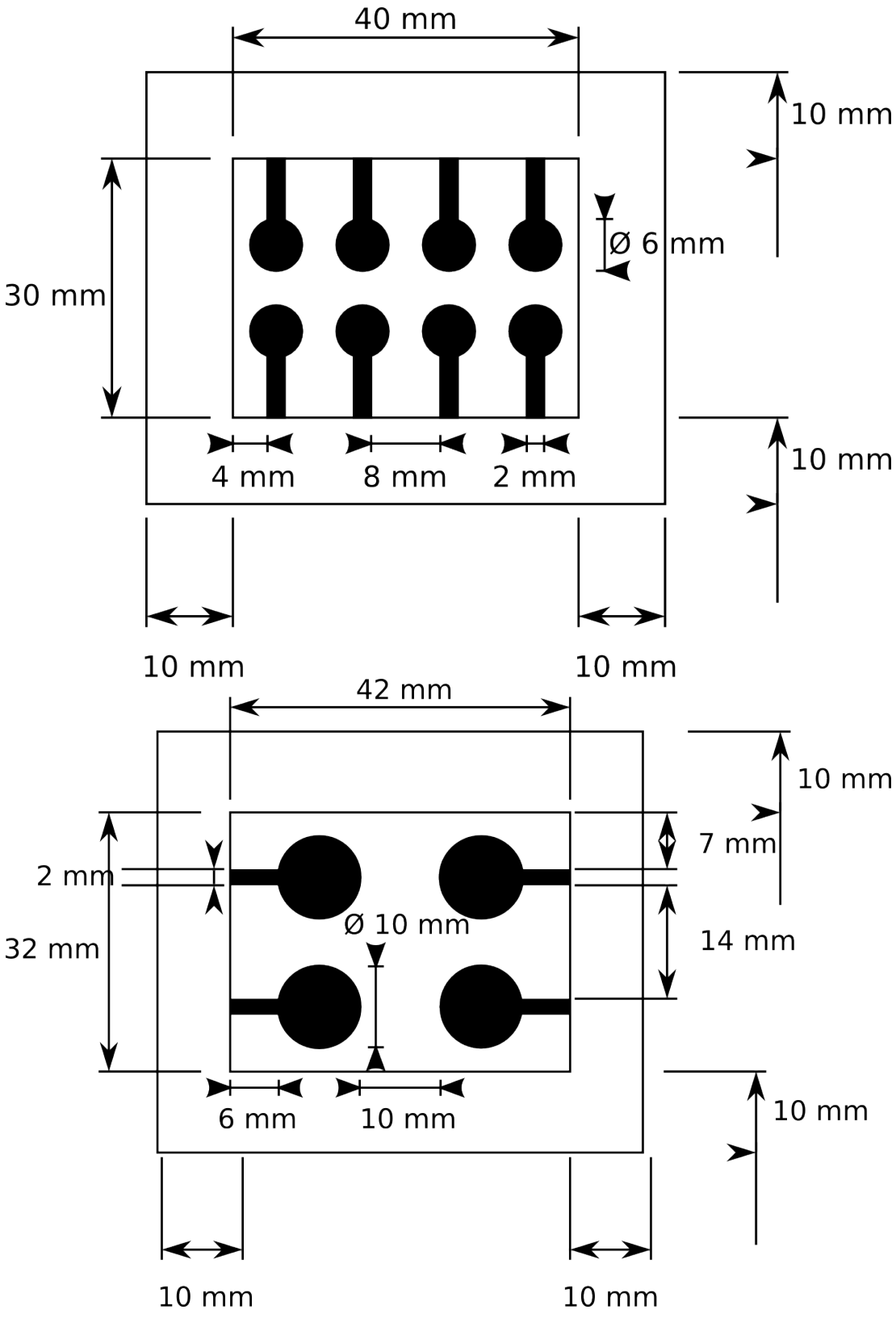

Figure 5.10 *Schematics of contact masks for evaporative deposition of cell counter electrodes. Filled areas represent regions where the metal has been cut away. The central region is inset so the substrate is held securely in the mask while evaporation takes place.*

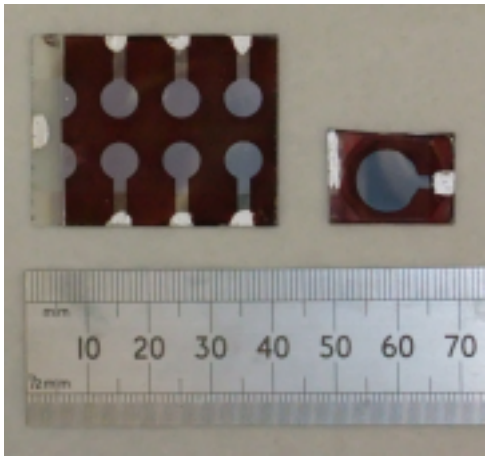

Figure 5.11 *Image of small and large completed cells. Small cells were usually left joined on the same substrate during testing due to the difficulty of separating them without shattering the glass.*

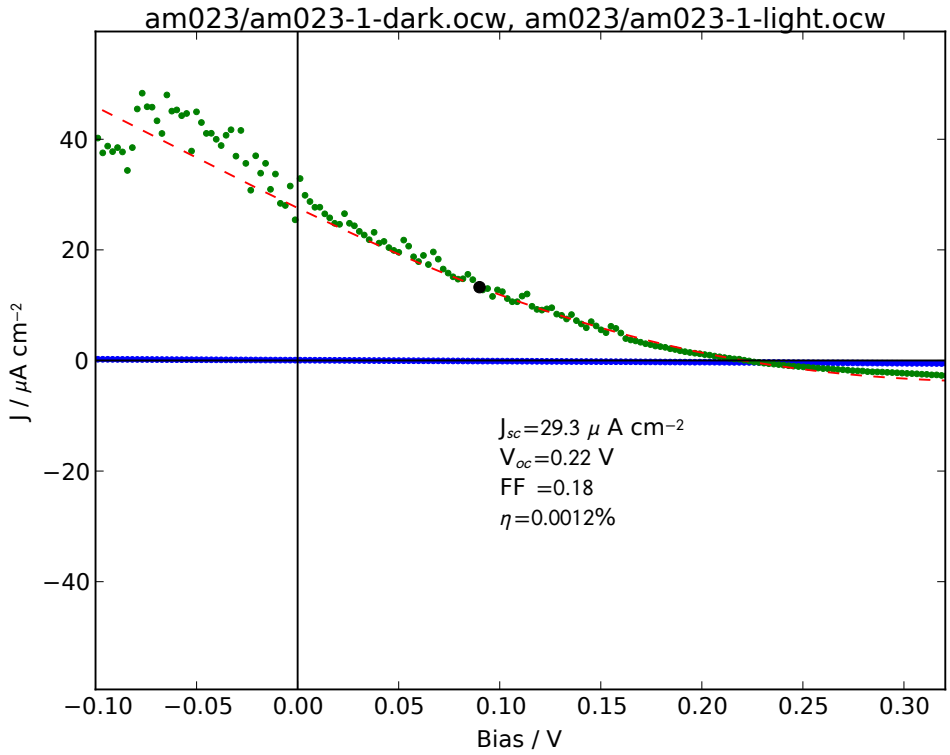

Figure 5.12 *Example IV curve of a real solid state cell (AM023-1). The performance of the cell in the dark is in blue, and the performance in the light in green. The black dot marks the maximum power point as calculated from a curve extrapolated from a fit to a high order polynomial (red dashes).*

quantum efficiency was not possible, no active area masking was employed, calibration of the light source was done without a standardised reference photodiode and the spectral mismatch of the light source was not known. However, the data gathered do provide a way of comparing the different devices fabricated in this study and are able to identify broad trends.

5.3 Results

Measured J_{sc} and V_{oc} for test devices are presented in table 5.1. The structure column reports the order in which the layers of the cell were deposited, beginning with the substrate:

FTO — 1mm thick glass substrate coated in fluorine doped tin oxide.

TiO_2 — Spray pyrolysed dense layer of titania.

PbS — Attachment of PbS dots to TiO_2 layer via mercaptopropanoic acid.

P3HT — Spin-cast layer of regioregular poly(3-hexylthiophene).

Al — Evaporation of a thin film ($\sim 100\,\text{nm}$) of aluminium under vacuum.

PEDOT — Spin-cast layer of PEDOT:PSS.

Blend — Spin-cast layer of a P3HT/TiO_2 composite.

Attempts were made to fabricate PEDOT:PSS/TiO_2 blend cells but no appreciable short circuit current was measured from any of the test cells. Variations in cell performance are small within a batch and large between batches (compare AM023, AM025, AM026 and AM027). This is a common issue when characterising a particular cell design

Table 5.1 *Table of short circuit current densities and open circuit voltages from IV measurements of complete cells under nominal* $1000\,\mathrm{W\ m^{-2}}$ *AM1.5G illumination. Fill factors were low (*≈ 0.25*)*

Cell	Structure	J_{sc} /µAcm^{-2}	V_{oc} /mV	P_{max} /mW m^{-2}	FF	η /10^{-6}
AM026	FTO/TiO_2/	9.9	127	4.1	0.32	4.1
	PbS/P3HT/Al	6.8	91	1.7	0.27	1.7
		9.1	43	0.9	0.24	0.9
AM025	FTO/TiO_2/	2.0	60	0.25	0.21	0.25
	PbS/P3HT/Al					
AM024	FTO/TiO_2/	0.5	20	0.03	0.25	0.03
	P3HT/Al	6.1	165			
AM023	FTO/TiO_2/	29.4	222	12.3	0.19	12.3
	PbS/P3HT/Al	33.8	213	15.1	0.21	15.1
AM022	FTO/TiO_2/	0.5	847	0.80	0.19	0.80
	P3HT/Al	0.6	794	0.84	0.19	0.84
		0.5	875	0.94	0.19	0.94
		0.7	987	1.6	0.22	1.6
AM021	FTO/PEDOT/	2.2	127	0.72	0.25	0.72
	P3HT/Blend/Al	2.0	173	0.88	0.25	0.88
AM020	FTO/TiO_2/	1.5	105	0.46	0.29	0.46
	Blend/PEDOT/Al	1.5	66	0.29	0.29	0.29
		1.2	37	0.13	0.30	0.13

Continued on next page...

Table 5.1 (Continued) *Table of short circuit current densities and open circuit voltages from IV measurements of complete cells under nominal* 1000 W m^{-2} *AM1.5G illumination. Fill factors were low (*≈ 0.25*)*

Cell	Structure	J_{sc} /µAcm^{-2}	V_{oc} /mV	P_{max} /mW m^{-2}	FF	η /10^{-6}
AM019	FTO/PEDOT/	4.3	67	0.75	0.26	0.75
	P3HT/Blend/Al	4.3	189	1.9	0.24	1.9
AM018[1, 2]	FTO/PEDOT/	1.0	110	0.27	0.26	0.27
	P3HT/Blend/Al	1.2	117	0.29	0.21	0.29
		1.3	177	0.65	0.28	0.65
AM017[1]	FTO/TiO_2/	0.7	177	0.34	0.27	0.34
	Blend/P3HT/Al	0.9	261	0.71	0.30	0.71
AM016[1]	FTO/TiO_2/	1.6	148	0.69	0.29	0.69
	Blend/PEDOT/Al	1.1	104	0.34	0.29	0.34
		1.4	171	0.56	0.23	0.56
		1.1	216	0.67	0.29	0.67
		1.0	184	0.58	0.31	0.58
AM015[1]	FTO/PEDOT/	5.4	150	2.0	0.25	2.1
	P3HT/Blend/Al	4.3	153	1.5	0.23	1.5
		4.0	115	1.2	0.25	1.2
		4.1	124	1.3	0.25	1.3
		5.1	160	2.0	0.24	2.0
		3.7	120	1.2	0.26	1.2
		3.3	125	1.1	0.26	1.1
		2.5	101	0.6	0.24	0.6

Continued on next page...

[1] P3HT and blend layers were not annealed for these devices.

[2] Blend for AM018 was two weeks old at time of spin-casting

Table 5.1 (Continued) *Table of short circuit current densities and open circuit voltages from IV measurements of complete cells under nominal* 1000 W m^{-2} *AM1.5G illumination. Fill factors were low (≈ 0.25)*

Cell	Structure	J_{sc} /µAcm^{-2}	V_{oc} /mV	P_{max} /mW m^{-2}	FF	η /10^{-6}
AM011	FTO/TiO_2/	0.4	323	0.24	0.21	0.24
	Blend[3]/PEDOT/Al	0.3	368	0.22	0.19	0.22
		0.3	406	0.23	0.17	0.23
		0.3	397	0.21	0.19	0.21
AM010	FTO/TiO_2/	0.7	404	0.64	0.24	0.64
	Blend[3]/PEDOT/Al	0.7	429	0.75	0.24	0.75
		0.6	401	0.53	0.24	0.53
		0.6	412	0.56	0.23	0.56
		0.5	391	0.41	0.22	0.41
		0.3	412	0.25	0.21	0.25
AM002[4]	FTO/PEDOT/	7.7	445	9.4	0.27	9.4
	Blend/Al	7.7	478	8.7	0.24	8.7
		8.2	497	9.6	0.24	9.6
		4.8	209	2.4	0.24	2.4
		4.9	319	3.8	0.24	3.8
		6.8	437	7.0	0.23	7.0
		5.8	423	6.0	0.25	6.0

[3] The blend spin program for these cells was 10 s/500 RPM and 60s/2000 RPM. The PEDOT:PSS layer also had an intermediate 10 s/3000 RPM step between the 500 RPM and 6000 RPM spin steps.

[4] PEDOT:PSS spin program was 10s/1800 RPM, 50s/6000 RPM and was annealed for 30 minutes at 150 °C in an oven. Regiorandom P3HT in chlorobenzene was used in the blend for this cell, and the blend was heated to 50 °C for 2 minutes to promote P3HT solvation.The blend spin program was 60s/1800 RPM followed by annealing at 150 °C for 45 minutes under vacuum.

For blend cells, it is expected that the kinetics of mixing and therefore the time after mixing before deposition of the blend layer will contribute to the device performance [91]. The approximate time after initial mixing of the P3HT and titania blends is summarised with performance data for the appropriate cells in

table 5.2. Performance parameters are mean values, with the reported error (for cell batches with four or more cells) being the standard error on the mean. Cell AM002 is omitted from this table as it was cast from chlorobenzene solution rather than chloroform.

Table 5.2 *Time between blend mixing and film deposition for P3HT/titania blends, compared with cell performance.*

Cell	Time / days	J_{sc}/µA cm^{-2}	V_{oc}/mV
Cells without TiO_2 blocking layer			
AM015	1	4.1(3)	131(7)
AM019[1]	5	4.3	128
AM021	5	2.1	150
AM018	17	1.2(1)	135(21)
Cells with TiO_2 blocking layer			
AM016	1	1.24(11)	165(19)
AM017	1	0.8	219
AM020	5	1.4(1)	69(20)
AM010	5	0.57(6)	408(5)
AM011	5	0.33(3)	374(19)

[1] Blend remixed prior to deposition.

There appears to be a downward trend in short circuit current with time in cells with no TiO_2 blocking layer, while cells with a TiO_2 blocking layer show no time dependence in their short circuit current. Open circuit voltage shows no time dependence for these cells. PbS sensitised cells exhibited high variability in short circuit current. For all cells, the short circuit current was higher than non-sensitised TiO_2/P3HT interfaces (except for one cell in the AM024 batch), indicating the PbS dots were successfully acting in concert with the P3HT as photocurrent sources.

5.4 Discussion

Cells based on a blend of P3HT and TiO_2 developed greater photocurrent when the blend layer was spun onto a PEDOT:PSS layer rather than a TiO_2 blocking

layer. Cells developed this way also demonstrated a possible dependence on the state of the blend layer at the time of deposition, while those deposited onto TiO_2 blocking layers did not demonstrate any time dependence. This indicates that performance limitations in devices with TiO_2 blocking layers are not related to the morphology of the active blend layer. When devices with blocking layers are sensitised by PbS dots an increase in photocurrent over blend devices without sensitisation but with a blend layer is observed. This also indicates that the blend layer is not contributing to the observed photocurrent in these cells.

It is possible that the top PEDOT:PSS layer is not acting as an adequate photoanode, perhaps due to the mismatch of work function with the aluminium electrode contacting it or an inadequate coating. It is difficult to tell from visual inspection if the PEDOT layer is present or not. Too thin a layer would result in a bad interface between the active blend and the metal electrode. Too thick a layer would reduce cell efficiency through resistive losses. The fact that PbS sensitisation results in a higher photocurrent indicates that electron transport can occur through the blocking TiO_2 layer.

The reduction in photocurrent with blend standing time for blend devices without a blocking layer can be explained by the gravitational sedimentation of the blend. The combination of van der Waals and depletion atttraction forces between TiO_2 colloids should result in strong aggregation. The enhanced viscosity of the polymer solution will kinetically slow the aggregation and sedimentation processes but not significantly inhibit it. As titania aggregates in the suspension sediment, the weight fraction of titania in the castable solution is reduced, which will result in less of the final film being within one exciton diffusion length of a P3HT/TiO_2 heterojunction and is also likely to result in a network with a lower connectivity.

The cell with an active layer cast from a remixed blend exhibited a similar photocurrent to more pristine blends, indicating that the expected irreversible aggregation of titania (which gentle remixing should not affect) within the blend must occur quickly, and later performance degradation is due to slower processes. The remixing also indicates that a chemical degradation mechanism (e.g. photodegradation of the P3HT) is not the cause of the change. Examining the above performance data more closely is difficult as the batch-to-batch variation in cell parameters cannot be adequately accounted for. This parameter is not well known due to the low statistical sampling of cell performance versus fabrication route.

The performance of all cells tested is lower than for similar cells reported in the literature, with photocurrents of the order of milliamps per centimeter squared for blend and dot sensitised cells [65, 86] (although the dot sensitised cell used CdS quantum dots; this study appears to be the first to use a PbS-sensitised TiO_2 interface with P3HT in a solid state sensitised cell geometry). Without standardised testing procedures (see subsection 5.2.7 "Characterisation") it is difficult to determine whether this is an effect of cell construction or testing procedure.

An important test of the solid state sensitised cell design would be to begin constructing cells with sintered, sensitised mesoporous layers, as studied in previous chapters. Once a repeatable protocol for depositing these layers is established structure-property relationships between cells and studied porous structures can be drawn.

5.5 Conclusions

Operational photovoltaic devices were constructed following two design patterns: TiO_2/P3HT bulk heterojunction and solid state PbS quantum dot sensitised solar cells. Bulk heterojunction cells demonstrated performance dependence with blend standing time, confirming this is an important factor to consider when fabricating BHJ cells. Devices including a TiO_2 blocking layer generated a smaller photocurrent than devices without, unless sensitised with PbS quantum dots.

The basic cell designs outlined in this chapter provide useful fabrication patterns to extend upon in the future. Study of these designs was not continued here due to a desire to work on related soft matter topics (the drying of titania films and formulation of titania suspensions) which were closer to the existing expertise present in the authors research group. Future work will need to establish a protocol with a known batch-to-batch performance variability to allow valid conclusions on morphology to be drawn, including the deposition of the suspensions formulated in the first chapter and knowledge of the drying process established in the second.

Chapter 6

Conclusions

Clustering of the titania whilst in suspension plays a central role in the behaviour of the material throughout the studies undertaken here. There are two regimes in suspension behaviour, as identified in chapter 2. First, when suspensions are prepared by setting the pH below 3.5 before mixing and at volume fractions $\phi < 0.0025$, samples exhibit size-limited clustering. For samples with a pre-mix pH of 4.5 or higher volume fractions, aggregation is observed. For volume fractions $\phi < 0.04$ gravitational collapse of the aggregated network occurs. The initial velocity of the sediment/supernatant interface follows a power-law relation with volume fraction, with an exponent consistent with an underlying fractal structure generated by reaction limited cluster aggregation (RLCA). For $\phi > 0.04$, the aggregated sample develops a yield stress sufficient to resist gravitational consolidation. This was found to be $11(1)\,\mathrm{Pa}$ at a volume fraction $\phi = 0.076$. These suspensions demonstrated shear-thinning behaviour, with a power law exponent ($\eta \propto \dot{\gamma}^{0.8}$) also consistent with an underlying fractal gel.

Some difficulties with controlling surface charge were encountered when setting the pH of the suspension before mixing. If the pH of the suspension is adjusted to 3 after mixing, a previously viscous sample becomes less viscous. In addition, the transition between stable clusters and aggregated collapse at pre-mix pH below 4.5 for increasing volume fraction was not expected if pre-mix behaviour was successfully controlling colloidal surface charge. This behaviour was explained by the uptake of H^+ ions by the titania surface during mixing, shifting the solution pH towards the isoelectric point of titania, causing the generated surface charge to be lower than expected, resulting in aggregation of the sample. Distinction

has to be made, therefore, between samples for which the solvent pH is set before mixing and those for which it is set after mixing.

It is clear, from the sedimentation and rheological data, that fractal structures persist at higher volume fractions, into the regime of self-supporting gels from which solar cell electrode pastes are formulated. The importance of fractal aggregates to the mechanical response and structure of the suspension was demonstrated in the drying studies carried out in chapter 3. Here the fluidisation of the fractally aggregated network at post-mix pH 3 was interpreted as a disruption of the aggregated network. This change from fractal aggregates to stable clusters resulted in a significant change in cracking dynamics.

At a post-mix pH of 3, gels formed from cluster-cluster aggregation (an equilibrium approach to gelation, see chapter 2, section 2.1.4). Residual cluster-cluster bonds are expected to be weaker than the bonds holding primary units together within a cluster. When exposed to a stress gradient after gelation (i.e. during drying), the small but finite length scale of the stable cluster allows crack formation to smoothly follow the gradient. In contrast, a fractally aggregated structure in the absence of stabilised clusters is by definition self-similar down to the length scale of the primary units that form the gel. Cracks therefore nucleate preferably at defects, where the self-similar structure of the gel is broken, causing the defect-following behaviour observed for post-mix pH 4 films. Post-mix pH 3 films experience a higher maximum stress during the drying process, as evidenced by the smaller final ratio of crack domain size to film thickness.

Interesting behaviour in the rate of mass loss with time was observed in the first phase of the drying process. To date, the rate during this phase was understood to be controlled by the conditions of the environment the sample is drying in. Given a controlled environment, the rate should therefore be constant. This study has found the rate to increase over significant periods of time (ca. 4000 s). There also appears to be a weak dependence of rate increase with pH, with pH 3 films exhibiting larger rate increases than pH 4 films. It has been postulated that this may be due to UV exposure of the titania colloid at the surface of the film resulting in a change of contact angle.

The usefulness of the DLS technique for studying cluster formation in situ has been demonstrated, and the simulation work undertaken in chapter 4 allows confident interpretation of real data for monomodal polydispersities of $\sigma < 0.4$. This is an improvement over existing, linear, fitting techniques and is the first time

the non-linear technique has been extensively validated using well characterised test data. Measurement of cluster sizes with this technique at low volume fraction show that dispersion down to primary particles (as measured from TEM) is not achieved using probe sonication, even at very low volume fractions and low pre-mix pH. This may be due to the pre-mix pH effect noted above.

Two interesting trends were noted in the solar cell performance data presented in chapter 5. First, a negative trend in cell performance with waiting time between mixing the active layer blend and depositing was noted, which was reversible if the blend was remixed before deposition. Second, devices incorporating a dense TiO_2 blocking layer exhibited lower performance than those without, a trend which goes against the expected efficiency improvements from reductions in cell shorting.

Due to difficulties in measuring layer thicknesses at the appropriate length scales, the observed bad cell performance may be due to either too thick or too thin layers being deposited on the device. This would explain the decrease in performance on addition of a TiO_2 blocking layer; too thick a layer would causes resistive current losses. An alternate explanation is that P3HT strongly wets TiO_2, preventing good contact between titania surfaces if brought together in the presence of the polymer. This increases resistive losses in the titania network, due to the poor electron conductivity of P3HT with respect to titania. This can be addressed in future by extending the current work into a solid-state dye-sensitised design, where a porous layer is deposited first and back-filled with pure polymer instead of depositing a BHJ-style active blend design. Here the contact between the dense TiO_2 film and the titania network is guaranteed before the polymer is added.

If an appropriate layer thickness has been deposited, then degradation of the blend, either through chemical processes such as photodegradation of the P3HT or physical processes such as aggregation of the TiO_2 or crystallisation of the P3HT may reduce efficiency through unfavourable structuring of the blend. This explains the decrease in cell performance with time and is confirmed by the increase of blend performance upon remixing.

6.1 Further Work

Confirmation of the role of clusters in film formation would be of interest in establishing a structure/property relationship for solar cell performance in one of the design patterns discussed in chapter 5. If thinner films, which do not crack, could be incorporated into operational cells then effect of this morphology on, for example, electron transport in fractal networks could be understood better [24]. Polymer infiltration, identified as an important issue in SDSC design [99], is also an interesting area for further work on these films as the void structures formed by clustered and non-clustered aggregation should exhibit different morphologies. If the clustering work can be extended to non-aqueous solvents then similar inroads can be made for BHJ cells. This would be a challenging proposition given that possibilities for electrostatic charging without ligand attachment are limited in a non-polar environment. For these to be viable research goals the issue of variability in the cell construction procedure and performance would need to be addressed. Factors including dust contamination of devices and materials and reliability of cell characterisation equipment will need to be addressed and indeed these are currently active research topics within the broader solar cell community [97]. With the introduction of roll to roll processing techniques [64] to the field the possibility of high-throughput manufacture and processing becomes a possibility for researchers as well as industrial interests.

There is also the possibility of exploring the third approach to gelation described in chapter 2, that of gelation through aggregation of low coordination number colloids. This is primarily an area which needs advances in titania colloid synthesis, as it requires tight control of colloid shape. Advances in simulation techniques to predict the properties of these 'patchy' materials have been made [54]. Oriented attachement, a form of 'patchiness' which arises due to the intrinsically faceted nature of nanocrystals, has already been observed in the titania system [80] where is has been shown to generate needle-like single crystals of anatase. It is likely this effect also plays a role in the low temperature 'sintering' process used to enhance conductivity in DSSC films. The 'stringy' nature of gels formed via directional interactions would affect electron transport by modifying diffusion from three to one dimensions. In addition, current work on nanocrystal:polymer cells in a BHJ pattern has shown that changing from spherical to rod- or tetrapod-like nanocrystals also affects cell performance [108]. Currently, performance improvements after switching to rod-like structures is

attributed to rapid electron transport through long crystalline rods but it may be that the macroscopic assembly of these structures is governed by gelation through directional interactions.

This thesis has explored the colloidal science of titanium dioxide suspensions and begun work on introducing this knowledge to real cell designs. Several currently unexplored avenues exist for linking third generation solar cell fabrication and current research topics in colloid and interface science, as exemplified by the interesting trends noted in constructed cells. Combining existing materials synthesis and fabrication know-how with further exploration of material interactions will enable the creation of cheap solar energy materials which could become ubiquitous in clothing and construction.

Appendix A

Fits to DLS Data

This appendix contains the raw DLS data measured for the time resolved DLS measurements in section 2.3.6 and tabulates the fit parameters calculated using the method described in chapter 4. Raw correlation curves are presented by concentration and day, and then all fit parameters are tabulated afterward. In the data tables, day, ϕ, R and F refer to the day of measurement, the sample volume fraction, the sample number and the fractionation number of the measurement respectively.

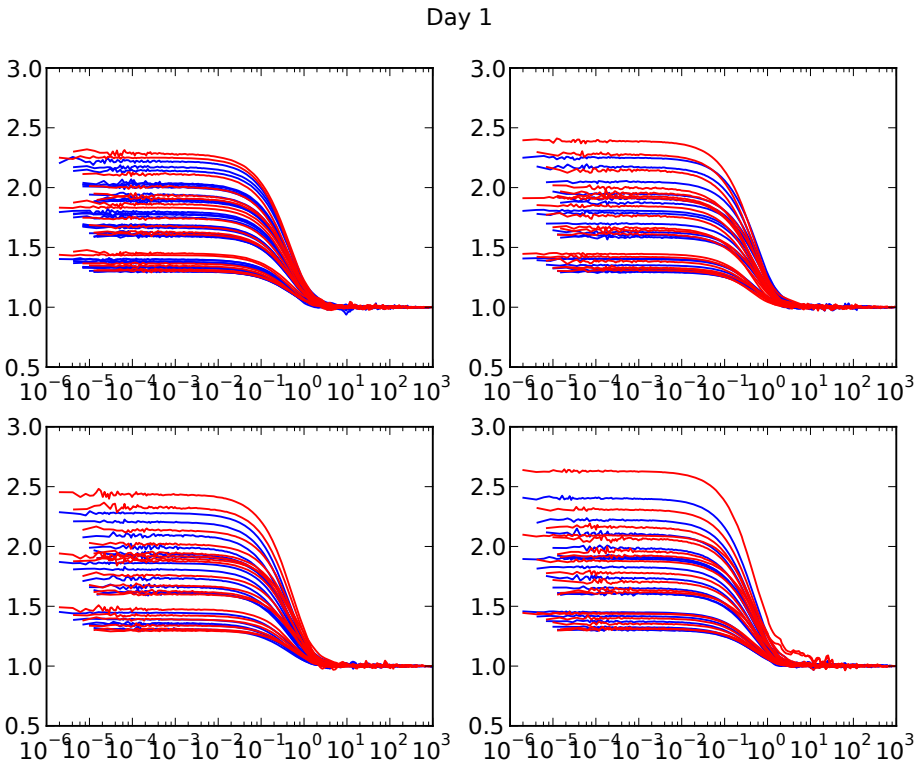

Figure A.1 *Raw DLS data for time-resolved, fractionated DLS experiment,* $\phi = 0.025\%$*, day 1.*

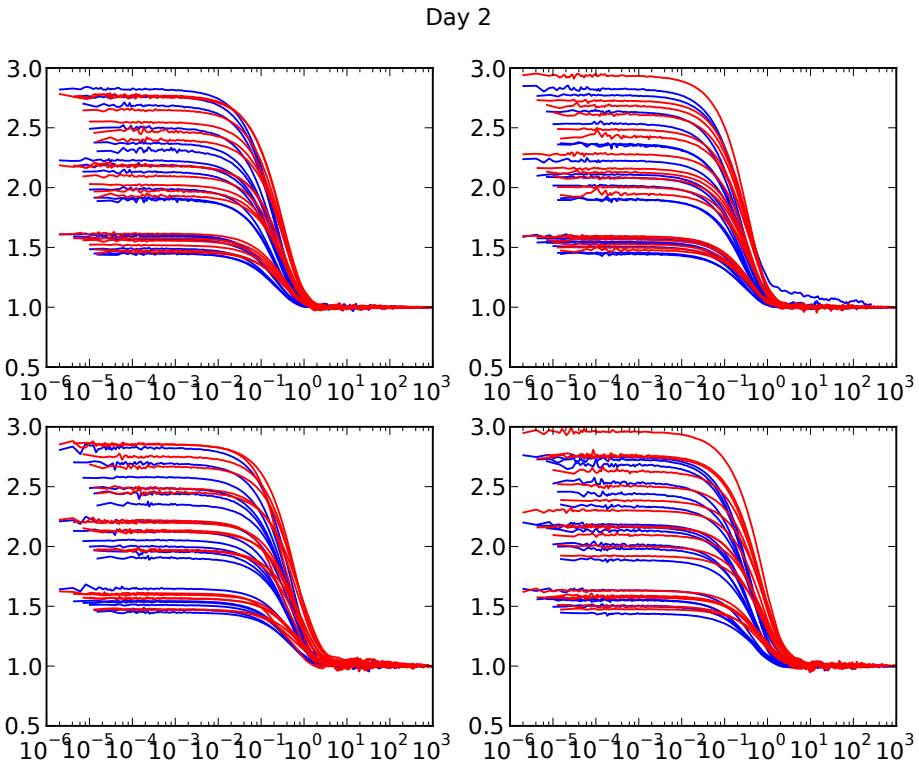

Figure A.2 *Raw DLS data for time-resolved, fractionated DLS experiment,* $\phi = 0.025\%$*, day 2.*

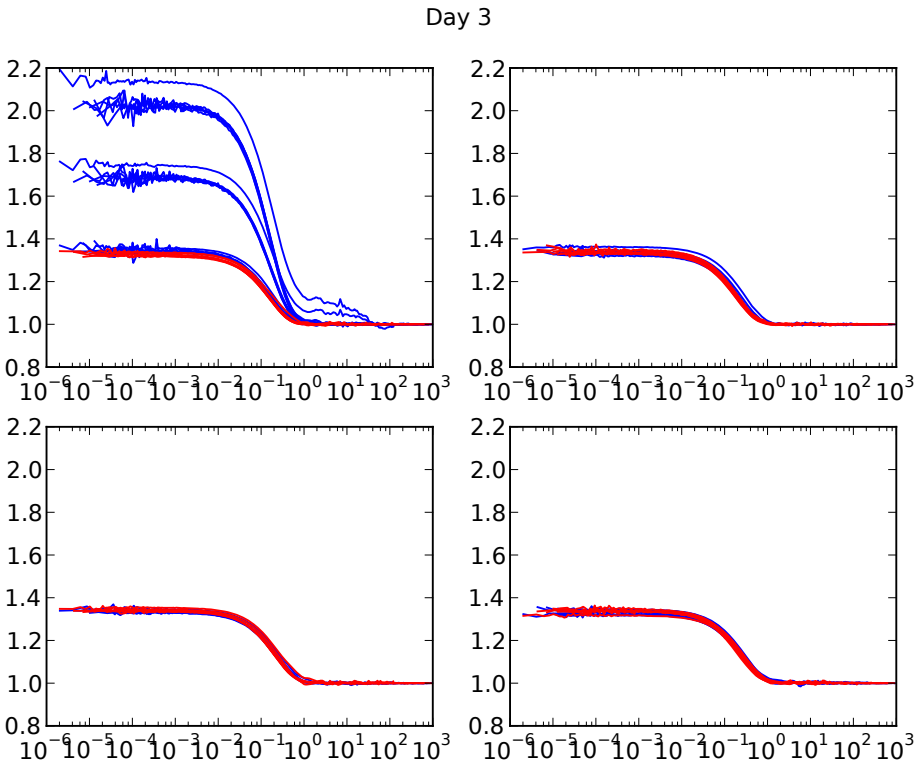

Figure A.3 *Raw DLS data for time-resolved, fractionated DLS experiment,* $\phi = 0.025\%$*, day 3.*

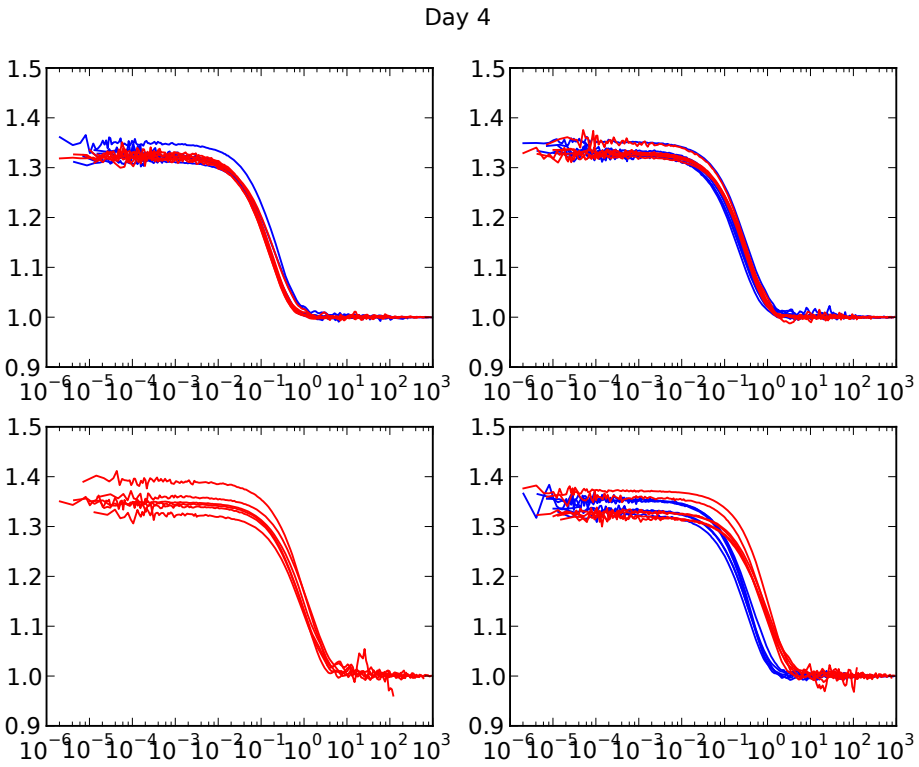

Figure A.4 *Raw DLS data for time-resolved, fractionated DLS experiment, $\phi = 0.025\%$, day 4.*

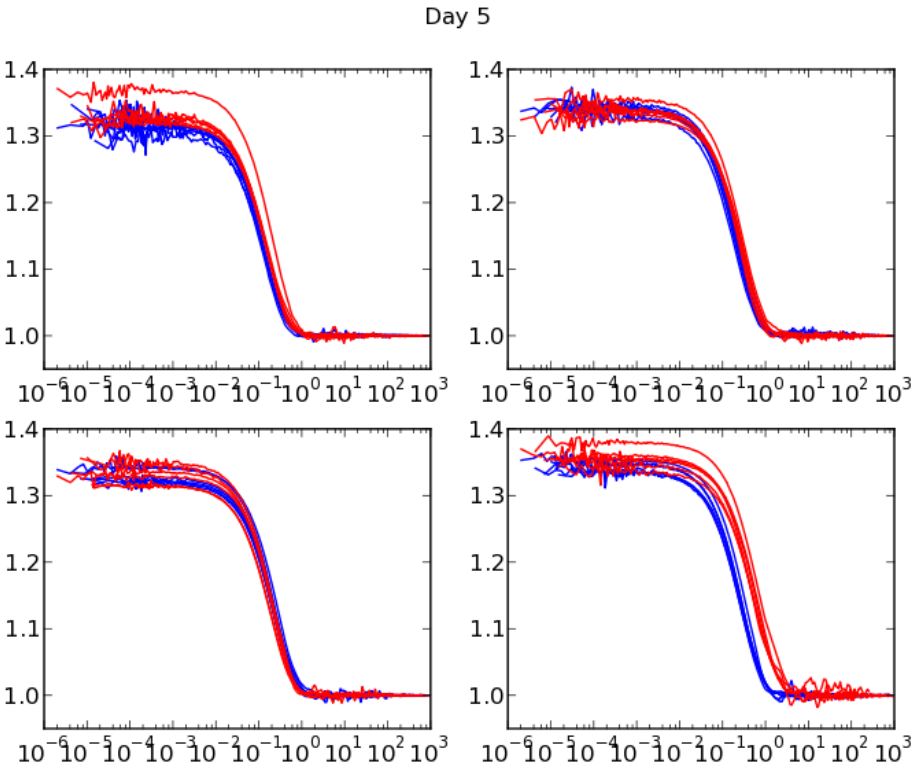

Figure A.5 *Raw DLS data for time-resolved, fractionated DLS experiment,* $\phi = 0.025$*, day 5.*

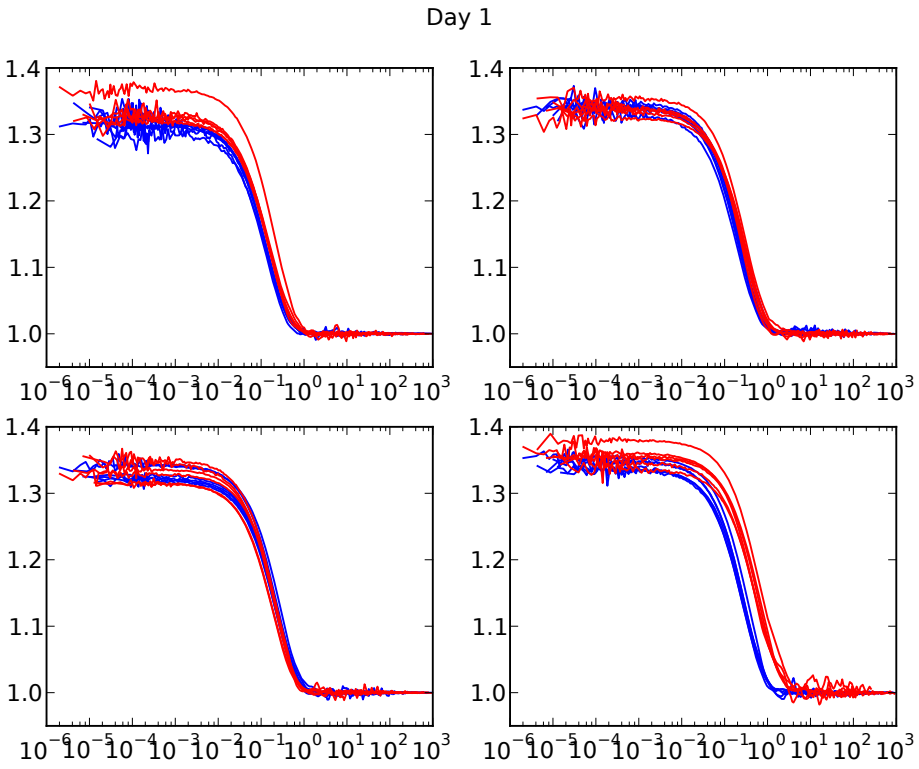

Figure A.6 *Raw DLS data for time-resolved, fractionated DLS experiment,* $\phi = 0.08\%$*, day 1.*

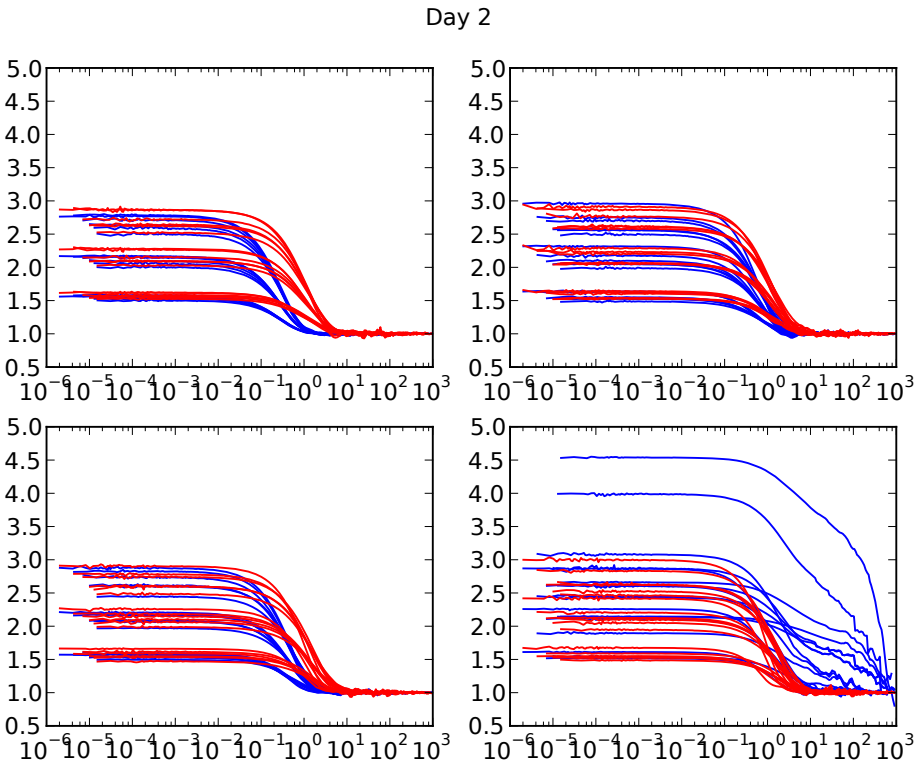

Figure A.7 *Raw DLS data for time-resolved, fractionated DLS experiment, $\phi = 0.08\%$, day 2.*

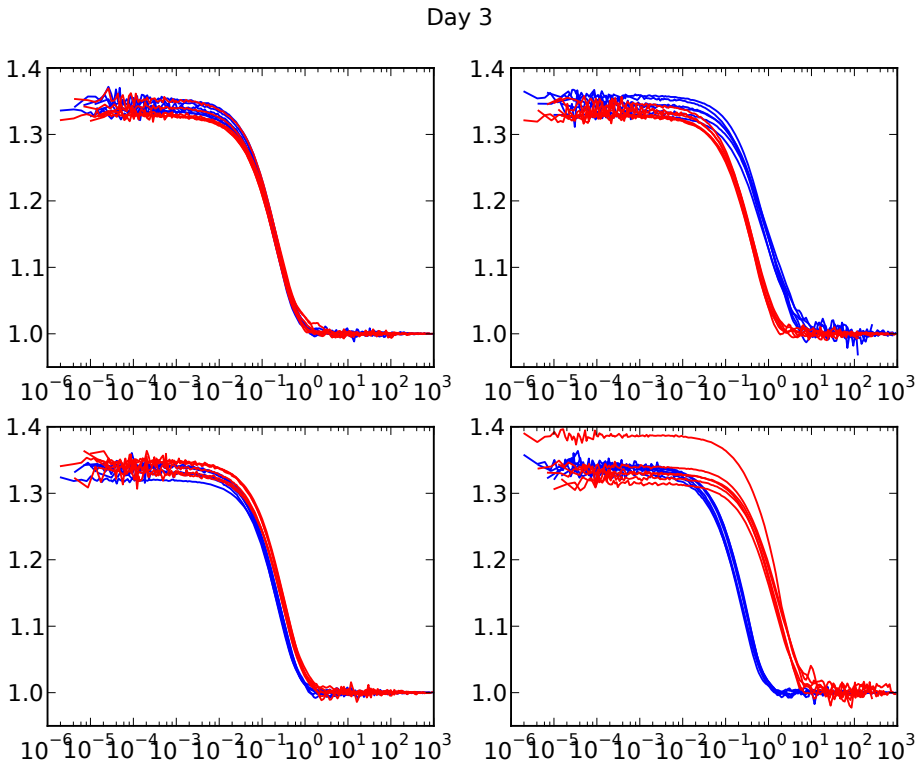

Figure A.8 *Raw DLS data for time-resolved, fractionated DLS experiment, $\phi = 0.08\%$, day 3.*

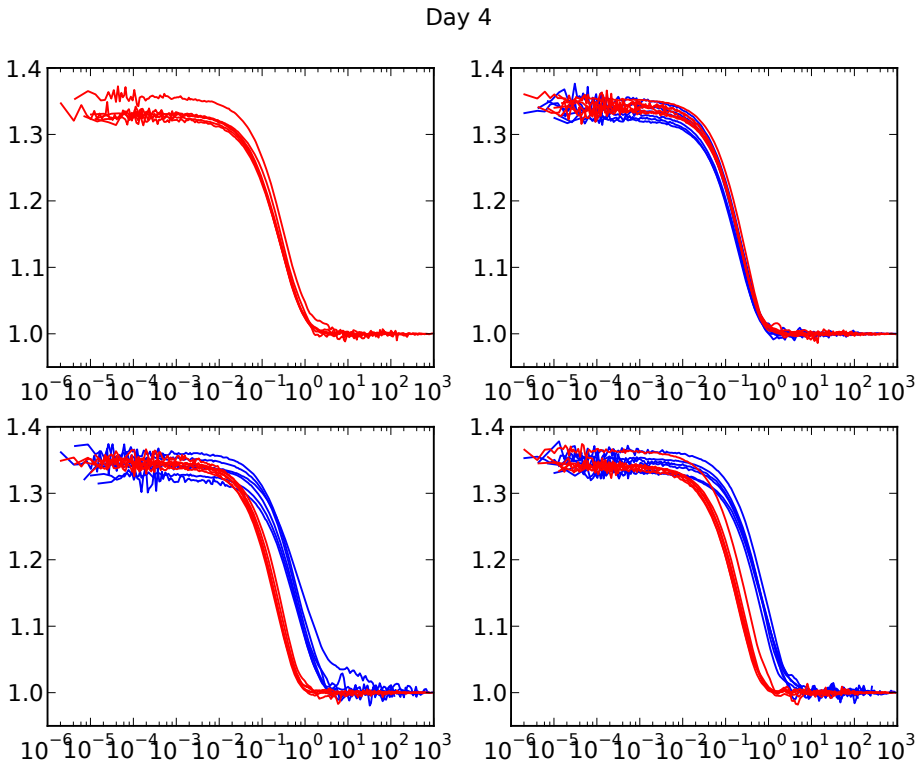

Figure A.9 *Raw DLS data for time-resolved, fractionated DLS experiment, $\phi = 0.08\%$, day 4.*

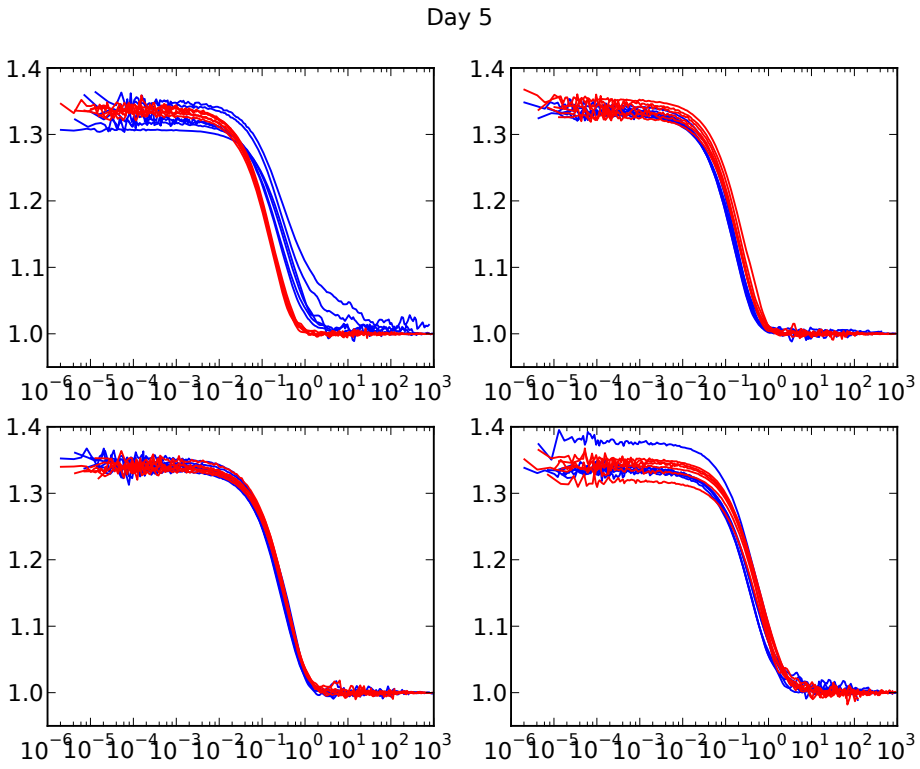

Figure A.10 *Raw DLS data for time-resolved, fractionated DLS experiment, $\phi = 0.08\%$, day 5.*

A.1 Tabulated Fit Results

Day	ϕ %	R	F	θ (°)	β	$\Delta\beta$	$\bar{\Gamma}$ (μs^{-1})	$\Delta\bar{\Gamma}$ (μs^{-1})	M_2	$\Delta(M_2)$	R_{eff} (nm)
1	0.025	1	1	40	0.4005		89		0		224.76
1	0.025	1	1	40	1.2200		83		15		241.04
1	0.025	1	1	40	0.7977		85		0		234.56
1	0.025	1	1	60	0.3965		157		0		271.15
1	0.025	1	1	60	0.7790		161		1		264.59
1	0.025	1	1	60	0.7738		164		1		259.11
1	0.025	1	1	60	1.1717		176		9925		242.42
1	0.025	1	1	60	1.1417		181		11763		235.24
1	0.025	1	1	60	0.3687		154		0		276.72
1	0.025	1	1	60	0.7501		161		1		264.93
1	0.025	1	1	60	0.3800		157		0		271.86

Continues on next page

Day	ϕ %	R	F	θ (°)	β	$\Delta\beta$	$\bar{\Gamma}$ (μs^{-1})	$\Delta\bar{\Gamma}$ (μs^{-1})	M_2	$\Delta(M_2)$	R_{eff} (nm)
1	0.025	1	1	80	0.3343		292		1		241.26
1	0.025	1	1	80	0.3283		287		1		245.5
1	0.025	1	1	80	0.6825		318		46472		221.31
1	0.025	1	1	80	1.0011		282		5		249.55
1	0.025	1	1	80	1.0380		310		39445		227.35
1	0.025	1	1	80	1.0132		315		33614		223.7
1	0.025	1	1	80	0.6723		278		1		253.65
1	0.025	1	1	80	0.3302		283		1		249.25
1	0.025	1	1	80	1.0292		320		28885		219.92
1	0.025	1	1	80	0.3361		290		1		242.49
1	0.025	1	1	80	0.6627		285		1		247.35
1	0.025	1	1	80	0.6853		288		1		244.73
1	0.025	1	1	100	0.9413		445		76268		224.6
1	0.025	1	1	100	0.6202		401		2		249.37

Continues on next page

Day	ϕ %	R	F	θ (°)	β	$\Delta\beta$	$\bar{\Gamma}$ (μs^{-1})	$\Delta\bar{\Gamma}$ (μs^{-1})	M_2	$\Delta(M_2)$	R_{eff} (nm)
1	0.025	1	1	100	0.3076		393		1		254.53
1	0.025	1	1	120	0.6018		557		130054		229.53
1	0.025	1	1	120	0.3010		544		146335		235.08
1	0.025	1	1	120	0.9037		562		132829		227.34
1	0.025	1	1	120	0.8977		564		131398		226.57
1	0.025	1	1	120	0.6025		573		159394		223.29
1	0.025	1	1	120	0.3022		564		156750		226.83
1	0.025	1	1	140	0.2987		579		227287		259.84
1	0.025	1	1	140	0.8848		589		208673		255.6
1	0.025	1	1	140	0.5935		579		194225		259.95
1	0.025	1	2	40	0.4060		68		0		294.39
1	0.025	1	2	40	1.2492		66		648		303.02
1	0.025	1	2	40	0.8060		64		0		309.57
1	0.025	1	2	60	0.7849		143		1		297.44

Continues on next page

Day	ϕ %	R	F	θ (°)	β	$\Delta\beta$	$\bar{\Gamma}$ (μs^{-1})	$\Delta\bar{\Gamma}$ (μs^{-1})	M_2	$\Delta(M_2)$	R_{eff} (nm)
1	0.025	1	2	60	1.1707		145		7		293.13
1	0.025	1	2	60	0.3999		142		0		299.44
1	0.025	1	2	80	1.0497		252		28781		279.37
1	0.025	1	2	80	0.6960		222		0		316.7
1	0.025	1	2	80	0.3502		230		0		305.93
1	0.025	1	2	100	0.9477		332		47946		301.3
1	0.025	1	2	100	0.3142		283		1		353.01
1	0.025	1	2	100	0.6284		332		48224		301.56
1	0.025	1	2	120	0.9087		445		82587		287.42
1	0.025	1	2	120	0.6029		450		85335		284.17
1	0.025	1	2	120	0.2988		458		106576		278.92
1	0.025	1	2	140	0.5865		484		138294		310.81
1	0.025	1	2	140	0.8736		468		117314		321.84
1	0.025	1	2	140	0.2943		485		134512		310.49

Continues on next page

Day	ϕ %	R	F	θ (°)	β	$\Delta\beta$	$\bar{\Gamma}$ (μs^{-1})	$\Delta\bar{\Gamma}$ (μs^{-1})	M_2	$\Delta(M_2)$	R_{eff} (nm)
1	0.025	1	3	40	0.4448		76		0		262.68
1	0.025	1	3	40	1.2768		79		35		251.47
1	0.025	1	3	40	0.8596		79		1		253.92
1	0.025	1	3	60	0.8058		176		1		242.23
1	0.025	1	3	60	1.2056		195		14158		219.12
1	0.025	1	3	60	0.3899		181		0		235.1
1	0.025	1	3	80	1.0933		332		24530		211.95
1	0.025	1	3	80	0.7310		308		2		228.87
1	0.025	1	3	80	0.3570		320		1		219.84
1	0.025	1	3	100	0.9931		484		95577		206.71
1	0.025	1	3	100	0.3431		418		1		239.08
1	0.025	1	3	100							
1	0.025	1	3	120	0.9366		577		147292		221.48
1	0.025	1	3	120	0.6176		589		167012		217.23

Continues on next page

Day	ϕ %	R	F	θ (°)	β	$\Delta\beta$	$\bar{\Gamma}$ (μs^{-1})	$\Delta\bar{\Gamma}$ (μs^{-1})	M_2	$\Delta(M_2)$	R_{eff} (nm)
1	0.025	1	3	120	0.3060		613		135110		208.59
1	0.025	1	3	140	0.6100		616		227468		244.22
1	0.025	1	3	140	0.9155		612		238011		245.79
1	0.025	1	3	140	0.3085		618		234958		243.72
1	0.025	1	4	40	0.4493		78		0		255.92
1	0.025	1	4	40	1.4033		82		2764		244.1
1	0.025	1	4	40	0.8952		77		1		258.88
1	0.025	1	4	60	0.8262		182		5082		234.72
1	0.025	1	4	60	1.2182		170		9		250.36
1	0.025	1	4	60	0.4168		174		0		245.35
1	0.025	1	4	80	1.1054		320		49876		220.45
1	0.025	1	4	80	0.7369		320		48605		220.4
1	0.025	1	4	80	0.3722		291		1		241.74
1	0.025	1	4	100	0.9880		464		92312		215.83

Continues on next page

Day	ϕ %	R	F	θ (°)	β	$\Delta\beta$	$\bar{\Gamma}$ (μs^{-1})	$\Delta\bar{\Gamma}$ (μs^{-1})	M_2	$\Delta(M_2)$	R_{eff} (nm)
1	0.025	1	4	100	0.3234		406		1		246.33
1	0.025	1	4	100	0.6525		456		92891		219.26
1	0.025	1	4	120	0.9148		570		158572		224.29
1	0.025	1	4	120	0.6076		567		146165		225.5
1	0.025	1	4	120	0.3069		553		139972		231.05
1	0.025	1	4	140	0.6072		625		209627		240.75
1	0.025	1	4	140	0.9075		626		206831		240.59
1	0.025	1	4	140	0.3028		649		232872		232.13
1	0.025	2	1	40	0.4353		81		0		245.39
1	0.025	2	1	40	1.2509		86		817		231.49
1	0.025	2	1	40	0.8333		85		721		233.82
1	0.025	2	1	60	0.8594		160		1		266.11
1	0.025	2	1	60	1.2804		166		9		256.28
1	0.025	2	1	60	0.4484		149		0		285.98

Continues on next page

Day	ϕ %	R	F	θ (°)	β	$\Delta\beta$	$\bar{\Gamma}$ (μs^{-1})	$\Delta\bar{\Gamma}$ (μs^{-1})	M_2	$\Delta(M_2)$	R_{eff} (nm)
1	0.025	2	1	80	1.1135		329		37362		214.27
1	0.025	2	1	80	0.7442		322		37613		218.74
1	0.025	2	1	80	0.3645		290		1		242.64
1	0.025	2	1	100	1.0074		466		82977		214.76
1	0.025	2	1	100	0.3463		469		105937		213.4
1	0.025	2	1	100	0.6757		466		96978		214.84
1	0.025	2	1	120	0.9348		559		131887		228.72
1	0.025	2	1	120	0.6289		564		145329		226.57
1	0.025	2	1	120	0.3145		562		163842		227.34
1	0.025	2	1	140	0.6098		614		199970		245.37
1	0.025	2	1	140	0.9108		610		197071		246.85
1	0.025	2	1	140	0.3040		621		221413		242.63
1	0.025	2	2	40	0.4454		83		0		240.4
1	0.025	2	2	40	1.3893		81		1647		245.78

Continues on next page

Day	ϕ %	R	F	θ (°)	β	$\Delta\beta$	$\bar{\Gamma}$ (μs^{-1})	$\Delta\bar{\Gamma}$ (μs^{-1})	M_2	$\Delta(M_2)$	R_{eff} (nm)
1	0.025	2	2	40	0.9109		77		1		258.7
1	0.025	2	2	60	0.8439		167		1		254.75
1	0.025	2	2	60	1.2744		166		9		256.92
1	0.025	2	2	60	0.4200		162		0		263.43
1	0.025	2	2	80	1.1464		307		31986		229.43
1	0.025	2	2	80	0.7661		306		30101		229.86
1	0.025	2	2	80	0.3832		277		1		254.52
1	0.025	2	2	100	1.0000		456		49365		219.41
1	0.025	2	2	100	0.3267		484		72397		206.87
1	0.025	2	2	100	0.6639		465		38673		214.99
1	0.025	2	2	120	0.9276		535		108305		239.03
1	0.025	2	2	120	0.6123		536		114292		238.74
1	0.025	2	2	120	0.3089		539		119638		237.04
1	0.025	2	2	140	0.6437		552		174444		272.9

Continues on next page

Day	ϕ %	R	F	θ (°)	β	$\Delta\beta$	$\bar{\Gamma}$ (μs^{-1})	$\Delta\bar{\Gamma}$ (μs^{-1})	M_2	$\Delta(M_2)$	R_{eff} (nm)
1	0.025	2	2	140	0.9549		545		171255		276.37
1	0.025	2	2	140	0.3301		548		187108		274.57
1	0.025	2	3	40	0.4751		71		0		280.08
1	0.025	2	3	40	1.4341		67		19		298.67
1	0.025	2	3	40	0.9195		71		1		279.03
1	0.025	2	3	60	0.8774		147		1		289.1
1	0.025	2	3	60	1.3268		162		8119		262.65
1	0.025	2	3	60	0.4228		141		0		301.94
1	0.025	2	3	80	1.1361		267		17059		263.8
1	0.025	2	3	80	0.7569		255		1		275.76
1	0.025	2	3	80	0.3904		255		2		276.51
1	0.025	2	3	100	1.0199		372		49825		269.27
1	0.025	2	3	100	0.3383		344		1		291.22
1	0.025	2	3	100	0.6730		379		47655		263.91

Continues on next page

Day	ϕ %	R	F	θ (°)	β	$\Delta\beta$	$\bar{\Gamma}$ (μs^{-1})	$\Delta\bar{\Gamma}$ (μs^{-1})	M_2	$\Delta(M_2)$	R_{eff} (nm)
1	0.025	2	3	120	0.9431		449		92420		284.84
1	0.025	2	3	120	0.6239		463		103879		275.92
1	0.025	2	3	120	0.3074		406		1		314.84
1	0.025	2	3	140	0.6007		444		113069		339.4
1	0.025	2	3	140	0.8960		449		113200		335.58
1	0.025	2	3	140	0.2963		460		134733		327.39
1	0.025	2	4	40	0.4382		76		0		264.18
1	0.025	2	4	40	1.6319		74		3503		270.5
1	0.025	2	4	40	1.0931		75		4211		265.27
1	0.025	2	4	60	0.8750		153		1		279.51
1	0.025	2	4	60	1.3097		180		13360		236.65
1	0.025	2	4	60	0.4372		145		0		293.65
1	0.025	2	4	80	1.1633		304		32090		231.7
1	0.025	2	4	80	0.7800		296		26174		238.04

Continues on next page

Day	ϕ %	R	F	θ (°)	β	$\Delta\beta$	$\bar{\Gamma}$ (μs^{-1})	$\Delta\bar{\Gamma}$ (μs^{-1})	M_2	$\Delta(M_2)$	R_{eff} (nm)
1	0.025	2	4	80	0.3984		277		1		254.16
1	0.025	2	4	100	1.0649		416		50854		240.26
1	0.025	2	4	100	0.3538		384		1		260.51
1	0.025	2	4	100	0.7058		409		45969		244.8
1	0.025	2	4	120	0.9616		519		96590		246.42
1	0.025	2	4	120	0.6365		529		83008		241.74
1	0.025	2	4	120	0.3137		471		1		271.76
1	0.025	2	4	140	0.6168		505		150283		298.18
1	0.025	2	4	140	0.9221		516		153167		291.87
1	0.025	2	4	140	0.3106		531		175089		283.4
1	0.080	1	1	40	0.5123		89		0		223.59
1	0.080	1	1	40	1.5499		85		13		235.7
1	0.080	1	1	40	1.0215		87		941		228.02
1	0.080	1	1	60	0.9940		186		4		229.31

Continues on next page

Day	ϕ %	R	F	θ (°)	β	$\Delta\beta$	$\bar{\Gamma}$ (μs^{-1})	$\Delta\bar{\Gamma}$ (μs^{-1})	M_2	$\Delta(M_2)$	R_{eff} (nm)
1	0.080	1	1	60	1.4857		204		10778		209.16
1	0.080	1	1	60	0.5056		185		1		230.43
1	0.080	1	1	80	1.2003		378		34898		186.18
1	0.080	1	1	80	0.7950		385		45105		182.99
1	0.080	1	1	80	0.3815		361		1		195
1	0.080	1	1	100	1.0865		538		85419		185.92
1	0.080	1	1	100	0.3661		475		1		210.88
1	0.080	1	1	100	0.7193		540		82220		185.45
1	0.080	1	1	120	0.9973		684		128111		187.11
1	0.080	1	1	120	0.6737		684		119576		186.86
1	0.080	1	1	120	0.3364		692		122792		184.79
1	0.080	1	1	140	0.6482		730		275171		206.41
1	0.080	1	1	140	0.9679		727		279044		207.11
1	0.080	1	1	140	0.3299		729		248774		206.63

Continues on next page

Day	ϕ %	R	F	θ (°)	β	$\Delta\beta$	$\bar{\Gamma}$ (μs^{-1})	$\Delta\bar{\Gamma}$ (μs^{-1})	M_2	$\Delta(M_2)$	R_{eff} (nm)
1	0.080	1	2	40	0.5082		88		0		226.01
1	0.080	1	2	40	1.6172		83		2320		240.36
1	0.080	1	2	40	1.0612		77		3		259.34
1	0.080	1	2	60	0.9650		178		3		238.94
1	0.080	1	2	60	1.4601		198		12864		215.27
1	0.080	1	2	60	0.4911		186		0		229.05
1	0.080	1	2	80	1.2576		352		37705		200.22
1	0.080	1	2	80	0.8295		319		1		220.62
1	0.080	1	2	80	0.4141		333		1		211.9
1	0.080	1	2	100	1.0872		535		91845		187.1
1	0.080	1	2	100	0.3681		489		1		204.78
1	0.080	1	2	100	0.7364		535		87857		187.21
1	0.080	1	2	120	0.9853		692		188050		184.93
1	0.080	1	2	120	0.6492		689		192176		185.74

Continues on next page

Day	ϕ %	R	F	θ (°)	β	$\Delta\beta$	$\bar{\Gamma}$ (μs^{-1})	$\Delta\bar{\Gamma}$ (μs^{-1})	M_2	$\Delta(M_2)$	R_{eff} (nm)
1	0.080	1	2	120	0.3284		675		153161		189.58
1	0.080	1	2	140	0.6399		735		280669		204.94
1	0.080	1	2	140	0.9539		745		288258		202.07
1	0.080	1	2	140	0.3216		736		263169		204.51
1	0.080	1	3	40	0.4957		77		0		259.49
1	0.080	1	3	40	1.5788		73		7		273.39
1	0.080	1	3	40	1.0528		71		3		279.4
1	0.080	1	3	60	0.9883		158		3		269.33
1	0.080	1	3	60	1.4974		176		10284		241.97
1	0.080	1	3	60	0.5161		151		0		282.81
1	0.080	1	3	80	1.2823		298		21584		236.46
1	0.080	1	3	80	0.8493		302		23824		233.61
1	0.080	1	3	80	0.4311		281		0		250.47
1	0.080	1	3	100	1.1019		432		70164		231.92

Continues on next page

Day	ϕ %	R	F	θ (°)	β	$\Delta\beta$	$\bar{\Gamma}$ (μs^{-1})	$\Delta\bar{\Gamma}$ (μs^{-1})	M_2	$\Delta(M_2)$	R_{eff} (nm)
1	0.080	1	3	100	0.3733		382		1		261.93
1	0.080	1	3	100	0.7424		438		78347		228.29
1	0.080	1	3	120							
1	0.080	1	3	120	0.6683		507		119565		252.09
1	0.080	1	3	120	0.3442		499		123403		256.19
1	0.080	1	3	140	0.6215		567		167870		265.41
1	0.080	1	3	140	0.9336		568		183317		265.13
1	0.080	1	3	140	0.3155		565		179467		266.48
1	0.080	1	4	40	0.4412		26		0		760.54
1	0.080	1	4	40	1.4597		24		0		842.18
1	0.080	1	4	40	0.9166		25		0		801.01
1	0.080	1	4	60	0.8628		42		0		1004.49
1	0.080	1	4	60	1.2944		47		631		905.47
1	0.080	1	4	60	0.4451		43		0		994.75

Continues on next page

Day	ϕ %	R	F	θ (°)	β	$\Delta\beta$	$\bar{\Gamma}$ (μs^{-1})	$\Delta\bar{\Gamma}$ (μs^{-1})	M_2	$\Delta(M_2)$	R_{eff} (nm)
1	0.080	1	4	80	1.1980		68		2706		1029.42
1	0.080	1	4	80	0.8044		61		0		1163.25
1	0.080	1	4	80	0.3987		58		0		1212.86
1	0.080	1	4	100	0.9726		89		3994		1119.15
1	0.080	1	4	100	0.3274		68		0		1465.42
1	0.080	1	4	100	0.6298		74		0		1351.17
1	0.080	1	4	120	0.9183		86		1		1479.81
1	0.080	1	4	120	0.6030		90		0		1418.76
1	0.080	1	4	120	0.2895		101		0		1266.96
1	0.080	1	4	140	0.5769		107		0		1409.76
1	0.080	1	4	140	0.8698		107		1		1412.04
1	0.080	1	4	140	0.2970		102		0		1470.42
1	0.080	2	1	40	0.5560		83		0		240.12
1	0.080	2	1	40	1.5998		92		91		217.55

Continues on next page

Day	ϕ %	R	F	θ (°)	β	$\Delta\beta$	$\bar{\Gamma}$ (μs^{-1})	$\Delta\bar{\Gamma}$ (μs^{-1})	M_2	$\Delta(M_2)$	R_{eff} (nm)
1	0.080	2	1	40	1.0830		89		781		224.25
1	0.080	2	1	60							
1	0.080	2	1	60	1.4878		231		10611		184.98
1	0.080	2	1	60	0.4917		219		1		194.82
1	0.080	2	1	80	1.3277		403		46394		174.8
1	0.080	2	1	80	0.8786		411		52969		171.54
1	0.080	2	1	80	0.4378		374		1		188.37
1	0.080	2	1	100	1.1716		587		105530		170.63
1	0.080	2	1	100	0.3959		585		122651		171.22
1	0.080	2	1	100	0.7839		585		107938		171.21
1	0.080	2	1	120	1.0646		773		228670		165.46
1	0.080	2	1	120	0.7070		777		206606		164.61
1	0.080	2	1	120	0.3591		769		175110		166.34
1	0.080	2	1	140	0.7003		869		425894		173.23

Continues on next page

Day	ϕ %	R	F	θ (°)	β	$\Delta\beta$	$\bar{\Gamma}$ (μs^{-1})	$\Delta\bar{\Gamma}$ (μs^{-1})	M_2	$\Delta(M_2)$	R_{eff} (nm)
1	0.080	2	1	140	1.0367		877		425988		171.79
1	0.080	2	1	140	0.3561		850		403735		177.17
1	0.080	2	2	40	0.5406		88		0		225.77
1	0.080	2	2	40	1.6363		86		8		233.28
1	0.080	2	2	40	1.0800		88		4		225.9
1	0.080	2	2	60	1.0079		189		4		225.74
1	0.080	2	2	60	1.5213		208		14142		205
1	0.080	2	2	60	0.5137		186		1		229.59
1	0.080	2	2	80	1.3128		368		54073		191.53
1	0.080	2	2	80	0.8747		372		57785		189.58
1	0.080	2	2	80	0.4311		330		1		213.77
1	0.080	2	2	100	1.1613		546		106982		183.38
1	0.080	2	2	100	0.3840		535		99274		187.24
1	0.080	2	2	100	0.7640		551		106385		181.77

Continues on next page

Day	ϕ %	R	F	θ (°)	β	$\Delta\beta$	$\bar{\Gamma}$ (μs^{-1})	$\Delta\bar{\Gamma}$ (μs^{-1})	M_2	$\Delta(M_2)$	R_{eff} (nm)
1	0.080	2	2	120	1.0333		690		187335		185.5
1	0.080	2	2	120	0.6769		696		182651		183.94
1	0.080	2	2	120	0.3399		690		196332		185.38
1	0.080	2	2	140	0.6753		727		287123		207.17
1	0.080	2	2	140	1.0231		734		298846		205.12
1	0.080	2	2	140	0.3448		736		303639		204.68
1	0.080	2	3	40	0.5073		40		0		499.56
1	0.080	2	3	40	1.6023		41		400		481.27
1	0.080	2	3	40	1.0411		40		2		494.89
1	0.080	2	3	60							
1	0.080	2	3	60	1.4808		85		3107		500.48
1	0.080	2	3	60	0.4997		76		0		562.12
1	0.080	2	3	80	1.2986		125		10701		564.87
1	0.080	2	3	80	0.8456		101		1		696.1

Continues on next page

Day	ϕ %	R	F	θ (°)	β	$\Delta\beta$	$\bar{\Gamma}$ (μs^{-1})	$\Delta\bar{\Gamma}$ (μs^{-1})	M_2	$\Delta(M_2)$	R_{eff} (nm)
1	0.080	2	3	80	0.4148		106		0		665.05
1	0.080	2	3	100	1.0490		161		21947		623.52
1	0.080	2	3	100	0.3483		142		0		703.71
1	0.080	2	3	100	0.7230		162		22940		619.24
1	0.080	2	3	120	1.0299		141		20130		907.08
1	0.080	2	3	120	0.7031		135		19551		944.6
1	0.080	2	3	120	0.3680		83		0		1535.12
1	0.080	2	3	140	0.6383		134		0		1120.58
1	0.080	2	3	140	0.9396		208		37618		722.67
1	0.080	2	3	140	0.3297		108		0		1389.41
1	0.080	2	4	40	0.5120		27		0		735.36
1	0.080	2	4	40	1.6884		23		106		875.98
1	0.080	2	4	40							
1	0.080	2	4	60	0.9664		35		577		1232.86

Continues on next page

Day	ϕ %	R	F	θ (°)	β	$\Delta\beta$	$\bar{\Gamma}$ (μs^{-1})	$\Delta\bar{\Gamma}$ (μs^{-1})	M_2	$\Delta(M_2)$	R_{eff} (nm)
1	0.080	2	4	60	1.5103		34		495		1266.55
1	0.080	2	4	60	0.4732		30		0		1411.54
1	0.080	2	4	80	1.2792		44		1028		1599.42
1	0.080	2	4	80	0.8997		35		0		2041.31
1	0.080	2	4	80	0.4448		42		0		1674.64
1	0.080	2	4	100	1.5831		16		423		6124.07
1	0.080	2	4	100	0.4606		25		787		4033.51
1	0.080	2	4	100	0.8157		21		0		4817.47
1	0.080	2	4	120	1.4607		14		338		9324.65
1	0.080	2	4	120	1.0562		3		0		40093.6
1	0.080	2	4	120	0.5314		8		121		16995.08
1	0.080	2	4	140	0.7029		24		0		6298.27
1	0.080	2	4	140	1.1901		26		1004		5874.67
1	0.080	2	4	140	0.4528		20		649		7700.98

Continues on next page

Day	ϕ %	R	F	θ (°)	β	$\Delta\beta$	$\bar{\Gamma}$ (μs^{-1})	$\Delta\bar{\Gamma}$ (μs^{-1})	M_2	$\Delta(M_2)$	R_{eff} (nm)
2	0.025	1	1	40	0.6061		180		0		110.94
2	0.025	1	1	40	1.8231		181		5390		109.99
2	0.025	1	1	40	1.2252		175		9		113.85
2	0.025	1	1	60	1.1891		390		24916		109.19
2	0.025	1	1	60	1.7636		392		20819		108.49
2	0.025	1	1	60							
2	0.025	1	1	80	1.6882		639		88703		110.21
2	0.025	1	1	80	1.1324		645		84426		109.07
2	0.025	1	1	80	0.5691		655		111927		107.46
2	0.025	1	1	100	1.5024		943		140421		105.99
2	0.025	1	1	100	0.4899		972		226481		102.79
2	0.025	1	1	100	0.9904		947		129729		105.5
2	0.025	1	1	120	1.3723		1184		204134		107.91
2	0.025	1	1	120	0.9109		1201		188315		106.37

Continues on next page

Day	ϕ %	R	F	θ (°)	β	$\Delta\beta$	$\bar{\Gamma}$ (μs^{-1})	$\Delta\bar{\Gamma}$ (μs^{-1})	M_2	$\Delta(M_2)$	R_{eff} (nm)
2	0.025	1	1	120	0.4502		1194		161893		106.97
2	0.025	1	1	140	0.9015		1325		251212		113.55
2	0.025	1	1	140	1.3161		1341		288542		112.17
2	0.025	1	1	140	0.4491		1274		4		118.01
2	0.025	1	2	40	0.5890		121		0		164.81
2	0.025	1	2	40	1.8254		127		4028		157.04
2	0.025	1	2	40	1.2213		116		6		171.26
2	0.025	1	2	60	0.5723		260		1		163.77
2	0.025	1	2	60	1.1108		299		24928		142.3
2	0.025	1	2	60	1.7734		268		46561		158.97
2	0.025	1	2	60	0.5461		279		1		152.55
2	0.025	1	2	80	1.6361		516		37997		136.35
2	0.025	1	2	80	1.0851		524		38994		134.23
2	0.025	1	2	80	0.5378		533		17945		132.15

Continues on next page

Day	ϕ %	R	F	θ (°)	β	$\Delta\beta$	$\bar{\Gamma}$ (μs^{-1})	$\Delta\bar{\Gamma}$ (μs^{-1})	M_2	$\Delta(M_2)$	R_{eff} (nm)
2	0.025	1	2	100	1.5360		735		59836		135.97
2	0.025	1	2	100	0.5057		710		3		140.73
2	0.025	1	2	100							
2	0.025	1	2	120	1.3650		976		238772		130.96
2	0.025	1	2	120	0.9029		971		217802		131.55
2	0.025	1	2	120	0.4556		960		164018		133.02
2	0.025	1	2	140	0.9020		1069		370244		140.72
2	0.025	1	2	140	1.3566		1062		326749		141.67
2	0.025	1	2	140	0.4452		1099		360627		136.91
2	0.025	1	3	40	0.6465		67		0		296.37
2	0.025	1	3	40	1.8252		82		1715		244.06
2	0.025	1	3	40	1.2116		74		15		267.78
2	0.025	1	3	60	1.1263		193		9558		221.09
2	0.025	1	3	60	1.6908		179		27		238.57

Continues on next page

Day	ϕ %	R	F	θ (°)	β	$\Delta\beta$	$\bar{\Gamma}$ (μs^{-1})	$\Delta\bar{\Gamma}$ (μs^{-1})	M_2	$\Delta(M_2)$	R_{eff} (nm)
2	0.025	1	3	60	0.5430		177		1		240.8
2	0.025	1	3	80	1.5800		321		25086		219.36
2	0.025	1	3	80	1.0537		329		25629		213.87
2	0.025	1	3	80	0.5355		302		0		233.05
2	0.025	1	3	100	1.4872		456		51898		219.09
2	0.025	1	3	100	0.5109		427		34415		233.93
2	0.025	1	3	100	1.0005		444		41752		225.13
2	0.025	1	3	120	1.4425		566		102059		225.93
2	0.025	1	3	120							
2	0.025	1	3	120	0.4716		578		109960		221.24
2	0.025	1	3	140	0.9049		604		181053		248.98
2	0.025	1	3	140	1.3524		599		176405		251.25
2	0.025	1	3	140	0.4493		621		157718		242.23
2	0.025	1	4	40	0.6341		88		0		225.92

Continues on next page

Day	ϕ %	R	F	θ (°)	β	$\Delta\beta$	$\bar{\Gamma}$ (μs^{-1})	$\Delta\bar{\Gamma}$ (μs^{-1})	M_2	$\Delta(M_2)$	R_{eff} (nm)
2	0.025	1	4	40	1.7463		89		5		223.61
2	0.025	1	4	40	1.1843		90		4		220.88
2	0.025	1	4	60	1.1625		205		3997		207.36
2	0.025	1	4	60	1.7275		212		5710		201.01
2	0.025	1	4	60	0.5539		214		0		199.15
2	0.025	1	4	80	1.6831		341		27164		206.24
2	0.025	1	4	80	1.1344		340		31768		207.13
2	0.025	1	4	80	0.5497		336		0		209.24
2	0.025	1	4	100	1.5358		507		95106		197.18
2	0.025	1	4	100	0.5045		502		111981		199.09
2	0.025	1	4	100	1.0169		508		103713		196.88
2	0.025	1	4	120	1.4411		596		125772		214.27
2	0.025	1	4	120	0.9819		581		127216		219.85
2	0.025	1	4	120	0.4992		574		141174		222.8

Continues on next page

Day	ϕ %	R	F	θ (°)	β	$\Delta\beta$	$\bar{\Gamma}$ (μs^{-1})	$\Delta\bar{\Gamma}$ (μs^{-1})	M_2	$\Delta(M_2)$	R_{eff} (nm)
2	0.025	1	4	140	0.8872		641		201061		234.57
2	0.025	1	4	140	1.3366		648		222677		232.25
2	0.025	1	4	140	0.4381		659		192562		228.42
2	0.025	2	1	40	0.6140		114		0		174.09
2	0.025	2	1	40	1.7690		122		9		163.97
2	0.025	2	1	40	1.1824		121		5		164.83
2	0.025	2	1	60	1.1835		256		6585		166.72
2	0.025	2	1	60	1.7598		256		9475		166.69
2	0.025	2	1	60	0.5776		244		1		174.6
2	0.025	2	1	80	1.6498		445		27860		158.07
2	0.025	2	1	80	1.0963		434		11		162.37
2	0.025	2	1	80	0.5562		433		6		162.77
2	0.025	2	1	100	1.5476		630		77424		158.8
2	0.025	2	1	100	0.5181		608		0		164.45

Continues on next page

Day	ϕ %	R	F	θ (°)	β	$\Delta\beta$	$\bar{\Gamma}$ (μs^{-1})	$\Delta\bar{\Gamma}$ (μs^{-1})	M_2	$\Delta(M_2)$	R_{eff} (nm)
2	0.025	2	1	100							
2	0.025	2	1	120	1.4730		793		153048		161.17
2	0.025	2	1	120	0.9750		799		167428		159.91
2	0.025	2	1	120	0.4743		795		130644		160.69
2	0.025	2	1	140	0.9320		861		252852		174.85
2	0.025	2	1	140	1.3993		850		202956		177.05
2	0.025	2	1	140	0.4618		876		231095		171.75
2	0.025	2	2	40	0.5941		116		0		171.51
2	0.025	2	2	40	1.9384		106		6		188.28
2	0.025	2	2	40	1.2815		108		1033		185.29
2	0.025	2	2	60	1.1603		224		3727		190.05
2	0.025	2	2	60	1.7271		228		7359		187.18
2	0.025	2	2	60	0.5851		219		1		194.46
2	0.025	2	2	80	1.6842		392		30747		179.46

Continues on next page

Day	ϕ %	R	F	θ (°)	β	$\Delta\beta$	$\bar{\Gamma}$ (μs^{-1})	$\Delta\bar{\Gamma}$ (μs^{-1})	M_2	$\Delta(M_2)$	R_{eff} (nm)
2	0.025	2	2	80	1.1280		393		20849		179.41
2	0.025	2	2	80	0.5657		396		25286		177.78
2	0.025	2	2	100	1.6141		560		79523		178.45
2	0.025	2	2	100	0.5265		572		57876		174.82
2	0.025	2	2	100	1.0820		558		91030		179.38
2	0.025	2	2	120	1.4864		701		126941		182.39
2	0.025	2	2	120	1.0047		696		111323		183.65
2	0.025	2	2	120	0.4993		720		124277		177.59
2	0.025	2	2	140	0.9503		808		228097		186.15
2	0.025	2	2	140	1.4315		798		215975		188.58
2	0.025	2	2	140	0.4785		790		195707		190.38
2	0.025	2	3	40	0.6106		95		138		210.74
2	0.025	2	3	40	1.8617		90		1561		220.9
2	0.025	2	3	40	1.2197		89		4		224.51

Continues on next page

Day	ϕ %	R	F	θ (°)	β	$\Delta\beta$	$\bar{\Gamma}$ (μs^{-1})	$\Delta\bar{\Gamma}$ (μs^{-1})	M_2	$\Delta(M_2)$	R_{eff} (nm)
2	0.025	2	3	60	1.1980		123		6		345.41
2	0.025	2	3	60	1.8561		130		6242		327.29
2	0.025	2	3	60	0.5964		125		0		340.76
2	0.025	2	3	80	1.7527		214		20235		329.35
2	0.025	2	3	80	1.1355		221		19660		318.77
2	0.025	2	3	80	0.5662		200		1		352.45
2	0.025	2	3	100	1.6664		286		35528		350.1
2	0.025	2	3	100	0.5620		239		0		418.34
2	0.025	2	3	100	1.1227		274		32783		365.66
2	0.025	2	3	120	1.4874		377		66357		338.92
2	0.025	2	3	120	0.9678		389		65087		328.66
2	0.025	2	3	120	0.4740		412		98280		310.55
2	0.025	2	3	140	0.9699		367		55887		409.61
2	0.025	2	3	140	1.4518		370		67547		406.56

Continues on next page

Day	ϕ %	R	F	θ (°)	β	$\Delta\beta$	$\bar{\Gamma}$ (μs^{-1})	$\Delta\bar{\Gamma}$ (μs^{-1})	M_2	$\Delta(M_2)$	R_{eff} (nm)
2	0.025	2	3	140	0.4706		331		1		454.98
2	0.025	2	4	40	0.6298		54		0		370.31
2	0.025	2	4	40	1.9594		51		559		388.91
2	0.025	2	4	40	1.3013		54		872		369.55
2	0.025	2	4	60	1.1646		118		5		360.23
2	0.025	2	4	60	1.7509		131		5450		324.96
2	0.025	2	4	60	0.5746		114		0		373.89
2	0.025	2	4	80	1.7625		204		14072		346.08
2	0.025	2	4	80	1.1646		206		12290		341.05
2	0.025	2	4	80	0.5858		185		1		380.37
2	0.025	2	4	100	1.6307		279		35636		357.92
2	0.025	2	4	100	0.5683		222		1		449.78
2	0.025	2	4	100	1.0969		273		36970		365.83
2	0.025	2	4	120	1.5048		353		50498		361.65

Continues on next page

Day	ϕ %	R	F	θ (°)	β	$\Delta\beta$	$\bar{\Gamma}$ (μs^{-1})	$\Delta\bar{\Gamma}$ (μs^{-1})	M_2	$\Delta(M_2)$	R_{eff} (nm)
2	0.025	2	4	120	0.9964		329		5		389.07
2	0.025	2	4	120	0.5012		362		37953		353.07
2	0.025	2	4	140	0.9202		363		59317		414.99
2	0.025	2	4	140	1.3844		365		65398		412.91
2	0.025	2	4	140	0.4750		338		55586		444.76
2	0.080	1	1	40	0.5622		143		1		139.58
2	0.080	1	1	40	1.7703		151		4476		132.23
2	0.080	1	1	40	1.1621		141		6		141.52
2	0.080	1	1	60	1.1681		316		27032		134.92
2	0.080	1	1	60	1.7862		305		25047		139.51
2	0.080	1	1	60	0.5786		291		0		146.23
2	0.080	1	1	80	1.7131		498		45812		141.35
2	0.080	1	1	80	1.1464		501		53461		140.69
2	0.080	1	1	80	0.5674		513		88914		137.33

Continues on next page

Day	ϕ %	R	F	θ (°)	β	$\Delta\beta$	$\bar{\Gamma}$ (μs^{-1})	$\Delta\bar{\Gamma}$ (μs^{-1})	M_2	$\Delta(M_2)$	R_{eff} (nm)
2	0.080	1	1	100	1.6365		681		94089		146.81
2	0.080	1	1	100	0.5478		676		103264		148.07
2	0.080	1	1	100							
2	0.080	1	1	120	1.5921		867		128921		147.37
2	0.080	1	1	120	1.0560		873		145580		146.36
2	0.080	1	1	120	0.5264		880		120834		145.26
2	0.080	1	1	140	1.0032		965		146527		155.97
2	0.080	1	1	140	1.5005		959		192750		156.97
2	0.080	1	1	140	0.5006		972		188431		154.78
2	0.080	1	2	40	0.6364		65		0		307.32
2	0.080	1	2	40	1.9605		64		0		311.18
2	0.080	1	2	40	1.3160		61		0		327.42
2	0.080	1	2	60	1.1748		132		6		323.29
2	0.080	1	2	60	1.7461		128		10		333.14

Continues on next page

Day	ϕ %	R	F	θ (°)	β	$\Delta\beta$	$\bar{\Gamma}$ (μs^{-1})	$\Delta\bar{\Gamma}$ (μs^{-1})	M_2	$\Delta(M_2)$	R_{eff} (nm)
2	0.080	1	2	60	0.6318		129		0		329.57
2	0.080	1	2	80	1.7028		222		18125		317.23
2	0.080	1	2	80	1.0982		223		13821		315.78
2	0.080	1	2	80	0.5483		210		0		335.32
2	0.080	1	2	100	1.5687		329		50293		303.7
2	0.080	1	2	100	0.5261		322		57200		310.2
2	0.080	1	2	100	1.0501		329		56769		303.72
2	0.080	1	2	120	1.5576		369		54669		346
2	0.080	1	2	120	1.0498		373		56596		342.71
2	0.080	1	2	120	0.5322		371		61384		344.34
2	0.080	1	2	140	0.9873		424		107536		355.19
2	0.080	1	2	140	1.4956		411		92064		365.88
2	0.080	1	2	140	0.4874		451		142777		333.41
2	0.080	1	3	40	0.5685		95		0		210.76

Continues on next page

Day	ϕ %	R	F	θ (°)	β	$\Delta\beta$	$\bar{\Gamma}$ (μs^{-1})	$\Delta\bar{\Gamma}$ (μs^{-1})	M_2	$\Delta(M_2)$	R_{eff} (nm)
2	0.080	1	3	40	1.8772		89		2354		224.98
2	0.080	1	3	40	1.2064		93		3387		215.1
2	0.080	1	3	60	1.1681		183		11		233.24
2	0.080	1	3	60	1.8278		193		12725		221.31
2	0.080	1	3	60	0.5762		199		1		213.89
2	0.080	1	3	80	1.7371		321		21611		219.67
2	0.080	1	3	80	1.1695		321		28065		219.17
2	0.080	1	3	80	0.5920		288		1		244.96
2	0.080	1	3	100	1.6145		428		45880		233.92
2	0.080	1	3	100	0.5337		429		41702		233.26
2	0.080	1	3	100	1.0797		397		10		251.69
2	0.080	1	3	120	1.6021		511		108250		250.24
2	0.080	1	3	120	1.0724		519		123484		246.12
2	0.080	1	3	120	0.5296		522		122565		245.04

Continues on next page

Day	ϕ %	R	F	θ (°)	β	$\Delta\beta$	$\bar{\Gamma}$ (μs^{-1})	$\Delta\bar{\Gamma}$ (μs^{-1})	M_2	$\Delta(M_2)$	R_{eff} (nm)
2	0.080	1	3	140	0.9707		558		168190		269.86
2	0.080	1	3	140	1.4457		563		161637		267.34
2	0.080	1	3	140	0.4953		539		148245		279.02
2	0.080	1	4	40	0.6118		32		0		614.17
2	0.080	1	4	40	1.8701		32		580		630.55
2	0.080	1	4	40	1.2598		30		468		666.18
2	0.080	1	4	60	1.4275		17		0		2437.59
2	0.080	1	4	60	2.0547		23		0		1855.01
2	0.080	1	4	60	0.8715		10		0		4236.86
2	0.080	1	4	80	1.6071		82		4117		859.56
2	0.080	1	4	80	1.1086		81		4341		865.2
2	0.080	1	4	80	0.5129		71		0		988.37
2	0.080	1	4	100	1.8234		35		1789		2867.81
2	0.080	1	4	100	0.5247		41		0		2452.2

Continues on next page

Day	ϕ %	R	F	θ (°)	β	$\Delta\beta$	$\bar{\Gamma}$ (μs^{-1})	$\Delta\bar{\Gamma}$ (μs^{-1})	M_2	$\Delta(M_2)$	R_{eff} (nm)
2	0.080	1	4	100	1.3637		9		0		11181.05
2	0.080	1	4	120	2.8724		10		194		12305.92
2	0.080	1	4	120	1.5318		19		637		6689.09
2	0.080	1	4	120	1.1029		8		134		15379.91
2	0.080	1	4	140	1.6004		7		111		20203.69
2	0.080	1	4	140	3.4749		5		46		32558.5
2	0.080	1	4	140	1.1263		5		59		27936.74
2	0.080	2	1	40	0.6140		33		0		599.84
2	0.080	2	1	40	1.8629		37		1		542.21
2	0.080	2	1	40	1.2770		37		163		546.22
2	0.080	2	1	60	1.2638		79		2507		538.16
2	0.080	2	1	60	1.8617		79		2086		541.36
2	0.080	2	1	60	0.6183		76		0		557.39
2	0.080	2	1	80	1.7195		120		4023		588.4

Continues on next page

Day	ϕ %	R	F	θ (°)	β	$\Delta\beta$	$\bar{\Gamma}$ (μs^{-1})	$\Delta\bar{\Gamma}$ (μs^{-1})	M_2	$\Delta(M_2)$	R_{eff} (nm)
2	0.080	2	1	80	1.1477		109		5		646.09
2	0.080	2	1	80	0.5801		103		0		685.46
2	0.080	2	1	100	1.6407		183		14893		546.49
2	0.080	2	1	100	0.5460		151		1		663.15
2	0.080	2	1	100	1.0921		183		17941		548.07
2	0.080	2	1	120	1.6180		221		21891		578.21
2	0.080	2	1	120	1.0905		221		23494		579.65
2	0.080	2	1	120	0.5642		169		1		759.01
2	0.080	2	1	140	1.0267		270		37613		557.92
2	0.080	2	1	140	1.5183		265		34757		568.97
2	0.080	2	1	140	0.5207		226		0		665.76
2	0.080	2	2	40	0.6404		36		0		549.69
2	0.080	2	2	40	1.9145		40		731		502.24
2	0.080	2	2	40	1.2901		41		948		485.63

Continues on next page

Day	ϕ %	R	F	θ (°)	β	$\Delta\beta$	$\bar{\Gamma}$ (μs^{-1})	$\Delta\bar{\Gamma}$ (μs^{-1})	M_2	$\Delta(M_2)$	R_{eff} (nm)
2	0.080	2	2	60	1.2304		65		240		651.64
2	0.080	2	2	60	1.8633		67		725		639.09
2	0.080	2	2	60	0.6275		65		0		657.85
2	0.080	2	2	80	1.7624		108		3489		651.29
2	0.080	2	2	80	1.1983		95		4		740.84
2	0.080	2	2	80	0.6019		103		0		684.18
2	0.080	2	2	100	1.6164		168		9764		596.71
2	0.080	2	2	100	0.5309		145		0		692.04
2	0.080	2	2	100	1.0493		154		4		649.36
2	0.080	2	2	120	1.6071		195		12070		654.51
2	0.080	2	2	120	1.0594		180		5		710.01
2	0.080	2	2	120	0.5263		174		1		734.19
2	0.080	2	2	140	1.0589		206		18473		732.46
2	0.080	2	2	140	1.5769		208		20775		722.4

Continues on next page

Day	ϕ %	R	F	θ (°)	β	$\Delta\beta$	$\bar{\Gamma}$ (μs^{-1})	$\Delta\bar{\Gamma}$ (μs^{-1})	M_2	$\Delta(M_2)$	R_{eff} (nm)
2	0.080	2	2	140	0.5314		167		1		903.73
2	0.080	2	3	40	0.6626		39		0		512.78
2	0.080	2	3	40	1.9080		39		0		507.12
2	0.080	2	3	40	1.2609		41		0		487.19
2	0.080	2	3	60	1.1811		68		3		623.61
2	0.080	2	3	60	1.7779		65		3		651.44
2	0.080	2	3	60	0.5887		67		0		632.44
2	0.080	2	3	80	1.7402		99		4305		712.89
2	0.080	2	3	80	1.1459		103		4443		681.64
2	0.080	2	3	80	0.6111		87		0		807.48
2	0.080	2	3	100	1.5972		140		6168		712.82
2	0.080	2	3	100	0.5470		134		4508		747.95
2	0.080	2	3	100	1.0967		130		5		769.91
2	0.080	2	3	120	1.5965		176		12700		724.87

Continues on next page

Day	ϕ %	R	F	θ (°)	β	$\Delta\beta$	$\bar{\Gamma}$ (μs^{-1})	$\Delta\bar{\Gamma}$ (μs^{-1})	M_2	$\Delta(M_2)$	R_{eff} (nm)
2	0.080	2	3	120	1.0560		155		5		827.28
2	0.080	2	3	120	0.5328		164		1		777.9
2	0.080	2	3	140	0.9790		160		3		942.93
2	0.080	2	3	140	1.4817		200		22329		754.5
2	0.080	2	3	140	0.4672		174		0		864.37
2	0.080	2	4	40	0.6787		48		0		417.02
2	0.080	2	4	40	2.0102		41		0		482.65
2	0.080	2	4	40	1.4274		43		0		467.16
2	0.080	2	4	60	1.2057		59		0		722.52
2	0.080	2	4	60	1.8338		56		2		758.13
2	0.080	2	4	60	0.5508		65		0		656.13
2	0.080	2	4	80	1.6237		88		2801		802.23
2	0.080	2	4	80	1.1220		74		3		947.07
2	0.080	2	4	80	0.5869		66		0		1068.91

Continues on next page

Day	ϕ %	R	F	θ (°)	β	$\Delta\beta$	$\bar{\Gamma}$ (μs^{-1})	$\Delta\bar{\Gamma}$ (μs^{-1})	M_2	$\Delta(M_2)$	R_{eff} (nm)
2	0.080	2	4	100	1.5235		118		1319		847.18
2	0.080	2	4	100	0.5266		112		0		891.55
2	0.080	2	4	100	1.0491		112		4		892.97
2	0.080	2	4	120	1.6274		138		6422		926.28
2	0.080	2	4	120	1.0943		128		5		996.42
2	0.080	2	4	120	0.5255		132		0		968.06
2	0.080	2	4	140	0.9426		142		2		1062.21
2	0.080	2	4	140	1.4627		158		9289		953.59
2	0.080	2	4	140	0.4855		141		0		1067.56
3	0.025	1	1	40	0.3573	0.0011	215	6	9668	3134	92.59
3	0.025	1	1	40	1.1377	0.0022	195	4	28422	2127	102.34
3	0.025	1	1	40	0.7466	0.0019	204	6	25166	3580	97.74
3	0.025	1	1	60	0.6855	0.0010	515	5	45435	6438	82.84
3	0.025	1	1	60	1.0258	0.0008	510	3	50739	3810	83.59

Continues on next page

Day	ϕ %	R	F	θ (°)	β	$\Delta\beta$	$\bar{\Gamma}$ (μs^{-1})	$\Delta\bar{\Gamma}$ (μs^{-1})	M_2	$\Delta(M_2)$	R_{eff} (nm)
3	0.025	1	1	60	0.3365	0.0007	522	8	14558	11351	81.69
3	0.025	1	1	80	1.0353	0.0011	876	5	202364	9706	80.43
3	0.025	1	1	80	0.6927	0.0007	873	6	211890	13674	80.74
3	0.025	1	1	80	0.3491	0.0011	872	14	166692	30072	80.78
3	0.025	1	1	100	1.0380	0.0007	1232	5	224977	15476	81.23
3	0.025	1	1	100	0.3433	0.0007	1223	15	264650	45853	81.82
3	0.025	1	1	100	0.6906	0.0012	1220	9	164330	25653	82.01
3	0.025	1	1	120	1.0263	0.0013	1619	8	390971	28709	79.01
3	0.025	1	1	120	0.6847	0.0007	1625	9	498514	35178	78.71
3	0.025	1	1	120	0.3478	0.0014	1609	25	644044	91355	79.47
3	0.025	1	1	140	0.6829	0.0012	1863	13	462991	51941	80.83
3	0.025	1	1	140	1.0155	0.0006	1882	6	523225	28506	80.01
3	0.025	1	1	140	0.3398	0.0006	1886	19	644344	88758	79.81
3	0.025	1	2	40	0.3623	0.0012	147	5	4079	1666	136.15

Continues on next page

Day	ϕ %	R	F	θ (°)	β	$\Delta\beta$	$\bar{\Gamma}$ (μs^{-1})	$\Delta\bar{\Gamma}$ (μs^{-1})	M_2	$\Delta(M_2)$	R_{eff} (nm)
3	0.025	1	2	60	0.3425	0.0009	350	7	4548	6415	121.96
3	0.025	1	2	80	0.3415	0.0008	658	10	53725	17005	107.01
3	0.025	1	2	100	0.3284	0.0006	978	12	174973	30605	102.33
3	0.025	1	2	120	0.3386	0.0006	1301	15	434328	48476	98.31
3	0.025	1	2	140	0.3217	0.0005	1554	16	539102	62006	96.88
3	0.025	1	3	40							
3	0.025	1	3	60	0.3404	0.0009	344	7	8564	6026	123.84
3	0.025	1	3	80	0.3469	0.0008	587	10	50896	14330	120.08
3	0.025	1	3	100	0.3314	0.0006	923	12	135345	28144	108.41
3	0.025	1	3	120	0.3296	0.0006	1203	14	195202	42346	106.31
3	0.025	1	3	140	0.3326	0.0006	1353	15	412641	51874	111.26
3	0.025	1	4	40	0.3187	0.0012	143	4	6092	1664	139.87
3	0.025	1	4	60	0.3451	0.0010	299	7	15111	5182	142.73
3	0.025	1	4	80	0.3448	0.0008	547	10	133833	13969	128.77

Continues on next page

Day	ϕ %	R	F	θ (°)	β	$\Delta\beta$	$\bar{\Gamma}$ (μs^{-1})	$\Delta\bar{\Gamma}$ (μs^{-1})	M_2	$\Delta(M_2)$	R_{eff} (nm)
3	0.025	1	4	100							
3	0.025	1	4	120	0.3232	0.0006	1097	13	333608	37515	116.58
3	0.025	1	4	140	0.3216	0.0005	1285	14	642802	48949	117.14
3	0.025	2	1	40	0.3365	0.0010	237	7	26545	4159	84.06
3	0.025	2	1	60	0.3366	0.0008	562	10	68160	13587	75.8
3	0.025	2	1	80	0.3183	0.0006	920	11	58662	26663	76.61
3	0.025	2	1	100	0.3211	0.0005	1357	15	247737	50744	73.77
3	0.025	2	1	120	0.3274	0.0005	1701	17	167724	71515	75.17
3	0.025	2	1	140	0.3220	0.0005	2017	18	530783	91590	74.66
3	0.025	2	2	40	0.3337	0.0011	206	6	13692	2969	96.79
3	0.025	2	2	60	0.3449	0.0009	420	8	19942	8279	101.41
3	0.025	2	2	80	0.3495	0.0009	702	11	27310	18612	100.37
3	0.025	2	2	100	0.3380	0.0006	1097	13	233645	36976	91.22
3	0.025	2	2	120	0.3295	0.0006	1458	16	265663	56579	87.7

Continues on next page

Day	ϕ %	R	F	θ (°)	β	$\Delta\beta$	$\bar{\Gamma}$ (μs^{-1})	$\Delta\bar{\Gamma}$ (μs^{-1})	M_2	$\Delta(M_2)$	R_{eff} (nm)
3	0.025	2	2	140	0.3332	0.0006	1721	17	445967	73901	87.52
3	0.025	2	3	40	0.3538	0.0013	160	5	13156	2228	124.47
3	0.025	2	3	60	0.3441	0.0008	348	4	0	1194	122.4
3	0.025	2	3	80	0.3352	0.0007	644	10	64903	16203	109.38
3	0.025	2	3	100							
3	0.025	2	3	120	0.3404	0.0007	1311	15	361725	49856	97.54
3	0.025	2	3	140	0.3381	0.0006	1544	17	751586	65327	97.51
3	0.025	2	4	40	0.3174	0.0011	150	5	7262	1870	133.08
3	0.025	2	4	60	0.3378	0.0009	308	7	16351	5173	138.4
3	0.025	2	4	80	0.3480	0.0008	581	9	17668	13411	121.38
3	0.025	2	4	100	0.3393	0.0007	892	12	128787	27500	112.14
3	0.025	2	4	120	0.3372	0.0007	1253	16	370770	48068	102.12
3	0.025	2	4	140	0.3372	0.0007	1400	17	817757	61799	107.55
3	0.080	1	1	40	0.3351	0.0011	171	5	7910	2165	116.42

Continues on next page

Day	ϕ %	R	F	θ (°)	β	$\Delta\beta$	$\bar{\Gamma}$ (μs^{-1})	$\Delta\bar{\Gamma}$ (μs^{-1})	M_2	$\Delta(M_2)$	R_{eff} (nm)
3	0.080	1	1	60	0.3542	0.0010	386	8	46833	7943	110.55
3	0.080	1	1	80							
3	0.080	1	1	100	0.3357	0.0007	977	13	194985	32043	102.42
3	0.080	1	1	120	0.3436	0.0007	1228	15	407203	46594	104.19
3	0.080	1	1	140	0.3396	0.0006	1411	16	581269	57779	106.73
3	0.080	1	2	40	0.3556	0.0014	35	14	0	738	574.2
3	0.080	1	2	60	0.3378	0.0002	64	3	1	0	669.3
3	0.080	1	2	80	0.3554	0.0013	193	7	26453	4099	365.9
3	0.080	1	2	100	0.3286	0.0010	258	8	50860	6351	388.52
3	0.080	1	2	120	0.3452	0.0011	293	8	62623	7055	436.57
3	0.080	1	2	140	0.3341	0.0012	336	9	97699	9543	448.11
3	0.080	1	3	40	0.3199	0.0011	141	4	203	2740	141.05
3	0.080	1	3	60	0.3327	0.0009	325	7	17493	5654	131.07
3	0.080	1	3	80	0.3416	0.0007	553	9	34775	12303	127.37

Continues on next page

Day	ϕ %	R	F	θ (°)	β	$\Delta\beta$	$\bar{\Gamma}$ (μs^{-1})	$\Delta\bar{\Gamma}$ (μs^{-1})	M_2	$\Delta(M_2)$	R_{eff} (nm)
3	0.080	1	3	100	0.3406	0.0007	878	12	181099	26773	114.03
3	0.080	1	3	120	0.3428	0.0007	1191	15	438706	44774	107.42
3	0.080	1	3	140	0.3317	0.0006	1344	16	599528	53759	112.08
3	0.080	1	4	40	0.3400	0.0013	135	4	286	1819	147.82
3	0.080	1	4	60	0.3420	0.0009	295	3	0	3872	144.71
3	0.080	1	4	80	0.3422	0.0009	530	9	46147	12096	133.02
3	0.080	1	4	100	0.3386	0.0007	842	12	122488	24405	118.87
3	0.080	1	4	120	0.3368	0.0007	1130	14	176740	39597	113.17
3	0.080	1	4	140	0.3298	0.0006	1292	16	573854	51373	116.57
3	0.080	2	1	40	0.3292	0.0011	167	5	12436	2202	119.66
3	0.080	2	1	60	0.3529	0.0010	396	8	73919	8549	107.68
3	0.080	2	1	80	0.3412	0.0007	673	10	124525	17669	104.77
3	0.080	2	1	100	0.3280	0.0006	941	12	181493	29535	106.41
3	0.080	2	1	120	0.3295	0.0006	1241	15	427816	46203	103.12

Continues on next page

Day	ϕ %	R	F	θ (°)	β	$\Delta\beta$	$\bar{\Gamma}$ (μs^{-1})	$\Delta\bar{\Gamma}$ (μs^{-1})	M_2	$\Delta(M_2)$	R_{eff} (nm)
3	0.080	2	1	140	0.3321	0.0006	1439	16	853207	60239	104.69
3	0.080	2	2	40	0.3271	0.0014	94	4	691	842	212.95
3	0.080	2	2	60	0.3292	0.0011	206	5	8986	2893	207.34
3	0.080	2	2	80	0.3464	0.0010	345	7	35467	6487	204.52
3	0.080	2	2	100	0.3376	0.0010	472	9	51202	10755	212.23
3	0.080	2	2	120	0.3349	0.0008	558	10	80081	13647	229.33
3	0.080	2	2	140	0.3265	0.0007	659	11	180388	19027	228.4
3	0.080	2	3	40	0.3475	0.0013	117	4	1958	1200	170.44
3	0.080	2	3	60	0.3294	0.0011	284	7	26729	4933	150.34
3	0.080	2	3	80	0.3488	0.0009	455	9	67969	10381	154.82
3	0.080	2	3	100	0.3478	0.0009	651	11	189567	18897	153.66
3	0.080	2	3	120	0.3402	0.0007	904	13	264998	29272	141.45
3	0.080	2	3	140	0.3327	0.0007	999	13	403090	34761	150.73
3	0.080	2	4	40	0.3852	0.0010	21	6	0	14	953.49

Continues on next page

Day	ϕ %	R	F	θ (°)	β	$\Delta\beta$	$\bar{\Gamma}$ (μs^{-1})	$\Delta\bar{\Gamma}$ (μs^{-1})	M_2	$\Delta(M_2)$	R_{eff} (nm)
3	0.080	2	4	60	0.3374	0.0006	45	8	0	19	953.69
3	0.080	2	4	80	0.3301	0.0014	99	4	2708	1027	714.65
3	0.080	2	4	100	0.3149	0.0012	149	5	10101	1948	672.33
3	0.080	2	4	120	0.3295	0.0012	164	6	16934	2533	781.73
3	0.080	2	4	140	0.3217	0.0010	182	5	1029	2275	825.94
4	0.025	1	1	40	0.3489	0.0012	181	5	12894	2540	109.89
4	0.025	1	1	60	0.3123	0.0008	414	8	78216	9330	102.99
4	0.025	1	1	80	0.3229	0.0007	861	12	198192	26738	81.79
4	0.025	1	1	100	0.3222	0.0007	1192	15	245336	44414	83.91
4	0.025	1	1	120	0.3266	0.0007	1530	18	572504	66881	83.56
4	0.025	1	1	140	0.3274	0.0006	1863	9	999999	213362	80.76
4	0.025	1	2	40							
4	0.025	1	2	60	0.3293	0.0009	328	7	39440	6095	129.9
4	0.025	1	2	80	0.3351	0.0009	535	11	155857	15160	131.54

Continues on next page

Day	ϕ %	R	F	θ (°)	β	$\Delta\beta$	$\bar{\Gamma}$ (μs^{-1})	$\Delta\bar{\Gamma}$ (μs^{-1})	M_2	$\Delta(M_2)$	R_{eff} (nm)
4	0.025	1	2	100	0.3260	0.0008	930	13	309945	31359	107.6
4	0.025	1	2	120	0.3271	0.0007	1113	15	650452	45188	114.83
4	0.025	1	2	140	0.3250	0.0007	1292	16	995731	169523	116.45
4	0.025	1	4	40	0.3500	0.0002	83	4	2	2	240.71
4	0.025	1	4	60	0.3553	0.0011	221	3	0	600	193.01
4	0.025	1	4	80	0.3529	0.0009	378	7	3558	7007	186.55
4	0.025	1	4	100	0.3336	0.0007	546	9	55922	12488	183.24
4	0.025	1	4	120	0.3238	0.0007	792	11	131339	22893	161.32
4	0.025	1	4	140	0.3325	0.0007	849	12	273222	26927	177.25
4	0.025	2	1	40	0.3194	0.0010	196	5	15532	2819	101.53
4	0.025	2	1	60	0.3253	0.0007	488	8	60923	10717	87.26
4	0.025	2	1	80	0.3310	0.0007	849	12	131290	25388	82.93
4	0.025	2	1	100	0.3280	0.0007	1214	15	325789	45423	82.37
4	0.025	2	1	120	0.3181	0.0007	1585	18	334243	69407	80.68

Continues on next page

Day	ϕ %	R	F	θ (°)	β	$\Delta\beta$	$\bar{\Gamma}$ (μs^{-1})	$\Delta\bar{\Gamma}$ (μs^{-1})	M_2	$\Delta(M_2)$	R_{eff} (nm)
4	0.025	2	1	140	0.3219	0.0006	1950	20	739060	93798	77.19
4	0.025	2	2	40	0.3258	0.0013	122	5	5721	1483	163.28
4	0.025	2	2	60	0.3211	0.0010	251	6	16775	4001	169.95
4	0.025	2	2	80	0.3500	0.0010	440	9	48253	9684	159.92
4	0.025	2	2	100							
4	0.025	2	2	120	0.3295	0.0007	866	12	152911	25562	147.67
4	0.025	2	2	140	0.3294	0.0006	992	13	295451	32912	151.75
4	0.025	2	3	40	0.3479	0.0022	41	2	891	276	490.43
4	0.025	2	3	60	0.3433	0.0002	80	4	2	1	532.62
4	0.025	2	3	80							
4	0.025	2	3	100	0.3406	0.0010	213	6	7208	3118	468.8
4	0.025	2	3	120	0.3238	0.0010	293	7	40678	5748	436.18
4	0.025	2	3	140	0.3582	0.0011	264	7	36009	5228	570.56
4	0.025	2	4	40	0.3711	0.0022	37	1	0	310	538.32

Continues on next page

Day	ϕ %	R	F	θ (°)	β	$\Delta\beta$	$\bar{\Gamma}$ (μs^{-1})	$\Delta\bar{\Gamma}$ (μs^{-1})	M_2	$\Delta(M_2)$	R_{eff} (nm)
4	0.025	2	4	60	0.3282	0.0013	101	4	769	950	422.37
4	0.025	2	4	80	0.3580	0.0013	173	5	10854	2409	407.85
4	0.025	2	4	100	0.3191	0.0010	234	6	17445	3656	428.1
4	0.025	2	4	120	0.3287	0.0010	285	7	40918	5625	449.1
4	0.025	2	4	140	0.3172	0.0009	375	9	94624	9568	401.42
4	0.080	1	2	40	0.3373	0.0011	174	5	6371	2216	114.8
4	0.080	1	2	60	0.3516	0.0010	363	4	0	4458	117.51
4	0.080	1	2	80	0.3437	0.0008	685	10	90957	17975	102.88
4	0.080	1	2	100							
4	0.080	1	2	120	0.3263	0.0005	1383	15	503944	53566	92.45
4	0.080	1	2	140	0.3312	0.0005	1541	16	459447	61371	97.72
4	0.080	1	3	40	0.3507	0.0008	53	14	1	315	377.04
4	0.080	1	3	60							
4	0.080	1	3	80							

Continues on next page

Day	ϕ %	R	F	θ (°)	β	$\Delta\beta$	$\bar{\Gamma}$ (μs^{-1})	$\Delta\bar{\Gamma}$ (μs^{-1})	M_2	$\Delta(M_2)$	R_{eff} (nm)
4	0.080	1	3	100	0.3275	0.0009	326	7	35998	6150	307.11
4	0.080	1	3	120							
4	0.080	1	3	140	0.3204	0.0009	513	10	104351	13654	293.29
4	0.080	1	4	40	0.3524	0.0018	57	3	436	393	352.66
4	0.080	1	4	60	0.3628	0.0016	109	4	5349	1211	389.58
4	0.080	1	4	80	0.3432	0.0011	203	6	11508	2981	347.6
4	0.080	1	4	100							
4	0.080	1	4	120	0.3476	0.0010	386	8	74074	8593	331.27
4	0.080	1	4	140	0.3322	0.0009	449	9	112646	11465	335.27
4	0.080	2	1	40	0.3302	0.0014	125	4	4691	1411	159.25
4	0.080	2	1	60	0.3560	0.0011	269	7	44319	5238	158.34
4	0.080	2	1	80							
4	0.080	2	1	100	0.3320	0.0007	747	12	250359	23484	133.95
4	0.080	2	1	120	0.3225	0.0006	972	14	422019	34760	131.61

Continues on next page

Day	ϕ %	R	F	θ (°)	β	$\Delta\beta$	$\bar{\Gamma}$ (μs^{-1})	$\Delta\bar{\Gamma}$ (μs^{-1})	M_2	$\Delta(M_2)$	R_{eff} (nm)
4	0.080	2	1	140	0.3308	0.0006	1183	15	690402	47705	127.25
4	0.080	2	2	40	0.3534	0.0012	154	5	1726	1953	129.44
4	0.080	2	2	60							
4	0.080	2	2	80	0.3356	0.0008	640	10	97104	16469	110.01
4	0.080	2	2	100	0.3414	0.0008	932	13	203566	30579	107.39
4	0.080	2	2	120	0.3466	0.0008	1172	15	256638	43488	109.13
4	0.080	2	2	140	0.3461	0.0007	1317	16	60484	50189	114.36
4	0.080	2	3	40	0.3470	0.0012	144	4	1832	1629	138.44
4	0.080	2	3	60	0.3446	0.0010	345	7	9954	6268	123.49
4	0.080	2	3	80	0.3387	0.0007	609	9	6969	14060	115.69
4	0.080	2	3	100	0.3480	0.0008	959	13	191240	31140	104.38
4	0.080	2	3	120	0.3541	0.0008	1208	15	185756	44390	105.9
4	0.080	2	3	140	0.3424	0.0008	1454	17	231007	60499	103.53
4	0.080	2	4	40	0.3635	0.0014	138	5	5081	1637	144.31

Continues on next page

Day	ϕ %	R	F	θ (°)	β	$\Delta\beta$	$\bar{\Gamma}$ (μs^{-1})	$\Delta\bar{\Gamma}$ (μs^{-1})	M_2	$\Delta(M_2)$	R_{eff} (nm)
4	0.080	2	4	60	0.3416	0.0008	347	7	1168	8116	122.88
4	0.080	2	4	80	0.3417	0.0008	655	10	63647	16776	107.61
4	0.080	2	4	100	0.3418	0.0007	979	13	176575	31532	102.24
4	0.080	2	4	120	0.3392	0.0007	1336	15	220803	50220	95.76
4	0.080	2	4	140	0.3367	0.0006	1616	18	836421	71984	93.2
5	0.025	1	1	40	0.3123	0.0010	240	6	6669	3513	82.83
5	0.025	1	1	60	0.3197	0.0009	619	10	78310	16310	68.57
5	0.025	1	1	80	0.3178	0.0009	1031	16	274168	38642	68.05
5	0.025	1	1	100	0.3171	0.0010	1473	20	461070	68199	67.69
5	0.025	1	1	120	0.3104	0.0011	1981	27	382245	116743	64.32
5	0.025	1	1	140	0.3007	0.0007	2161	11	1000000	13360	69.43
5	0.025	1	2	40	0.3397	0.0012	149	5	6634	1801	133.12
5	0.025	1	2	60	0.3482	0.0010	370	8	35052	7339	114.75
5	0.025	1	2	80	0.3439	0.0007	628	10	60150	16097	111.76

Continues on next page

Day	ϕ %	R	F	θ (°)	β	$\Delta\beta$	$\bar{\Gamma}$ (μs^{-1})	$\Delta\bar{\Gamma}$ (μs^{-1})	M_2	$\Delta(M_2)$	R_{eff} (nm)
5	0.025	1	2	100	0.3410	0.0007	948	13	195136	30482	105.13
5	0.025	1	2	120	0.3292	0.0007	1318	16	429252	52411	96.66
5	0.025	1	2	140	0.3395	0.0007	1467	17	535492	61284	102.29
5	0.025	1	3	40	0.3414	0.0011	152	4	4882	1803	131.06
5	0.025	1	3	60	0.3440	0.0009	370	7	22247	7057	114.88
5	0.025	1	3	80	0.3225	0.0006	606	5	0	12947	115.94
5	0.025	1	3	100	0.3208	0.0006	933	12	157600	28494	106.89
5	0.025	1	3	120	0.3265	0.0006	1153	14	444648	42623	110.49
5	0.025	1	3	140	0.3180	0.0005	1384	15	207950	50620	108.4
5	0.025	1	4	40	0.3538	0.0013	114	2	0	298	174.77
5	0.025	1	4	60	0.3359	0.0009	295	7	19378	4972	144.02
5	0.025	1	4	80	0.3477	0.0009	486	9	27380	10658	144.6
5	0.025	1	4	100							
5	0.025	1	4	120	0.3373	0.0007	943	13	59500	28721	135.22

Continues on next page

Day	ϕ %	R	F	θ (°)	β	$\Delta\beta$	$\bar{\Gamma}$ (μs^{-1})	$\Delta\bar{\Gamma}$ (μs^{-1})	M_2	$\Delta(M_2)$	R_{eff} (nm)
5	0.025	1	4	140	0.3351	0.0007	1160	15	380427	42895	129.42
5	0.025	2	1	40							
5	0.025	2	1	60	0.3197	0.0008	519	9	92051	12474	81.93
5	0.025	2	1	80							
5	0.025	2	1	100	0.3275	0.0007	1304	16	439645	51714	76.5
5	0.025	2	1	120	0.3327	0.0008	1679	20	831588	79990	75.92
5	0.025	2	1	140	0.3219	0.0006	1994	9	1000000	56434	75.29
5	0.025	2	2	40	0.3240	0.0012	121	2	0	544	163.76
5	0.025	2	2	60	0.3554	0.0011	283	7	26314	4952	150.06
5	0.025	2	2	80	0.3341	0.0007	520	9	39335	11718	134.96
5	0.025	2	2	100	0.3415	0.0007	774	6	0	6403	128.82
5	0.025	2	2	120	0.3388	0.0008	939	13	203956	30724	135.77
5	0.025	2	2	140	0.3380	0.0007	1065	14	275140	36616	140.97
5	0.025	2	3	40	0.3287	0.0011	169	2	0	425	117.58

Continues on next page

Day	ϕ %	R	F	θ (°)	β	$\Delta\beta$	$\bar{\Gamma}$ (μs^{-1})	$\Delta\bar{\Gamma}$ (μs^{-1})	M_2	$\Delta(M_2)$	R_{eff} (nm)
5	0.025	2	3	60	0.3355	0.0008	385	7	12945	7396	110.38
5	0.025	2	3	80	0.3502	0.0008	647	10	22990	16708	108.64
5	0.025	2	3	100							
5	0.025	2	3	120	0.3157	0.0005	1364	15	370194	50327	93.48
5	0.025	2	3	140	0.3152	0.0005	1641	16	513875	67511	91.5
5	0.025	2	4	40	0.3589	0.0002	67	3	1	1	298.24
5	0.025	2	4	60	0.3799	0.0024	128	3	8545	1760	333.28
5	0.025	2	4	80							
5	0.025	2	4	100	0.3530	0.0010	326	7	24746	5870	306.03
5	0.025	2	4	120	0.3360	0.0009	454	9	71797	10481	280.81
5	0.025	2	4	140	0.3457	0.0009	584	11	171995	16606	257.1
5	0.080	1	1	40	0.3047	0.0002	82	4	1	1	243.56
5	0.080	1	1	60							
5	0.080	1	1	80	0.0285	0.0000	3	0	11	0	23606.23

Continues on next page

Day	ϕ %	R	F	θ (°)	β	$\Delta\beta$	$\bar{\Gamma}$ (μs^{-1})	$\Delta\bar{\Gamma}$ (μs^{-1})	M_2	$\Delta(M_2)$	R_{eff} (nm)
5	0.080	1	1	100	0.3227	0.0009	785	13	348707	28085	127.08
5	0.080	1	1	120	0.0337	0.0000	2	0	8	0	62995.41
5	0.080	1	1	140	0.3224	0.0008	1142	17	921830	53199	131.53
5	0.080	1	2	40	0.3435	0.0011	219	5	5844	3187	90.65
5	0.080	1	2	60	0.3288	0.0007	492	8	56839	10842	86.37
5	0.080	1	2	80	0.0086	0.0000	1	0	3	0	49023.26
5	0.080	1	2	100	0.3357	0.0006	1287	15	340718	48233	77.56
5	0.080	1	2	120	0.3345	0.0006	1626	17	352822	68874	78.46
5	0.080	1	2	140	0.3380	0.0006	1872	18	614635	85082	80.25
5	0.080	1	3	40	0.3462	0.0015	102	4	897	1054	195.33
5	0.080	1	3	60	0.3532	0.0011	264	6	19748	4319	161.19
5	0.080	1	3	80	0.3337	0.0008	437	8	62925	9510	160.71
5	0.080	1	3	100	0.3421	0.0008	640	10	69498	16130	155.92
5	0.080	1	3	120	0.3395	0.0008	856	13	186159	26852	149.11

Continues on next page

Day	ϕ %	R	F	θ (°)	β	$\Delta\beta$	$\bar{\Gamma}$ (μs^{-1})	$\Delta\bar{\Gamma}$ (μs^{-1})	M_2	$\Delta(M_2)$	R_{eff} (nm)
5	0.080	1	3	140	0.3409	0.0007	1009	14	409163	36441	148.93
5	0.080	1	4	40	0.3311	0.0001	66	3	1	0	301.84
5	0.080	1	4	60	0.3770	0.0018	159	7	18145	3359	267
5	0.080	1	4	80	0.3355	0.0011	315	9	76724	8394	223.38
5	0.080	1	4	100	0.3388	0.0009	518	10	179563	14876	192.63
5	0.080	1	4	120	0.3378	0.0008	647	12	233482	21151	197.24
5	0.080	1	4	140	0.3322	0.0008	759	12	345407	25686	198
5	0.080	2	1	40	0.3404	0.0011	220	6	12526	3182	90.36
5	0.080	2	1	60	0.3340	0.0007	496	8	44154	10938	85.75
5	0.080	2	1	80	0.3299	0.0007	857	12	110752	25301	82.05
5	0.080	2	1	100	0.3421	0.0007	1157	14	237710	41706	86.37
5	0.080	2	1	120	0.3387	0.0007	1414	16	43475	54342	90.29
5	0.080	2	1	140	0.3348	0.0006	1718	18	649951	75683	87.51
5	0.080	2	2	40	0.3520	0.0012	148	5	3792	1708	134.23

Continues on next page

Day	ϕ %	R	F	θ (°)	β	$\Delta\beta$	$\bar{\Gamma}$ (μs^{-1})	$\Delta\bar{\Gamma}$ (μs^{-1})	M_2	$\Delta(M_2)$	R_{eff} (nm)
5	0.080	2	2	60	0.3471	0.0010	370	8	30654	7352	115.13
5	0.080	2	2	80	0.3317	0.0007	661	10	102196	17322	106.46
5	0.080	2	2	100	0.3435	0.0008	922	13	40044	28886	108.41
5	0.080	2	2	120	0.3260	0.0005	1196	13	209269	41313	106.78
5	0.080	2	2	140	0.3367	0.0007	1429	17	454047	58858	105.22
5	0.080	2	3	40	0.3388	0.0014	100	4	1188	1038	198.5
5	0.080	2	3	60	0.3366	0.0011	231	6	13222	3534	183.87
5	0.080	2	3	80	0.3350	0.0008	398	8	40285	7928	176.68
5	0.080	2	3	100	0.3425	0.0008	552	9	59552	12812	180.89
5	0.080	2	3	120	0.3505	0.0008	686	11	92165	18352	186.19
5	0.080	2	3	140	0.3422	0.0008	797	12	143895	23502	188.72
5	0.080	2	4	40	0.3399	0.0003	60	5	1	1	332.53
5	0.080	2	4	60	0.3518	0.0013	145	5	12164	2122	294.07
5	0.080	2	4	80	0.3187	0.0010	262	6	41313	4755	269.01

Continues on next page

Day	ϕ %	R	F	θ (°)	β	$\Delta\beta$	$\bar{\Gamma}$ (μs^{-1})	$\Delta\bar{\Gamma}$ (μs^{-1})	M_2	$\Delta(M_2)$	R_{eff} (nm)
5	0.080	2	4	100	0.3341	0.0010	344	8	59696	7415	290.9
5	0.080	2	4	120	0.3472	0.0010	406	9	96979	10361	314.67
5	0.080	2	4	140	0.3448	0.0010	482	10	122390	13499	312.05

Appendix B

Tables of Sedimentation Velocities

pH	ϕ	v_A µm s^{-1}	v_B µm s^{-1}	τ_{AB} s	h_{AB} mm	h_0 mm	h_f mm	ϕ_f %
3.1	0.8 %	22.3	25.6	250	29.1	31.8	10.8	2.43
		22.8	27.7	320	28.3	32.8	10.7	2.52
		22.3	31.5	240	29.4	32.0	10.8	2.43
		23.8	29.4	280	27.8	31.3	11.1	2.29
		23.2	23.7	440	25.9	33.7	11.4	2.41
		21.4	34.3	290	30.1	34.0	11.6	2.38
	μ	22.6	29	300	28.4	32.6	11.1	2.41
	σ	0.8	4	70	1.5	1.1	0.4	0.07
	2.5 % [a]	1.3	1.22	2300	32.5	34.1	24.3	3.54
		1.39	1.27	2400	32.1	33.7	24.4	3.47
		1.57	1.43	1900	33.5	35.4	24.7	3.59
		1.37	1.26	2500	33.7	35.4	26.0	3.42
		1.46	1.35	2100	33.6	35.2	25.3	3.49
		1.57	1.43	2300	33.1	34.9	25.4	3.45
	μ	1.44	1.33	2300	33.1	34.8	25.0	3.49
	σ	0.11	0.09	200	0.6	0.7	0.7	0.06

pH	ϕ	v_A µm s^{-1}	v_B µm s^{-1}	τ_{AB} s	h_{AB} mm	h_0 mm	h_f mm	ϕ_f %
3.5	0.8 %	29.3	25	320	26.9	32.3	11.0	2.38
		20.7	32.2	310	30.4	34.2	11.8	2.34
		31.4	28.1	330	27.1	32.8	11.3	2.35
		26.6	19.5	430	24.8	32.2	11.3	2.32
		21.5	26.7	370	28.5	34.0	11.7	2.36
	μ	26	26	350	28	33.1	11.4	2.35
	σ	5	5	50	2	0.9	0.3	0.02
	2.5 % [a]	1.44	1.34	2200	33.9	35.3		
		1.39	1.24	2400	32.9	34.2		
		1.48	1.38	2100	33.5	35.0		
		1.32	1.18	2700	32.3	33.7		
		1.42	1.32	2200	34.1	35.5		
		1.44	1.28	2500	32.9	34.2		
	μ	1.41	1.29	2300	33.3	34.7		
	σ	0.06	0.07	200	0.7	0.7		

pH	ϕ	v_A µm s^{-1}	v_B µm s^{-1}	τ_{AB} s	h_{AB} mm	h_0 mm	h_f mm	ϕ_f %
4.5	0.25 %	288	441	58	38.6	45.5		
		173	315	50	42.9	46.7		
		215	388	48	40.8	44.1		
		228	343	51	36.3	39.5		
	μ	230	370	52	40	44		
	σ	50	60	4	3	3		
	0.6 %	53.5	65.4	150	29.8	33.0	9.6	2.22
		36.2	42.3	97	33.7	35.3	10.3	2.20
		45.2	51.4	120	31.6	33.6	9.7	2.22
		42.6	66.9	140	31.6	35.1	9.8	2.30
		51.2	73.6	170	30.3	35.6	10.3	2.21
		37.8	42.2	82	34.2	35.5	10.3	2.22
	μ	44	60	130	32	34.7	10.0	2.23
	σ	7	14	30	2	1.1	0.3	0.04
	0.8 %	23.6	16.7	490	25.1	33.9	11.6	2.39
		24.7	18.6	480	25.3	34.0	12.0	2.31
		21.9	17.1	480	26.0	34.0	11.7	2.37
		23.3	16.3	500	24.9	33.6	11.8	2.33
		20.5	15.8	560	24.1	35.8	11.8	2.47
	μ	22.8	16.9	500	25.1	34.2	11.8	2.37
	σ	1.6	1.0	40	0.7	0.9	0.2	0.06
	1.2 %	8.95	9.49	570	32.1	35.4	16.1	2.62
		9.01	8.79	320	32.6	33.6	15.2	2.63
		10.1	9.45	410	32.9	35.1	15.5	2.69
		9.45	8.65	560	31.3	34.5	15.0	2.74
		9.63	7.95	560	32.7	35.5	16.1	2.62
		9.15	8.09	420	33.8	35.0	15.5	2.69
	μ	9.4	8.7	470	32.6	34.8	15.6	2.67
	σ	0.4	0.7	110	0.8	0.7	0.5	0.05

Table continues on next page...

Continued...

pH	ϕ	v_A µm s^{-1}	v_B µm s^{-1}	τ_{AB} s	h_{AB} mm	h_0 mm	h_f mm	ϕ_f %
	1.7 % [a]	4.89	5.77	440	34.8	35.5		
		4.17	3.85	890	32.5	34.5		
		2.78	4.43	550	34.0	34.6		
		4.72	4.57	720	31.7	33.4		
		3.1	4.04	580	34.7	35.2		
		3.95	3.69	920[b]	32.8	34.5		
	μ	3.9	4.4	680	33.4	34.6		
	σ	0.9	0.8	190	1.3	0.8		
	2.5 %	1.38	1.2	2400	29.1	30.7	22.5	3.42
		1.39	1.2	2700	31.5	33.7	24.5	3.45
		1.42	1.23	2600	32.7	34.6	25.1	3.44
		1.3	1.07	3000	30.5	32.4	24.5	3.30
		1.44	1.23	2600	32.0	34.1	24.7	3.47
		1.3	1.11	2900	31.3	33.0	24.8	3.34
	μ	1.37	1.17	2700	31.2	33.1	24.4	3.40
	σ	0.06	0.07	200	1.2	1.4	0.9	0.06
	3.2 %	0.62	0.44	4.85	33.4	34.9	29.4	3.82
		0.57	0.39	5.92	34.5	36.6	30.9	3.80
		0.50	0.34	5.67	32.5	33.9	33.9	
		0.53	0.36	6.36	32.7	35.0	29.7	3.79
		0.67	0.51	4.21	33.5	35.6	29.5	3.87
	μ	0.58	0.41	5.4	33.3	35.2	30.7	3.82
	σ	0.07	0.07	0.9	0.8	1.0	1.9	0.04

[a] Determination of v_B relies on adequate sampling of the sedimentation velocity for long times. For these data, due to a short window of data being available and/or extremely slow sedimentation velocities, the accuracy with which the end of the initial velocity period can be determined is low. As such values for τ_{AB} and v_B should be treated with caution for these samples.

[b] The time after sonication had to be estimated from the loading completion time for this sample. Therefore τ_{AB}, which depends on an absolute time scale, may be incorrect for this sample.

Table continues on next page...

Continued...

pH	ϕ	v_A µm s^{-1}	v_B µm s^{-1}	τ_{AB} s	h_{AB} mm	h_0 mm	h_f mm	ϕ_f %
	3.9 %	0.14	0.12	11 000	34.1	35.0	32.9	4.14
		0.19	0.1	9800	32.7	33.9	31.6	4.18
		0.18	0.13	9500	34.7	35.6	33.3	4.17
		0.06	0.04	16 000	34.6	35.4	34.0	4.05
		0.13	0.08	13 000	34.2	35.1	33.1	4.14
		0.22	0.14	9300	36.1	37.1	34.5	4.19
	μ	0.15	0.10	12 000	34.4	35.4	33.2	4.14
	σ	0.06	0.04	3000	1.1	1.1	1.0	0.05
	4.3 %	0.06	0.02	19.2	34.2	35.2	33.5	4.53

Appendix C

Code Listings

This appendix lists the ImageJ plugin code, written in the Java programming language, used to perform edge detection on images and OCR on stopwatch 7 segment displays.

C.1 Edge_Detector.java

```
import ij.*;
import ij.process.*;
import ij.gui.*;
import java.awt.*;
import ij.plugin.filter.*;
import java.util.Vector;
import ij.plugin.frame.RoiManager;
import java.awt.event.*;
import ij.measure.ResultsTable;
import java.util.Comparator;
import java.util.Collections;

// This ImageJ plugin sums pixel values row-wise and attempts to find maxima in
    the resulting profile
public class Edge_Detector implements PlugInFilter {
        ImagePlus imp;
        long threshold;
        long toSeek;

        // This method is run as soon as the user runs the plugin
        public int setup(String arg, ImagePlus imp) {
                this.imp = imp;
                ImageStack is = imp.getImageStack();
                ImageProcessor ip = is.getProcessor(imp.getCurrentSlice());
```

```
Rectangle roi = imp.getRoi().getBounds();

double[] xs = new double[roi.height];
double[] lineTotals = new double[roi.height];
// IJ.log("ROI rectangle: " + roi.toString());
for (int i = roi.y; i < roi.y + roi.height; i++) {
        double[] line = ip.getLine(roi.x, i, roi.x + roi.width,
            i);
        xs[i - roi.y] = i - roi.y;
        for (int j = 0; j < line.length; j++) {
                lineTotals[i - roi.y] += line[j];
        }
}

// Here we display a profile of the line totals in the current
    selection
// to enable choosing of a threshold value
Plot p = new Plot("Profile", "xPosition", "Grey value", xs,
    lineTotals);
final PlotWindow pw = p.show();
final Thread currentThread = Thread.currentThread();
pw.getCanvas().addMouseListener(new MouseAdapter() {

        public void mouseClicked(MouseEvent e) {
                int x = e.getX();
                int y = e.getY();
                int offscreenX = pw.getCanvas().offScreenX(x);
                int offscreenY = pw.getCanvas().offScreenY(y);
                // IJ.log("mousePressed: "+offscreenX+","+
                    offscreenY + " " + x + "," + y);
                currentThread.interrupt();
        }
});
pw.addWindowListener(new WindowAdapter() {

        public void windowClosing(WindowEvent e) {
                // IJ.log("Window Closing");
                currentThread.interrupt();
        }
});

try {
        while(!pw.isClosed()) {
                Thread.sleep(100);
        }
} catch (InterruptedException e) { }

if (pw.isClosed()) {
        return DONE;
}

// Here we ask for a threshold value and a number of edges to
    seek
double thresh = IJ.getNumber("Threshold value:", 5000);
if (thresh == IJ.CANCELED) {
        return DONE;
}
```

```
        double seek = IJ.getNumber("Number of edges to seek:", 3);
        if (seek == IJ.CANCELED) {
                return DONE;
        }
        threshold = Math.round(thresh);
        toSeek = Math.round(seek);
        pw.close();

        return DOES_8G + DOES_STACKS + ROI_REQUIRED;
}

// This method is run for each image in the image sequence
public void run(ImageProcessor ip) {
        Rectangle roi = ip.getRoi();

        double[] xs = new double[roi.height];
        double[] lineTotals = new double[roi.height];

        // sum the pixels for each line
        for (int i = roi.y; i < roi.y + roi.height; i++) {
                double[] line = ip.getLine(roi.x, i, roi.x + roi.width,
                    i);
                xs[i - roi.y] = i - roi.y;
                for (int j = 0; j < line.length; j++) {
                        lineTotals[i - roi.y] += line[j];
                }
        }

        // The following performs the peak recognition routine.
        // The index of the highest value in the totals array is chosen
            as a starting point.
        // This value is marked to be excluded from future searches.
        // The values either side of the maximum are then looked at. If
            they are higher than the threshold,
        // they are also excluded from future searches.
        // Eventually the algorithm hits the threshold value or the end
            of the selection above and below the maximum.
        // The algorithm is repeated for the next maximum until enough
            edges have been found
        Vector<PeakMatch> maxes = new Vector<PeakMatch>();
        double max = lineTotals[0];
        do {
                int maxIndex = 0;
                max = lineTotals[maxIndex];
                for (int i = 0; i < xs.length; i++) {
                        if (lineTotals[i] >= max) {
                                maxIndex = i;
                                max = lineTotals[i];
                        }
                }
                // IJ.log("Found a new local best: " + max);
                boolean searchLow = true;
                boolean searchHigh = true;
                int iLow = maxIndex;
                int iHigh = maxIndex;
                do {
                        if (searchLow) {
```

```
                        lineTotals[iLow] = 0;
                        iLow--;
                        if (iLow >= 0) {
                                if (lineTotals[iLow] < threshold
                                    ) {

                                        searchLow = false;
                                    // IJ.log("searchLow
                                        terminate at " +
                                        iLow + " " +
                                        lineTotals[iLow]);
                                } else {
                                    // IJ.log(" - searchLow
                                        continues at " +
                                        iLow + " " +
                                        lineTotals[iLow]);
                                }
                        } else {
                                searchLow = false;
                                // IJ.log("searchLow terminate
                                    at " + iLow);
                        }
                }
                if (searchHigh) {
                        lineTotals[iHigh] = 0;
                        iHigh++;
                        if (iHigh < lineTotals.length) {
                                if (lineTotals[iHigh] <
                                    threshold) {
                                        searchHigh = false;
                                        // IJ.log("searchHigh
                                        terminate at " +
                                        iHigh + " " +
                                        lineTotals[iHigh]);
                                } else {
                                        // IJ.log(" - searchHigh
                                         continues at " +
                                        iHigh + " " +
                                        lineTotals[iHigh]);
                                }
                        }
                        else {
                                searchHigh = false;
                                // IJ.log("searchHigh terminated
                                     at " + iHigh);
                        }
                }
        } while (searchLow || searchHigh);
        maxes.add(new PeakMatch(maxIndex, Math.round((float)max)
            , iHigh - iLow));
        //IJ.log("Found maximum " + max + " at index " +
            maxIndex + " got maxes: " + maxes.size());
} while(maxes.size() < toSeek);

IJ.log("Finished search");

int label = 1;
```

```
        int peakNum = 1;
        RoiManager roiMan = RoiManager.getInstance() == null ? new
            RoiManager() : RoiManager.getInstance();
        ResultsTable results = ResultsTable.getResultsTable();
        results.incrementCounter();
        Collections.sort(maxes, maxes.firstElement().indexComparator);
        imp.setSliceWithoutUpdate(ip.getSliceNumber());
        for (PeakMatch peak : maxes) {
                // IJ.log("" + xs[index.intValue()] + " " + lineTotals[
                    index.intValue()]);
                Roi l = new Line(roi.x, roi.y + peak.index, roi.x + roi.
                    width, roi.y + peak.index);
                roiMan.add(imp, l, label);
                label++;
                results.addValue("Peak " + peakNum + " index", peak.
                    index);
                //results.addValue("Peak " + peakNum + " intensity",
                    peak.maxValue);
                //results.addValue("Peak " + peakNum + " width", peak.
                    width);
                peakNum++;
        }
        results.show("Results");
}

private class PeakMatch {

        public int index;
        public int maxValue;
        public int width;

        public PeakMatch(int i, int v) {

                this.index = i;
                this.maxValue = v;
                this.width = 0;

        }

        public PeakMatch(int i, int v, int w) {
                this(i, v);
                this.width = w;
        }

        public final Comparator<PeakMatch> indexComparator = new
            Comparator<PeakMatch>() {

                public int compare(PeakMatch peak1, PeakMatch peak2) {

                        return peak1.index - peak2.index;

                }

        };

        public final Comparator<PeakMatch> valueComparator = new
            Comparator<PeakMatch>() {
```

```
                        public int compare(PeakMatch peak1, PeakMatch peak2) {

                                return peak1.maxValue - peak2.maxValue;

                        }

                };
        }

}
```

C.2 Seven_SegementDetector.java

```
import ij.*;
import ij.process.*;
import ij.gui.*;
import java.awt.*;
import ij.plugin.filter.*;
import java.awt.Rectangle;
import ij.plugin.frame.RoiManager;
import java.util.Vector;
import java.util.Arrays;
import java.util.*;
import ij.measure.ResultsTable;
import ij.gui.Overlay;
import ij.gui.Roi;

public class Seven_SegmentDetector2 implements PlugInFilter, ImageListener {
        ImagePlus imp;
        ResultsTable results;
        private final int defaultInsets = 15;
        private final double defaultThresh = 125.0;

        private int insets = defaultInsets;
        private double thresh = defaultThresh;
        private SSDigit digit;

        public void imageOpened(ImagePlus impOpen) { }
        public void imageClosed(ImagePlus impClose) {

                if (impClose == this.imp) {
                        ImagePlus.removeImageListener(this);
                }

        }

        public void imageUpdated(ImagePlus impUpdated) {

                if (impUpdated == this.imp) {
                        if (this.digit != null) {
                                overlayThresh(this.digit, this.currentThresh);
                        }
                }
```

```
}

private double currentThresh = defaultThresh;

GenericDialog threshChoose;
public int setup(String arg, ImagePlus imp) {
        this.imp = imp;
        ImagePlus.addImageListener(this);
        this.results = ResultsTable.getResultsTable();
        GenericDialog insetsChoose = new GenericDialog("Set digit inset
            length");
        insetsChoose.addNumericField("Inset length:", defaultInsets, 0);
        insetsChoose.addDialogListener(new DialogListener() {
                public boolean dialogItemChanged(GenericDialog gd,
                    AWTEvent e) {
                        int insets = (int)gd.getNextNumber();
                        if (gd.invalidNumber()) {
                                return false;
                        } else {
                                overlayInsets(insets);
                        }
                        return true;
                }
        });
        overlayInsets(insets);
        insetsChoose.showDialog();
        if (insetsChoose.wasCanceled()) {
                this.imp.getOverlay().clear();
                this.imp.repaintWindow();
                ImagePlus.removeImageListener(this);
                return DONE;
        }
        this.insets = (int)insetsChoose.getNextNumber();
        this.digit = new SSDigit(this.imp.getRoi().getBounds(), this.
            insets);

        // TODO: Live feedback on setting threshold value e.g.
            dynamically highlight detected segments
        threshChoose = new NonBlockingGenericDialog("Set digit threshold
            value");
        //Rectangle longSeg = digit.rectangles.get(1).getBounds();
        //int maxGrey = longSeg.width * longSeg.height * 255;
        threshChoose.addSlider("Threshold value:", 0.0, 255.0,
            defaultThresh);
        threshChoose.addDialogListener(new DialogListener() {
                public boolean dialogItemChanged(GenericDialog gd,
                    AWTEvent e) {
                        currentThresh = threshChoose.getNextNumber();
                        if(gd.invalidNumber()) {
                                return false;
                        } else {
                                overlayThresh(digit, currentThresh);
                        }
                        return true;
                }
        });
```

```
        overlayThresh(digit, thresh);
        threshChoose.showDialog();
        if (threshChoose.wasCanceled()) {
                this.imp.getOverlay().clear();
                this.imp.repaintWindow();
                ImagePlus.removeImageListener(this);
                return DONE;
        }
        this.thresh = currentThresh;
        //this.thresh = (int)IJ.getNumber("Threshold value:",
            defaultThresh);
        ImagePlus.removeImageListener(this);
        return DOES_8G + DOES_STACKS + NO_CHANGES + ROI_REQUIRED;
}

ImageProcessor ip;
public void run(ImageProcessor ip) {

        this.ip = ip;


        SSDigit myDigit = new SSDigit(ip.getRoi().getBounds(), this.
            insets);

        this.results.incrementCounter();
        String det = myDigit.detectDigit(ip, thresh);
        if (det == null) {
                results.addValue("value", Double.NaN);
        } else if (det == "␣") {
                IJ.log(ip.getSliceNumber() + ":␣No␣digit");
                results.addValue("value", 0.0);
        }else {
                results.addValue("value", Double.parseDouble(det));
        }
        results.show("Results");
        this.imp.getOverlay().clear();
        this.imp.repaintWindow();
}

private Overlay ov;
private void overlayInsets(int insets) {

        Rectangle currentBounds = this.imp.getRoi().getBounds();
        Rectangle insetBounds = (Rectangle)currentBounds.clone();
        insetBounds.grow(-insets, -insets);
        ov = new Overlay(new Roi(insetBounds));
        ov.setStrokeColor(Color.GREEN);
        this.imp.setOverlay(ov);

}

private final Color segmentColor = new Color(0.0f, 0.0f, 1.0f, 0.9f);

private void overlayThresh(SSDigit test, double thresh) {
        ImageProcessor ip = imp.getProcessor();
        for (Roi r: test.rectangles) {
                r.setStrokeColor(Color.BLUE);
```

```
                if (test.thresholdSegment(ip, r, thresh)) {
                        r.setFillColor(segmentColor);
                } else {
                        r.setFillColor(null);
                }
                ov.add(r);
                this.imp.setOverlay(ov);
        }

}

private class SSDigit {

        private Roi s1, s2, s3, s4, s5, s6, s7;
        public Vector<Roi> rectangles = new Vector<Roi>();

        public final Map<Integer, String> codeMap = new HashMap<Integer,
             String>() {{
                put(0, "␣");
                put(111111, "0");
                put(110, "1");
                put(1011011, "2");
                put(1001111, "3");
                put(1100110, "4");
                put(1101101, "5");
                put(1111101, "6");
                put(111, "7");
                put(1111111, "8");
                put(1101111, "9");
        }};

        public SSDigit(Rectangle digitBounds, int inset) {
                int hDigitWidth = digitBounds.width - 2 * inset;
                int vDigitHeight = (digitBounds.height - 3 * inset) / 2;

                // Digit coding:
                //          1
                //          _
                //       6 |_| 2        middle = 7
                //       5 |_| 3
                //
                //          4
                s1 = new Roi(new Rectangle(digitBounds.x + inset,
                                digitBounds.y,
                                        hDigitWidth, inset));
                s2 = new Roi(new Rectangle(digitBounds.x + hDigitWidth +
                     inset, digitBounds.y + inset,
                    inset,       vDigitHeight));
                s3 = new Roi(new Rectangle(digitBounds.x + hDigitWidth +
                     inset, digitBounds.y + vDigitHeight + 2*inset,
                    inset,       vDigitHeight));
                s4 = new Roi(new Rectangle(digitBounds.x + inset,
                                digitBounds.y + 2*vDigitHeight + 2*
                    inset, hDigitWidth, inset));
                s5 = new Roi(new Rectangle(digitBounds.x,
                                        digitBounds.y + vDigitHeight
                    + 2*inset,  inset,       vDigitHeight));
```

```
                s6 = new Roi(new Rectangle(digitBounds.x,
                                           digitBounds.y + inset,
                                       inset,       vDigitHeight));
                s7 = new Roi(new Rectangle(digitBounds.x + inset,
                                    digitBounds.y + vDigitHeight + inset,
                        hDigitWidth, inset));
                rectangles.addAll(Arrays.asList(new Roi[] {s1, s2, s3,
                    s4, s5, s6, s7}));
        }

        public void addToROIMan() {
                RoiManager roiMan = RoiManager.getInstance() == null ?
                    new RoiManager() : RoiManager.getInstance();
                roiMan.addRoi(s1);
                roiMan.addRoi(s2);
                roiMan.addRoi(s3);
                roiMan.addRoi(s4);
                roiMan.addRoi(s5);
                roiMan.addRoi(s6);
                roiMan.addRoi(s7);
        }

        public String detectDigit(ImageProcessor im, double threshold) {
                int digitVal = 1;
                int digitID = 0;
                for (Roi r : rectangles) {
                        //IJ.log(digitVal + ": " + total);
                        if (thresholdSegment(im, r, threshold)) digitID
                            += digitVal;
                        digitVal = digitVal * 10;
                }
                //IJ.log("" + digitID + "=" + codeMap.get(digitID));
                String ret = codeMap.get(digitID);
                if (ret == null) { IJ.log(im.getSliceNumber() + "=" +
                    digitID + "␣(not␣recognised)"); }
                return ret;
        }

        public boolean thresholdSegment(ImageProcessor im, Roi roi,
            double threshold) {
                Rectangle r = roi.getBounds();
                double area = r.width*r.height;
                double total = 0;
                for (int x = r.x; x < r.x + r.width; x++) {
                        for (int y = r.y; y < r.y + r.height; y++) {
                                total += im.getPixel(x, y);
                        }
                }
                return total/area < threshold;
        }

    }
}
```

Appendix D

Mathematical Treatment of the Schultz Distribution

The Schultz distribution is defined as:

$$G(\Gamma) = \frac{1}{\bar{\Gamma}} \frac{(z+1)^{z+1}}{z!} \left(\frac{\Gamma}{\bar{\Gamma}}\right)^{z} \exp\left[-\frac{\Gamma}{\bar{\Gamma}}(z+1)\right] \tag{D.1}$$

It is useful to be able to analytically calculate the nth moment about the mean $\langle(\Gamma - \bar{\Gamma})^n\rangle$. This quantity will be an nth order polynomial in the expectation of the nth power of Γ, e.g. for $n = 2$,

$$\langle(\Gamma - \bar{\Gamma})^2\rangle = \langle\Gamma^2\rangle - \bar{\Gamma}^2 \tag{D.2}$$

It is therefore useful to derive an expression for the expectation of the nth power of Γ for the Schultz distribution.

$$\langle\Gamma^n\rangle = \int_0^\infty \Gamma^n \frac{1}{\bar{\Gamma}} \frac{(z+1)^{z+1}}{z!} \left(\frac{\Gamma}{\bar{\Gamma}}\right)^{z} \exp\left(-\frac{(z+1)}{\bar{\Gamma}}\Gamma\right) d\Gamma \tag{D.3}$$

$$= \frac{1}{\bar{\Gamma}} \frac{(z+1)^{z+1}}{z!} \left(\frac{\Gamma}{\bar{\Gamma}}\right)^{z} \int_0^\infty \Gamma^{(n+z)} \exp\left(-\frac{(z+1)}{\bar{\Gamma}}\Gamma\right) d\Gamma \tag{D.4}$$

$$= \frac{1}{\bar{\Gamma}} \frac{(z+1)^{z+1}}{z!} \left(\frac{\Gamma}{\bar{\Gamma}}\right)^{z} (z+n)! \left(\frac{\bar{\Gamma}}{(z+1)}\right)^{z+n+1} \tag{D.5}$$

$$= \left(\frac{\bar{\Gamma}}{(z+1)}\right)^{n} \prod_{i=1} n(z+i) \tag{D.6}$$

Noting that $\sigma^2 = \langle(\Gamma - \bar{\Gamma})^2\rangle = \bar{\Gamma}^2/(z+1)$:

$$= \frac{1}{\bar{\Gamma}^n}\sigma^{2n}\prod_{i=0}^{n-1}\left(\frac{\bar{\Gamma}^2}{\sigma^2} + i\right) \tag{D.7}$$

Bibliography

[1] Abramoff, M. D., P. Magalhaes, and S. Ram. "Image Processing with ImageJ." *Biophotonics International* 11, 7: (2004) 36–42.

[2] Abrusci, A., I. Ding, M. Al-Hashimi, T. Segal-Peretz, M. D. McGehee, M. Heeney, G. L. Frey, and H. J. Snaith. "Facile infiltration of semiconducting polymer into mesoporous electrodes for hybrid solar cells." *Energy & Environmental Science* 4, 8: (2011) 3051. http://pubs.rsc.org.ezproxy.webfeat.lib.ed.ac.uk/en/Content/ArticleLanding/2011/EE/c1ee01135a.

[3] Adda-Bedia, M., and M. Amar. "Fracture Spacing in Layered Materials." *Physical Review Letters* 86, 25: (2001) 5703–5706. http://link.aps.org/doi/10.1103/PhysRevLett.86.5703.

[4] Allain, C., M. Cloitre, and M. Wafra. "Aggregation and Sedimentation in Colloidal Suspensions." *Phys. Rev. Lett.* 74, 8: (1995) 1478–1481.

[5] Allain, C., and L. Limat. "Regular patterns of cracks formed by directional drying of a colloidal suspension." *Physical Review Letters* 74: (1995) 2981–2985.

[6] American Society for Testing and Materials. "ASTM G173-03 Tables: Extraterrestrial Spectrum, Terrestrial Global 37 deg South Facing Tilt & Direct Normal + Circumsolar." published by the ASTM at http://www.astm.org, available for free at the following URL., . http://rredc.nrel.gov/solar/spectra/am1.5/. Relevant ISO standard: ISO 9845-1, 1992.

[7] Annica Andersson, Nicklas Johansson, Per Bröms, Nu Yu, Donald Lupo, and William R. Salaneck. "Fluorine Tin Oxide as an Alternative to Indium Tin Oxide in Polymer LEDs." *Advanced Materials* 10, 11: (1998) 859–863. http://dx.doi.org/10.1002/(SICI)1521-4095(199808)10:11<859::AID-ADMA859>3.0.CO;2-1.

[8] Archer, M. D., and A. J. Nozik. *Nanostructured And Photoelectrochemical Systems For Solar Photon Conversion*, volume 3 of *Series On Photoconversion Of Solar Energy*. Imperial College Press, 2008, 1st edition. http://www.worldscibooks.com/chemistry/p217.html.

[9] Bai, T., D. D. Pollard, and H. Gao. "Explanation for fracture spacing in layered materials." *Nature* 403, 6771: (2000) 753–6. http://www.ncbi.nlm.nih.gov/pubmed/10693800.

[10] Barnard, A. S., and L. A. Curtiss. "Prediction of TiO_2 Nanoparticle Phase and Shape Transitions Controlled by Surface Chemistry." *Nano Letters* 5, 7: (2005) 1261–1266. http://dx.doi.org/10.1021/nl050355m.

[11] Bevington, P. R., and D. K. Robinson. *Data reduction and error analysis for the physical sciences.* McGraw-Hill, 2003.

[12] Bohn, S., B. Andreotti, S. Douady, J. Munzinger, and Y. Couder. "Constitutive property of the local organization of leaf venation networks." *Physical Review E* 65, 6: (2002) 1–12. http://link.aps.org/doi/10.1103/PhysRevE.65.061914.

[13] Bohn, S., S. Douady, and Y. Couder. "Four Sided Domains in Hierarchical Space Dividing Patterns." *Physical Review Letters* 94, 5: (2005) 3–6. http://link.aps.org/doi/10.1103/PhysRevLett.94.054503.

[14] Bohn, S., L. Pauchard, and Y. Couder. "Hierarchical crack pattern as formed by successive domain divisions." *Physical Review E* 71, 4: (2005) 1–7. http://link.aps.org/doi/10.1103/PhysRevE.71.046214.

[15] Bohn, S., J. Platkiewicz, B. Andreotti, M. Adda-Bedia, and Y. Couder. "Hierarchical crack pattern as formed by successive domain divisions. II. From disordered to deterministic behavior." *Physical Review E* 71, 4: (2005) 1–7. http://link.aps.org/doi/10.1103/PhysRevE.71.046215.

[16] Bouclé, J., S. Chyla, M. Shaffer, J. Durrant, D. Bradley, and J. Nelson. "Hybrid bulk heterojunction solar cells based on blends of TiO_2 nanorods and P3HT." *Comptes Rendus Physique* 9, 1: (2008) 110–118. http://linkinghub.elsevier.com/retrieve/pii/S1631070507002502.

[17] Bouclé, J., and J. Ackermann. "Solid-state dye-sensitized and bulk heterojunction solar cells using TiO_2 and ZnO nanostructures: recent progress and new concepts at the borderline." *Polymer International* 61, 3: (2011) 355–373. http://onlinelibrary.wiley.com.ezproxy.webfeat.lib.ed.ac.uk/doi/10.1002/pi.3157/abstract.

[18] Bradshaw, G., and A. Hughes. "Etching methods for indium oxide/tin oxide films." *Thin Solid Films* 33, 2: (1976) L5 – L8. http://www.sciencedirect.com/science/article/B6TW0-46J3KJX-CD/2/4df47629e98d3e062f6db08408d678a0.

[19] Burns, J. L., Y.-d. Yan, G. J. Jameson, and S. Biggs. "A Light Scattering Study of the Fractal Aggregation Behavior of a Model Colloidal System." *Langmuir* 13, 24: (1997) 6413–6420. http://pubs.acs.org/doi/abs/10.1021/la970303f.

[20] Buscall, R. "The sedimentation of concentrated colloidal suspensions." *Colloids and Surfaces* 43, 1: (1990) 33–53. http://linkinghub.elsevier.com/retrieve/pii/016666229080002L.

[21] ———. "The rheology of concentrated dispersions of weakly attracting colloidal particles with and without wall slip." *Journal of Rheology* 37, 4: (1993) 621. http://link.aip.org/link/?JOR/37/621/1\&Agg=doi.

[22] ———. "Letter to the Editor: Wall slip in dispersion rheometry." *Journal of Rheology* 54, 6: (2010) 1177. http://journalofrheology.org/resource/1/jorhd2/v54/i6/p1177_s1?view=fulltext.

[23] Buscall, R., and L. R. White. "The consolidation of concentrated suspensions. Part 1. The theory of sedimentation." *Journal of the Chemical Society, Faraday Transactions 1* 83, 3: (1987) 873. http://xlink.rsc.org/?DOI=f19878300873.

[24] Buxton, G. A., and N. Clarke. "Predicting structure and property relations in polymeric photovoltaic devices." *Physical Review B* 74, 8: (2006) 085,207. http://link.aps.org/doi/10.1103/PhysRevB.74.085207.

[25] Chen, D., and M. Doi. "Simulation of aggregating colloids in shear flow. II." *Journal of Chemical Physics* 91, 4: (1989) 2656–2663.

[26] Coakley, K., Y. Liu, M. McGehee, K. Frindell, and G. Stucky. "Infiltrating Semiconducting Polymers into Self-Assembled Mesoporous Titania Films for Photovoltaic Applications." *Adv. Funct. Mater.* 13, 4: (2003) 301–306. http://dx.doi.org/10.1002/adfm.200304361.

[27] Comings, E., and T. Sherwood. "The Drying of Solids. VII Moisture Movement by Capillarity in Drying Granular Materials." *Industrial Engineering Chemistry* 26, 10: (1934) 1096–1098.

[28] Coussot, P., Q. D. Nguyen, H. T. Huynh, and D. Bonn. "Viscosity bifurcation in thixotropic, yielding fluids." *Journal of Rheology* 46, 3: (2002) 573. http://link.aip.org/link/JORHD2/v46/i3/p573/s1\&Agg=doi.

[29] Cramer, H. *Mathematical Methods of Statistics (PMS-9).* Princeton University Press, 1946.

[30] Derjaguin, B., and L. Landau. "Theory of the stability of strongly charged lyophobic sols and of the adhesion of strongly charged particles in solutions of electrolytes." *Acta Physico Chemica URSS* 14: (1941) 633.

[31] Dhont, J. *An Introduction to Dynamics of Colloids.* Elsevier, 1996.

[32] Domingos, R. F., M. a. Baalousha, Y. Ju-Nam, M. M. Reid, N. Tufenkji, J. R. Lead, G. G. Leppard, and K. J. Wilkinson. "Characterizing manufactured nanoparticles in the environment: multimethod

determination of particle sizes." *Environmental science & technology* 43, 19: (2009) 7277–84. http://www.ncbi.nlm.nih.gov/pubmed/19848134.

[33] Dufresne, E., E. Corwin, N. Greenblatt, J. Ashmore, D. Wang, a. Dinsmore, J. Cheng, X. Xie, J. Hutchinson, and D. Weitz. "Flow and Fracture in Drying Nanoparticle Suspensions." *Physical Review Letters* 91, 22: (2003) 1–4. http://link.aps.org/doi/10.1103/PhysRevLett.91.224501.

[34] Dufresne, E. R., D. J. Stark, N. A. Greenblatt, J. X. Cheng, J. W. Hutchinson, L. Mahadevan, and D. A. Weitz. "Dynamics of fracture in drying suspensions." *Langmuir : the ACS journal of surfaces and colloids* 22, 17: (2006) 7144–7. http://www.ncbi.nlm.nih.gov/pubmed/16893207.

[35] Dzyaloshinskii, I. E., E. M. Lifshitz, and L. P. Pitaevskii. "General Theory of van der Waals' Forces." *Soviet Physics Uspekhi* 4, 2: (1961) 153–176. http://iopscience.iop.org/PU1961v004n02ABEH003330.

[36] Fisher, R., S. Perkins, A. Walker, and E. Wolfart. "Hypermedia Image Processing Reference." URL, 2012. http://homepages.inf.ed.ac.uk/rbf/HIPR2.

[37] Fitzgibbons, E. T., K. J. Sladek, and W. H. Hartwig. "TiO_2 Film Properties as a Function of Processing Temperature." *Journal of The Electrochemical Society* 119, 6: (1972) 735–739. http://link.aip.org/link/?JES/119/735/1.

[38] Frisken, B. J. "Revisiting the Method of Cumulants for the Analysis of Dynamic Light-Scattering Data." *Applied Optics* 40, 24: (2001) 4087. http://www.opticsinfobase.org/ao/abstract.cfm?uri=AO-40-24-4087.

[39] Gisler, T., R. Ball, and D. Weitz. "Strain Hardening of Fractal Colloidal Gels." *Physical Review Letters* 82, 5: (1999) 1064–1067. http://link.aps.org/doi/10.1103/PhysRevLett.82.1064.

[40] Goehring, L., W. J. Clegg, and A. F. Routh. "Wavy cracks in drying colloidal films." *Soft Matter* 7, 2: (2011) 7984–7987. http://xlink.rsc.org/?DOI=c1sm05979c.

[41] Grätzel, M. "Photoelectrochemical cells." *Nature* 414, 6861: (2001) 338–44. http://www.ncbi.nlm.nih.gov/pubmed/11713540.

[42] Green, M. A., K. Emery, Y. Hishikawa, W. Warta, and E. D. Dunlop. "Solar cell efficiency tables (version 39)." *Progress in Photovoltaics: Research and Applications* 20, 1: (2012) 12–20. http://onlinelibrary.wiley.com/doi/10.1002/pip.2163/abstract.

[43] Guijarro, N., T. Lana Villarreal, I. Mora Seró, J. Bisquert, and R. Gómez. "CdSe Quantum Dot-Sensitized TiO2 Electrodes: Effect of Quantum Dot

Coverage and Mode of Attachment." *The Journal of Physical Chemistry C* 113, 10: (2009) 4208–4214. http://dx.doi.org/10.1021/jp808091d.

[44] Guinier, A., and G. Fournet. *Small-Angle Scattering of X-Rays*. Chapman and Hall, Ltd., London, 1955.

[45] Guo, J. J., and J. A. Lewis. "Aggregation Effects on the Compressive Flow Properties and Drying Behavior of Colloidal Silica Suspensions." *Journal of the American Ceramic Society* 82, 9: (1999) 2345–2358. http://doi.wiley.com/10.1111/j.1151-2916.1999.tb02090.x.

[46] Hassan, P., and S. Kulshreshtha. "Modification to the cumulant analysis of polydispersity in quasielastic light scattering data." *Journal of Colloid and Interface Science* 300, 2: (2006) 744–748. http://linkinghub.elsevier.com/retrieve/pii/S0021979706002980.

[47] Hillhouse, H., and M. Beard. "Solar cells from colloidal nanocrystals: Fundamentals, materials, devices, and economics." *Current Opinion in Colloid & Interface Science* .

[48] Huh, J. Y., M. L. Lynch, and E. M. Furst. "Poroelastic Consolidation in the Phase Separation of Vesicle-Polymer Suspensions." *Industrial & Engineering Chemistry Research* 50, 1: (2011) 78–84. http://pubs.acs.org/doi/abs/10.1021/ie1004543.

[49] Hunter, R. J. *Foundations of Colloid Science*. Oxford University Press, USA, 1992, 1 edition.

[50] Hyun, B.-R., Y.-W. Zhong, A. C. Bartnik, L. Sun, H. D. Abru na, F. W. Wise, J. D. Goodreau, J. R. Matthews, T. M. Leslie, and N. F. Borrelli. "Electron Injection from Colloidal PbS Quantum Dots into Titanium Dioxide Nanoparticles." *ACS Nano* 2, 11: (2008) 2206–2212. http://dx.doi.org/10.1021/nn800336b.

[51] ISO - International Organization for Standardization. "ISO 22412:2008 Particle size analysis – Dynamic light scattering (DLS).", . http://www.iso.org/iso/iso_catalogue/catalogue_tc/catalogue_detail.htm?csnumber=40942.

[52] Israelachvili, J. N. *Intermolecular and Surface Forces*. Academic Press, 1992.

[53] James, F., and M. Roos. "Minuit: A System for Function Minimization and Analysis of the Parameter Errors and Correlations." *Computer Physics Communications* 10: (1975) 343. http://inspirehep.net/record/101965. DOI:10.1016/0010-4655(75)90039-9.

[54] Jankowski, E., and S. C. Glotzer. "Screening and designing patchy particles for optimized self-assembly propensity through assembly pathway engineering." *Soft Matter* 8, 10: (2012) 2852. http://pubs.rsc.org/en/Content/ArticleLanding/2012/SM/c2sm07101k.

[55] Jiang, J., G. Oberdorster, and P. Biswas. "Characterization of size, surface charge, and agglomeration state of nanoparticle dispersions for toxicological studies." *Journal of Nanoparticle Research* 11, 1: (2009) 77–89.

[56] Jones, E., T. Oliphant, P. Peterson, and others. "SciPy: Open Source Scientific Tools for Python.", 2001. http://www.scipy.org/.

[57] Jones, R. A. L. *Soft Condensed Matter*. Oxford University Press, 2002.

[58] Karthikeyan, C. S., and M. Thelakkat. "Key aspects of individual layers in solid-state dye-sensitized solar cells and novel concepts to improve their performance." *Inoranica Chimica Acta* 361, 3: (2008) 635–655.

[59] Kätzel, U., M. Vorbau, M. Stintz, T. Gottschalk-Gaudig, and H. Barthel. "Dynamic Light Scattering for the Characterization of Polydisperse Fractal Systems: II. Relation between Structure and DLS Results." *Particle & Particle Systems Characterization* 25, 1: (2008) 19–30. http://doi.wiley.com/10.1002/ppsc.200700005.

[60] Ladislav Kavan, and Michael Grätzel. "Highly efficient semiconducting TiO2 photoelectrodes prepared by aerosol pyrolysis." *Electrochimica Acta* 40, 5: (1995) 643 – 652. http://www.sciencedirect.com/science/article/B6TG0-3YS8BCM-BN/2/89496164b93b3399823d76f6c3d0e3bf.

[61] Kim, A. Y., and J. C. Berg. "Fractal Aggregation: Scaling of Fractal Dimension with Stability Ratio." *Langmuir* 16, 5: (2000) 2101–2104. http://pubs.acs.org/doi/abs/10.1021/la990841n.

[62] Kosmulski, M. "The significance of the difference in the point of zero charge between rutile and anatase." *Advances in Colloid and Interface Science* 99, 3: (2002) 255–264.

[63] Kotlarchyk, M., R. B. Stephens, and J. S. Huang. "Study of Schultz distribution to model polydispersity of microemulsion droplets." *The Journal of Physical Chemistry* 92, 6: (1988) 1533–1538. http://dx.doi.org/10.1021/j100317a032.

[64] Krebs, F. C., T. Tromholt, and M. Jørgensen. "Upscaling of polymer solar cell fabrication using full roll-to-roll processing." *Nanoscale* 2, 6: (2010) 873. http://pubs.rsc.org.ezproxy.webfeat.lib.ed.ac.uk/en/Content/ArticleLanding/2010/NR/b9nr00430k.

[65] Kwong, C. Y., W. C. H. Choy, A. B. Djurišić, P. C. Chui, K. W. Cheng, and W. K. Chan. "Poly(3-hexylthiophene):TiO_2 nanocomposites for solar cell applications." *Nanotechnology* 15, 9: (2004) 1156. http://stacks.iop.org/0957-4484/15/i=9/a=008.

[66] Kenneth L. Hardee, and Allen J. Bard. "Semiconductor Electrodes." *Journal of The Electrochemical Society* 122, 6: (1975) 739–742. http://link.aip.org/link/?JES/122/739/1.

[67] Larson, R. G. *The Structure and Rheology of Complex Fluids (Topics in Chemical Engineering)*. OUP USA, 1999. http://www.amazon.co.uk/Structure-Rheology-Complex-Chemical-Engineering/dp/019512197X.

[68] Lattuada, M., H. Wu, and M. Morbidelli. "Estimation of fractal dimension of colloidal gels in the presence of multiple scattering." *Physical review. E, Statistical, nonlinear, and soft matter physics* 64, 6 Pt 1: (2001) 061,404. http://www.ncbi.nlm.nih.gov/pubmed/11736182.

[69] Lawn, B. *Fracture of Brittle Solids*. Cambridge: Cambridge University Press, 1993, 2nd ed. edition. http://ebooks.cambridge.org.ezproxy.webfeat.lib.ed.ac.uk/ebook.jsf?bid=CBO9780511623127\# http://ebooks.cambridge.org/ref/id/CBO9780511623127.

[70] Lazarus, V., and L. Pauchard. "From craquelures to spiral crack patterns: influence of layer thickness on the crack patterns induced by desiccation." *Soft Matter* 7, 6: (2011) 2552. http://xlink.rsc.org/?DOI=c0sm00900h.

[71] Lewis, J. A. "Colloidal Processing of Ceramics." *Journal of the American Ceramic Society* 83, 10: (2000) 2341–2359.

[72] Lide, D. R. *CRC Handbook of Chemistry and Physics*. CRC Press, 2008, 89th edition.

[73] Macosko, C. W. *Rheology: Principles, Measurements, and Applications (Advances in Interfacial Engineering)*. Wiley-VCH, 1994. http://www.amazon.com/Rheology-Measurements-Applications-Interfacial-Engineering/dp/0471185752.

[74] Moneta, L. "pyminuit – Minuit numerical function minimization in Python." hosted on Google Code, . http://code.google.com/p/pyminuit/.

[75] Nazeeruddin, M. K., E. Baranoff, and M. Grätzel. "Dye-sensitized solar cells: A brief overview." *Solar Energy* 85, 6: (2011) 1172–1178. http://www.sciencedirect.com/science/article/pii/S0038092X11000351.

[76] Jenny Nelson. *The Physics of Solar Cells*. Imperial College Press, 2003, 1st edition.

[77] Oosterhout, S. D., M. M. Wienk, S. S. v. Bavel, R. Thiedmann, L. J. A. Koster, J. Gilot, J. Loos, V. Schmidt, and R. A. J. Janssen. "The effect of three-dimensional morphology on the efficiency of hybrid polymer solar cells." *Nature Materials* 8, 10: (2009) 818–824. http://www.nature.com.ezproxy.webfeat.lib.ed.ac.uk/nmat/journal/v8/n10/abs/nmat2533.html.

[78] O'Regan, B., and M. Gratzel. "A Low-Cost, High-Efficiency Solar-Cell Based On Dye-Sensitized Colloidal Tio2 Films." *Nature* 353, 6346: (1991) 737–740.

[79] Bin Peng, Gert Jungmann, Claus Jäger, Dietrich Haarer, Hans-Werner Schmidt, and Mukundan Thelakkat. "Systematic investigation of the role of compact TiO_2 layer in solid state dye-sensitized TiO2 solar cells." *Coordination Chemistry Reviews* 248, 13-14: (2004) 1479 – 1489. http://www.sciencedirect.com/science/article/B6TFW-4CPD7RB-1/2/78cdbc4f6f3d93aa9be6e9a872f1dc89. Michael Graetzel Festschrift, a tribute for his 60th Birthday, Dye Sensitized Solar Cells.

[80] Penn, R., and J. F. Banfield. "Morphology development and crystal growth in nanocrystalline aggregates under hydrothermal conditions: insights from titania." *Geochimica et Cosmochimica Acta* 63, 10: (1999) 1549–1557. http://www.sciencedirect.com/science/article/pii/S001670379900037X.

[81] Perez, F., and B. E. Granger. "IPython: A System for Interactive Scientific Computing." *Computing in Science & Engineering* 9, 3: (2007) 21–29. http://ipython.org/citing.html.

[82] Poon, W. C. K., E. R. Weeks, and C. P. Royall. "On measuring colloidal volume fractions." *Soft Matter* 8, 1: (2012) 21. http://pubs.rsc.org/en/content/articlehtml/2012/sm/c1sm06083j.

[83] Pusey, P. N. "Static and Dynamic Light Scattering." In *5th European Summer School on "Scattering Methods Applied to Soft Condensed Matter"*. Vacation centre "Les Bruyeres", Carcans-Maubuisson, 2000.

[84] Pusey, P. N., D. E. Koppel, D. E. Schaefer, R. D. Camerini-Otero, and S. H. Koenig. "Intensity fluctuation spectroscopy of laser light scattered by solutions of spherical viruses. R17, Q.beta., BSV, PM2, and T7. I. Light-scattering technique." *Biochemistry* 13, 5: (1974) 952–960. http://dx.doi.org/10.1021/bi00702a020.

[85] Python Software Foundation. "Python 2.6.6.", 2002–2012. http://www.python.org.

[86] Qian, J., Q. Liu, G. Li, K. Jiang, L. Yang, and Y. Song. "P3HT as hole transport material and assistant light absorber in CdS quantum dots-sensitized solid-state solar cells." *Chemical Communications* 47, 22: (2011) 6461. http://pubs.rsc.org.ezproxy.webfeat.lib.ed.ac.uk/en/Content/ArticleLanding/2011/CC/c1cc11595b.

[87] Royall, C. P., R. v. Roij, and A. v. Blaaderen. "Extended sedimentation profiles in charged colloids: the gravitational length, entropy, and electrostatics." *Journal of Physics: Condensed Matter* 17, 15: (2005) 2315–2326. http://iopscience.iop.org/0953-8984/17/15/005.

[88] Rueb, C. J., and C. F. Zukoski. "Viscoelastic properties of colloidal gels." *Journal of Rheology* 41, 2: (1997) 197. http://link.aip.org/link/?JOR/41/197/1\&Agg=doi.

[89] Russel, W. B. "Mechanics of drying colloidal dispersions: Fluid/solid transitions, skinning, crystallization, cracking, and peeling." *AIChE Journal* 57, 6: (2011) 1378–1385. http://doi.wiley.com/10.1002/aic.12651.

[90] Saunders, B. R., and M. L. Turner. "Nanoparticle-polymer photovoltaic cells." *Adv. Colloid Interface Sci.* 138, 1: (2008) 1–23.

[91] Saunders, B. R. "Hybrid polymer/nanoparticle solar cells: Preparation, principles and challenges." *Journal of Colloid and Interface Science* 369, 1: (2012) 1–15. http://www.sciencedirect.com/science/article/pii/S0021979711015050.

[92] Scharber, M. C., D. Mühlbacher, M. Koppe, P. Denk, C. Waldauf, A. J. Heeger, and C. J. Brabec. "Design Rules for Donors in Bulk-Heterojunction Solar Cells - Towards 10 % Energy-Conversion Efficiency." *Advanced Materials* 18, 6: (2006) 789–794.

[93] Shorlin, K. a., J. R. de Bruyn, M. Graham, and S. W. Morris. "Development and geometry of isotropic and directional shrinkage-crack patterns." *Physical review. E, Statistical physics, plasmas, fluids, and related interdisciplinary topics* 61, 6 Pt B: (2000) 6950–7. http://www.ncbi.nlm.nih.gov/pubmed/11088387.

[94] Silbert, L. E., J. R. Melrose, and R. C. Ball. "The rheology and microstructure of concentrated, aggregated colloids." *Journal of Rheology* 43, 3: (1999) 673. http://link.aip.org/link/doi/10.1122/1.551028/html http://link.aip.org/link/JORHD2/v43/i3/p673/s1\&Agg=doi.

[95] Smestad, G. P., F. C. Krebs, C. M. Lampert, C. G. Granqvist, K. Chopra, X. Mathew, and H. Takakura. "Reporting solar cell efficiencies in Solar Energy Materials and Solar Cells." *Solar Energy Materials and Solar Cells* 92, 4: (2008) 371–373. http://www.sciencedirect.com/science/article/pii/S0927024808000093.

[96] Snaith, H. J., and L. Schmidt Mende. "Advances in Liquid-Electrolyte and Solid-State Dye-Sensitized Solar Cells." *Advanced Materials* 19, 20: (2007) 3187–3200. http://dx.doi.org/10.1002/adma.200602903.

[97] Snaith, H. J. "How should you measure your excitonic solar cells?" *Energy & Environmental Science* 5, 4: (2012) 6513–6520. http://pubs.rsc.org.ezproxy.webfeat.lib.ed.ac.uk/en/content/articlelanding/2012/ee/c2ee03429h.

[98] Snaith, H. J., A. J. Moule, C. Klein, K. Meerholz, R. H. Friend, and M. Gratzel. "Efficiency Enhancements in Solid-State Hybrid Solar Cells via Reduced Charge Recombination and Increased Light Capture." *Nano Letters* 7, 11: (2007) 3372–3376. http://pubs.acs.org/doi/abs/10.1021/nl071656u.

[99] Snaith, H., and L. Schmidt-Mende. "Advances in Liquid-Electrolyte and Solid-State Dye-Sensitized Solar Cells." *Advanced Materials* 19, 20: (2007) 3187–3200. http://doi.wiley.com/10.1002/adma.200602903.

[100] Starrs, L., W. C. K. Poon, D. J. Hibberd, and M. M. Robins. "Collapse of transient gels in colloid-polymer mixtures." *Journal of Physics: Condensed Matter* 14, 10: (2002) 2485–2505. http://stacks.iop.org/0953-8984/14/i=10/a=302?key=crossref.a765e9123d93636de32c03c9238f0050.

[101] Stevens, N., C. I. Priest, R. Sedev, and J. Ralston. "Wettability of Photoresponsive Titanium Dioxide Surfaces." *Langmuir* 19, 8: (2003) 3272–3275. http://dx.doi.org/10.1021/la020660c.

[102] Tang, C. "Multilayer organic photovoltaic elements." US Patent 4,164,431, 1979.

[103] Tang, H., K. Prasad, R. Sanjines, P. Schmid, and F. Levy. "Electrical and Optical-Properties of TiO_2 Anatase Thin-Films." *Journal of Applied Physics* 75, 4: (1994) 2042–2047.

[104] Thévenaz, P., and M. Unser. "User-Friendly Semiautomated Assembly of Accurate Image Mosaics in Microscopy." *Microscopy Research and Technique* 70, 2: (2007) 135–146.

[105] Verduin, H., B. J. de Gans, and J. K. G. Dhont. "Shear Induced Structural Changes in a Gel-Forming Suspension Studied by Light Scattering and Rheology." *Langmuir* 12, 12: (1996) 2947–2955. http://pubs.acs.org/doi/abs/10.1021/la951504r.

[106] Verwey, E. J. W., and J. T. G. Overbeek. *Theory of the stability of lyophobic colloids*. Elsevier, 1948.

[107] Wang, M., and X. Wang. "P3HT/TiO2 bulk-heterojunction solar cell sensitized by a perylene derivative." *Solar Energy Materials and Solar Cells* 91, 19: (2007) 1782–1787. http://www.sciencedirect.com/science/article/pii/S0927024807002371.

[108] Weickert, J., R. B. Dunbar, H. C. Hesse, W. Wiedemann, and L. Schmidt-Mende. "Nanostructured Organic and Hybrid Solar Cells." *Advanced Materials* 23, 16: (2011) 1810–1828. http://onlinelibrary.wiley.com/doi/10.1002/adma.201003991/abstract.

[109] Wessel, R., and R. C. Ball. "Fractal aggregates and gels in shear flow." *Physical Review A* 46, 6: (1992) R3008–R3011.

[110] Zaccarelli, E. "Colloidal gels: equilibrium and non-equilibrium routes." *Journal of Physics: Condensed Matter* 19, 32: (2007) 323,101 (50pp). http://stacks.iop.org/0953-8984/19/323101.